3-24-2016

Enhanced Flow Migration in Full Annular Ultra Compact Combustor

Nicholas A. Gilbert

ENHANCED FLOW MIGRATION IN FULL ANNULAR ULTRA COMPACT COMBUSTOR

THESIS

Nicholas A. Gilbert, Captain, USAF

AFIT-ENY-MS-16-M-211

DEPARTMENT OF THE AIR FORCE
AIR UNIVERSITY

AIR FORCE INSTITUTE OF TECHNOLOGY

Wright-Patterson Air Force Base, Ohio

AFIT-ENY-MS-16-M-211

ENHANCED FLOW MIGRATION IN FULL ANNULAR ULTRA COMPACT COMBUSTOR

THESIS

Presented to the Faculty

Department of Engineering Physics

Graduate School of Engineering and Management

Air Force Institute of Technology

Air University

Air Education and Training Command

in Partial Fulfillment of the Requirements for the

Degree of Master of Science

Nicholas A. Gilbert, BS

Captain, USAF

March 2016

AFIT-ENY-MS-16-M-211

ENHANCED FLOW MIGRATION IN A FULL ANNULAR ULTRA COMPACT COMBUSTOR

Nicholas A. Gilbert, BS
Captain, USAF

Committee Membership:

Marc D. Polanka, PhD
Chair

Mark F. Reeder, PhD
Member

Andrew W. Caswell, PhD
Member

Abstract

Since combustion efficiency in modern jet engines has stabilized, attention has turned to improving the combustor by improving the thrust-to-weight ratio. The Ultra Compact Combustor (UCC) is a means to reduce the weight of the combustor while ensuring exhaust meets increasingly stringent government emission standards. Combustion occurs within the UCC under a g-load in the circumferential direction, which maintains combustion efficiency while decreasing axial combustor length. Previous analysis optimized the combustion chamber flame characteristics with a common upstream air source. Previously, issues for the UCC were inspired by integration into a traditional axial turbojet. The focus of this investigation was to increase migration of the hot combustion products to the middle of the hybrid vane's exit plane. This was done by varying the dimensions of the UCC combustion cavity, the air driver configuration into the cavity, as well as adding a radial vane cavity into the center-body guide vanes. In order to accomplish this, a temperature measurement collection technique called thin filament pyrometry was implemented to obtain high fidelity data. Also, the AFIT UCC required an accurate initial emissions baseline to be established; this baseline consisted of collecting five different gaseous species for each considered geometry. The temperature profile within the primary zone and exit plane, as well as the emissions data were then compared against each other and previously collected temperature values. From these comparisons, a geometric configuration that shifted the air more into the outer diameter and incorporated a radial vane cavity in the hybrid vane center-body was found to offer the greatest improvement in exit temperature profiles and efficiency.

Acknowledgments

This thesis was made possible by the contributions and assistance of many individuals that enabled my success. This thesis was a group effort and their work allowed me to do my best. I'd like to first thank the AFIT Machine Shop personnel. Their work was always impeccable, on-time, and showed the great pride they take in their job. Their willingness to discuss all my rough ideas, fix my crude SolidWork drawings, interpret what I really wanted from my parts, and the overtime they worked to get the RVC component and Compound Drivers delivered early ensured that I made all of my deadlines. Without these three gentlemen, my thesis would have been sunk. Similarly, the ENY lab tech team were always willing to help the COAL Lab get work done and accommodate our unique facilities. At multiple times they dropped everything to help me troubleshoot a problem, update our documentation, assemble a part, or get the right tool.

The contractors at ISSI also provided their expertise and assistance to me during this project. I would like to thank Dr. Larry Goss and Corey Goss on helping the COAL Lab restart PIV measurements, as well as helping the COAL Lab with the initial equipment start-up of thin filament pyrometry data. Without their support and their help post processing the data, we would not have been able to acquire such accurate readings for the temperature profiles. Also, other personnel within ISSI was instrumental in diagnosing the different issues with the CAI Emissions Analyzer, and providing procedures to troubleshoot the device. Other members of ISSI working at AFRL/RQT also pointed out the published sources to ensure correct error analysis for the emissions indices. Also, the personnel of AFRL/RQTC were very supportive in the designs of the new multi-channel emissions probe, providing drawings for the previous

version and guidance on necessary construction requirements, as well as keeping up communication and collaboration with the AFIT COAL Lab.

At AFIT, I would like to thank my advisor for advising me throughout this process and ensuring that I had the data I needed to graduate. His patience with my learning curve and sarcasm were greatly appreciated. I also would like to thank the PHD student who worked with me during my time in the COAL Lab for all his help in training me with the UCC operations, bouncing ideas off me, and just being around to vent to on occasion. His friendship, advice, and CFD were instrumental to my understanding of the UCC and sanity. I want to thank the "Group of 9" that formed in Turbulence and assisted each other throughout this eighteen months. Their thoughtful feedback and discussion greatly improved my thinking and the quality of this thesis. Finally, my mustached 2Lt compadre in the COAL Lab was instrumental in testing the UCC, coming in during the weekend and late hours of the week, and occasionally allowing me the use of the 9/16 inch combination wrench.

Finally, I would like to thank the most important person to this endeavor: my wife. Her constant support, sympathy, dinner making, patience, flexibility, and unleashing her supreme grammar correction skills on all my long papers. Not many spouses are willing to wake up at 0800 on a weekend and sit in a lab while their husband works, much less sacrifice two different anniversaries to Finals. She is the perfect complement for me, and I hope that I will begin to repay all the help she has given me these last 18 months, and I love her with all my heart.

Table of Contents

List of Figures

APPENDIX FIGURES Page

List of Tables

TABLE Page

Nomenclature

AFIT	Air Force Institute of Technology
AFRL	Air Force Research Laboratory
APCRC	Atmospheric Pressure Combustion Research Center
ARP	Aerospace Recommended Practice
CAI	California Analytical Instruments, an emissions analyzer
CCW	Counter Clockwise
cDAQ	Compact Data Acquisition Unit
CFD	Computational Fluid Dynamics
CLP	Combustion Loading Parameter
Cmpd Drvr	Compound Driver, driver holes have added axial angle into cavity
CO	Carbon Monoxide, a type of pollutant emission
CO_2	Carbon Dioxide, a product of combustion
COAL	Combustion Optimization and Analysis LASER (Lab)
csv	Comma Separate File
CW	Clockwise
Da	Damköhler number
DAQ	Data Acquisition
EI	Emissions Index
EPA	Environmental Protection Agency
F_g	Buoyancy Force
g	g-loading factor, the magnitude a force is greater than the normal gravitational force exerted by earth
h	Convective heat transfer coefficient
H_2O	Water, a product of combustion
HPT	High Pressure Turbine
HRR	Heat Release Rate
HVOF	High Velocity Oxygen Fuel
IAW	In Accordance With
ID	Inner Diameter
I_R	Intensity Ratio
IR	Infra-Red
ITB	Inter-Turbine Burner
LBO	Lean Blow Out
LLCB	Low Loss Centerbody Hybrid Vane Passage
LLCB	Low Loss Center-Body
LLP	Longwell Parameter
M	Mach Number
$\dot{m}$	Mass flow (kg/m^3)
N_2	Atmospheric Nitrogen molecule
NAAQS	National Ambient Air Quality Standards
NI	National Instruments, maker of LabView and associated hardware
NO_x	Nitrous Oxide Family, a type of pollutant emission
OD	Outer Diameter
OFAR	Overall fuel-to-air ratio

P	Pressure (Pa)
PIV	Particle Image Velocimetry
PLIF	Planar Laser-Induced Fluorescence
RAM	Random Access Memeory
RVC	Radial Vane Cavity
S S_t	Turbulent Flame Length (m)
SAE	Society for Aeronautical Engineers
SiC	SiliconCarbide, used as TFP filaments
S_L	Laminar Flame Length
SLPM	Standard Liters Per Minute
T	Temperature (Kelvin)
$\bar{T}$	Time-averaged Temperature (K)
T_3	Turbine Inlet Temperature (K)
T_4	Averaged (bulk) temperature exiting combustor, both spatial and temporal
TCB	Tapered Center-Body, original hybrid vane used in UCCv2
T_f	Filament Temperature
TFP	Thin Filament Pyrometry
THC	Total (unburned) Hydrocarbons present (ppm) – Specifically Propane for the CAI Gas Analyzer
Thrust-to-Weight	$\frac{F}{W} = \frac{Engine\ Thrust}{Engine\ Weight}$
T_{max}	Maximum recorded temperature
TSFC	Thrust Specific Fuel Consumption (1/hr)
UCC	Ultra Compact Combustor
UCCv1	60° Sector Model of UCC
UCCv2	First Full Annular Model of UCC at AFIT
UCCv3	UCC version 3, has driver holes only oriented tangentially to the bulk flow
UHC	Unburned Hydrocarbon
UHC	Unburned Hydrocarbons, both propane and hydrocarbon radicals
v'_{rms}	Root mean square, velocity perturbation (m/s)
V	Volume (m^3)
VAC	Volts – Alternating Current source
VDC	Volts – Direct Current source
VI	Virtual Interface
XX/YY (i.e. 70/30)	Core air percentage of inlet flow to cavity air percentage of inlet flow split
δ	Flame thickness
λ	Core blockage ratio
Φ	Air to Fuel Ratio
Φ_{cavity}	Air to Fuel Ratio within UCC Combustion Cavity
$\theta_{profile}$	Local Profile Factor
θ_r	Radial angle of air driver hole to original UCCv3 radial hole
θ_t	Tangential angle of air driver hole to centerline of combustion cavity

I. Introduction

Mattingly [1] states that the primary purpose of the combustor is to add thermal energy to the air-fuel mixture of the core engine flow. This enables the turbine to convert thermal energy into mechanical work, extracted by turbine blades in order to drive the compressor, which feeds the combustor with high-pressure air. Much research has been devoted to increasing the thrust of the engine, but these measures typically increase weight. Recently, the Ultra Compact Combustor (UCC) has been proposed as an alternative to enhance jet engine thrust-to-weight characteristics by reducing the weight and size, rather than increasing thrust. Current issues for a UCC revolve around integrating the centrifugal flow combustor concept into a traditional axial turbojet and determining the effects of altering the combustion cavity upon the temperature profiles and exit emissions. This investigation will focus on experimentally determining ways to enhance the migration of the hot combustion products across a hybrid vane radial span.

1.1. Basics of Combustors

Combustors use chemical reactions to increase the thermal energy of the core flow through an engine. The basic chemical formula is a set of molecules, termed reactants, chemically reacting with each other in order to form products [2]. For practical air-breathing combustion, this reaction most often consists of a mole of hydrocarbon based fuel (propane, JP8) mixing with the oxygen in air to produce water, carbon dioxide and nitrogen. Certain conditions must be met, such as activation energy, proper pressure conditions, and appropriate ratio of fuel and oxygen to sustain combustion. When these conditions no longer exist, the flame is quenched and ceases to exist. The conditions of the air can also affect the formation of other products, termed free radicals, that are undesirable with respect to efficiency as well as to the environment.

To prevent these pollutants from forming and decreasing the component efficiency, the effects of changing flow patterns throughout the combustor must be understood.

The combustor on an aircraft engine uses the thermal energy provided by the combustion chemical reaction to power the turbine section, which converts it into mechanical energy that powers the compressor. Combustors operate in a trade-space of competing requirements for optimal performance. Mattingly [1] identifies some of these requirements as: complete combustion, low total pressure loss, stability of combustion process, freedom from flameout, easy ability to relight extinguished flames, proper temperature distribution at exit plane, short length and small cross-section, and operation over a wide range of flow conditions with minimal degradation of performance. Early combustor development focused on ensuring complete combustion and flame stability. Within subsequent generation of engines, more efficient combustion led to elevated exit temperatures making proper temperature distribution across the turbine blades paramount. Without the proper distribution, the turbine blades experienced extremely short lifecycles due to melting and other structural failures. Eventually, combustors had their efficiency increased during off-design flight conditions in excess of 90% [1]. All these parameters increased the thrust and engine reliability, which were the emphasis of customer requirements. Combustor efficiency has plateaued since the 1990s and improvements have instead focused on meeting ever-increasing emissions restrictions from government agencies.

1.2. Ultra Compact Combustor

The Ultra Compact Combustor (UCC) seeks to improve the Thrust-to-Weight ratio of an engine by focusing on weight reduction, as opposed to thrust improvement. It does this by axially shortening the combustor section by wrapping the flow path around the outer annulus of the vane. This diverted flow is forced in a tangential direction within the primary combustion

zone, which imparts a centrifugal force that accelerates heavy particles to the outer diameter. This imparts a high-g load on the fuel-air mixture, which increases flame speed, decreases residence time, and decreases axial combustor length. Lewis [3] first demonstrated that high-g circumferential loads in combustion environments between 500 g and 3500 g increase flame speeds. Now the UCC must sustain operations within traditional aircraft jet engine environments while meeting environmental requirements.

Previous research by Zelina *et al.* [4] catalogued the effect of high g-loading within a UCC and confirmed the trends seen by Lewis [3]. Wilson *et al.* [5] constructed a fully-functional combustor and test stand at the Air Force Institute of Technology (AFIT) Combustion Optimization and Analysis LASER (COAL) Laboratory. Cottle and Polanka [6] recently used a common air inlet source to supply the core and cavity flows simultaneously; they found that insufficient air was being routed to the combustion chamber during low reaction flows. Computations led to a blockage plate design that balanced the pressure distribution and achieved appropriate combustor operating ranges. Further experiments are now required to determine the effect on the exit temperature profile under combustion conditions. Similar research is also being performed at the Air Force Research Laboratory (AFRL) [7] and Spytek Industries [8].

1.3. Research Objectives

The purpose of this experiment is to determine the effect of varying the combustion cavity and vane geometry upon emissions, exit flow characteristics and the combustion product's flow path through the UCC. The data will quantify which geometric configurations enable exit conditions for the UCC that match typical combustor exit profiles. This will allow for eventual integration of the UCC into existing aircraft engines. These experiments will also establish an emissions baseline for the AFIT UCC, and then quantify the effect of varying the geometry upon

emissions at the exit plane. These results will then be used to refine the computational model currently in development. To acquire accurate temperature measurements, the thin filament pyrometry (TFP) technique and thermocouples were used to obtain the time-averaged temperature at the UCC exit plane. TFP places a filament of silicon carbide into the flow and determines the temperature of the gas by comparing the radiation intensity of the filament to a baseline. This technique allows for more accurate data that is also across the entire channel width with enhanced spatial resolution.

1.3.1. Objective 1: Impact of Increasing Size of Combustion Cavity

The initial change made to the UCC was to alter the geometry of the combustion cavity from previous designs. These included modifications to the air injection ports into the combustion chamber, the cross-sectional flow area within the combustor, the aspect ratio of the chamber, and making the air driver holes evenly distributed around the entire front plate. Temperature values within the combustion cavity were acquired in order to aid in the understanding of temperature migration from the combustion cavity to the exit plane. This data was then compared to previously collected temperature values for a previous incarnation of the AFIT UCC rig. The normalized pattern factor and local profile factors at the exit plane were also calculated to show the feasibility of integrating this combustor into existing jet engines. In order to integrate the UCC into existing aircraft jet engines, the exit temperatures must not exceed the material limits of the components behind it.

Finally, an accurate emissions baseline for the AFIT UCC with the larger cavity was established by taking the concentrations of five different gaseous species for this geometry. This baseline of experimental data is sought in order to improve future computational models ability to track both species and temperatures. To determine emissions and efficiency, a new multi-port

emissions probe was designed. This probe interfaced with the COAL Lab's revitalized California Analytical Instruments (CAI) emissions analyzer to determine exit gas concentrations and combustor efficiency. All emissions data was calculated by the methods outlined in ARP 1533 [9], the common standard for aircraft emissions.

1.3.2. Objective 2: Impact of Adding a Radial Vane Cavity to the Hybrid Vane

Next, the hybrid-vane geometry was varied by adding a radial vane cavity (RVC), and the effects on the combustion cavity, exit temperature profile, as well as the emissions were investigated. The purpose of this modification was to focus the peak exit temperatures in the mid-span region and away from the outer span as had been noted in previous center-body vane designs. The collected data for this geometry was then compared to the previous geometric configuration to determine if the RVC had the intended effect. The existing AFIT UCC test rig allowed this by having significant optical access via quartz windows that enable the flow properties and temperature profile within the combustion chamber to be taken.

1.3.3. Objective 3: Impact of Compound Angled Holes on Cavity Combustion

The next objective found that altering the axial angle of the air driver geometry also alters the residence time of the fuel, temperature profile and emissions of the UCC. This geometry was first considered analytically by Cottle *et al.* [10] and showed the potential to increase residence time, which warranted its experimental validation. This has the effect of increasing the amount of combustion within the UCC, and lowering the temperature magnitude at the exit for certain cases. It is also shown through emissions measurements that increasing the residence time also increased the efficiency of the UCC. However, this modification did not alter the UCC exit temperature profile into the desired shape.

1.3.4. Objective 4: Compound Driver – RVC

The final geometry investigated was a combination of RVC center-body with the Compound Driver air injection scheme. Through this experiment, it was determined that the hybrid vane design strategy within the UCC is valid for integration with existing engines. This configuration had sufficient temperature profile and efficiency improvements to warrant continuing research into this design. It was also shown that this permutation produced the most effective exit temperature profiles and efficiencies of the four geometries.

II. Literature Review

Jet engine design has progressed quickly in the first century of its existence. Since the 1940s, the primary goal has been to increase engine thrust through compressor efficiency, which is constrained by the amount of power the turbine can extract after combustion [1]. Due to the nature of aircraft, the space and weight are primary design concerns with aircraft; the heavier the engine, the less weight is available for the aircrafts primary functions. The non-dimensional engine parameters used to compare engine performance are thrust specific fuel consumption (TSFC) and thrust-to-weight ratio $\left(\frac{F}{W}\right)$ [1]. The most prevalent way to increase the thrust-to-weight ratio over the last 50 years has been to focus on increasing engine thrust. Research has focused on increasing compressor pressure ratio, increasing the temperature limits of the turbine to increase potential power extraction, and increasing the chemical efficiency of the combustor. However, decreasing the length and weight of the combustor has a positive influence on this parameter, as well as reduce the air losses required to cool the combustor.

Exemplary combustor performance requires a series of interrelated and contrasting parameters. Two parameters that illustrate this juxtaposition best are the desire for complete combustion with low total pressure losses versus short length with a small cross section. The latter produces lower weight and material cost while decreasing complexity and the area required for cooling. To achieve the former, it is preferred to have a long combustor, where the chemical reaction is given more time (which is proportional to distance) to progress. Complete combustion also needs the correct proportion of oxygen to fuel at a high-pressure condition to occur. A short combustor does not provide adequate time for the combustion to occur and incurs losses that reduce the total pressure of the section.

The Ultra Compact Combustor (UCC) seeks to accommodate these seemingly opposed design requirements. It increases the residence time of the gas by circumferentially spinning the flow around the combustion chamber, thus decreasing the required axial length, while varying the cross-sectional area in the center-body appropriately in order to maintain the appropriate circumstances for combustion. Also, due to the density gradient caused by the high-g loading upon the flow, the heavier hydrocarbon fuel molecules are spun towards the outer rim of the circumferential cavity (gray boxes in below figure). This increases the residence time of the fuel while the high-temperature, low-density products and N_2 are forced out through the exit vane [3].

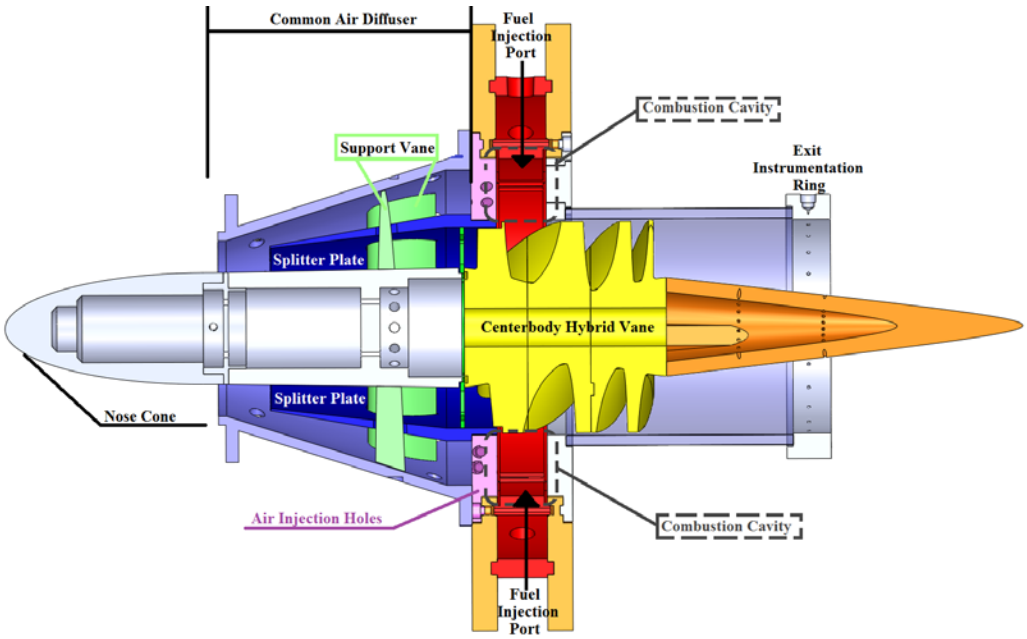

Figure 2.1: AFIT UCC Basic Part Nomenclature

Previous experiments have proven the viability and nature of high-g flows and have been incorporated into AFIT UCC test rig. Work remains to integrate the concept into a modern aircraft engine design. This includes routing the flow into the combustion cavity, ensuring complete combustion, and flow migration back into the core flow. To ascertain the practicality of the UCC, the flow path within the combustion chamber through to the exit must be designed

to achieve high combustion efficiencies. As such, the emissions data at various axial points and the exit temperature profile of the combustor must be collected. Previous experiments have been performed in combustion environments, to include both sectional and full-annular UCC designs and had their flows characterized. Also, methods for obtaining and analyzing emissions, temperature profiles and flow parameters will be discussed.

2.1. UCC Basics

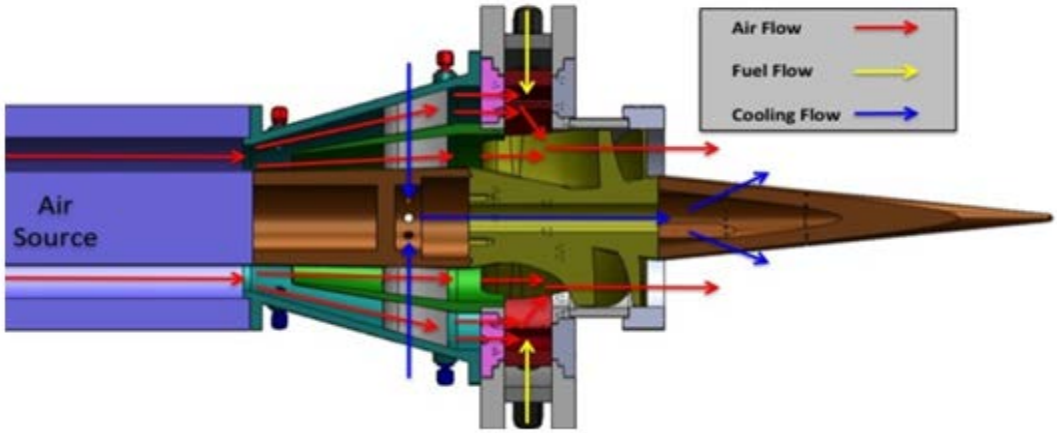

Figure 2.2: AFIT UCC Mass Flow Path with Common Air Source [6]

Fundamentally, the UCC concept is different from traditional combustors and a brief definition of the components of the current AFIT UCC configuration is included for the reader's reference. Figure 2.2 shows the AFIT UCC, where air is introduced into the common core air source, it is split between the main core flow and circumferential combustion cavity. The diffuser (inner green colored part in Figure 2.2) diverts the appropriate mass flow split into the combustion chamber and core flow section. The bypass flow then progresses radially outward within the diffuser until it reaches the air injection panels (pink colored part in Figure 2.2). These panels inject the core flow at a tangential angle into the circumferential combustion chamber. This tangential flow places circumferential forces between 500-2000 g upon the

mixture and swirls the combustion cavity [5]. The products are then entrained by the hybrid vane (yellow colored part in Figure 2.2), which migrates the hot gases out of the UCC combustion cavity into the core flow. Within the hybrid vane, the combustion gases mix with the remainder of the core flow, lowering the overall equivalence ratio in what is termed a quick-quench, lean-burn process. This process will be discussed more fully in Section 2.4.1. An added benefit of the high-g swirl is the density gradient causing the heavier reactants to be thrown outward and increase residence time [11]. Combustion is completed in these passages, while the flow is turned to the appropriate exit velocity angle.

2.2. Combustion Fundamentals

Combustion, as defined by Turns, is "the rapid oxidation of a gas generating heat and light" [2]. Typically this involves the reaction of a hydrocarbon-based fuel and air into water, carbon-dioxide, Nitrogen gas and free radicals that result from incomplete combustion. If there are no free radicals produced and the atoms are conserved between reactants and products, then the reaction is said to be stoichiometric. The non-dimensional parameter used to quantify the actual fuel-to-air relation to the stoichiometric condition in combustor and augmenter environments is the equivalence ratio, Φ [2], which is defined as:

$$\Phi \equiv \frac{A/F|_{stoich}}{A/F} = \frac{\dot{m}_{air}}{\dot{m}_{fuel}} = \frac{\nu_{air} MW_{air}}{\nu_{fuel} MW_{fuel}} \tag{1}$$

where A/F is the mass ratio of Air to fuel, $A/F|_{stoich}$ is the mass ratio of air to fuel for stoichiometric reaction conditions, $\dot{m}$ is the mass flow of the species (kg/s), ν is the stoichiometric coefficient for chemical reaction, and MW is the molecular weight of the molecule. Traditional axial combustors require fuel-lean environments (Φ < 1) in order to

sustain the flame while not exceeding the material properties of the combustor lining and turbine blades [1].

Combustion can result from one of two processes: deflagration and detonation. As Turns [2] summarizes, detonation occurs when the combustion wave propagates and sustains itself at supersonic speeds. Deflagration, which the AFIT UCC uses to maintain combustion, produces and relies on flames to propagate the combustion event from one localized area throughout the entire chamber. All flames, whether they are turbulent or laminar, have the common characteristics of flame speed (S_x) and flame thickness (δ). The flame speeds for laminar and turbulent non-premixed flames are [2]:

Laminar

$$S_L = \left[-\frac{2\alpha(\nu+1)\overline{\dot{m}}_F'''}{\rho_u} \right]^{\frac{1}{2}} \quad (2)$$

Turbulent

$$S_t = \frac{\dot{m}_{reactant}}{\overline{A}\rho_u} \approx 3.5 S_L \left(\frac{v'_{rms}}{S_L} \right)^{.7} \quad (3)$$

where α is the thermal diffusivity, ν is the molar ratio of oxygen-to-fuel, $\overline{\dot{m}}_F'''$ is the mean volumetric mass flow rate, $\rho_u$is the density of the unburned mixture and $\overline{A}$ is the time-averaged area of the flame. Since turbulent flames increase the mixing of the reactants, they also increase the total flame speed while decreasing residence time and required combustor length. For this reason, combustors predominately use turbulence in order to reduce chemical residence time.

Within the UCC, the flame thickness is not of primary importance because the flame is constrained by the physical geometry of the combustion chamber and flow exiting the hybrid vane. Therefore, the flame speed is the focus of combustor design as it relates to residence time. The non-dimensional parameter that shows this relation is the Damköhler number (Da) which is defined as [2]:

$$Da \equiv \frac{\tau_{flow}}{\tau_{chem}} = \frac{l_0/v'_{rms}}{\delta_L/S_L} \tag{4}$$

where l_0 is the integral length scale of the turbulence eddy, v'_{rms} is the root mean square of the turbulence intensity chemical time is a function of the laminar flame values, and α is the thermal diffusivity of the reactant mixture. Applying Turns simplified analysis for laminar, premixed flame, he shows that $\delta_L = 2\alpha/S_L$, therefore *Da* can be simplified to:

$$Da = \frac{l_0 \, S_L^2}{2\alpha v'_{rms}} \tag{5}$$

If *Da* is >>1, then it is fast-chemistry regime, and the residence time of the gas is slow. However, if *Da* is <<1, then the regime is dominated by the flow and the residence time is much quicker. Therefore, it is the goal of a combustor to increase the turbulence intensity with respect to the laminar flame speed in order to reduce residence time.

One parameter used to quantify the stability of the combustor component is the Combustor Loading Parameter (*CLP*) which Mattingly [1] defines as:

$$CLP = \frac{\dot{m}}{P^n V} \tag{6}.$$

The *CLP* relates the flow properties within a combustor to the temperature and Φ required to maintain combustion [1]. The term "n" is based on the rate of the combustion process and for hydrocarbon gases (i.e. propane), *n* = 1.8, while JP-8+100 is represented by a bimolecular reaction and, thusly [1], uses a value of *n* = 2.0. Since the AFIT UCC uses gaseous propane as its source, 1.8 is the value used in post processing experimental results. A high CLP correlates to

large mass flow versus the amount of mechanical energy lost within the combustor. Put another way, the higher the loading parameter, the greater the efficiency of the engine.

An alternative loading parameter also used in combustor analysis is the Longwell Loading Parameter (*LLP*). Anthenien *et al.* [16] originally used the *LLP* in lieu of the *CLP* due to its accounting of the combustor temperature performance. The *LLP* was also originally used since it was derived for use within Well-Stirred Reactors environments, which only consider the potential enthalpy of a system. Anthenien used the values:

$$LLP = \frac{P^{1.75} V e^{\frac{T}{300}}}{\dot{m}_{A_{cav}}} \tag{7}.$$

Where P is pressure, V is volume, T is Temperature (in units of K) and $\dot{m}_{A_{cav}}$ is the mass flow rate supplied to the combustion cavity. Due to this reciprocal nature of the *LLP*, for traditional combustors the higher the loading parameter the less efficient the engine performs. However, for the UCC, this was reversed so that higher *LLP* values corresponded to increased efficiency. Therefore, the AFRL UCC performed most efficiently at a Longwell Parameter around the order of magnitude of 10^7.

Another effect that occurs within the UCC is free convection. Free convection occurs due to the difference between densities within the same fluid, or in combustion, between high-temperature (low density) products and low temperature reactants [3]. The buoyant force that drives this is defined as:

$$F_B = g(\rho_a - \rho_f) \tag{8}$$

where g is the centrifugal force applied to the gas (normally 9.80 $\frac{m}{s^2}$), $\rho_a$is the density of the cold reactants and $\rho_f$is the density of the hot products. As Lewis [3] notes, this term is normally

insignificant compared to the forced convection term—equating to only 0.280 Newtons for a cubic foot of gas increasing from 300 K to 2200 K at ambient pressure and normal earth gravity.

Lewis [3] theorized that the flow speed within a combustion chamber could be enhanced within a centrifugal combustion chamber. Using an enclosed rotating tube to induce centrifugal forces, he determined that g-loads above 200 g and up to 3500 g increased the observed flame speed. Figure 2.3 shows the observed flame speed of a propane-air mixture for varying Φ over the range of g-forces that provided improvement.

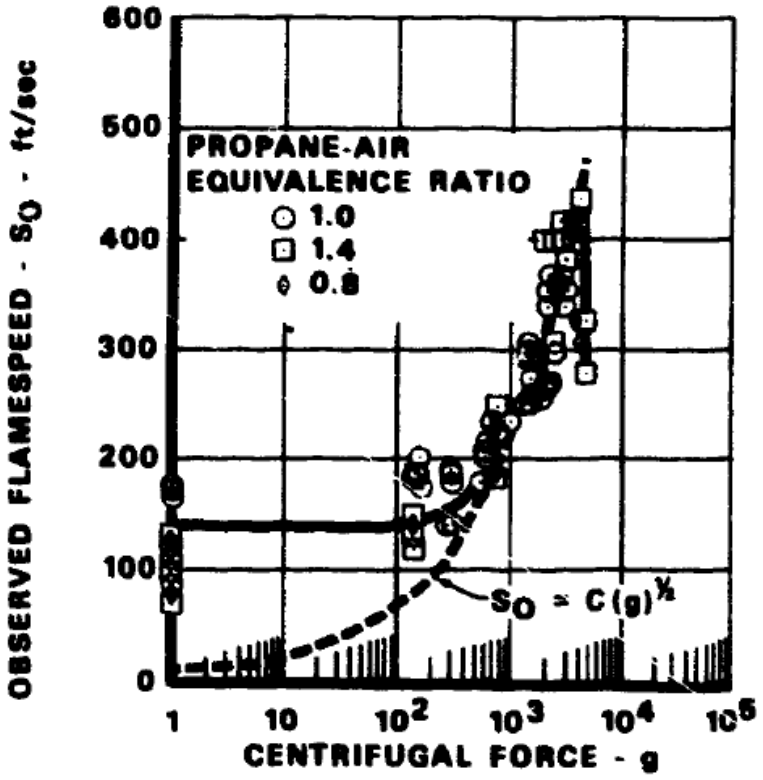

Figure 2.3: Centrifugal Forces Effects upon Fuel-Air Combustion Environments [3]

Zelina [11] later confirmed these trends within a modular UCC, and extended Lewis' previous work by determining the fuel operability limits for the entire component. Zelina [17] previously had showed that the g-load within the combustion cavity was most influenced by the injector air mass flow rate into the combustion cavity. This enabled him to fix the g-load

condition while varying the combustion cavity equivalence ratio. From these results, Zelina determined that the highest increase in efficiency occurred between 3500–4000 g but combustion would continue up until a condition of approximately 7000 g. His specific data points are shown in Figure 2.4.

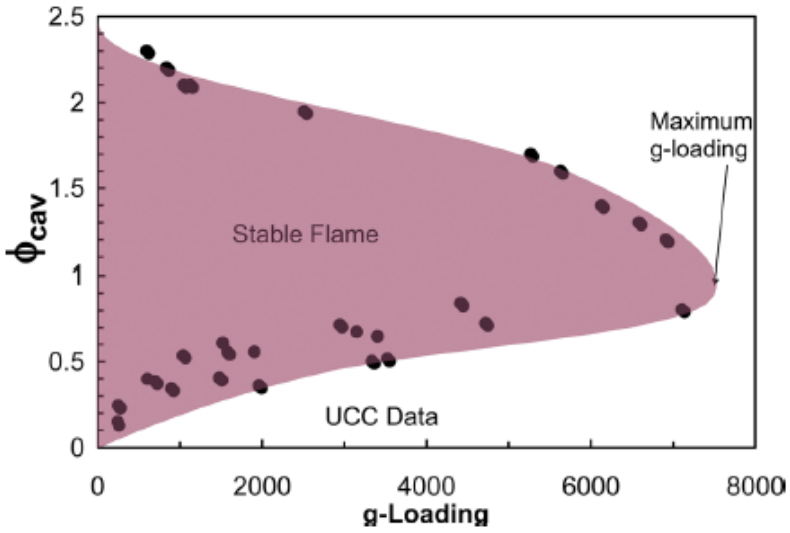

Figure 2.4: UCC Stability Map Based upon Cavity g-Load [11]

Figure 2.5 pictorially demonstrates how the density gradient between the low density flame (dark circle) and the higher density fuel-air mixture affects the apparent flame speed. During an incremental step in time, Δt, the fuel-air mixture will move a distance, $\Delta t * S_B$, where S_B is termed the "bubble velocity" by Lewis [3]. The bubble velocity is driven by the free convection force and progresses much slower than the turbulent flame over the same time increment. However, when the g-load is increased upon the combustion gases, the bubble "races ahead," as shown by the middle picture of Figure 2.5. This causes the rate of flame propagation to increase, meaning that the higher of the two velocities should be used to calculate reaction rates. The right-most picture depicts a high-g load upon the flame, but within a non-air environment so the flame does not progress ahead of the bubble velocity.

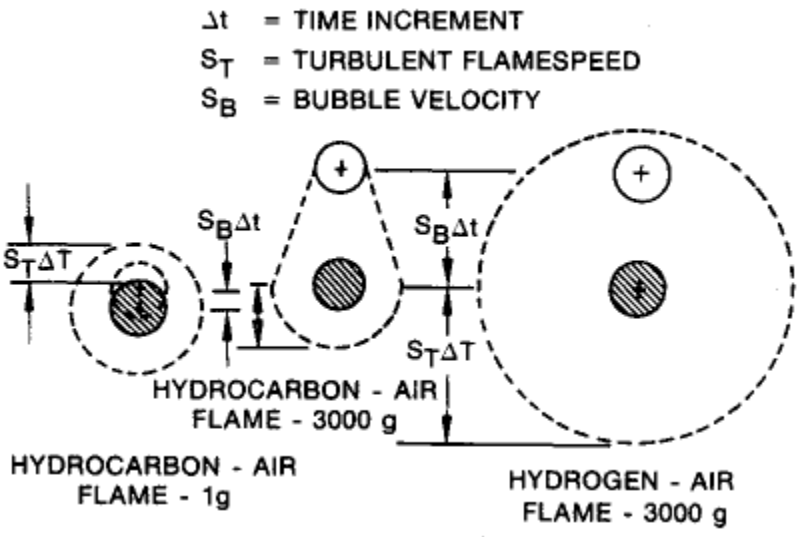

Figure 2.5: Pictorial Representation of Lewis' Theory about Bubble Transport Phenomenon [3]

Briones et al. [12] sought to confirm Lewis' bubble transport theory using a scale-adaptive, unsteady Reynolds-Averaged Navier-Stokes, 2-D simulation. This analysis considered the three different hydrocarbon fuel sources used by Lewis using their own specific global reaction model. The model showed good agreement between the values reported in the published literature and confirmed the trends seen in g-loading and flame propagation velocity. However, they determined that the centrifugal force was not a primary actor on the turbulent flame speed; rather it was the density differences combining with the centrifugal force encouraging Rayleigh-Taylor instabilities. Rayleigh-Taylor instability, as explained by Erdmann et al. [13] explains the progress of lower density (i.e. hot) fluids through a higher density (i.e. cold) fluid. Put another way, it says that hot air will rise because it cold air will follow the acceleration force applied on it by the earth. Normally, this force is trivial in modern combustors due to their large axial length encouraging convective mixing and turbulence. However, if a

sufficiently large enough acceleration is applied (such as the centrifugal force seen in a UCC), the Rayleigh-Taylor instability can dominate the other flame effects and increase the flame propagation velocity.

The pressure wave originating from the presence of the g-forces also provides a secondary mechanism to increase flame speed [12]. This wave encourages additional wrinkling and corrugation of the flame that enhance the Landau-Darrieus (hydrodynamic) instability at the flame front which creates a faster propagating, corrugated flame. These instabilities combined with the thermal expansion to increase the flame speed in the tube away from the original flame source. However, this stretching has an optimal point between 2000-3000 g's that, if exceeded will cause the flame to stretch so much that it will locally extinguish. It is also worth noting that the UCC uses the geometry of the combustion cavity and center-body to impose a centripetal force upon the fluid, where Lewis' [3] experiment imparted a centrifugal force on the fluid by rotating the fluid about a centroid.

2.3. Combustor Fundamentals

In order to maximize the energy extracted by the turbine, initial developmental focus was placed on maximizing the efficiency of combustion and finding the appropriate air-to-fuel mixture [1]. Combustor development and efficiency have plateaued since the 1970—where engines achieved efficiencies in excess of 90% for on- and off-design conditions. Since that time, a can-annular (a.k.a. turbo-annular) design has primarily been used, due to its lower weight, highly efficient design, and ease to incorporate a series of independent combustor "cans." The individual components are typically split into five main sections as depicted in Figure 2.6 the diffuser, primary zone, intermediate zone, dilution zone and discharge nozzle. The outer annulus provides additional cooling and oxygen-rich air into the primary combustor flow in order to

maintain the proper reactant ratios. Air enters from the compressor and is slowed by the diffuser. Some of the flow is routed into the outer and inner annulus to be reintroduced further downstream. The remainder is directed into the primary zone where the flow is initially tripped to turbulence by various means. Fuel is then introduced and fully mixed with the oxygenated core flow via the turbulent vortices with the flame anchored in the primary zone in Figure 2.6). The primary zone is followed by the intermediate zone, where more air is added from the annulus flows in order to ensure more complete combustion and reduce soot by quenching the fluid. The dilution zone reduces the temperature of the combustion products by adding in the remaining diverted air to quick quench the main flow, limiting chemical reactions by lowering the energy of the fluid below conditions favorable for combustion. The products are then forced into the discharge nozzle in order to achieve the optimal exit velocity and temperature profile for the first turbine stage.

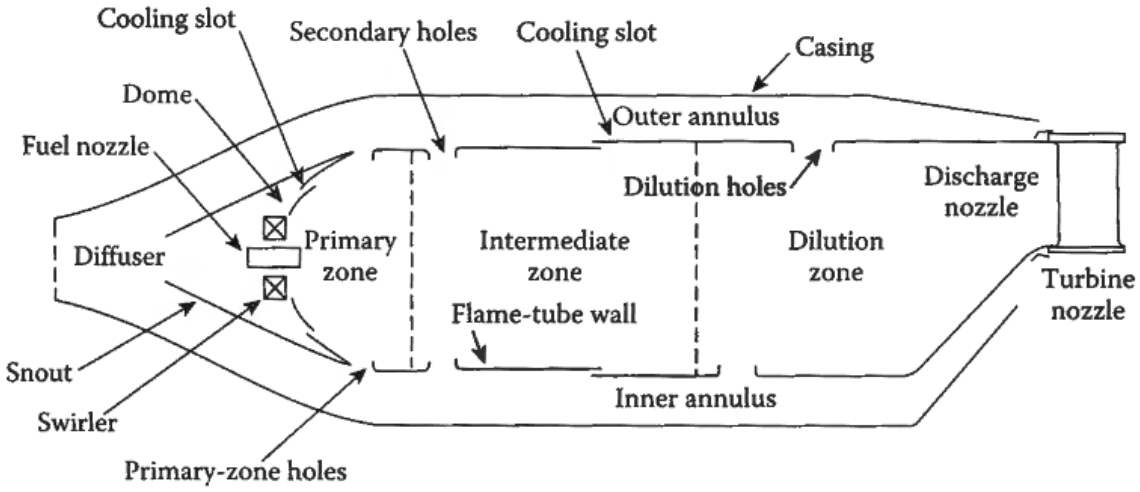

Figure 2.6: Basic Combustor Design and Zones [14]

The UCC has these four distinguishing regions as well. As Figure 2.7 shows, the air is split by the diffuser into the primary core flow and the annulus. A significant percentage of air flow is required to drive the flow within the combustion cavity circumferentially. The outer ring

encapsulating the front-most part of the hybrid vane is the primary zone, and all the diverted air from the diffuser is reintroduced here. Prior to the introduction of the core flow, the combustion cavity flow rotates about the intermediate zone where the density gradients delay the fuel molecules exit until they have reacted. Due to this, the primary zone is designed to be the component most radially outward. The intermediate zone, where burning still takes place but the number or reactions are reduced from the reintroduction of the cooler air, occurs where the combustion ring products are swirled into the hybrid vane cavities within the core flow (seen as the green section in Figure 2.7) [11].

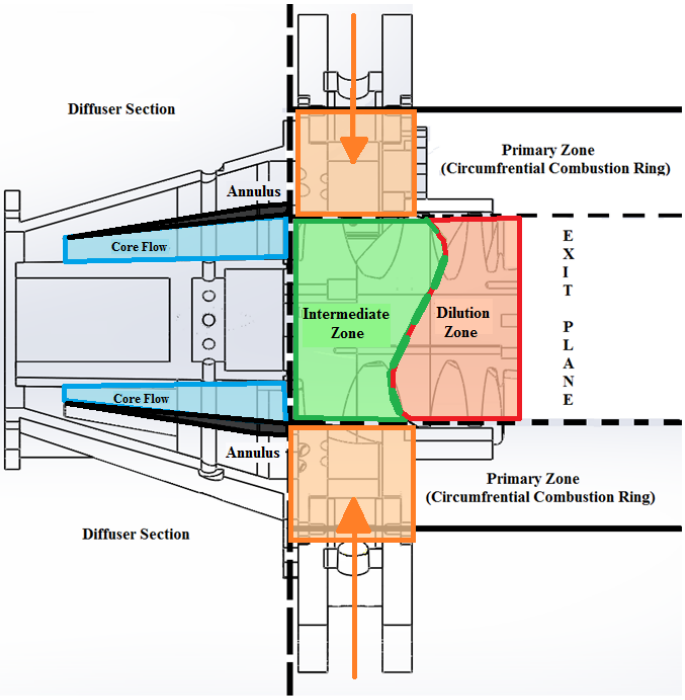

Figure 2.7: AFIT UCC mass flow path with common air source

Within the intermediate zone, a portion of the combustion cavity flow is sucked into the hybrid vane passages where the chemical reaction is quenched by the introduction of colder air. In an axial combustor this occurs when cool air jets are placed a specific distance downstream and quenches the flow. However, the quick-quench lean-burn process within the UCC does not have

a definite transition point between the intermediate zone and the dilution zone. Rather, the swirling flow in the vane and the vortices that occur there result in different chemistry at the same axial locations, so the point is not finite as with a traditional axial combustor. To illustrate this phenomenon, the interface in Figure 2.7 is curved. The dilution zone occurs around and within the later portion of the hybrid vane. It is here that the core flow cools the hot combustion products and migrates them out of the combustor with the appropriate temperature distribution. In this way, the UCC is opposite of a traditional combustor; its diverted flow feeds the chemical reaction and its core flow cools.

2.4. UCC Development

The UCC was initially investigated as an auxiliary power source for on-board aircraft electrical systems [15]. The electronic systems onboard modern aircraft are powered exclusively by their engines converting the chemical power of the fuel into mechanical power within the turbine and then to electrical power with an AC/DC converter. This means that in addition to providing thrust for the aircraft, the engines are relied on to feed the avionics, hydraulics and pilot-aiding computers. This electrical power requirement subtracts energy, and therefore thrust, away from the engine. As more electronics are added to modern systems, such as the future AWACS system updated RADAR unit, the potential exists that these systems will reduce the thrust sufficiently to preclude certain mission environments. Even worse, this loss of thrust could prevent aircraft from taking off.

It was this conundrum that led Sirignano and Liu [15] to speculate that an inter-turbine burner (ITB) could add the requisite energy back into the engine flow so that the electrical systems could be powered while maintaining sufficient thrust for all mission profiles. The major dilemma with this idea was that adding another traditional combustor to the aircraft engine

would detrimentally increase the weight. As with rocket engines, where every one pound of rocket needs two pounds of fuel to propel it, aircraft engines have a similar relationship with their fuel source. Eventually, the combustor weight would reach the point where its presence would offset any power benefit by significantly decreasing the range of the aircraft. Therefore, a new, more compact combustor from then unknown technology would be required to implement this idea. Sirignano's and Liu's [15] design focused on stabilizing combustion around the turbine stators to create a constant temperature burn and approximate an ideal Carnot Cycle.

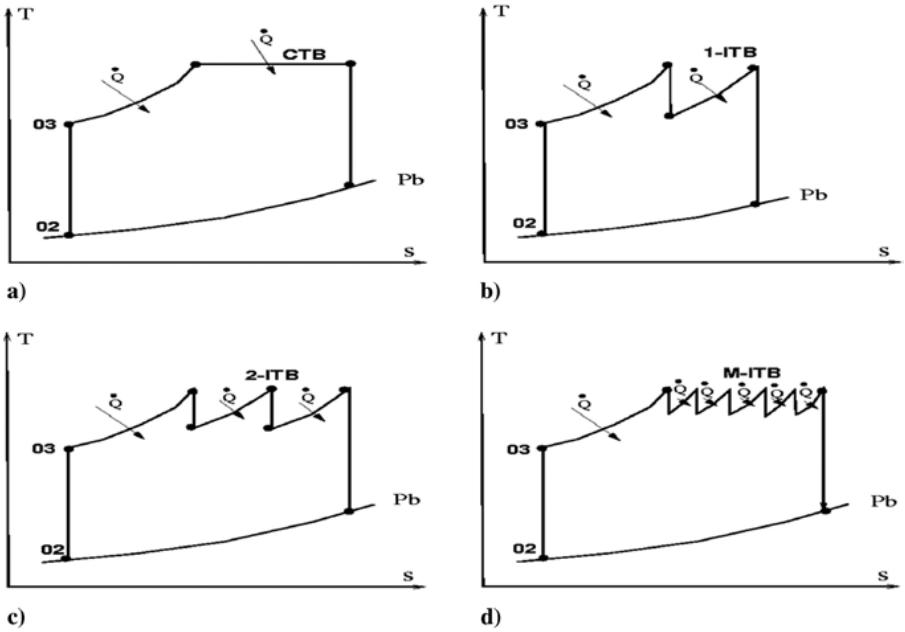

Figure 2.8: Carnot Cycle Comparisons between a) Ideal b) Single-Stage ITB c) Dual-Stage ITB and d) Multi-Stage ITB with burning at every HPT stator [15]

Figure 2.8 shows Sirignano's and Liu's ultimate goal: to increase the temperature after each extraction of energy by turbine stage back to the max temperature limit. By doing this, the turbine behavior could be approximated as a constant temperature burn, allowing for more power extraction and greater engine efficiency. Therefore their designs focused on cavity burning and cooling the turbine sufficiently. However, others began to speculate that a single, reduced size combustor could also provide the necessary power.

2.4.1. Initial UCC Development at AFRL

Based on the idea of Sirignano and Liu [15], and the promising work of Lewis *et al.* [3], Anthenien *et al*. [16] began formulating the concept of an UCC in 2001. Their concept sought to burn around a single stage of turbine stators in order to provide the requisite residence time for combustion. The turbine stators, or vanes, would then entrain the combustion products out of the cavity and into the main flow. Within the combustion cavity, the design would make use of the g-loads seen by Lewis [3] to provide more efficient combustion within fuel rich and vitiated environment. A vitiated environment is one in which there is a reduced amount of oxygen from ambient air; in the case of the ITB, one where oxygen has been previously consumed in combustion process within the main combustor.

Anthenien team's [16] hope was to use the swirl generated by the incoming flow to stir the products and create the turbulence required for air-fuel mixing within the chamber, and thereby require no additional components other than the combustion cavity housing. Using ethanol and JP-8 [16], the AFRL initial UCC design had fuel sprayed from six jet ports using a liquid fuel source that was atomized into gas by a pressure nozzle. Anthenien *et al.* [16] original publication featured two combustion cavity designs. The first cavity design had the air introduced into the cavity from six equal-distant ports around the outer ring of the cavity, as well as 15° off-center air jets on the front wall of the combustion cavity. Upon optimizing the AFRL design for its small size, the front plate air jets were removed so the only swirl in the combustion cavity came from the six outer ring jets oriented at a radial angle 45° to the core flow. Initial tests performed on the initial and optimized design used ethanol, but subsequent tests [11] also used a variety of liquid fuels.

Efficiency for the AFRL UCC was calculated by analyzing the Emissions Index (EI) of the combustion products. The ethanol gas saw initial efficiencies range between 80%–92%, which is lower than the typical efficiency of combustors. This lower efficiency was attributed the small size of the AFRL UCC rig, which had its front-wall air jet spacing too close to the fuel injector to ensure proper flame characteristics. The subsequent design removed these air driver plates, aligning the fuel jets with the outer wall air jets and enhancing combustion. This change in the air driver location increased the efficiency to 99+% with both ethanol and JP-8 fuels at the same loading parameters that had previously seen efficiencies within the 80% –90% range.

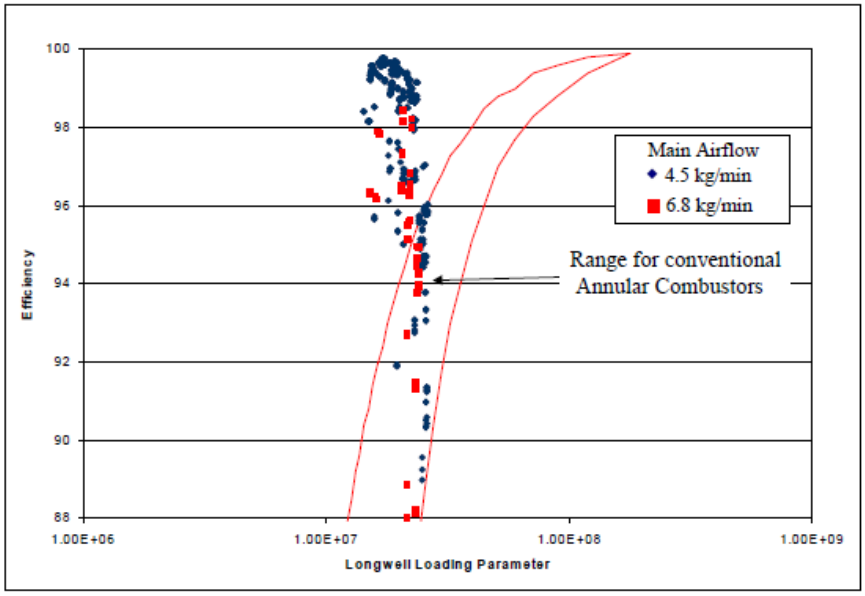

Figure 2.9: Efficiency vs. Longwell Parameter for Different UCC Main Airflow Rates and conventional combustors [19]

The lowest sustained Longwell Parameter (radial Loading Parameter) of $1x10^7$ corresponded to an average residence time of approximately 5 micro-seconds. Anthenien *et al*. also [16] saw that as the Longwell Parameter decreased, Φ and efficiency increased, which is atypical in traditional can-annular combustor. The red trend lines seen in Figure 2.9 show the typical increase in efficiency for conventional combustors as loading parameter is increased. These

positive results encouraged the research team at AFRL to further study the behaviors of the UCC design and seek ways to integrate it with existing engine technology.

Once Anthenien's design at the AFRL Atmospheric Pressure Combustion Research Center (APCRC) was completed, and its baseline was established, Joseph Zelina lead a battery of tests that further defined the operational environment of the UCC. In June 2004, Zelina *et al*. [17] presented their research into optimizing the operational range for the AFRL UCC. The center-body employed by AFRL was a straight body, symmetric airfoil and the experiment sought to determine the optimal geometry of a radial vane cavity (RVC) in order to coax the exhaust gas from the combustion cavity into the core flow. Examples of the RVC geometries used by AFRL in this study can be seen in Figure 2.10. The study found that there was a trade-off between lean blowout performance, emissions characteristics and exit temperature profiles. Subsequent research has focused on the blowout performance and emissions characteristics, but the changes required for improving exit temperature profiles has been marginal; most changes have been incidental finds or have been found to degrade performance. The RVC was shown to be effective in translating the cavity airflow into the core flow for a symmetric airfoil.

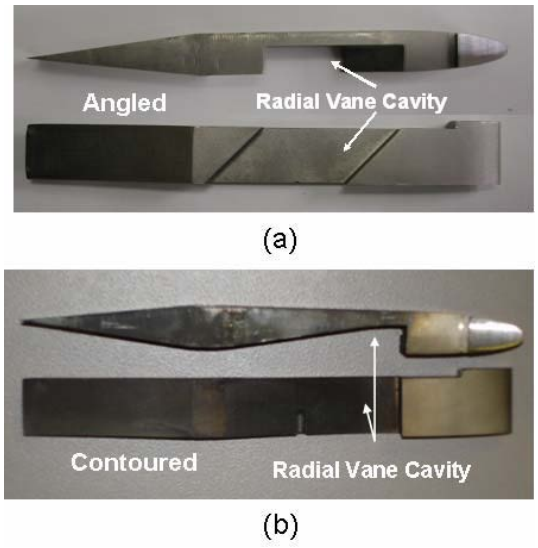

Figure 2.10: Two Radial Vane Cavity Geometries Employed by Zelina et al. [18]

In the same paper, Zelina *et al*. [17] quantified the benefits of the density gradient caused by the g-forces within a compact combustion chamber. By varying the air-jet and fuel-jet injection ratios, they were able to vary the g-loading and Φ within the combustion cavity from 500 g to 4000 g. For g-loads between 550 g and 1250 g, the density gradient caused by the high-g forces was insufficient to separate the fuel particles from what Lewis termed their "speed bubbles". The lack of a density gradient meant that flame stability could not be maintained, and either blowout or inefficient combustion occurred. Therefore, it was determined that the tangent velocity component introduced into the combustion cavity by the air jets should incur a minimum g-force greater than 1250 g.

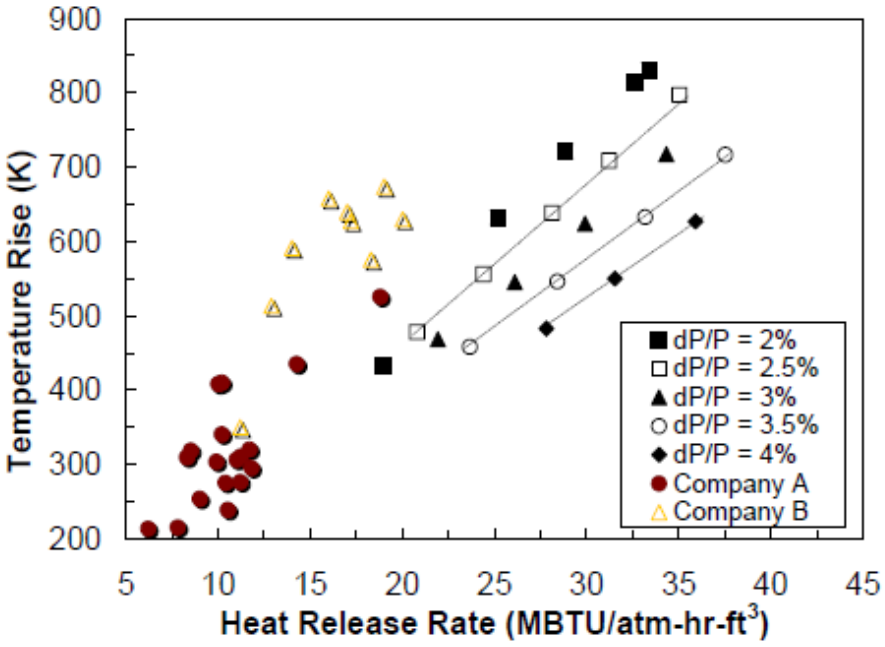

Figure 2.11: HRR for Full Annular UCC compared to Conventional Combustors [4]

Zelina *et al.* [4] next found that the decreased volume of the UCC correlated to higher heat release rates (HRR) than a traditional combustor. Predictably, the temperature rise across the combustion cavity, which functions as the primary zone, increased as the HRR was increased. As expected, lower pressure drops led to a higher temperature rise (i.e. more efficient

combustion) as the increased pressure drop encouraged more combustion within the cavity. Overall, the UCC required a lower temperature rise to supply the same heat release within the primary zone. The UCC also has a lower stability limit than traditional combustors; traditional combustors are placed "on-design" for the cruise condition at high altitude, which has low air pressures and densities. To ensure relight during engine failure, there must be sufficient length and residence time for the fuel-air mixture to reignite.

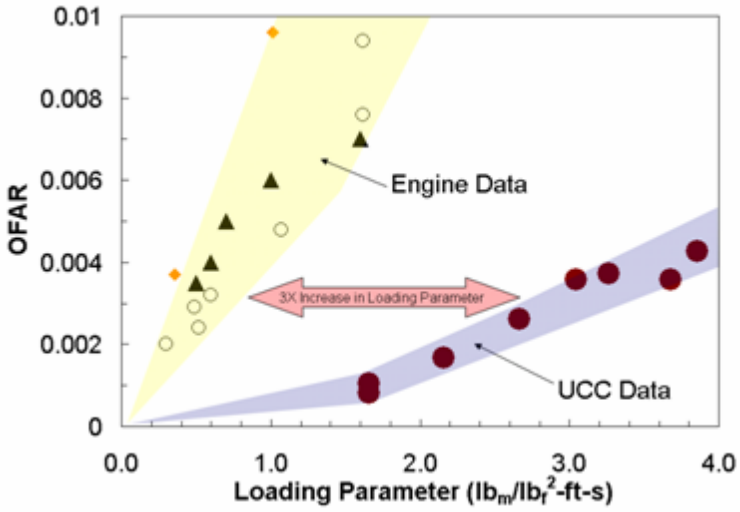

Figure 2.12 Stability Comparison between UCC and In-Service Engines [4]

As Figure 2.12 shows, the UCC maintains its flame better at low oxygen points due to its high g-loading parameter. Whether this is at high altitude cruise or in the vitiated flow behind a primary combustor, the UCC could outperform traditional combustor performance and increase safety. For this reason, Zelina *et al.* [4] then postulated that the UCC could function not only as an ITB but as a main combustor. Figure 2.12 graphically shows this fact, how the UCC can perform and maintain combustion while greatly decreasing pressure losses. In this diagram, Zelina *et al.* [4] choose to show the overall fuel-to-air ratio (OFAR) instead of equivalence ratio. As the Loading Parameter increases, less mechanical energy (i.e. pressure) is required by the combustor to sustain the flame, which increases the overall efficiency of the component. If the

loading parameter for a combustor is higher at the same OFAR (or fuel flow rate), then the combustor can increase the temperature of the flow over a wider range of equivalency ratios and extract more energy. Therefore, as seen above, the UCC can operate at the same fuel flow rates as a traditional combustor but with much less power loss. This means that the UCC can not only increase the amount of energy extracted by the turbine, but also allow the combustor to sustain a flame over a wider range of pressure drops.

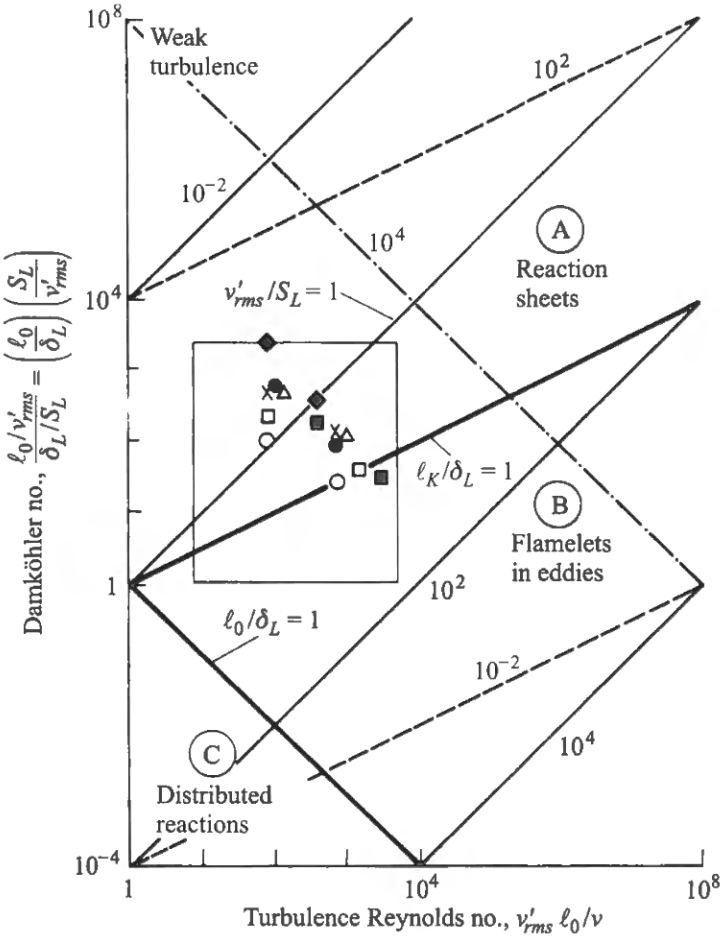

Figure 2.13: Parameters Characterizing Turbulent Premixed Combustion [2],
Note: data points are not from UCC but from original source. UCC operates in region (B).

Anthenien and Zelina [19] then sought to characterize the flame and flow characteristics within the UCC. Their aim was to determine and use the appropriate models of flame speed and length in computational analysis. Using the regimes and criteria proffered by Borghi [20] they speculated that these regimes occurred in the distributed reaction regime. However, upon comparing Borghi's terminology with Figure 2.13 in Turns [2], it was determined that the data actually corresponded to the flamelet in eddies regime. This makes sense for the UCC since the combustion chamber has high turbulence within it and wrinkled flame, which are the primary features of flames in the flamelet in eddies regime. It is of note that the below figure is taken from an experiment referenced by Turns in his text that shows where the different flame regions occur, and not the UCC. Flamelet in eddies reactions occur when the turbulence integral length alters the geometry of the flame so that the turbulent wrinkles are larger than the laminar flame. Also essential to modeling and understanding this regime is the Damköhler number since the turbulent scale (v'_{rms}) dominates the combustion time.

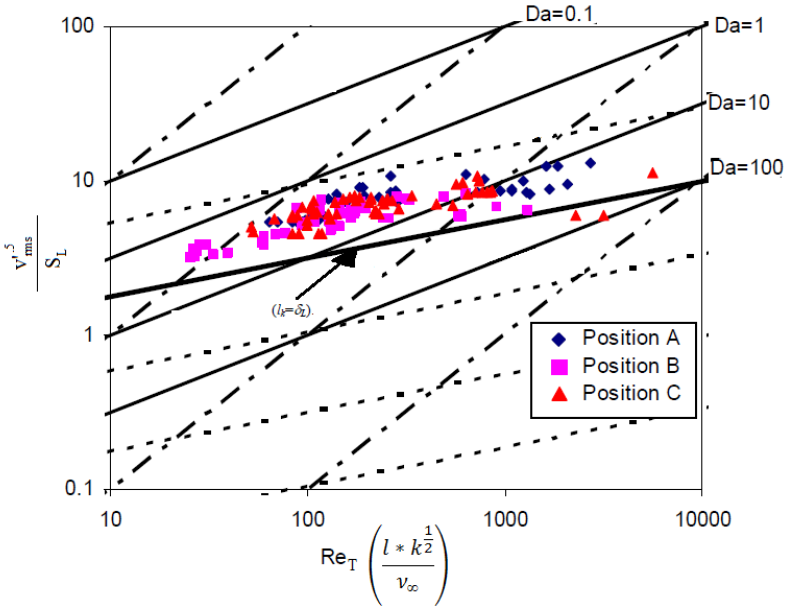

Figure 2.14: Parameters Characterizing Combustion within the UCC. [19]

By plotting their data in Figure 2.14 they concluded that the vast majority of the data points taken at three different locations were above the Klimov-Williams Criterion. This criterion asserts that laminar flames cannot exist in these flow environments due to the high turbulent flow gradients dominating the flame structure. The turbulent Reynolds numbers considered by Anthenien and Zelina [19] were between 50 and 1000. Reynolds numbers below this range caused the cavity to be loaded such that the flow re-laminarized within the cavity, thereby reducing the flame speed and extinguishing the combustion. Also, almost all of the Damköhler numbers were less than 100 while the turbulent Reynolds numbers were similarly small, placing the UCC squarely within the flamelet in eddy regime. Future UCC designs and models have therefore accounted for the characteristics of this regime within the combustion cavity.

2.4.2. AFIT UCC Development

Based on the promising results seen by AFRL, the Air Force Institute of Technology (AFIT) increased the level of partnership in research with the UCC and began to develop their own UCC test rig. This AFIT rig has gone through three major combustion chamber redesigns in its history, as well as two air source configurations in that time. The original UCC Combustion cavity (UCC version 1 or UCC v1) was a 60° sector model of the combustion chamber seen in Figure 2.16. Lebay [21] was the last individual to predominately use this rig and he accomplished flow characterizations within the visual section of the 60° section by performing PLIF and PIV within the core flow and outer cavity flow.

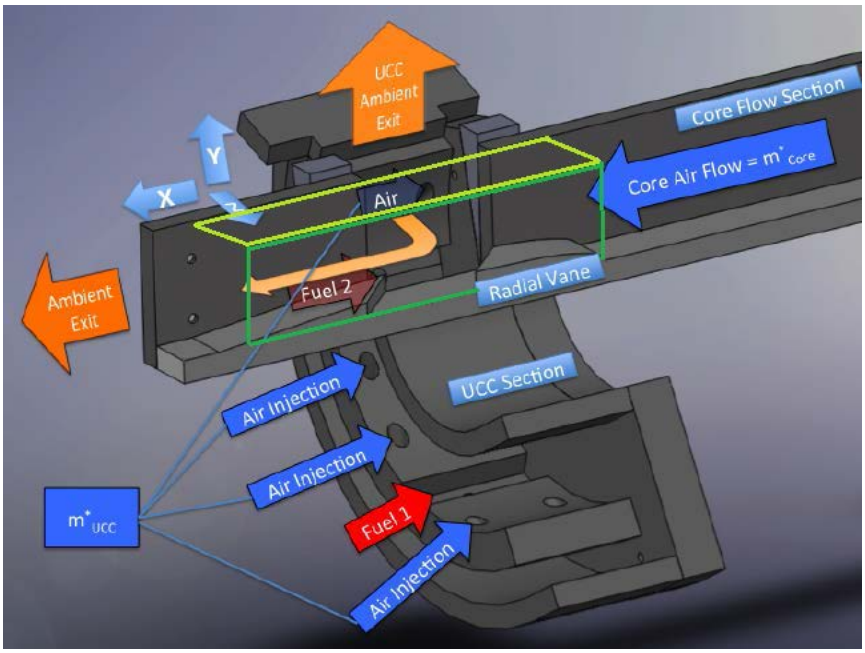

Figure 2.15: AFIT Sectional UCC (UCC v1). [21]
Note: The walls of the rig were clear to allow visibility within the colored box

This concept then progressed to a full-annular design analytically started by Bohan and Polanka [22] who considered the feasibility of a UCC as the main combustor within a fighter-sized aircraft. Wilson and Polanka [5] reduced the scale of the Bohan computational design from a 20-vane to a 6-vane test rig size. This design, called UCC version 2 (UCC v2), maintained a fixed combustion chamber height and width but altered many features within it, to include the air injection driver location, center-body vane geometry and exit plane instrumentation. The most significant of these changes was the work of Conrad [28] and Cottle et al. [6][23] to transition from a discrete (i.e. separate) air source with the air injection holes around the outer annulus (as shown by the air injection arrows in Figure 2.16) to a common air source (i.e. diffuser) with the air drivers on the front plate [6].

A third version of the UCC (UCCv3) was recently constructed by Cottle et al. [23] which increased the aspect ratio of the combustion chamber, and increased the uniformity of the air injection scheme by evenly distributing the air injection holes around the entire

circumference, as opposed to UCC v2 which had gaps in coverage where the plates were placed. This geometry is more fully discussed in Section 3.1.2.3.

2.4.2.1. Hybrid Vane Development

The original AFIT UCC was a 60° representation of the fully annular, 360° combustor. This "sectional model" greatly increased optical access into all sections of the combustor and allowed for easy parts exchange for optimization studies. Based on the previously mentioned results of AFRL, Bohan and Polanka [22] began investigating the construction of a fully annular UCC at AFIT. They used sectional model results to inform their design, and conceived of a new hybrid vane concept that they added into their analysis. Typically, the combustor has a compressor stator preceding it and a fixed inlet guide vane following the discharge nozzle. The last compressor stator reorients the flow entering the combustor, and the inlet guide vane re-swirls the flow prior to the turbine rotor. The hybrid vane Bohan designed employed these two flow guidance devices into one under the combustor section. The computational model also suggested that there would be a reduction in pressure loss across the blended space when compared to the total pressure losses across all three components.

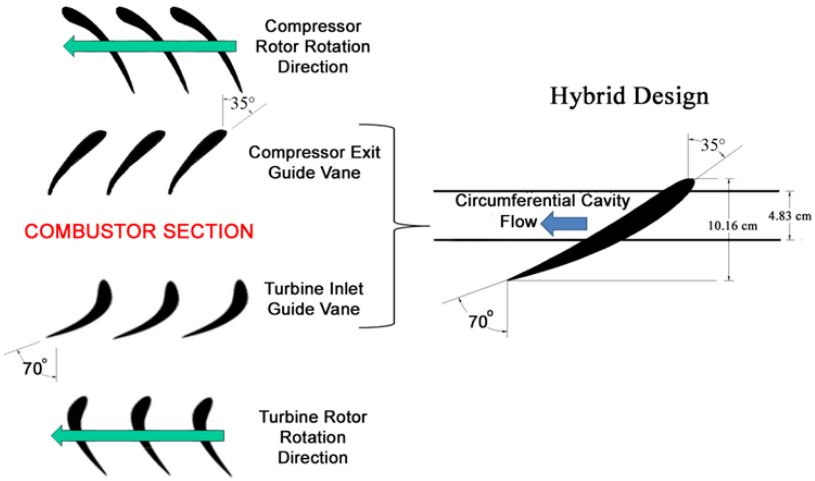

Figure 2.16: Bohan's Design of the Hybrid Vane [22]

Bohan and Polanka [22] also employed a computational model to vary the number of inlet radial vanes and the geometry within the UCC for a fighter sized aircraft. Modifying the cross-sectional area of the hybrid vanes, the number of hybrid vanes, the solidity (the ratio of the former two parameters), or combustion cavity volume did not register any distinguishable variance upon the g-load. However, the 20 vane configuration was found to have the lowest pressure losses of 5.9% static and 4.7% total pressure loss values and a flame length of approximately 33 cm. These values are all lower than a traditional combustor and were even more impressive since they included the losses due to the turning of the compressor and turbine stators, which are not normally accounted for in combustor efficiency calculations. The number of vanes was shown to affect the exit temperature the most, with more vanes resulting in a higher inner turbine temperature profile while decreasing the magnitude of the time fluctuations. The 20 vane, 28.75 cm^2 area air inlet also provided the best temperature and velocity profile, due to the decreased number of inlets within the combustor and large inlet cross-sectional area.

Upon the completion of Bohan's preliminary research, a full 360° UCC was designed, constructed, and assembled by Wilson et al. [24][25] at the AFIT COAL Lab based on a smaller diameter version of Bohan and Polanka's [22] geometry. Wilson et al. [24] scaled the size down from a 20-vane model to a six-vane test model. This reduction also required significantly less mass flow rates, which the AFIT complex could accommodate, and allowed for increased modularity as well as optical access within the combustion cavity. Modularity was sought in order to switch operation of the UCC between a main combustor and an ITB configuration. The modular design also eased integration efforts with future modifications and improvements. The increased optical access allowed for non-intrusive fluid measurements to be taken within the turbulent and high temperatures of the combustion cavity.

Wilson *et al.* [24] ascertained the Lean Blow Out (LBO) conditions of the AFIT UCC by igniting the engine at a high Φ case and, subsequently, decreasing the equivalence ratio until blow out occurred. These tests were performed at different core-flow-to-cavity-flow air splits ranging from 87/13 to 60/40. The LBO was found to be dependent on the cavity g-loading parameter and cavity equivalence ratio; increasing the cavity g-load necessitated the increase of Φ_{Cavity} as well. Wilson *et al.* [24] also found that modifying the air injection scheme consequently altered combustor performance. The air injection holes were drilled into the radial edge of the combustion chamber with varying hole diameters of 0.35 cm, 0.45 cm and 0.65 cm at a tangent angle of 35°; the flow direction was also toggled between clockwise (CW) and counter-clockwise (CCW) for all hole schemes as viewed from looking aft-to-forward. Their results confirmed earlier computational findings that larger hole diameters decreased the tangential velocity components within the combustion cavity. This in turn lowered the g-load and required a higher mass flow through the air injection holes in order to sustain combustion. An example of their findings can be seen in Figure 2.17 for the specific case of a high Φ, a constant core $\dot{m}$ of 3.24 kg/min while varying air driver diameter and the cavity flow mass flow.

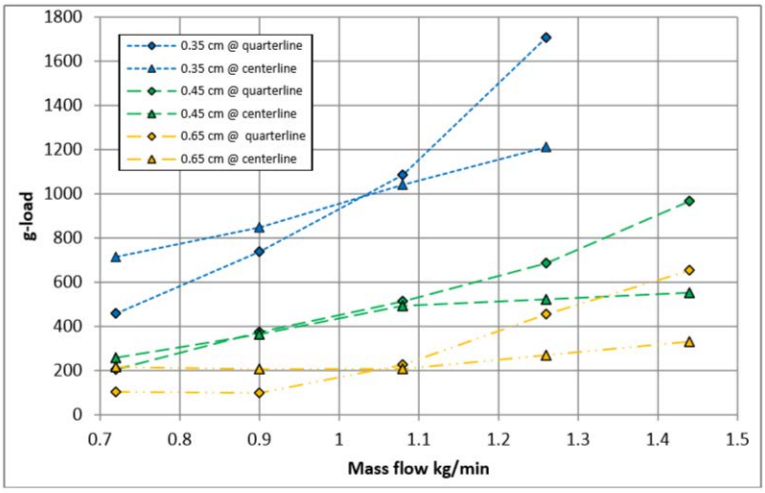

Figure 2.17: G-Loading Data for Various Hole Diameters for the AFIT UCC Model [24]

While this data shows that the smaller the jet size, the larger the g-load imparted within the cavity, the higher g-loads did not correlate with increased stability. As Wilson *et al.* [25] reveal in their text, the smallest hole diameter of 0.35 cm experienced LBO far earlier than the other jets despite the high g-load present. This phenomenon was investigated by placing a second probe at the quarter-line position, informing how the g-load at high air injection flows begins to diverge in value from the centerline position. The air flow and density gradients caused by the circumferential flow impacting the fuel jet, causing a substantial velocity gradient, increased mixing, and instability within the cavity. These conditions lowered the tangential velocity component at the centerline of the cavity. They also found that blowout occurred sooner for the 0.65 cm jet diameter than the 0.45 cm diameter. Therefore, it was determined to use the 0.45 cm hole-size diameter in future design iterations of the UCC with this air injection scheme.

Wilson *et al.* [24] likewise tested the effect of altering the orientation of the flow within the combustion cavity. The CW flow was oriented such that it struck the suction side of the hybrid vane airfoil (traditionally viewed as the upper portion of a 2-D airfoil); the CCW flow struck the pressure side of the radial vane airfoil (traditionally viewed as the bottom portion of a 2-D airfoil). The CCW flow resulted in the core flow turning the cavity flow (as shown by the red arrow in Figure 2.17) in order to accommodate the flow passages. This turning caused unsteadiness and varied g-loads within the cavity, exacerbating pressure losses by 50%. Therefore, while having the hot gases strike the pressure side of the airfoil would have been preferable as it would be easier to cool, CW combustion cavity flow was determined to be the way forward.

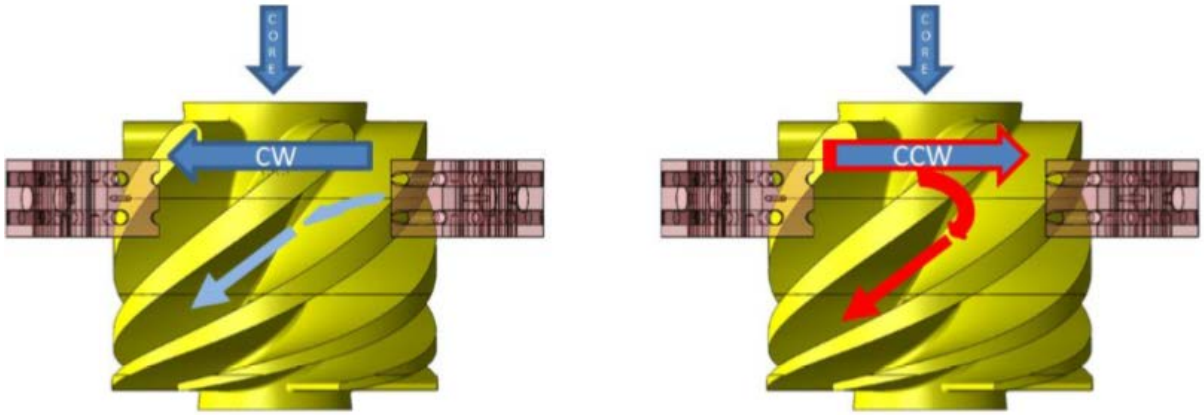

Figure 2.18: Cavity Flow Orientation as Originally Described by Wilson [24]

Wilson and Polanka [5] discovered during modeling and construction that the original constant radius hybrid vane resulted in high Rayleigh losses through the intermediate zone. Rayleigh losses are the high total pressure loss of a flow through a channel when there is significant heat transfer out of that flow [26]. They typically occur when there is sustained heat generation through a channel of fast moving air (Mach > 0.30), such as the combustion chamber and the flow through the hybrid vane. Saad [26] developed Equation (9) relating the losses in Mach (which corresponds to the pressure loss) to the area and total temperature (T_t) of the chamber:

$$\frac{dM}{M} = \frac{1 + \frac{\gamma - 1}{2} M^2}{M^2 - 1} \frac{dA}{A} - \frac{(\gamma M^2 + 1)\left(1 + \frac{\gamma - 1}{2} M^2\right)}{2(M^2 - 1)} \frac{dT_t}{T_t} \tag{9}$$

While Radtke *et al.* [27] found that the AFRL UCC small sectional model resulted in only a 2% pressure drop due to Rayleigh losses, Bohan [22] later found that the full annular UCC resulted in losses near 12%. To combat this pressure loss, Wilson designed with a 2-D MATLAB model a low-loss center body (LLCB) hybrid vane with variable radial height and cross-sectional area. These modifications improved the combustion efficiency and reduced the

local Mach number, thereby decreasing pressure losses. Downward flow migration was also increased allowing more of the combustion products to experience the quick-quench process. This change also helped migrate the high temperature exhaust flow away from the inner diameter, which was a previously noted problem. The LLCB also resulted in the Rayleigh losses being reduced from 10% to a maximum value of 4.2% [25].

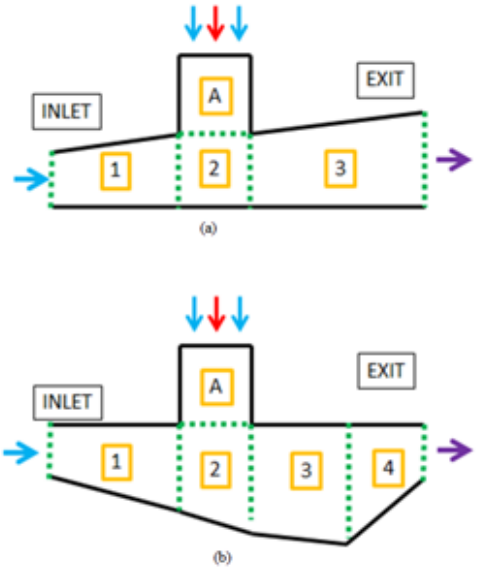

Figure 2.19: Wilson's (a) Tapered Center-body (TCB) Design and (b) Low Loss Center-body (LLCB) Design [25]

2.4.2.2. Common Air-Source Diffuser Development

Conrad *et al.* [28] integrated a common core diffuser that supplied the air for both the core air flow and air injection holes. The air injection scheme was transitioned from Wilson's original design with six air ports feeding the air driver jets around the outer ring to a single source feeding the core flow and three plates with multiple rows of small angled holes on the forward face of the combustion chamber. These angled holes can have varying diameters (from 0.35 cm to 0.65 cm) and angles (from 35° to 55°) to impart the requisite swirl within the combustion chamber to incur a g-load. For Conrad's work, these values were held constant at

0.45 cm and 35°. The diffuser that Conrad designed diverted a certain percentage of the inlet mass flow to the core flow and outer cavity flow, which he denoted as "70/30" for when 70% of the total inlet mass flow was diverted to the core cavity and 30% of the total inlet mass flow was diverted to the combustion cavity air injection plates. For clarity, this presentation of the mass flow split is maintained throughout the rest of this document. Conrad [28] then computationally researched what the appropriate core-to-cavity air flow ratio should be in order to aid in future design of the diffuser geometry. This analysis used the commercially available CHEMKIN reaction modeling software.

In order to determine the separation criteria for the diffuser geometry, Conrad used Reneau *et al.* [29] Diffuser Design Manual to prevent stall within the cavities and reduce pressure losses. In order to accomplish this, Conrad used the existing constraints of the inner core diameter to determine the height of the middle diameter splitter plate. From this, the axial length was determined to be 12.7 cm and the geometry was determined by the equation:

$$\log(AR) = 0.1950 \log\left(\frac{L}{H}\right) + 0.1647 \tag{10}$$

where AR is the cross-sectional area ratio between the outer (cavity) flow path and inner (core) flow path, L is the length of the diffuser from the aft of the channel to the tip of the splitter plate, and H is the distance from the inner diameter outer radius to the tip of the splitter plate.

Conrad then sought to determine the air flow split that would produce the balance high thermal efficiency with low pollutant emissions (NO_x, CO, and THC). He analytically validated the design using the commercially available CHEMKIN chemical reaction model to test the emissions and efficiency performance of the theoretical diffuser split. His model used Dodecane, which he showed could be used to approximate kerosene and JP-8 combustion. The UCC was modeled as a well-stirred reactor in this model due to its previously noted high

efficiency and high density gradients. He obtained data for the air-fuel split ranges of 80/20, 70/30, and 60/40.

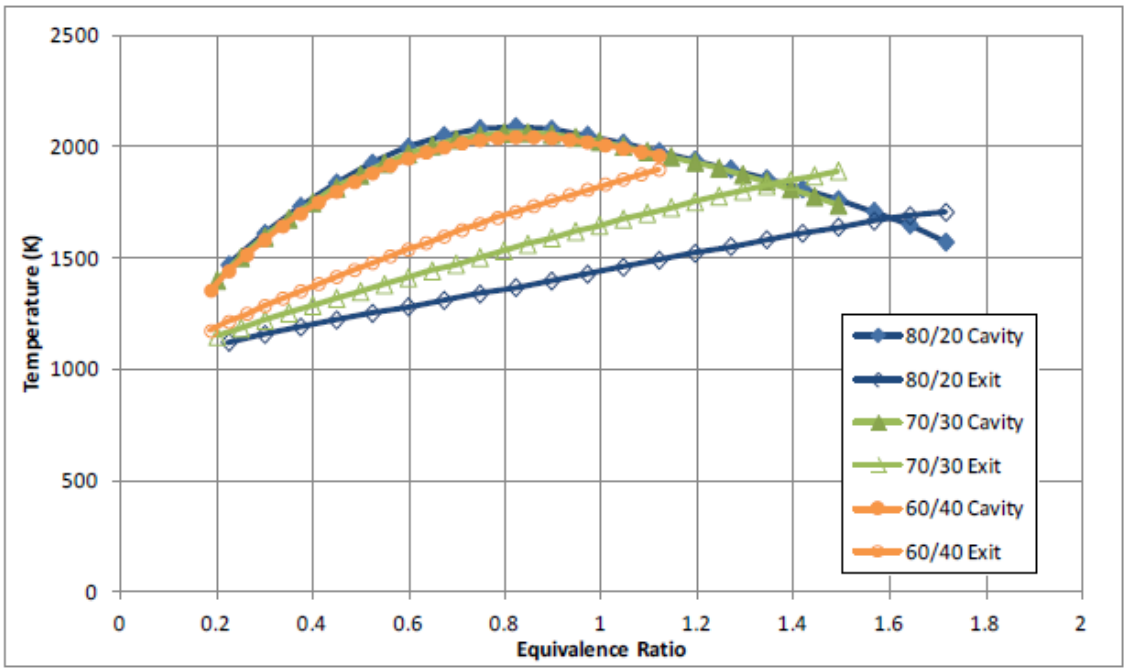

Figure 11: Cavity and Exit Temperatures

Figure 2.20: Predicted Cavity and Exit Temeratures [28]

By balancing the "best blend of efficiency and emissions output", Conrad [28] determined the predicted ideal flow split to be 70/30. This design point maintained the peak efficiency values seen using the 80/20 split while also significantly decreasing the pollutant emissions from the UCC. A summary of his emission results that keyed this accommodation can be seen in Figure 2.20 and Table 2.1.

Table 2.1: CHEMKIN Predicted Emissions Results at Exit Plane [28]

Core / Cavity Split	80/20	70/30	60/40
Equivalence Ratio	0.67	0.45	0.34
Temperature (K)	1310	1319	1318
NO_x (ppm)	63.98	38.74	33.92
THC (ppm)	0.15	1.14	7.03
CO (ppm)	2865	1803	1828

Cottle [6] then characterized this new diffuser using the 70/30 splitter plate. In order to perform a proper characterization of the diffuser, he performed both computational fluid dynamics (CFD) and an experimental characterization on the common source diffuser. From this, it was determined that the diffuser design suffered from separation regions and pressure losses when the diffuser had only air passing through it ("cold flow") or combusting ("hot flow"). These large recirculation regions in the outer diameter cavity reduced the mass flow and velocity into the combustion cavity, which prevented combustion from occurring and limited the operating range of the UCC.

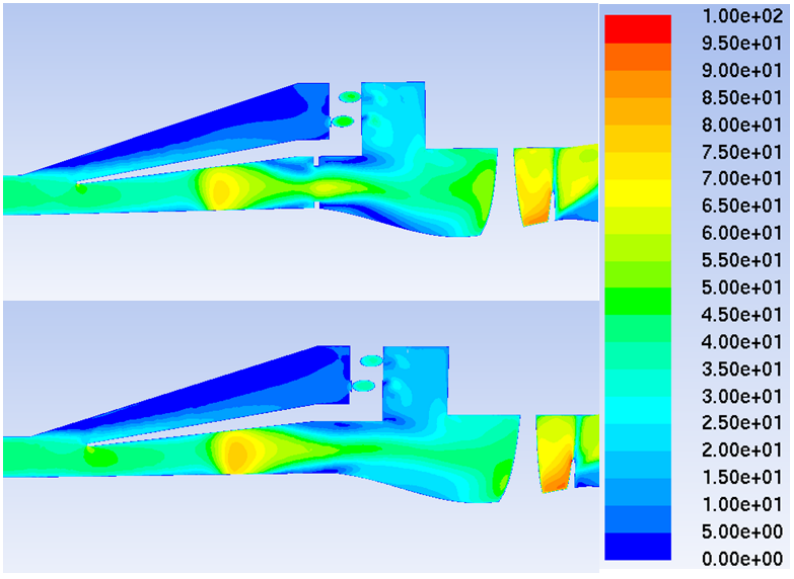

Figure 2.21: CFD velocity contours [in m/s] demonstrating the effects of no flow blockage (bottom), and the more "optimal" flow blockage (top) at inlet mass flow of 0.18 kg/s [6]

Figure 2.21 shows the effect of these large recirculation regions in the cavity flow. The bottom picture shows the velocity within the entire diffuser and combustion cavity section, while the top shows the same view only with a blockage plate installed. The velocity in the outer cavity (bottom picture) of the diffuser is zero for over half the area, and has minimal mass flow to the upper set of air injection holes. This stagnation region is the result of the diffuser plate's failure to create a sufficient pressure gradient to redirect the air flow out of the core and into the outer passage. This in turn limits the air provided to the air-jet driver holes and reduces the exit velocity from the injection drivers. This phenomenon occurred over the entire test range of total inlet mass flows from 0.12 kg/s to 0.24 kg/s. To help assuage this problem, Cottle [6] designed a "channel plate" which reduced the cross-sectional area open to the core flow. This created additional back pressure in the core flow that propagated upstream and forced more air into the outer cavity, as can be seen in the top-most cross-section of Figure 2.21. The area restricted by the channel plate was defined in the paper as the non-dimensional ratio (λ), which related the ratio of the two cross-sectional areas to the total annular area available. This equation was:

$$\frac{A_{channelPlate}}{A_{core}} = \lambda \frac{A_{injectionHoles}}{A_{cavity}} \tag{11}.$$

Cottle [6] first published his CFD and experimental results for cold flow, in which the model predicted an optimal value of $\lambda_{70} = 4.6$ (where λ_{70} is defined as the area ratio required to achieve a 70/30 split). However, the experimentally determined value was subsequently found to be $\lambda_{70} = 4.0$ [30]. These values helped improved the fidelity of the CFD model and were used to predict the effects with combustion ("hot flow"). A λ_{70} value of 5.0 was found to be optimal with the Cottle CFD combustion model [23]. The higher ratio value for hot flow was expected since the combustion event increases the back pressure within the combustion cavity.

This in turn increases the back-pressure seen at the splitter plate, which means a smaller hole in the blockage plate is needed to achieve the same core-to-cavity split seen for cold flow.

2.5. Temperature Measurements and Thin Filament Pyrometry

The main purpose of a combustor is to add chemical energy into the flow through an engine; this chemical energy is converted to mechanical energy that provides thrust, power to onboard systems, and drive to the compressor. With increased exit temperature comes increased potential energy; as discussed in Section 2.4, the temperature magnitude is not the only point of concern, but the exit profile as well. Temperatures within the combustion chamber are also of primary interest, as it is in here that the majority of chemical reactions occur. As Turns [2] notes, the temperature of combustion keys different reactant chains and mechanisms that can alter the emissions, especially Nitrous-Oxide production and to a lesser sense Carbon Monoxide. Therefore, a fine resolution of the temperature profile both within the combustion cavity and the exit plane are desired.

Traditional temperature measurements use a thermocouple to find a point measurement. According to the Omega [31], thermocouples join two dissimilar metals at the location of the measurement. The voltage across these two metals changes as the temperature applied at the measurement location changes, and this change can be measured and correlated to a specific temperature. This phenomenon between two different metals is called the Seebeck effect.

An alternative method of temperature acquisition is Thin Filament Pyrometry (TFP). According to Vilimpoc, Goss and Sarka [32], this method places a thin rod of heat resistant material normal to the flow of interest. The rod then glows (like an incandescent bulb) and its intensity is captured by a high speed camera (known as the intensity-ratio method). If the material is assumed to be a gray body, then Planck's Equation can be used to determine a

relation between temperature, angle, wavelength and emissivity. The authors show that β-Silicon Carbide (β-SiC) has a high emissivity and a weak relation between temperature and the wavelength, and angle of the filament. They found that there was a less than 1.0% error in the temperature measurement so long as the image was captured at an angle normal to the wire within ±45°. Each filament requires individual calibration, a process that requires placing it within a flame of known temperature (such as a propane-air premixed flame) and acquiring the signal of the flame. The flame's signal is then used to normalize and calibrate the filaments using the curve in Figure 2.22 or Equation (12).

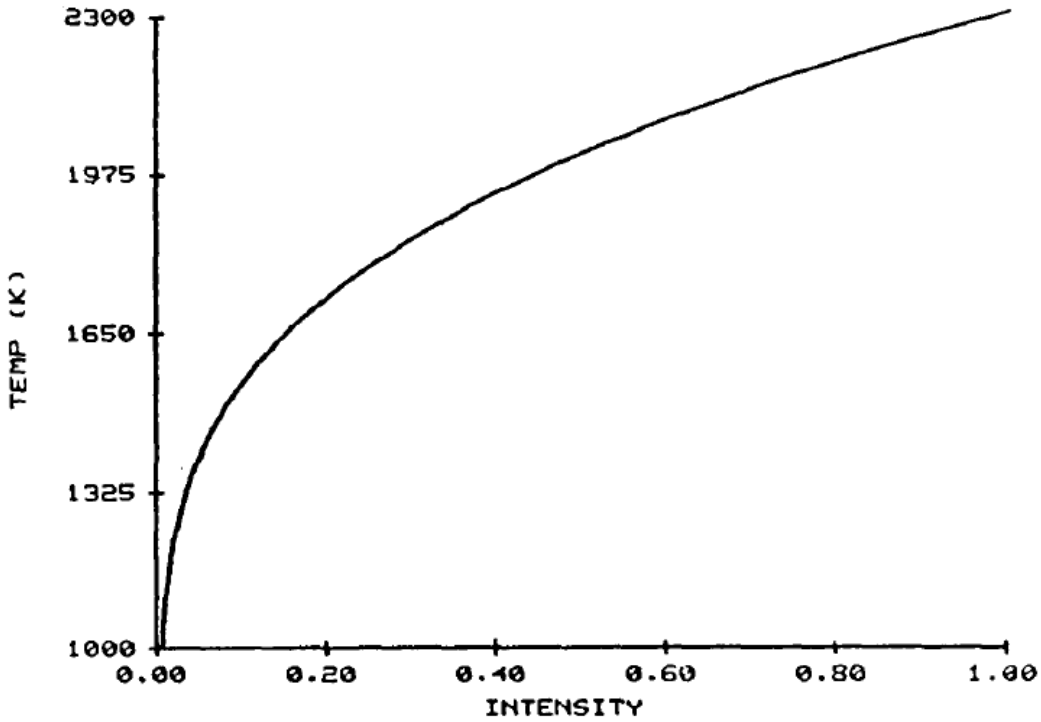

Figure 2.22 Calibration Curve used by Vilimpoc *et al.* to calibrate β-SiC filaments [32]

$$I_R = \frac{\epsilon I_b(\lambda, T)}{\epsilon I_b(\lambda, T_0)} = e^{\frac{c_2}{\lambda}\left(\frac{1}{T_0}-\frac{1}{T}\right)} \tag{12}$$

In the above equation, I_R is the Intensity ratio of the filament at its calibrated temperature, $I_b$is the spectral radiance calculated by Planck's equation for wavelength λ and temperature *T*, *T* is the measured filament temperature, T_0 is the calibration reference temperature, and C_2 is Planck's second constant.

Also considered in this method was the correction needed to equate the filament's temperature with the local gas temperature [32]. The filament temperature is actually lower than the surrounding gas temperature, and this reduction is due mostly to radiative heat loss. Conductive heat loss both into the mounting apparatus and across the filament is minimal as β-SiC has a low thermal conductivity (3.6 $W*cm^{-1}*K^{-1}$) and therefore were neglected in the analysis. Initially, only the losses to the gas were considered, however, in subsequent research the radiative effects of the walls surrounding the filaments were also accounted for [33]. To do this, a model developed originally by Mossey et al. [34] in FORTRAN for thermocouples was converted to a Microsoft Excel file to account for six different heat fluxes seen by the filament: Convection of the gas temperature into the filament, radiation to the surroundings, radiation from gas to surrounds, stem conduction, Boundary Layer distortion, and surface reaction. The equation that converted the filament temperature to the gas temperature was:

$$T_g = \frac{\epsilon\sigma(T_f^4 - T_\infty^4)}{h} + T_f \tag{13}$$

where T_g is the gas temperature (desired), T_f is the measured value of the filament or thermocouple probe, ϵ is the emissivity, σ is the Boltzmann Constant, *h* is the convective heat transfer coefficient, which is dependent on the thermodynamic properties and velocity of the flow. It was found by Goss [51] that for a gas temperature of 1000 K, the radiation correction was 5 K while for a gas temperature of 2000 K, the correction increased substantially to

approximately 100 K. The conversion between the filament temperature and the gas temperature is given by the blue data set and trend-line in Figure 2.23, with the lower limit of TFP given by the solid black line and the upper limit of the data shown with the dotted black line. As the data shows, the correction adds between 2 K at low temperatures and 87 K for the highest temperatures sampled.

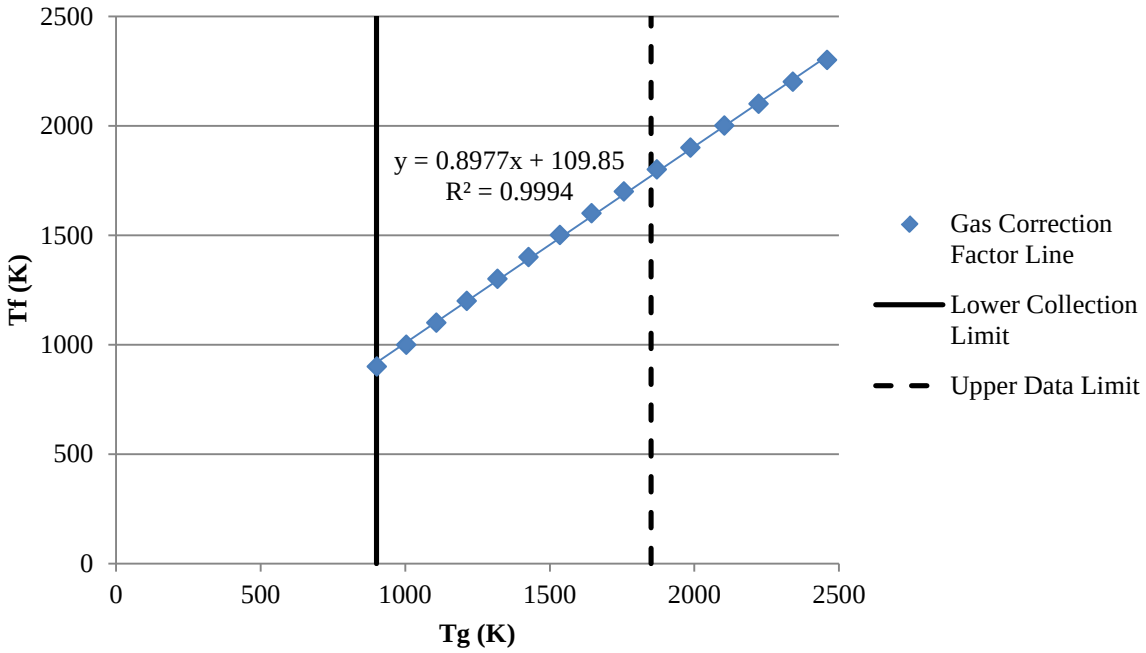

Figure 2.23: Filament to Gas Temperature Correction Curve for UCC experiment Calculated by Goss [51] using the methods of Mossey *et al.* [34]

The benefits of TFP are great compared to thermocouples. For example, the filament provides temperatures across the entire span of the cable, rather than at a single point value with a thermocouple. It also is very responsive to changes, with the calculated response time being 1.9 ms (equivalent to 500 Hz). The spatial resolution along the filament was noted by Vilimpoc, Goss and Sarka [32] to be 120 microns in length for this experiment, while the width was diameter of the filament. Finally, it allows for full span characteristics within combustion environments.

2.6. Temperature Profiles and Pattern Factors

One concern with UCC operation is whether the primary combustion zone can still produce the same pattern factors and profile factors found in traditional jet engines. As Samuelson [35] explains, temperature profile shapes are used to analyze average and maximum distributions across turbine stages in order to protect the component's structural integrity. Samuelson [35] defines the pattern factor and profile factor to characterize the combustor exit temperature profile across the span of a turbine component.

$$Pattern\ Factor = \frac{T_{max} - T_4}{T_4 - T_3} \tag{14}$$

$$Profile\ Factor\ = \frac{T_{mean} - T_4}{T_4 - T_3} \tag{15}$$

In Equations (14) and (15), T_{max} is the maximum recorded temperature, T_3 is defined as the average combustor inlet temperature, and T_4 is the average combustor exit temperature (or bulk temperature). Therefore, the pattern and profile as defined by Samuelson [35] are single point, non-dimensional values that expresses the deviation of the maximum temperature from the bulk temperature of the combustor and the deviation of the bulk exit temperature from the inlet temperature (respectively). Data collection apparatuses are traditionally placed immediately at the exit plane of the combustor since this is where the turbine section starts and must come contact with the hot exhaust gases.

Since the region of interest is the entire span of the exit plane, where the combustion flow strikes the inlet guide vanes, a different value was sought to graphically normalize the flow. To do this, Lefebvre and Ballal's [14] textbook (Samuelson's source for the Profile Factor) was consulted. The book stipulates that these factors are best used when the exit-temperature distribution is ideal (constant value across the span), which is not the case in modern jet engines.

Therefore, a new parameter was created to normalize the values of the temperature across the entire span. This equation uses the same denominator as the three factors given by Lefebvre and Ballal's [14] to normalize the factor to order unity, and the numerator uses the average exit temperature value to show where values are lower than the average (negative) or higher (positive) and the percent the temperature deviates from the average. Equation (16) shows the computation used:

$$Local\ Profile\ Factor\ = \frac{T_{4_{Local}} - \overline{T_4}}{\overline{T_4} - T_3} \tag{16}$$

where $T_{4_{Local}}$ is the local time averaged value of temperature, T_3 is defined as the time averaged combustor inlet temperature, and $\overline{T_4}$ is defined as the time and span-wise averaged combustor exit temperature (or bulk temperature).

Large variations of the local temperature from the axial location's mean value in both the radial and circumferential directions can lead to hot spots, which weaken structural integrity and reduce part lifetime. Typically, the local temperatures at the inner and outer radius locations are reduced below that of the center, mean value. The inner radius is the more critical of the two, as it secures the component to the rotating shaft [35]. High temperatures near the tip of the blade are also not preferable since the leakage causes heat transfer into the engine wall and burns up the tip of the blade [36]. This additional heat must be cooled with either complex liquid systems or bleed air from the compressor core flow; both options increase the complexity of the engine and decrease performance. Therefore, the combustion gases must be designed to migrate through the turbine section to focus the hottest gases into the mid-span region of the turbine, but with a slight skew to the outer diameter.

Damele *et al*. [37], using two independent, discrete air sources where air was supplied by six holes around the combustion cavity ring, alternating between the six fuel jets, confirmed upon the full annular UCC the trends seen by Lebay *et al*. [36] in the sectional UCC: increasing cavity equivalence ratio increases the temperature, but not the overall temperature profile shape. However, Damele et al. [37] also showed that the discrete air source produced undesirable temperature profiles that had the highest temperatures skewed to the outer diameter. Figure 2.24 shows how the same temperature bias toward the outer diameter was found to exist for all flow splits and all flow conditions.

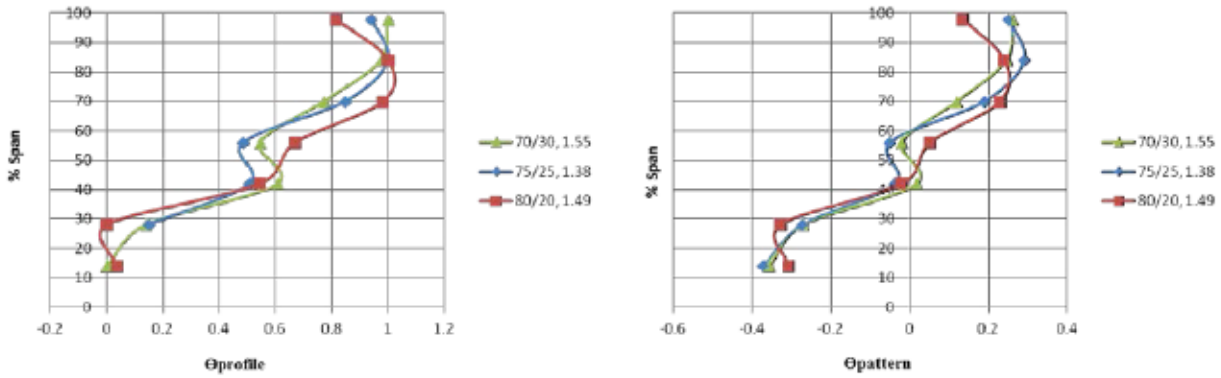

Figure 2.24: Pattern and profile factors of varying flow splits for AFIT UCC [37]

The one factor noted to prominently change the temperature profile was the mass flow split. The greater the mass flow split favored the core flow, the further the peaks for the temperature profile and pattern factors were pushed outward. Therefore, in order to improve the integration of the UCC into an aircraft jet engine, more hot gas must be allowed to penetrate deeper into the radial vane channel while keeping the 70/30 core split, which has been shown to have optimal combustion efficiency [28] and operation range [37]. Damele *et al.* [37] recommended altering the internal geometry of the engine in order to encourage the pattern

factor to resemble those employed in modern aircraft engines, thereby accommodating existing turbine cooling schemes.

Previous work by Mawid *et al.* [38] show potential means for improving the exit temperature profile of the UCC. Their initial assessments considered the most favorable shape of radial vane cavities (RVC). The three geometries considered were a backward facing step on the suction side (where the thickest portion of the cut was closer to the front), forward facing step on the suction side (where the thickest portion of the cut is closer to the aft), and a dual rectangular cavity, where there was an RVC of equal depth extending one-fourth of the chord in on both the suction and pressure side. Figure 2.25 is provided to depict these three geometries.

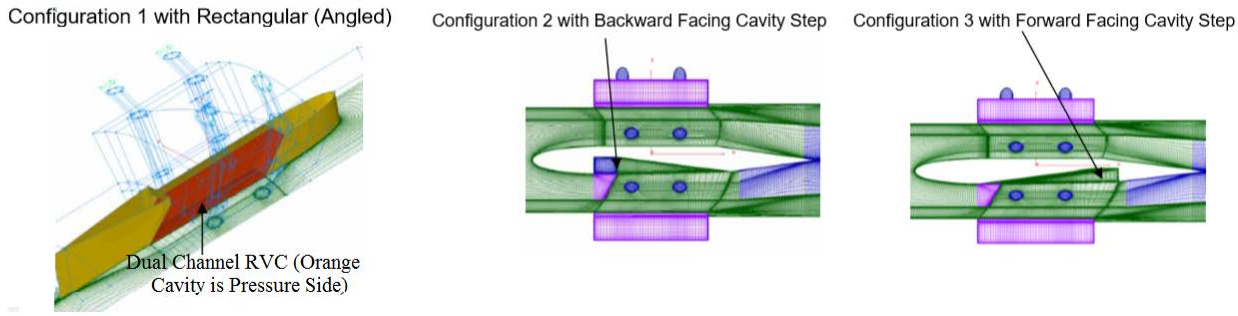

Figure 2.25 RVC Geometries analytically considered by Mawid *et al.* [38]

Mawid et al. [38] performed CFD upon the AFRL UCC rig using straight vane geometries and three different RVC geometries. Their CFD analysis used a large Reynolds number k-ε turbulence model, with the JP-8 fuel source modled by a stochastic (non-steady state source) STAR-CD sub-routine liquid spray model and a simplified two-step chemical reaction scheme. This reaction sequence used was taken from past studies wih JP-8 and consisted of:

$$4\ C_{12}H_{23} + 35.5\ O_2 \rightarrow 48\ CO + 46\ H_2O \quad (17)$$

$$CO + 0.5O_2 \rightarrow 48\ CO_2 \quad (18)$$

The computational grid also was fine enough to resolve the viscous boundary layers and was built using the GRDGEN software package. From these inputs, they were able to track the time-averaged: axial, tangential and total velocities within the UCC; temperature distribution; and the fuel, air and cavity mass concentrations rates at the exit plane and within the cavity. When considering all this data, they found that the RVC was successful in migrating the combustion cavity flow radially inward. The Backward Facing Cavity was too effective in doing this however, allowing for uncombusted fuel to escape the cavity. Figure 2.26 shows how the Backward Facing Step had the same magnitude of fuel-to-air as the other two conditions for span heights below 40%, but significantly higher fuel concentrations in the outer diameter.

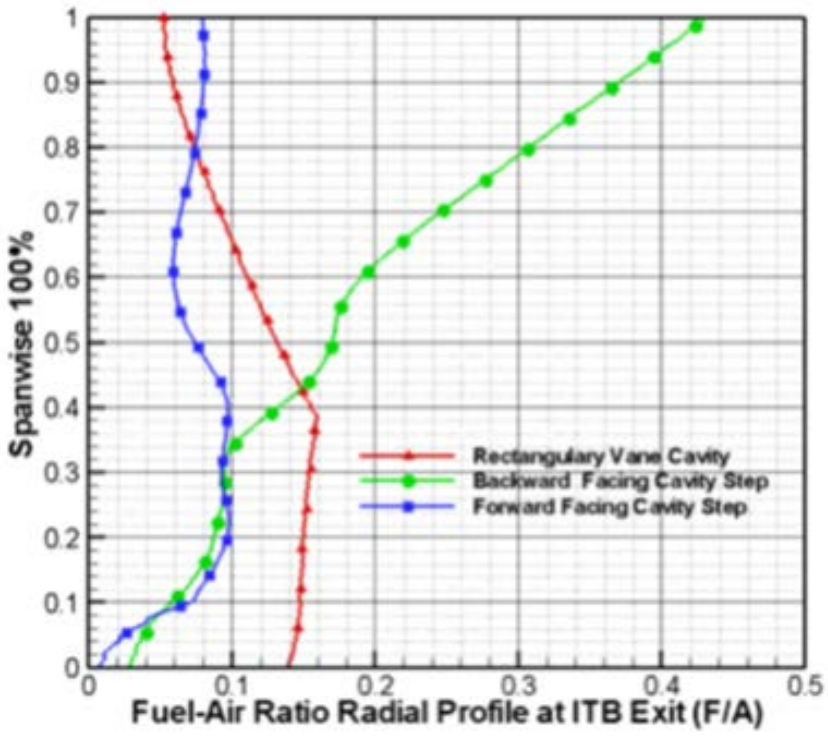

Figure 2.26: Computed ratio of Fuel Mass to Air Mass Ratio at UCC/ITB Exit Plane [38]

The fuel escaping greatly reduced the efficiency of the combustor section and lowered the temepratures seen throughout the combustor. Also, this problem could lead to burning within

multiple components of the turbine, which would increase the thermal fatigue of the turbomachinery. Therefore this was not a viable option for optimizing the profile factor.

The single Forward Facing Cavity also presented problems when simulated. This RVC created a pressure bubble which decreased the flow out of the combustion cavity. This in turn increased the average residence time of the gas, which normally is desired. However, the back pressure created by the cavity also limited the migration of the products radially inward, confining most of the thermal energy to the upper 30% of the span as seen in Figure 2.27.

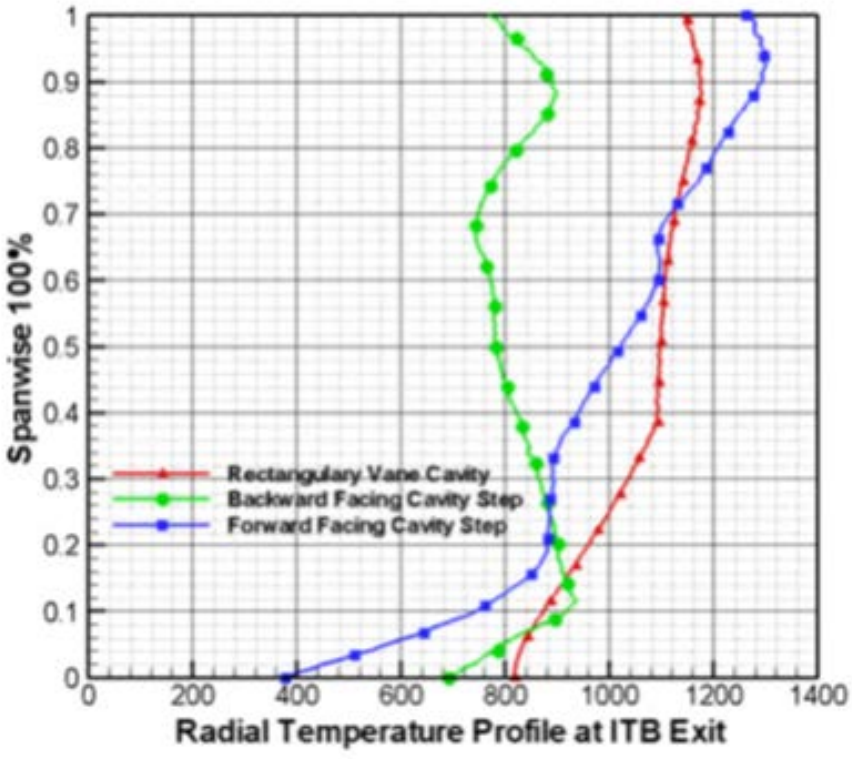

Figure 2.27 Radial Temperature (K) Profile at UCC/ITB Exit Plane [38]

This temperature distirbution is also as it is too biased to the upper profile. However, by using the combination of both a backward facing step and forward facing step, the benefits upon the temperature profile also combined to shift the temperature distributing away from the outer

radius. This RVC will increase the pressure drop within the cavity and its magnitude of loss and affects on combustion stability were to be clarified in subsequent tests.

Providing further insight into the anticipated behavior of the AFRL UCC, Thornburg e*t al.* [39] also executed numeric analysis to determine the effect of altering the combustion cavity flow direction around curved vanes with a single RVC. The airfoil was considered in three configurations: no radial cavity, a RVC placed on the suction side (upper side of a traditional 2-D airfoil) and a RVC placed on the pressure side (lower side of a traditional 2-D airfoil). The flow orientation was also varied between CW and CCW (looking forward from the back). Note, due to the AFRL rig, which Thornburg modeled, having its air jet drivers positioned in the opposite orientation of the AFIT rig, Thornburg's version of CW equates to Wilson's *et al.* [24] CCW definition in Figure 2.18. Thornburg et al. [38] determined that the RVC placed on the suction side with a CCW cavity flow direction was optimal compared to all other combinations. The suction side CW and pressure side CW were the worst performers. The optimal position was due to the escaping cavity flow impacting the suction side of the airfoil, which Wilson *et al.* [24] showed requires less turning by the core flow. The suction side cavity also migrates the hot products down the airfoil span more effectively so the temperature peak occurs at the desired middle radial height position. The authors do concede that further alterations to the air injection scheme and RVC geometry could further increase the optimization of the temperature profile, but more CFD analysis is required. Also, they noted that large hot spots occurred within the RVC, specifically on the aft wall. No experimental data has been published that corroborates these results due to the difficulty in constructing the vanes.

2.7. Emissions

Emissions data is of great concern in the modern aircraft engine operational environment. As Turns [2] notes, emissions regulations began in the 1950s with automobiles and greatly increased under the implementation of the Clean Air Act it of 1990. Pollutant emissions, such as nitrous-oxides, carbon-monoxide and carbon dioxide have negative effects upon the environment, to include altered weather patterns, deterioration of soil and vegetation, as well as increasing the morbidity and mortality of humans [40]. Since the chemical composition is changed primarily in the combustor, the gaseous emissions of the UCC must be isolated and categorized in order to ensure that it meets existing government standards. By categorizing the emissions data, future integration efforts are eased between the UCC and modern aircraft engine components.

The Department of Defense is interested in combustor emissions for two reason. As Sturgess *et al*. [41] explains, U.S. Military aircraft are typically exempted from EPA standards governing commercial aircraft. However, they must comply with the National Ambient Air Quality Standards (NAAQS) and State Implementation Standards, which regulate the amount of emissions of departing aircraft. Furthermore, most aircraft engines are derivatives or commercial-off-the-shelf copies of civilian aircraft jet engines, which must be designed to comply with EPA regulations. Since combustors are the primary producers of pollutants, the U.S. Military and engine developers must concentrate their efforts on combustor emissions while maintaining its efficiency.

The difficulty that engine designers face is the inherent trade-offs between emissions control and performance. Sturgess *et al*. [41] summarizes that the two basic types of trade-offs are those between emissions and combustor performance and secondly between the different

emission species themselves. Emissions generation has a dichotomous relationship between efficiency and the different gaseous components that comprise it. For example, the high pressure increase seen in modern combustors increases the efficiency of the engine, and therefore decreases the CO_2 levels produced. However, high-pressure, low-Φ combustion events also leads to increased NO_x production, which is strictly regulated by the U.S. Environmental Protection Agency (EPA).

Sturgess *et al*. [41] summarized the Federal statutes enacted by the EPA, who determined carbon monoxide (CO), unburned hydrocarbons (UHC), oxides of nitrogen (NO_x), and smoke warranted regulation. The Society for Aeronautical Engineers (SAE) [42] concurred and also added the measurement of carbon dioxide (CO_2) to deduce emission indices, fuel-air ratio, combustion efficiency, and exhaust gas thermodynamic properties. In order to properly relate these emissions impact on the environment to the amount of fuel consumed, the emissions index is used (EI). The EI of species "z" is defined as

$$EI_z \equiv \left[\frac{\dot{m}_Z}{\dot{m}_{fuel}}\right] * 1000 = \left[\frac{moles\ of\ z}{moles\ of\ fuel}\right]\left[\frac{MW_z}{MW_{fuel}}\right] * 1000 \qquad (19).$$

Of note is that SAE specifies that when calculating the EI of all oxidized nitrogen molecules, the average molecular weight of all nitric oxide radicals (NO, NO_2, NO_3) is used, which equals the molecular weight of nitrogen dioxide (30.006 g/mol). From emissions data, the isentropic efficiency of the combustor can be calculated. This is accomplished by performing an enthalpy balance of the combustion products and subtracting the EI of CO and UHC normalized by the heat of combustion of those species. The equation is given by SAE [42] as (for SI and English units respectively):

$$\eta_b = \left[1.00 - 10109\frac{EI_{CO}}{H_c} - \frac{EI_{C_xH_y}}{1000}\right] * 100 \quad (20)$$

$$\eta_b = \left[1.00 - 4.346\frac{EI_{CO}}{H_c} - \frac{EI_{C_xH_y}}{1000}\right] * 100 \quad (21)$$

Sturgess *et al.* [41] performed a series of experiments in different combustor types in order to establish common trends for hydrocarbon-based combustion. In a well-stirred reactor the hydrocarbon consumption was ten times the consumption rate of CO when set to idle power. However, the two species are not totally controlled by the same mechanisms. As Figure 2.28 shows, as combustor power is initially increased (moving right to left) the EI of CO and UHC decrease exponentially. This trend continued until the amount UHC remains constant while the amount of CO decreased. Data were taken using a variety of engine sizes and manufacturers, and correlated well between the different types. This trend suggests that, while some of the mechanisms that lead to UHC formation and CO formation are related, CO was dependent upon additional parameters.

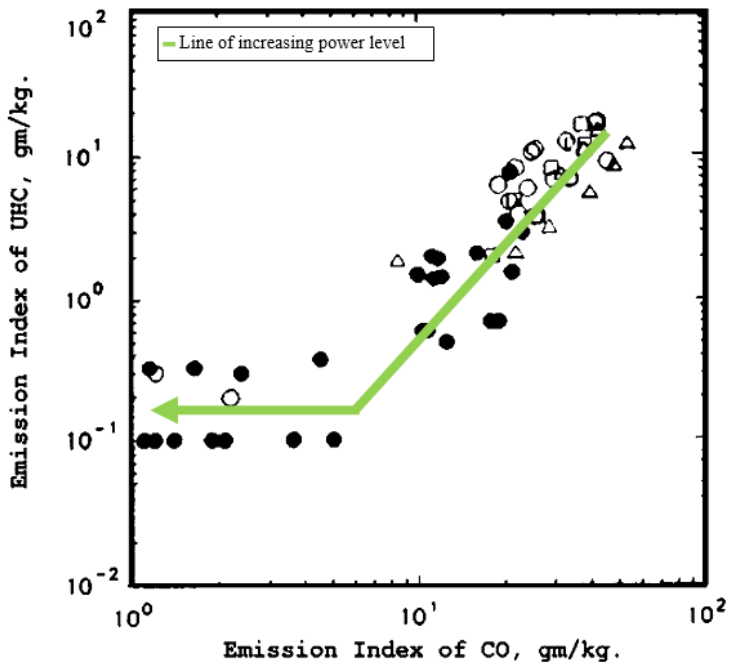

Figure 2.28: Relationship Between CO and UHC Emissions for Several Engines Down an Engine Operating Line [41]

Another combustor design Sturgess *et al.* [41] used to categorize emissions was the Rich-Quench-Lean Combustion (RQL). The purpose of this design was to lower the NO_x emissions of the combustor. Feinmore [43] postulated that combustion at high temperatures in oxygen lean environments ($\Phi < 1$) increased the reaction rate between nitrogen and hydrocarbons to produce NO_x. The high temperature lends enough energy to disassociate an N_2 molecule and have it bond with a free-floating hydrocarbon molecule (typically CH). This leaves one unbound nitrogen that can then collide with a free oxygen atom from the normal combustion reaction. The RQL seeks to rapidly lower the temperature of the gas within the combustor by having it operate at a low Φ during idle operations and high Φ during primary flight operations. This is why the majority of the "cool" air is added in the Dilution Zone in a traditional combustor. Within the UCC, since the core flow mass flow is greater than the combusting circumferential mass flow, a process known as quick-quench, lean-burn occurs between the interface between

the primary zone and the intermediate zone [41]. This process has the hot combustion products rapidly cooled and mixed in with a high amount of oxygen, which provides two mechanisms to encourage combustion to cease. With the lower temperatures, nitrogen does not have enough energy to dissociate or bond with the hydrocarbons, meaning the chemical reaction chain of NO_x never begins.

Zelina *et al.* [11] used straight, symmetric center-body airfoils with both Radial Cavity Vanes and normal airfoil cavity vanes within a UCC to ascertain the emissions characteristics of the engine. The UCC had the minimum EI occur at a higher Φ value than expected for both airfoil profiles. Typically, CO is minimized during near stoichiometric conditions ($\Phi = 1$) but the minimum amount of CO was produced at $\Phi = 1.5$ for the symmetric airfoil and $\Phi = 2.0$ for the RVC. Figure 2.29 shows the EI of CO across all operating conditions for Zelina's experimental rig.

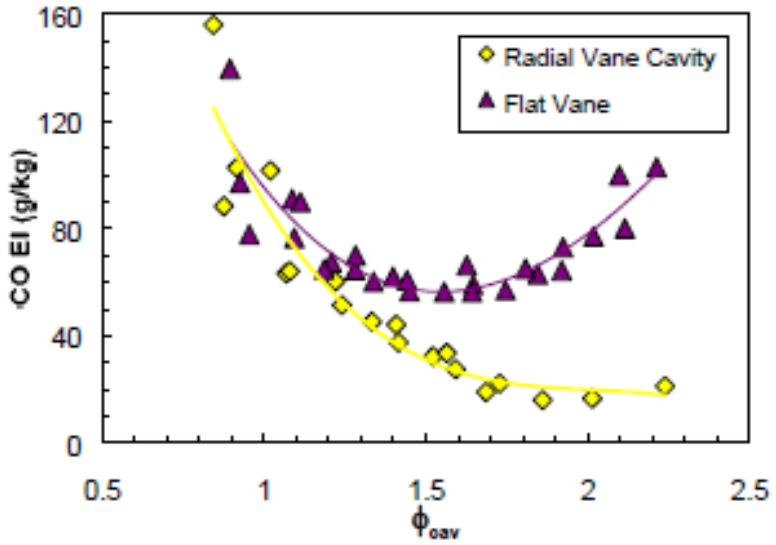

Figure 2.29: CO EI for AFRL UCC with Flat Vane and RVC geometry [11]

This shift was due to the combustor's efficiency also not occurring at $\Phi \approx 1.05$, as is typical of combustion reactions [17] but instead at a $\Phi \approx 1.5$ for the flat vane geometry. In order to confirm this result, the effect of g-loading parameter on emissions was also analyzed in Figure 2.30. The results show that for several different g-load conditions, the optimal fuel-equivalence ratio is 1.5 for this engine, and an increase in g-load also increases CO emissions. These results suggest that because the flow path and body forces within the UCC are different, it does not operate at the same optimal point as a traditional combustor. Also, Figure 2.30 shows that in order to reduce CO emissions, g-load should be held to less than 4000 g.

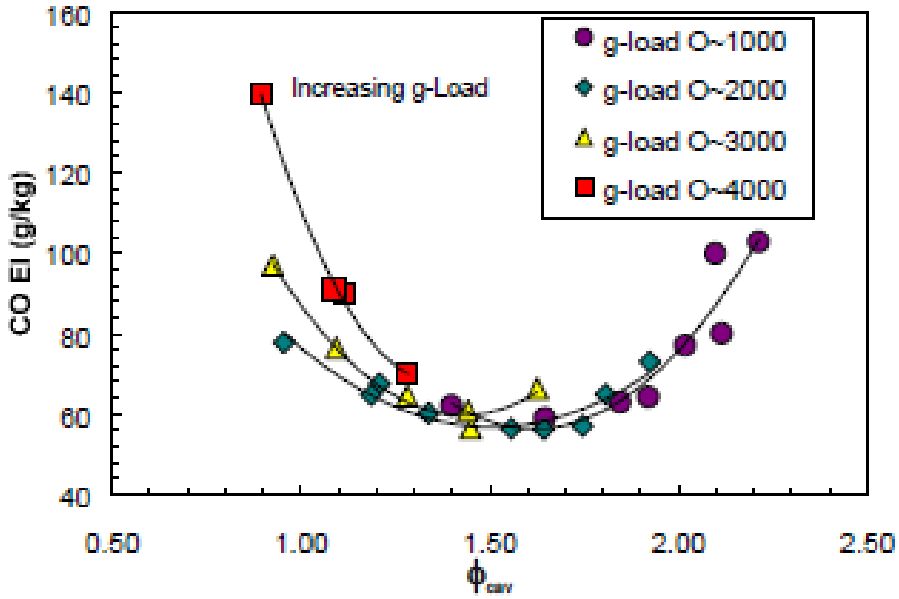

Figure 2.30: Flat Vane CO EI for AFRL UCC at Different g-loads [11]

Anderson *et al.* [44] conducted experiments with a four-vane sectional UCC at the AFRL APCRC that looked at the combustion efficiency and emissions of a radial vane cavity. Their experiment used a single port emissions probe and varied liquid fuel, flow direction (CW and CCW), and radial vane geometry. The combustion efficiency of the sectional UCC was found to

range from 68% when $\Phi = 0.8$, to >99% for all $\Phi \geq 1.2$. This compared favorably to previous experiments in a fuel-rich cavity [11]. While there were inconclusive differences between the Fischer-Tropsch and JP-8 fuels, the direction that the flow was introduced did impact combustor performance. The CCW swirl — impacting the pressure side of the guide vane first — improved the stability limits by creating a secondary region of stability within the radial vane cavity (cut out section in Figure 2.31).

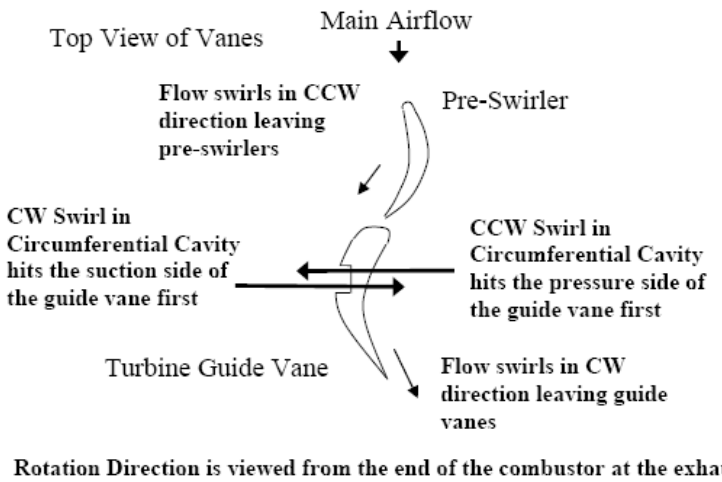

Figure 2.31 Picture of Radial Vane Cavity and Different Flow Paths Based on Swirl [44]

Emissions data was also taken from the AFRL APCRC and can be seen in Figure 2.32 and Figure 2.33. As Anderson *et al*. [44] found in Figure 2.32, there was little correlation found between the generation of emissions and either the aerodynamics (i.e. swirl direction and mass flow intensity) of the combustion cavity section, or the fuel type used. These trend results can be used for comparison with the AFIT UCC, but since it runs on a different fuel source the actual numerical values will be different due to set-up and fuel type differences.

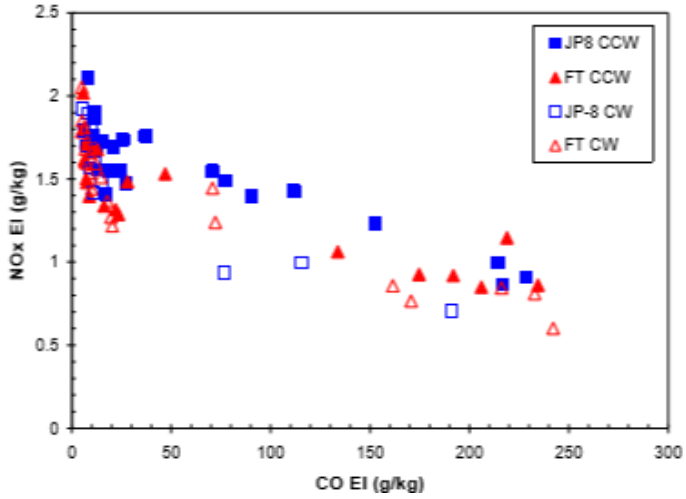

Figure 2.32 Emissions Trade Curve for NO_x and CO for AFRL UCC [44]

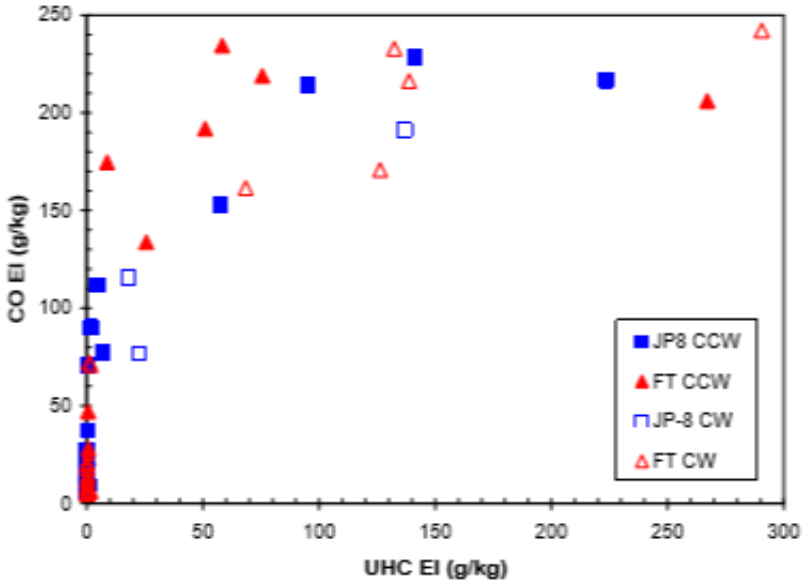

Figure 2.33 Emissions Trade Curve for CO and UHC for AFRL UCC [44]

2.8. Shortfalls of Existing Research

Alterations are now required to improve upon the AFIT UCC baseline. The emissions profile of the AFIT UCC has not been properly characterized or annotated and no outside source exists to confirm the AFRL UCC results. AFRL used emissions data primarily to calculate combustor efficiency. They did not publish how their variations in design affected emissions,

nor did they compare them to current aircraft jet standards. Spytek [45] only performed a preliminary emissions analysis of his UCC design and did not isolate his results from the main combustor flow. All of the emissions data presented in his paper focused on the profile and pattern factors incurred by the UCC acting as an ITB. He did note that with the ITB running in conjunction with the main combustor, the CO and UHC ppm decreased, while CO_2, NO, and NO_x concentrations increased. Jeschke and Penkner [46] presented preliminary research from 2015 into a rotating combustor imparting g-forces upon a trapped vortex chamber. However, they also omitted emissions data, instead focusing on polytropic efficiencies, *F/W,* and TSFC.

Also, as discussed in Section 2.5, there are no experiments investigating ways to optimize the pattern or profile factor exiting the UCC. Alterations now must focus on changing the shape of the pattern factor of the UCC, which is too highly biased to the outer diameter of the Dilution Zone. One way to encourage this migration of hot gases is to change the geometry, specifically the cross-sectional area, of the hybrid vane center-body. The effect of solidity (the number and spacing of blades) was previously researched by Bohan and Polanka for only two configurations [22]. Wilson's study [25] on the effect of area was confined to geometry's effect on Rayleigh losses and used a rudimentary 2-D analysis. Cottle *et al*. [6] have developed a CFD model to allow for multiple geometries to be analyzed. Previous published work with the model only focused on non-reacting flows within the combustor, but the next iteration of the model is to account for combustion, which requires greater refinement of grid. Once the model consistently produces reliable results, different hybrid vane designs are compared analytically, with the most promising results constructed and experimentally validated.

III. Experimental Methods

The UCC test rig used in these experiments is located in the Combustion Optical Analysis and LASER Laboratory (COAL Lab) at the Air Force Institute of Technology (AFIT). This facility accommodated the original sectional combustor design and through a series of upgrades has grown to accommodate the full annular rig now in use. The full annular combustor itself was initially constructed by Wilson *et al.* [24][25] in 2011 and has been incrementally improved since then.

To accomplish the experiments required for this research, several modifications and additions were made to the UCC. The changes primarily focused on the creation of an emissions collection system that obtained accurate data and interfaced with the data collection computer. These additions included a multi-channel probe, sample line, LabView data collecting VI, as well as repairing and establishing operating procedures for the emissions analyzer. The diffuser required a new nose cone in order to seal the hollowed out center. Also for this thesis, two new air injector plates were created and tested. Several designs that altered the hybrid vane geometry were also designed, of which one was produced with additive manufacturing, showing the feasibility of this process for use within the UCC. The test instrumentation has also evolved in order to increase data collection capabilities, most recently with the addition of a large cut-out for a quartz visual port insert at the aft of the combustion cavity. This window also allowed for the taking of TFP data within the combustion cavity.

3.1. AFIT UCC

The AFIT full-annular UCC is a six-vane, reduced-scale representation of the combustor required for a fighter-sized aircraft [22]. The design of the AFIT UCC version 2 was conducted primarily by Wilson [24][25] based upon the fighter-scale sized UCC numerical analysis of

Bohan and Polanka [24]. These models used code provided by Anthenien *et al.* [16] as a baseline. The entire UCC is 43.2 cm long from inlet to the aft of the instrumentation ring and has a maximum diameter of 25.4 cm (around the combustion cavity). Air enters into the common air diffuser (front portion in Figure 3.1) and is split to go into the core (inner) flow and the combustion cavity (outer) flow. This splitter plate is the dark blue plate in Figure 3.1.

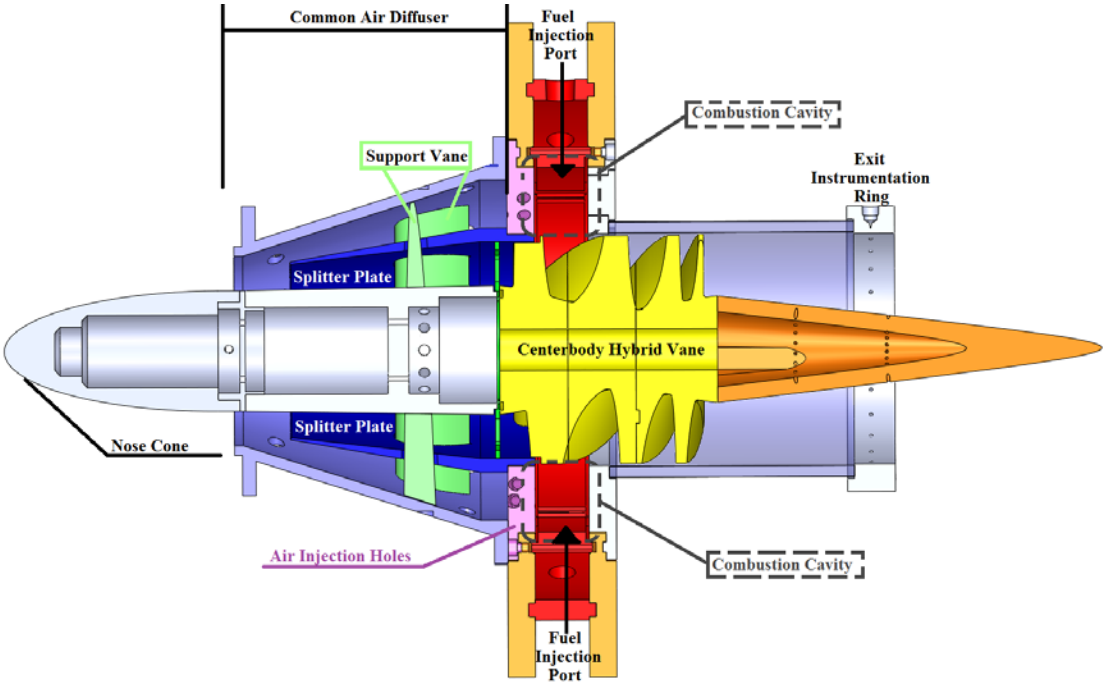

Figure 3.1: AFIT UCC (Version 3) Mass Flow Path with Common Air Source

The outer flow, once diverted, is routed into the air injector holes which consist of two rows of holes oriented at an angle tangent to the radial combustion flow. The cavity itself extends from the inner diameter of the Inner (Combustion) Ring to the top of the hybrid-vane center-body. The primary combustion zone occurs within the combustion cavity between the fluid interface of the core flow and the cavity flow. This interface occurs near the top of the hybrid vane (yellow colored part in Figure 3.1). The cavity flow has a clockwise orientation, as depicted in Figure 2.18 so that it strikes the suction side of the hybrid vane.

This tangential flow swirls the combustion cavity flow and creates a circumferential force between 500-2000 g's upon the mixture [6]. Products were then entrained by the hybrid vane, which migrated the hot gases out of the UCC combustion cavity into the core flow. Within the hybrid vane, the combustion gases mix with the remainder of the core flow, lowering the overall equivalence ratio. The inlet and outlet Mach number and flow angle conditions were designed to represent the typical values modern jet engine combustors experience. The current inlet condition is an ambient air mass flow setting of 6.48 kg/s. The exit plane conditions were determined using the turbine rotor inlet requirements of Mach = 0.8 with a swirl angle of approximately 70° [22]. However, due to facility constraints the exit Mach number was set instead to 0.5 upon construction [24]. An instrumentation ring secures the exhaust vent onto the UCC and has Omega Type-K Thermocouples positioned in the exit plane in order to obtain the pattern factor and annotate the radial flow migration.

3.1.1. Diffuser

Figure 3.2 shows the core components of the AFIT UCC diffuser section, which are common to both UCC version 2 and version 3. The diffuser was secured to the combustion chamber by four 7.94 mm (5/16-inch) steel bolts, one each placed at the 2 o'clock, 4 o'clock, 8 o'clock and 10 o'clock positions; the air inlet pipe was secured to the front face of the outer diameter. The inner diameter was a solid aluminum annulus 0.64 cm thick and secured to the hybrid vane by three bolts. Fourteen aluminum support vane airfoils extend radially from the inner diameter to the middle diameter, "splitter plate", before bolting into recessed holes in the outer diameter. The splitter plate was intersected and secured in place by these support vanes. The outer diameter was the casing that housed all of these components and attached the diffuser section to the inlet air duct (a PVC pipe 12 cm in diameter).

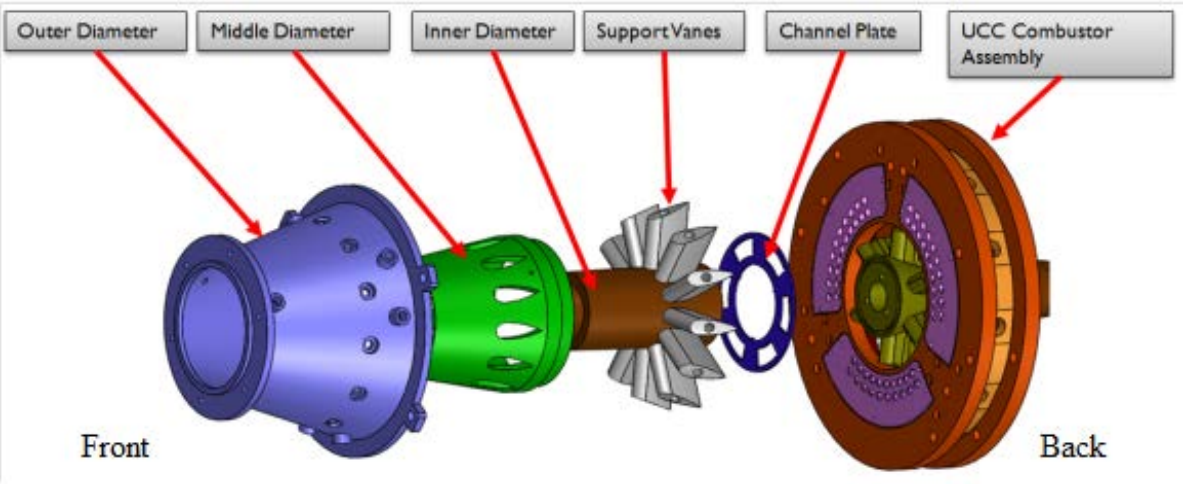

Figure 3.2: Part breakout and exploded view of AFIT UCC diffuser section [50]

Conrad [19] designed the common air source to integrate with Wilson's second design iteration of the combustion cavity [25]. The design mass flow was set at 0.45 kg/s, which was consistent with the small turbine engine in the AFIT COAL lab: a JetCat P-200 turbojet engine. The diffuser was designed as a modular part for easy alteration of the configuration between the ITB (with JetCat installed) and main burning configuration (JetCat uninstalled). The splitter plate can be removed and replaced with different plate heights in order to change the amount of air diverted into the combustion cavity. The 70/30 plate which Cottle [6] showed to be optimal was the one used for this investigation.

The inner diameter (ID) also had a hole in its center which is 4.19 cm in diameter to secure the JetCat P-200 when the UCC is functioning as an ITB. However, when the UCC was functioning in the main combustor mode, this hole needed to be blocked to prevent the air from penetrating into the central cavity. Further, the inside flowpath of the rig required a nose cone adapter to smoothly create the desired flow annulus. This nose cone was manufactured out of 2024-T3 aluminum and can be seen in Figure 3.3.

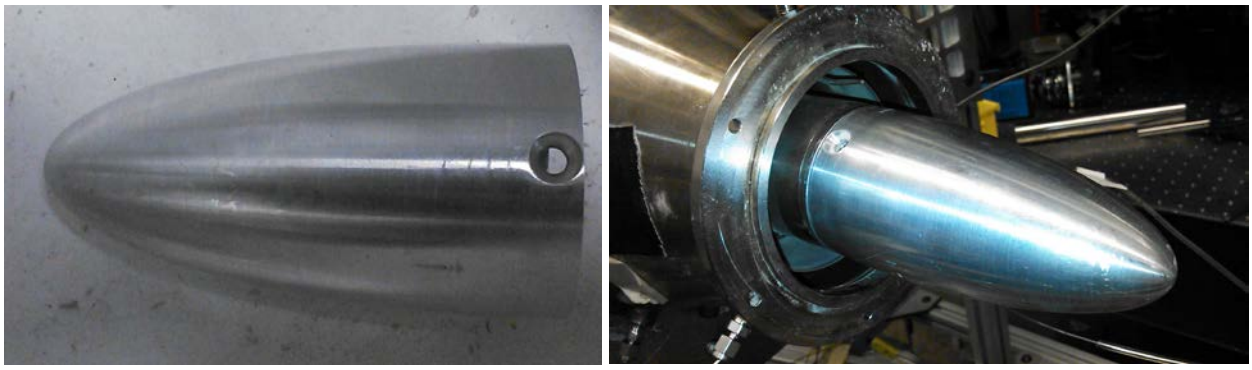

(a) (b)

Figure 3.3: (a) New Nose Cone cover for UCC, Main Combustor Configuration, (b) Nose Cone Installed on Diffuser Section with Union

3.1.2. Centrifugal Combustor Cavity

The centrifugal combustion cavity is the primary zone within the UCC for combustion. Figure 3.4 shows the breakout of the different parts of this section for UCC version 2 including the core flow section whose flow field and pressure distribution alter the combustion cavity physics. Note that while the air injection panels (plates) are the pink-colored parts that take the diverted air from the outer diffuser flow; they inject and swirl the air it into the outer diameter of the combustion cavity. The core channel restriction plate is the dark purple part that was optimized by Cottle [6] for the initial combined core configuration. This part creates a blockage in the core flow that ensures sufficient mass flow into the combustion cavity. The inner ring is the surface that secures the diffuser to the combustor, and has the air injection holes in it. The outer ring is the surface to which the fuel jets and optical access windows are secured. Inside this outer ring is the inner combustion ring that forms a plenum. This feature is a legacy item from efforts prior to the common airflow diffuser. The outer ring and inner ring also connect and secure the front plate and back plate together. The back plate is designed with several cutouts that allow for visual access and instrumentation blocks into the combustion cavity. The back plate also has the attachment port for the igniter in it (black circle on black plate).

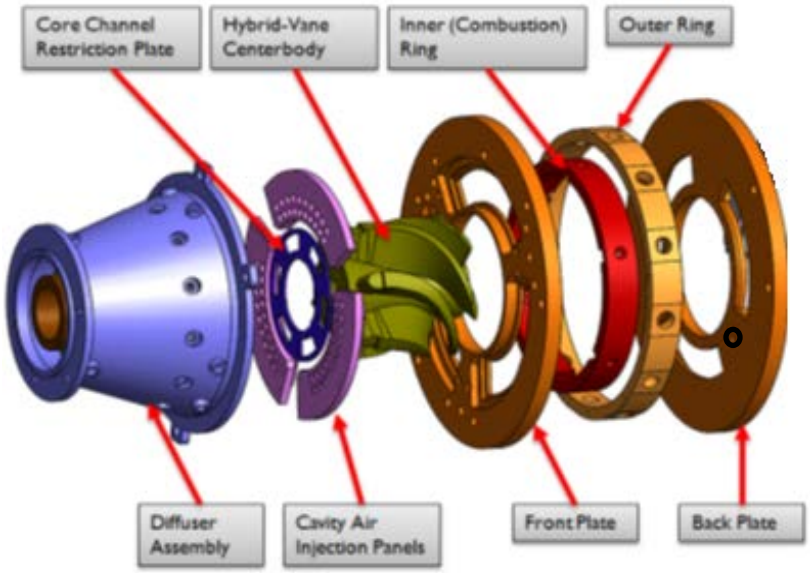

Figure 3.4: Part breakout and exploded view of AFIT UCC v2 combustion chamber [6]

The fuel injection scheme used for all configurations is identical and uses gaseous propane. Fuel is injected by six hollowed-out bolts that screw into the outer ring and rest within a countersink of the inner ring. The fuel is further dissipated by an eight-hole baffle plate, shown in Figure 3.5, which reduces the surface area of the fuel molecules further and decreases the evaporation time of the fuel. Originally, the gap between the fuel injector and baffle plate resulted in flame leaking out of the combustion cavity. The solution that Damele [47] implemented was to manufacture an I-shaped fuel baffle addition. This addition had a divot placed under the injection hole that diverted the fuel away from the stagnation region in the center of the baffle plate (where there is no hole). This scattered the fuel further towards the eight holes (seen in the rectangular plate in Figure 3.5) and increased the pressure drop of the fuel flow, ensuring the appropriate pressure seal for non-leaking operations.

3.1.2.1. Discrete Source Combustion Cavity Configuration

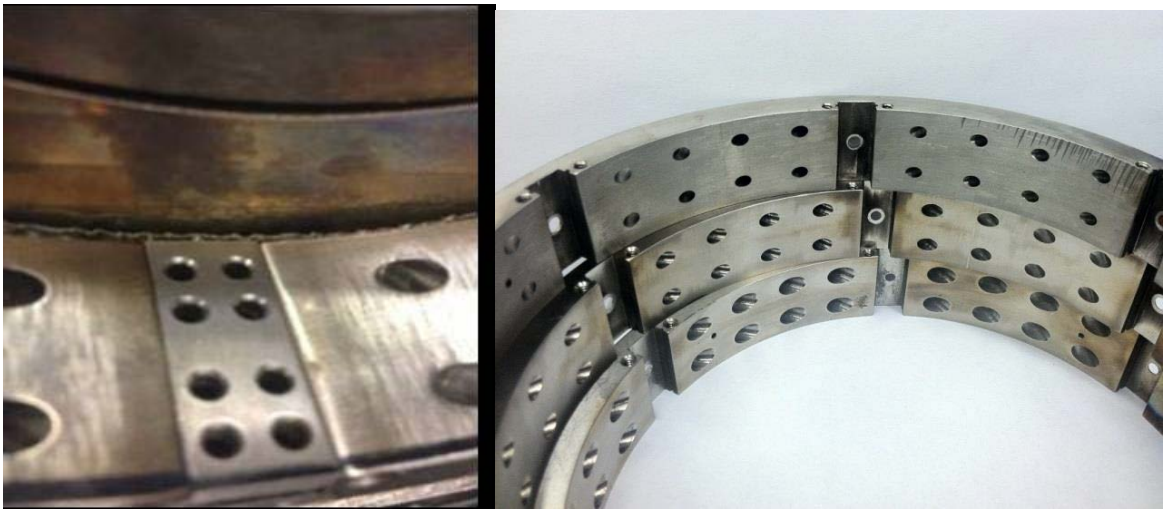

Figure 3.5: Close view of (left) Fuel Baffle Plate [37] and (right) side air injection holes for Discrete Air Source Configuration [25]

Prior to Conrad's [28] and Cottle *et al.* [6][48] incorporation of the common air-source diffuser, Wilson [25] and Damele [37] also anchored six air injection ports to the outer cavity for the discretely sourced air configuration. This configuration was used exclusively with the original UCC combustion cavity geometry (UCC v2), and these six air ports pressurized the air within the plenum created between the inner and outer ring. The air was then shot through the air injection holes on the inner ring at an angle 35° tangent to the existing flow within the combustion chamber. Figure 3.5 shows the original air injection driver holes in the outer ring, while Figure 3.6 shows the full annular flow path of both the air from the injection ports, into the outer plenum, through the air driver holes, and into the combustion cavity.

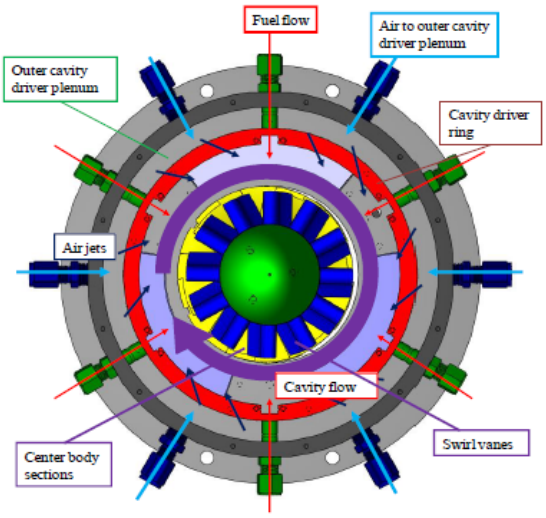

Figure 3.6: Discrete Source Combustion Cavity Air and Fuel flow path [25]

The combustion cavity height and width for the discrete source injection scheme were set in accordance with the values in Table 3.1. The geometric dimensions of the combustion cavity was deemed the second version of the UCC (UCC v2) and is abbreviated as such in this document. With the holes being in the outer ring, none were required or located on the front plate. This design also required a separate air source which enabled independent control of the flow split between core and cavity. However, the goal was to integrate the UCC into a turbine engine where all the available flow originated from the compressor. To accomplish this integration step, the aforementioned diffuser was designed.

Table 3.1: Geometric Differences between Previous Common Source Combustion Cavity UCC (v2) and current Common Source Combustion Cavity UCC (v3)

Ring Dimensions			Air Drivers		
	v2	v3		v2	v3
Cavity Height [cm]	5.2	6.4	Lower Row Diameter [cm]	12.827	12.941
Cavity OD [cm]	15.9	17.0	Upper Row Diameter [cm]	13.780	13.729
Plenum ID [cm]	17.8	18.9	Cav OD - Upper Row [cm]	2.121	3.289
Plenum OD [cm]	20.3	23.3	Hole Row Spacing [cm]	0.953	0.787
Volume [cm^3]	139.6	190.3	Hole Diameter [cm]	0.450	0.493
			Number of Holes	60	48
			Total Hole Area [cm^2]	9.52	9.15
			Angle [cm]	30	55

3.1.2.2. Initial Common Source Combustion Cavity (UCC v2)

When the common core diffuser was completed after Damele's [37] research, several changes to the geometry of the combustion cavity were required. The six air driver holes used to charge the air plenum were plugged by metal bolts. The inner combustion ring was replaced with a new, solid piece of Hastelloy (i.e., has no air driver hole feeding the plenum cavity in the combustion chamber). The baffle designed for the fuel jets was retained, as well as the same cavity dimensions as the discrete air driver configuration. In order to test different air driver schemes, the original air drivers were also a series of three plates of varying angles and size. The original geometry of these plates are displayed in Table 3.1, as well as the combustion chamber dimensions.

During the implementation of UCC v2, there were repeated issues with fuel and flames leaking out of the combustion cavity because the fuel leaked into and through the outer air plenum to the UCC exterior. The reason this had not been a noted problem before was the air being pumped into the outer plenum created a high pressure environment that acted as a seal to the fuel. When the high pressure environment was removed, the fuel was able to leak through all the part interfaces, and eventually into the outer atmosphere. The propane would stagnate

around the combustor but be drawn aft slowly by the exhaust fan. Then the flame exiting out of the UCC would come in contact with this pocket of gas and ignite. To fix this conundrum, high temperature, flame resistant sealant was placed in all the interfaces between the inner ring, outer ring, front plate and back plate. This solution fixed this recurring issue and was implemented around all interfaces near the combustion chamber (i.e. around the optical access windows). Through trial and error, it was found that VersaChem Exhaust System Joint and Crack Sealer (available at any auto parts store) was most effective at preventing flame leakages without igniting itself.

3.1.2.3. Increased Aspect Ratio Combustion Cavity (UCCv3)

The combustion cavity has gone through three major design iterations, the last of which was completed in August of 2015. While the newer version of the UCC resembles the previous version, it has several key differences in the geometry. Table 3.1 highlights the differences between the current combustion chamber geometry and the one used previously by Damele *et al.* [37] and Cottle *et al.* [55]. This changed the aspect ratio (height-to-width) from 2.04 to 2.51. Also modified is that the air drivers are no longer three sectional plates angled 30° tangentially to the combustion chamber flow. Rather, the entire front plate is one solid piece with constant spacing of 0.787 cm and air driver holes oriented 55° tangentially to the combustion chamber flow. This was done to decrease the axial velocity component and increase the tangential velocity throughout the entire combustion chamber, and therefore increase the g-loading. Mechanical seals, depicted in were added to help seal the combustion chamber from the outside and prevent air and gas leaks. This was the combustion cavity used exclusively in the experiments performed for this thesis, though it was compared to legacy data with UCC v2 discrete source configuration.

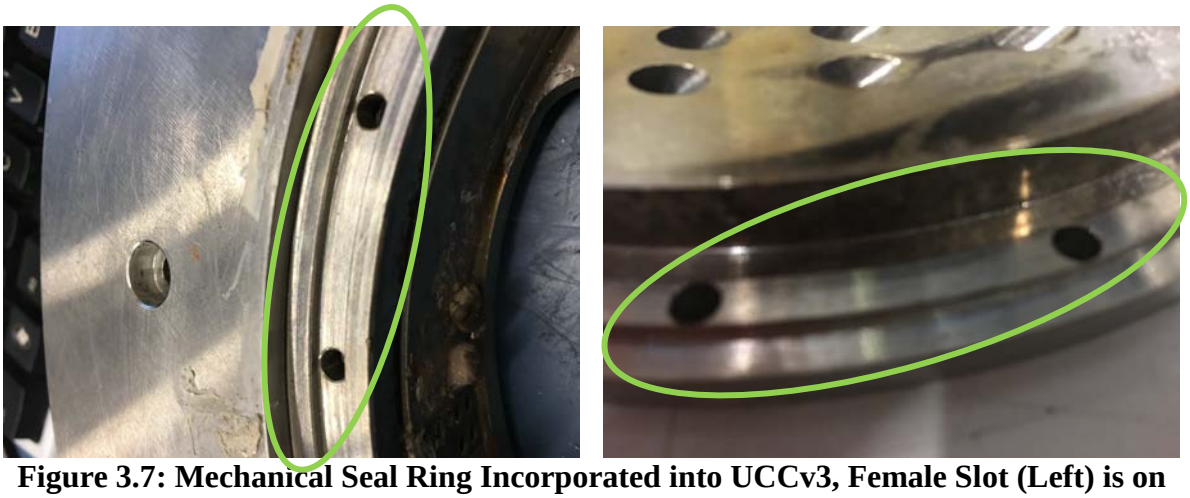

Figure 3.7: Mechanical Seal Ring Incorporated into UCCv3, Female Slot (Left) is on Outer Ring and Male Slot (Right) is on Driver Plate and Instrument Plate

3.1.2.4. Compound Air Driver Geometry

During computational analysis of the AFIT UCC, Cottle et al. [55] noticed that there was a reduced amount of combustion occurring within the upper height of the cavity. This was found to exist due to the cavity flow and fuel flow being sucked out by the core flow before they could ignite fully in this region. In order to increase the mass flow into this area, the mixing of the air and fuel, and the residence time of the combustion process, the air drivers for the basic UCCv3 geometry were angled 10° radially. This drove the cavity air radially outward toward the inner ring (viewed as the ceiling of the combustion cavity). This angle was determined by finding the slant that would cause the top row to point directly at the junction of the inner ring and back plate [50]. Figure 3.8 shows how this compound angle was derived. The UCCv3 was used as the baseline condition, and the air driver hole was altered by angling the hole angle radially outward (θ_r) from the UCCv3 air driver hole centerline (labeled Axis 2). The tangent angle is defined as the angle between the centerline of the core flow (Axis 1) and the centerline of the air jet driver hole. This creates a 35° drill angle, or a 55° tangent angle to the flow (θ_t) with the front plate wall.

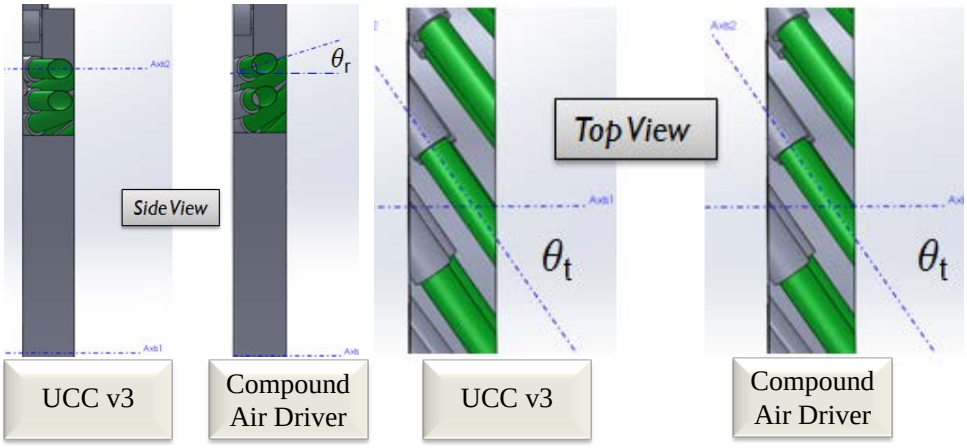

Figure 3.8: Orientation of UCC Air Driver Holes with Respect to (Side View) Original Hole Geometry Centerline and (Top View) Core Centerline Axis [55]

3.1.3. Hybrid Vane

Within the hybrid vane, the combustion gases were entrained into the core flow. Combustion was completed in these passages by a quick-quench, lean-burn process, which rapidly lowers the fluid temperature below those conducive for reaction while simultaneously lowering the equivalence ratio below flammability limits. The vane center-body was also designed to turn the inlet flow from the compressor; the exit swirl angle was set by Bohan [22] to a representative turbine inlet guide vane exit value of 70°. Figure 3.9 shows the hybrid vane's substantial turning, and how it should look when assembled.

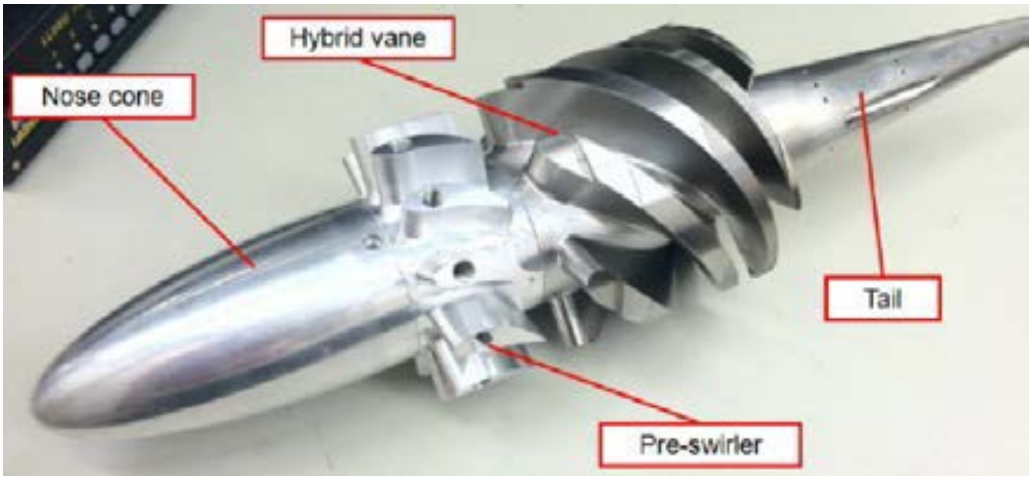

Figure 3.9: Low-Loss Hybrid Vane Geometry (Geometry 1)

3.1.3.1. Low Loss Center-body

As stated previously, Bohan and Polanka [22] developed the hybrid vane concept that has continued to be the baseline of AFIT research since its manufacture. The initial Tapered Center Body (TCB) designed by Wilson experienced appreciable Rayleigh losses during experimental testing. The Low-Loss Center Body (LLCB), also designed by Wilson [5] for the discrete source UCC v2 geometry, was a method to reduce these loses and was the primary hybrid vane design of this investigation. Wilson [5] also included a pre-swirler to duplicate conditions seen exiting a compressor rotor blade and a tail cone that was designed to ease the exhaust into the 20.32 cm diameter port for the dual fan, 1.0 kg/s, ventilation system, which all can be seen in Figure 3.9. In order to facilitate the manufacturing of the center-body, the vane had to be cut into three parts, the breakout of which can be seen in Figure 3.10. The cross-sectional view and research completed for this design is extensively covered at the end of Section 2.4.2.1.

3.1.3.2. Radial Vane Cavity

It was noted by Damele *et al.* [37] that the combustion products within the AFIT UCC do not fully migrate down the span of the vane and create a local hot-spot on the vane. In order to

alleviate these issues as well as those observed by Wilson and Polanka [5], Mawid *et al.* [38], and Thornburg et al. [39], a Radial Vane Cavity (RVC) center-body was designed, manufactured and integrated into the existing LLCB design.

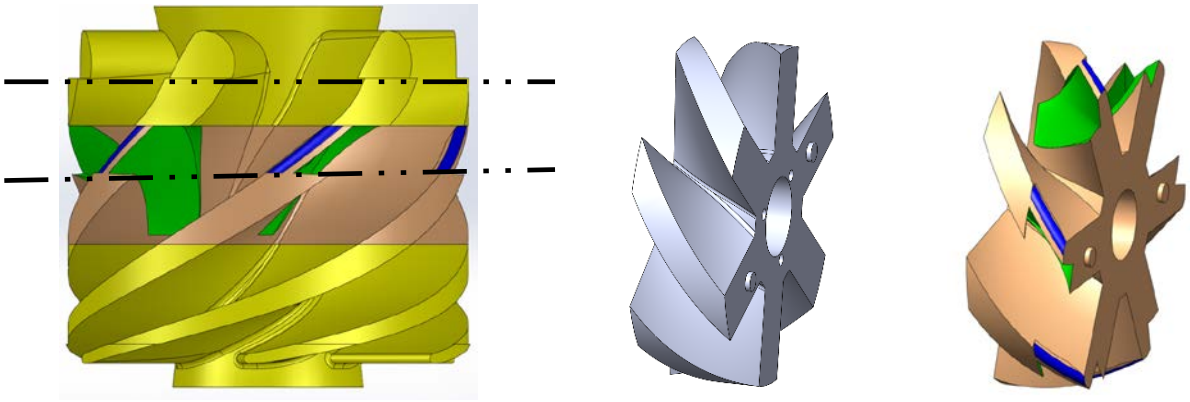

(a) (b) (c)

Figure 3.10: (a) Full RVC center-body assembly with (b) original LLCB middle piece and (c) modified LLCB piece with RVC cut-out (green) and chamfered edge (blue)

Previous work investigating how to affect the radial distribution of the combustion gases was accomplished at AFIT by Parks [49]. His work was performed in the 60° sector version of the UCC (UCC v1) and focused on a straight body vane similar to the AFRL vane used by Zelina *et al.* [11]. He modified the test profile between a straight vane, a RVC, and a new variant he termed the "tiger-claw". The tiger-claw was a series of backward-facing steps that blended the profile of the airfoil designed migrate the hot gases of the combustion chamber more effectively. The goal of the step design was to distribute portions of the cavity flow into various radial heights. However, the tiger-claw proved relatively ineffective when the cavity-to-core mass flow ratio was greater than 0.3, which equates to 76.9%/23.1% split as defined in this thesis. This geometry also significantly increased all emissions production which in turn reduced the efficiency of the tiger-claw design. This was due to the tiger claw having no backward facing step as detailed by Mawid *et al.* [38] and so significant amounts of unburned hydrocarbons were removed from the combustion cavity before they could react.

The finalized design for this RVC can be seen in Figure 3.10 where the combustion cavity location around (i.e. “over”) the hybrid vane is shown by the two black dotted lines. The cavity was designed with primary consideration for the findings of Mawid *et al.* [38] that a rectangular face was the most desirable face for a RVC. By creating a partial back wall, the reduction in efficiency seen by Parks [49] could be avoided while still migrating the flow toward the inner diameter. The rectangular cut-out was then fluted towards the aft in order to prevent the hot spots observed by Thonburg *et al.* [39] as well as guide the flow out and into the middle span region. There is also a chamfered edge (blue cut out in Figure 3.10) on the pressure side that alleviates pressure blockages and hot spots seen on that edge in analytical analysis [50]. These considerations were implemented into the second section of the hybrid vane as indicated in Figure 3.9. This new second section was constructed by Bastech Inc. in Dayton, OH as a Direct Laser Metal Sintered part made out of Stainless Steel 15-5.

As previously mentioned, Wilson [25] experienced challenges during the construction of the LLCB which necessitated the hybrid vane being split into three different pieces. Whether by coincidence or design, the cut and subsequent mate between the bow and middle pieces occur right at the 50% channel location under the combustion cavity. Most of the combustion within the UCC occurs in the aft half of the combustion cavity, which corresponds to the front 1.27 cm of middle section of the hybrid vane. Therefore, in order to prevent too much entrainment of the combustion cavity flow and lower residence time, the RVC cutout was only applied to the center piece. The flute finished 3.8 mm from the end in order to ensure the flow was fully integrated into the core flow prior to impacting on the aft part and causing an additional hot spot. This decision, coupled with the decision to use additive manufacturing to grow the part, expedited

production of the RVC middle piece from 12 weeks to 4 weeks. The finalized middle part is shown in Figure 3.11 with the RVC cutout on the forward face highlighted with yellow circles.

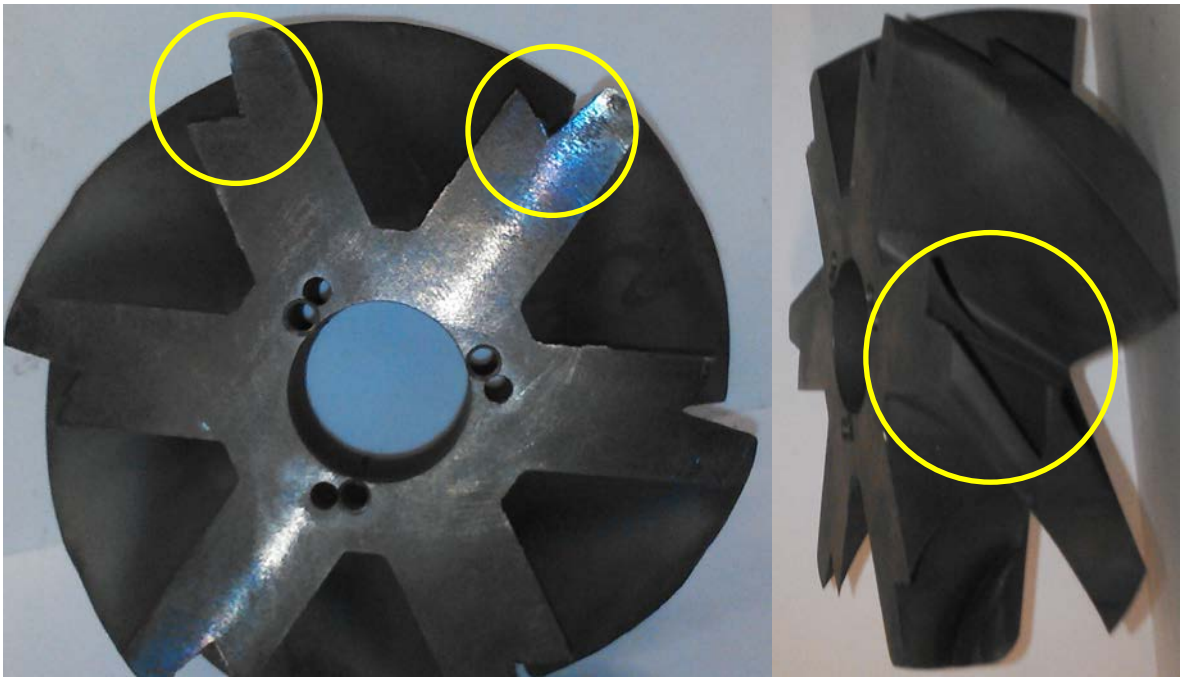

Figure 3.11: Final Low-Loss Hybrid Vane with RVC Channel Incorporated into Center-body as Grown by Bastech Inc.

3.1.4. Exit Plane Instrumentation Ring

The exit plane instrumentation ring was constructed and characterized primarily by Damele *et al.* [37] in order to ascertain the pattern factor and profile factor of the UCC. This ring was designed for an experiment set that used the discrete source air driver configuration within the UCC v2 combustion chamber (abbreviated UCCv2 in the results). This instrument ring was designed to capture the temperature values of the swirled flow exiting the hybrid vanes. The original ring was designed for the LLCB dimensions, but the thermocouple heights are adjustable for experimental needs by loosening the Swagelok fittings along the outside of the ring and adjusting the radial height as required. Figure 3.12 shows the first version of the

instrumentation ring set up to take temperature measurements only. In this configuration, each probe is an Omega K-type thermocouple.

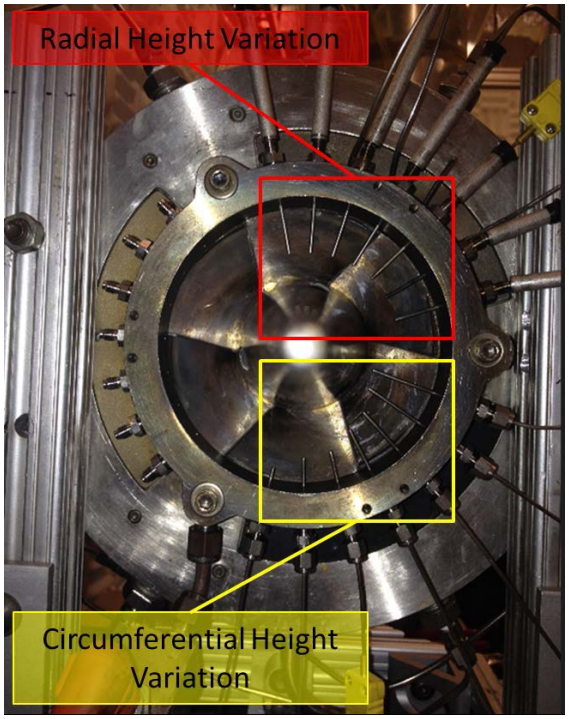

Figure 3.12: Damele Exit Plane Instrumentation Ring [37]

The instrumentation ring is divided into three sections, and the probes are inserted into holes spaced 0.357 cm apart. The first set of probes has the circumferential height increased from a radial height of 3.9 cm to 9.9 cm. This allowed for the pattern factor and profile factor to be found based on radial channel height. The second grouping is placed at the same angular distance from the vane exit but at the same radial height in order to determine the wake effects and flow variations at each radial height. These variations helped find a geometric average across the middle radial height but at different angle variations after the vane exit so the different heights could be compared appropriately. The instrument ring has since been modified by reducing the visual profile of the un-instrumented third of the ring (cut-out from 1 o'clock to 4 o'clock position in Figure 3.13. This allows for greater optical resolution and high speed

photography of the exit flame. The instrument ring can also have total pressure ports made from 0.75 mm stainless steel tubing or United Sensor PCA-8-KL 1514 pitot-static probes inserted into the holes to make pressure and velocity measurements within the exit-plane regime. Though not used in these experiments, one of these can be seen in the 10 o'clock position of the instrument ring.

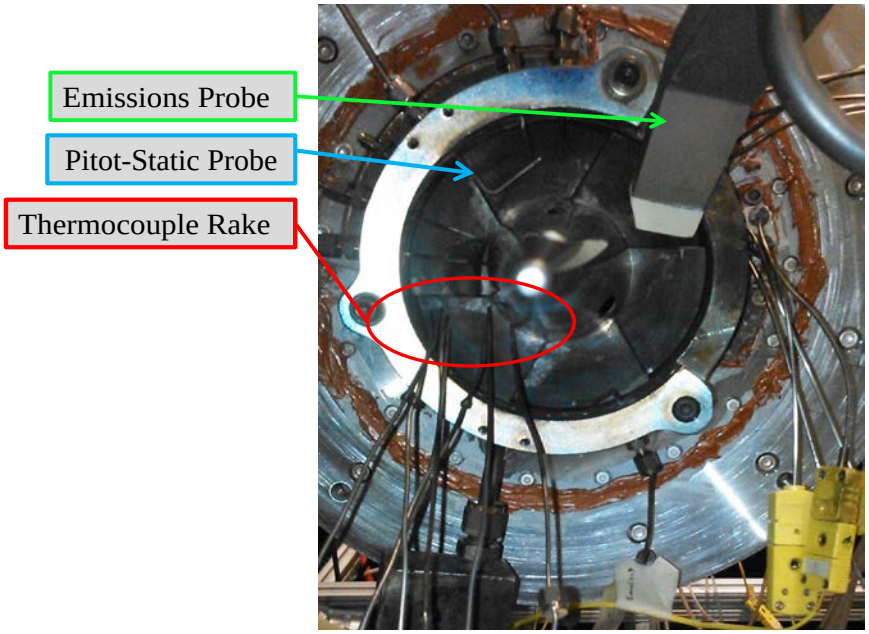

Figure 3.13: Current Instrumentation Ring with Cutout for Emissions Probe

It was discovered by Cottle [50] using his CFD Model that the radial instrumentation ring used by Damele may not be getting accurate results. This was confirmed during an experiment where one of the probes was left in and measured. This probe was the front-most probe immediately following the cut-out which would yield the largest error. A preliminary experiment was conducted to test this theory by placing a thermocouple in the ring and one in the rake formation. The former was at a radial height of 14.24 mm but was placed approximately 40° circumferentially (25 mm) away from the exit plane while the latter was at radial height of 14.66 mm exactly at the exit plane (i.e. 0° circumferential). It was found that the exit flow was

swirling so much at the exit that the flow was shot through the large gap in the instrumentation ring instead of being confined. Furthermore, this probe should have been reading the vane passage 100° away, not 40° as originally thought. Therefore, the flow that should have impacted the probe escaped and caused a difference in reading for the same radial height (but different circumferential position) of approximately 400 K. This result would affect at least the first three probe positions in the ring. For this reason a temperature rake was created in order to get the exit temperatures exactly at the plane of exit and avoid any loses or distortion in position due to the circumferential velocity component. Figure 3.13 shows the general set-up for simultaneous temperature and emissions collection, while Figure 3.14 shows a zoomed-in view of the tips.

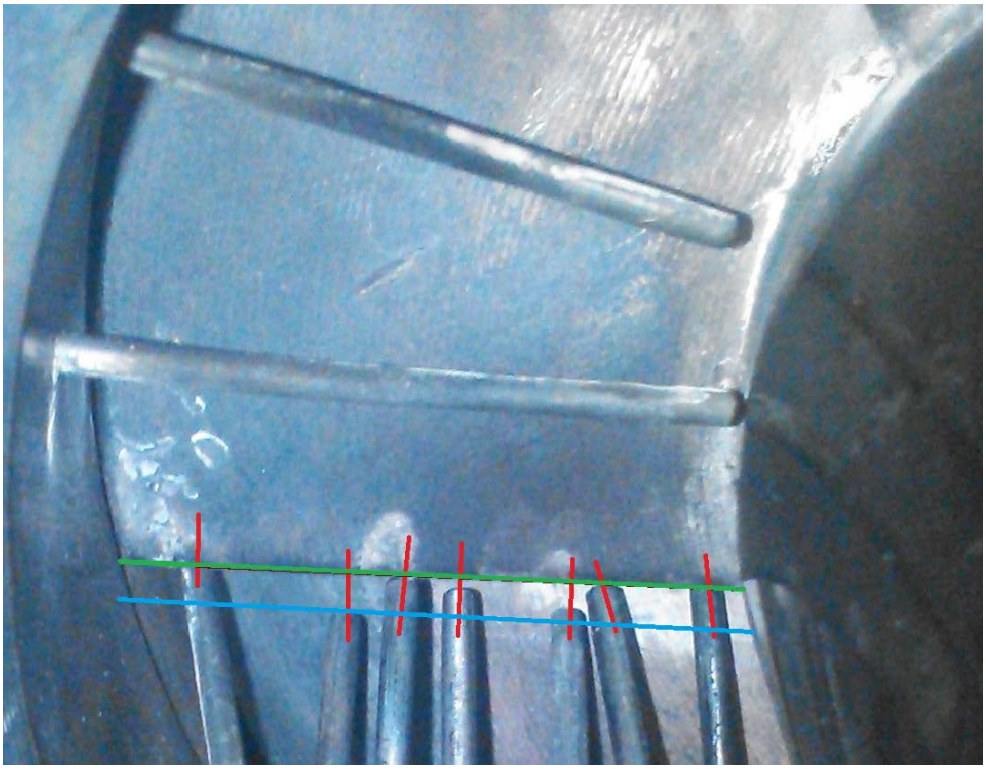

Figure 3.14: Zoomed-In View of Thermocouple Rake at Exit Plane

The location of the probes was determined using dimensional analysis and comparing the known length of the exit span and probe diameter, and finding a pixel to mm conversion factor. Figure 3.15 shows how the span width (known to be 30.575 mm from SolidWorks drawings) and the

probe diameter (a measured 1.60 mm) were used to find an average pixel-to-mm conversion factor. This ratio was unique to each day of tests and probe position, and thus was taken prior to every test. The probes were always ± 1.5 mm of the exit plane (green line), and this crieteria is shown with the blue line in Figure 3.14. The probes were checked intermittenly and after the conclusions of test to ensure no movement occurred, and if so was noted in the day's notes and post processing code. Figure 3.15 shows different instance of this process but with the probes positions numbered, along with their pixel displacement from the inner diameter, calculated position, and resultant spanwise location.

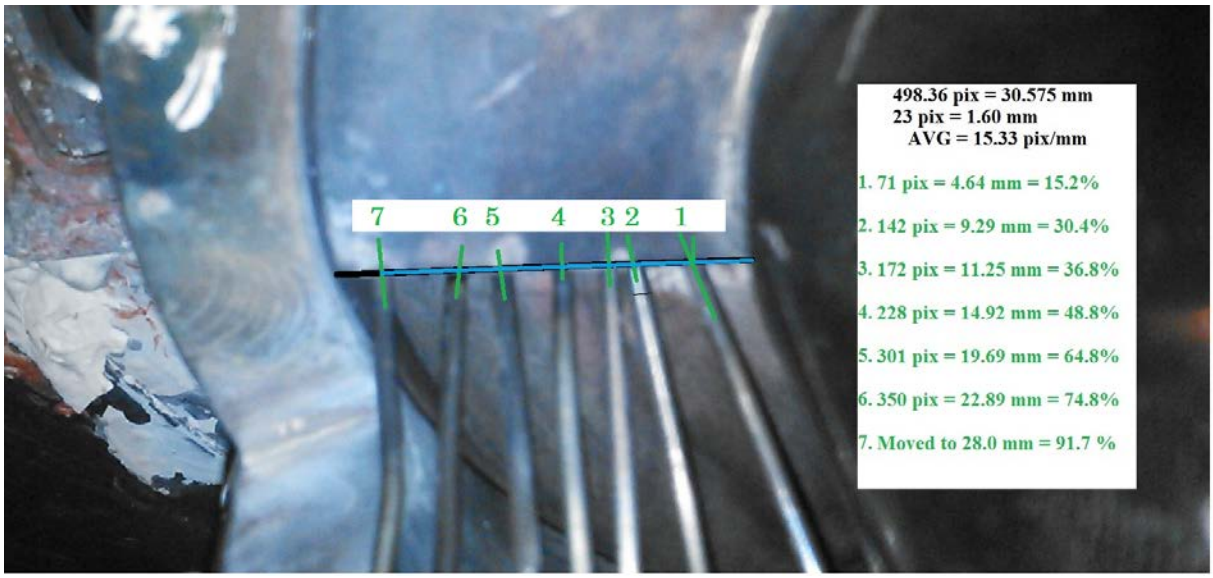

Figure 3.15: Dimensioned Zoomed in View of Thermocouple Rake at Exit Plane

3.1.5. Emissions Probe

Previous work with the AFIT UCC relied on a single channel port that could only take a small mass sample at a single point. The probe was also only able to traverse in one dimension, which was not parallel to the exit angle of the hybrid vane. Therefore, to get multiple points of data, run times often exceeded practical limits. To enable simultaneous data collection across multiple points and reduce run time, a four-channel (a.k.a. four-port) emissions probe was

designed, constructed and added to the COAL Lab arsenal of equipment. The probe was constructed out of Stainless Steel 316L bar extrusion and maintains a thickness of 1.52 mm on all exterior surfaces. A CAD drawing of the probe is provided below for reference, as well as how it is positioned in the exhaust flow of the UCC hybrid vane.

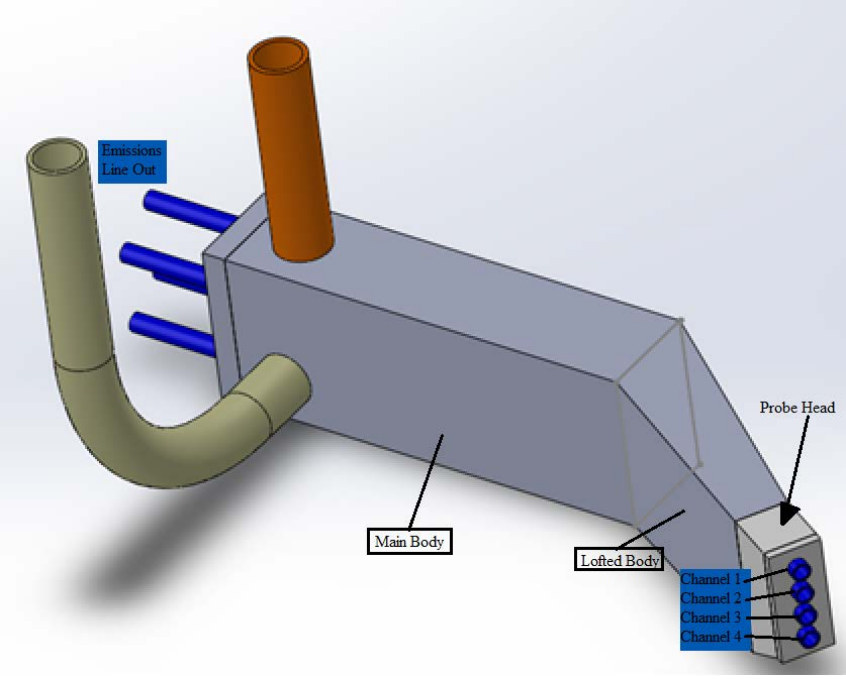

Figure 3.16: AFIT UCC Four-Channel Emissions Probe

The probe is comprised of a front mounting plate, head cavity, lofted body extrusion, main body, end cap and two 0.80 cm ID, 0.95 cm OD tubes, all of which are welded together in order to seal the surfaces. The four ports lines are 0.33 cm OD, 316L Stainless Steel tube that run from the probe face through the channels within the probe and out the end cap. The two 0.95 cm tubes provide a flow path for coolant oil heated to a temperature of 150 °C to progress through the entire probe and around the emission lines. This oil supplies convective heat transfer that extracts heat away from the probe face which is exposed to temperatures approaching 1200 K. The presenting face of the probe is 0.91 cm x 2.03 cm and flares to the overall probe height of

2.8 cm. The front mounting plate and head cavity are also coated in a 0.051 cm ceramic thermal protective coating (TPC) applied by M&M Coatings of Walton, Kentucky to provide additional protection (colored white). The lofted body extrusion and main body have a splitter plate 0.091 cm thick and placed 1.27 cm down from the top face of the probe in order to create a recirculating flow of the coolant fluid. Flow enters into the probe from the top (orange tube) and is extracted from the bottom side (tan tube). The probe is approximately 13 cm in total length.

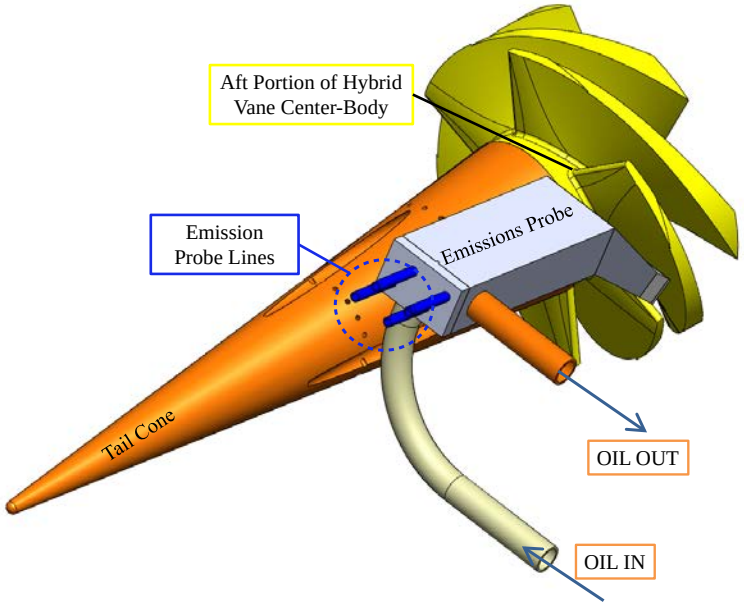

Figure 3.17: Four-Channel Emissions Probe Relative Placement in Hybrid Vane Wake

Initially the probe was designed to simultaneously thermally and sonically quench the flow by drawing it through a weak shock wave. To do this, the emissions gas would have to be drawn through a hole of 0.610 mm in diameter. This probe design was based on the probe used by Zelina *et al.* [11] at AFRL. This required a small hole size but would cease all chemical reactions upon entering the into the probe. Therefore, the emissions gas sample line originally had the entire tip on the probe head welded over and a hole 0.610 mm in diameter was drilled through the material with the wire EDM machine located at the AFIT Machine Shop. However, when the probe was used in conjunction with the CAI Emissions Analyzer at atmospheric

conditions, an insufficient pressure drop occurred in order to cause the shock wave; the measured drop was only -6.03 psig as opposed to the minimum required drop of -7.64 psig. This pressure drop became more pronounced if multiple ports were opened simultaneously. The small port-hole size also restricted the mass flow through the port hole, causing low concentration readings of all emissions species. Therefore, since the vacuum was insufficient to cause a shock, the port-hole diameter was increased in order to alleviate the mass flow problem. As expected, the mass flow increased to the requisite amount for measurements while the total pressure drop was reduced to -3.8 psig.

Since the flow was not choked upon entry into the probe, the probe had to thermally quenched the sampled emission gas. This was accomplished by a series of temperature control devices working in concert to cool the sample and then maintain its temperature to prevent condensation of the sample. Starting with the temperature control devices in the probe, a Mokon HTF-350 oil pump system was used to heat and transport the coolant fluid (Durathem 600 Oil) through the probe at a rate of 10 gal/min. By using the flow rate of the machine, the velocity used by Damele [47] to cool his probe could be calculated and was used as a baseline to calculate the requisite velocities. The minimum velocity calculated in the four-channel probe was 3.91 m/s, which is greater than the slowest velocity of the Damele probe value of 2.92 m/s. Also, the flow velocity at the probe head is of prime importance at this portion of the probe since it resides within in the flame. Therefore, if the velocity was high enough at the probe head, then the Reynolds numbers and heat transfer coefficients would also be greater than his design, and sufficient to ensure proper cooling. Also, the center divide plate was extended further forward in the multi-channel probe to reduce the amount of large, stagnant flow seen within the Damele probe. In order to ensure thermal quenching, an IR TELOPS camera was set to look at the

exhaust plane of the UCC and confirmed that the probe's temperature returned to the set temperature of 420 K within 10 cm of the probe head. Therefore, assuming that the temperature of the exterior of the probe was the temperature of the oil (which is reasonable given that the probe is only 1.5 mm thick), which also was the temperature of the sample (which is separated only by an oil layer 4.3 mm thick), the flow is rapidly thermally quenched.

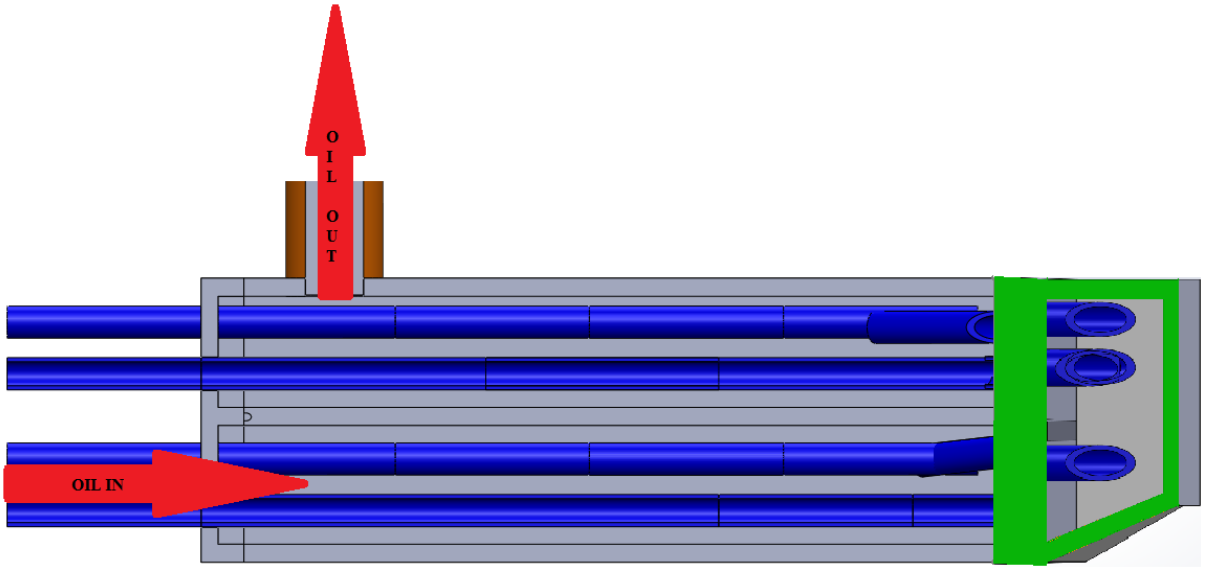

Figure 3.18: Flow Path of Coolant in Multi-Channel Probe
Note: critical flow region is surrounded in green

After the emissions samples leave the probe, it progressed through a 1.21 meter section of flexible stainless steel lines with a 316L core weave and 304 jacket. This section of the line was heated with an Omega HTWC102-010, 2.54 cm wide heating tape which provides 118 W/m of energy into the emissions line. This tape was wrapped with 0.635 cm thick layer of fiberglass tape and protected further with 5.84 cm of fiberglass insulation. A K-type thermocouple was inserted into one of the emissions line to monitor the gaseous temperature. Due to the density of the wrap and the non-perfect contact surface, the correct power setting had to be experimentally

determined. The power setting required to maintain the desired internal emission line temperature of approximately 150 °C was found to be between 15%-20%.

The emissions must be routed to the CAI Emissions Analyzer, which has a single sample input line. This integration of the different samples was accomplished by the addition of an AtmoSeal six-channel manifold switch pictured in Figure 3.19. The flow entered through a 3.3 mm OD tube (bottom of Figure 3.19) and is combined into one flow. Any number of channels from 0-6 may be open at any one time and combined prior to their exit out the top, though only channels one through four should be open with the current probe configuration. The six-channel manifold was internally heated in order to maintain a constant temperature of 150 °C and regulated by an independent control device. In order to open the manifolds, a 24 VDC signal with a minimum of 250 mA was required; this signal was regulated by the NI 9472 cDAQ channel selector. The channel selector essentially functions as a computer operated light switch that turns on or off a common source 24 VDC power supply that opens the manifold when power was supplied, and closes it when power was extinguished. This power was then transferred from the NI 9472 to the manifold switch board, through the bundle of wires occupying the upper right portion of the manifold. The emissions line that routes the gas to the CAI (large black insulated pipe and fitting in the top center of Figure 3.19) can also be seen in Section 3.2.4.

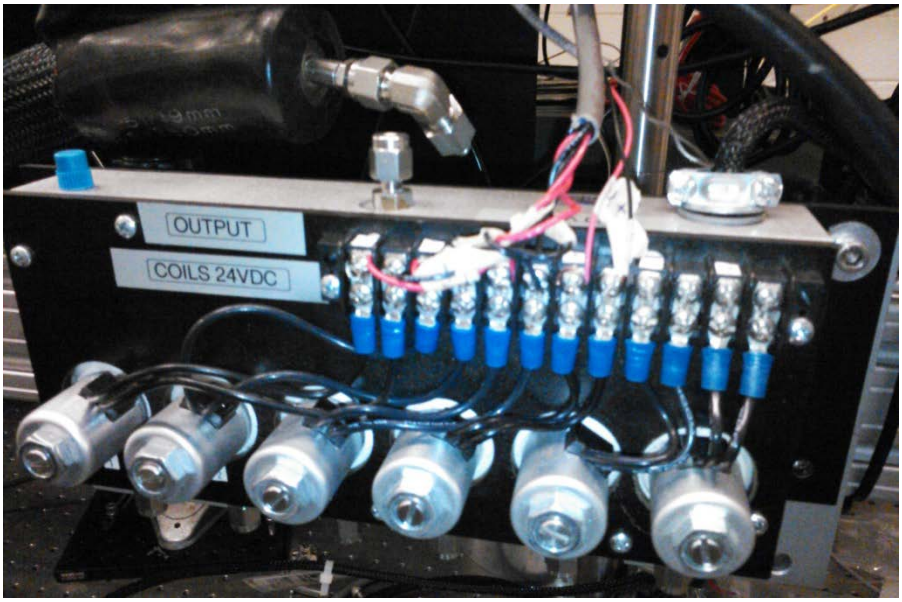

Figure 3.19: AtmoSeal Six-Channel heated manifold switch

The emissions species temperature must be stabilized to cool the flow at a point where the temperature of the gas remains constant so equilibrium may be maintained. The more pressing concern with this data collection method is ensuring the entropy stays constant so the number of free radicals in the emission gas is not reduced. Since the emissions line connecting the probe to the CAI resides approximately 10 meters apart, the flow temperature had to be controlled for the entire length. Therefore, maintaining the temperature of the emissions throughout the entire routing line is paramount to reduce experimental error.

As the gas progresses from the six-channel manifold into the CAI collection line the entire length of hose was also wrapped with a heating tape. This line was provided by CAI at the time of delivery and was calibrated then to ensure an internal temperature between 0-200 °C. This hose has a temperature gauge that allows feedback between the inner diameter of the tube and the control panel upon the CAI, and was set to a temperature of 150 °C during emissions collection. It was assumed that since none of the connectors were more than 5 cm in length, the

temperature loss over these sections was insufficient to warrant consideration as both sides of the connector are heated.

3.1.6. Visual Access Points

The UCC was designed not only to be modular in design but to have extensive visual access points. The third iteration, which was just assembled, added to these optical access points by converting the ports which had previously been used for the discretely-sourced air injection into windows. This was accomplished by designing a seal plate which held a 1.59 cm diameter quartz window over the cavity. A protective layer of Fiberfrax® Unifrax 3.2 mm thick was placed around the window and anchor points to prevent the stress concentration points from causing cracking during thermal expansion. This still led to flame leakages around the edges, so the use of automotive high-temperature RTV and exhause line sealant were used to seal all interfaces. This included the windows, mates between the cavity plates and inner and outer rings, as well as the exhaust tube.

These views allow for extensive non-intrusive measurement techniques such as high-speed flame photography and PIV. This window allows for a LASER beam to enter into the combustion cavity and strike seeded flow with light, enabling PIV measurements to be taken. The seed particles are captured by a Phantom V12.1 high speed digital camera through a second arch-shaped window positioned on the back wall of the combustion chamber.

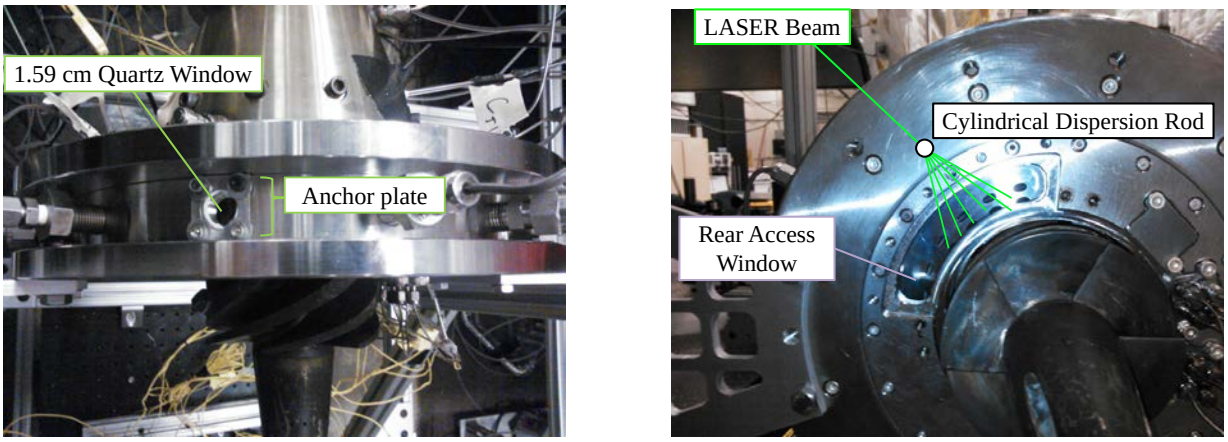

(a) (b)

Figure 3.20: PIV LASER (a) Access Window Anchor Plate and (b) Seed View-Window with LASER Dispersion Sheet Shown

3.1.7. Pressure Measurements

Pressure measurements were required in these experiments in order to determine the local point velocity values at various points within the UCC. The primary means of measurement was a DTC Initium 32 channel pressure scanner. The DTC Initium system uses an advanced analog circuit design that uses Wheatstone Bridges to measure a differential pressure from a reference sample. This sample is standardized and after calibration (right clicking the "re-zero" button on the Initium LabView VI) can provide a 1200 Hz sample with an accuracy within $\pm$ 0.05 %.

Providing the pressure to the initium are two different configuration of probes. The first configuration uses a United Sensor PCA-8-KL Pitot-Static probe. This probe is designed in the classical Pitot-Static probe style with total port at the tip and a static port located on the side of the probe. Both the total and static measurements are individually connected to an Initium channel via a flexible 1.159 mm (1/16 inch) diameter Tygon tube. These probes however are very delicate and difficult to install within the cramped confines of the UCC, specifically it is difficult to insert the probe through a Swagelok fitting into the area of interest and seal the fitting. Also, due to the swirling nature and non-uniform flows seen within the UCC, it is

difficult to orient the probe perfectly normal to the flow. Finally, these probes cannot survive the high temperatures seen in the combustion chamber or exit plane (max temperature of fitting is 480 °F), and can only be used in the diffuser section or inlet.

For this reason, the primary measurement device of for pressure was to use two separate stainless steel pipes as a total port and static port. The total port was inserted as a straight piece of tube into a Swagelok fitting, and then bent into an angle that would make it normal to the incoming flow IAW with the bend radius limits of United Sensor PCA-8-KL Pitot-Static probe. The outer part of the port was bent at a slight angle in the same direction of the total port bend, in order to see the probes position from outside the UCC. The static port was placed at the same axial position as the radial spur of the total port, and flush with the wall to prevent any "cylinder in a cross flow" tip vortices from distorting the pressure entering the static port. Both of these ports were also connected to the Initium pressure scanner via flexible 1.159 mm (1/16 inch) inner diameter Tygon tube. The flexible tubing was placed around the stainless steel tubing concentrically and form a seal. Random seals were checked for leaks by placing soapy water around the interfaces to see if leaked air would produce bubbles. When no bubbles appeared, the seating was deemed secure enough to prevent leaks. Error analysis for the pressure equipment was also previously accomplished by Wilson [24] with the same system, set-up and software. In it, he determined that the error from the initium on the velocity and Mach number measurements were 0.17 m/s and the Mach number was 2.15E-7, which translates to 0.09% for velocity and 8.26E-4% for Mach number for a velocity of 18 m/s.

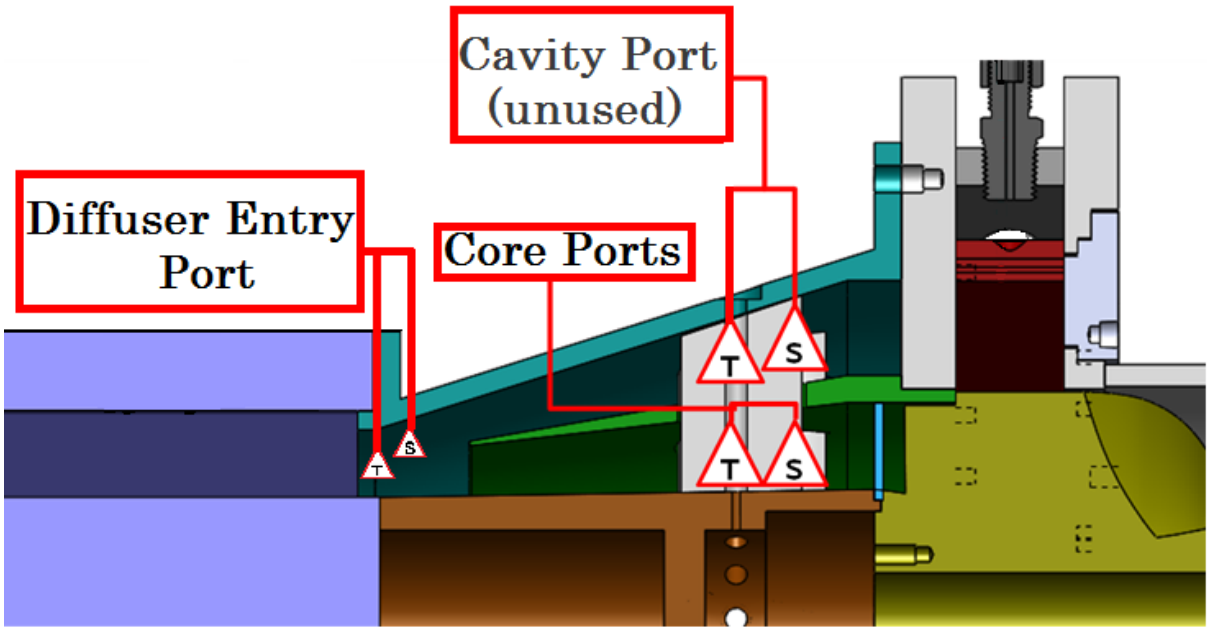

Figure 3.21: Placement of Pressure Ports for these experiments within UCC

3.1.8. Thin Filament Pyrometry

The filaments used for this experiment were 125 micron diameter rods of β-Silicon Carbide (β-SiC) crystals. This material was chosen due to its high emissivity (0.9) and purity of sample. Other mixes of silicone-carbide have lower tolerances for material composition, and will sometimes emit other materials in analysis, increasing error. This alters the emissivity of the material and also shifts the emission spectrum away towards more of the green wave-length, reducing the accuracy of measurements [51]. Data collection was performed by two Bobcat, Imprex monochrome cameras utilizing a 75 mm lens and a 990 nm filter (10 nm bandwidth), with one of the cameras looking directly at the filaments and one for calibration. The two serial numbers for these cameras were 280072 and 280087. The single point calibration for the wires was performed for each experiment at the highest temperature condition (a $\Phi \cong 1.00$) in both view pictures. A DFP 2000 Disappearing Filament Optical Pyrometer from Spectodyne, Inc. with a central wavelength of 655 nm was attached over the lens of the second camera and

recorded. The pyrometer uses a NIST traceable algorithm that allows for the simultaneous test point collection and calibration so that the effects of fluctuating flames can be accounted for. This is especially important with the UCC since it operates in the flamelet in eddies regime.

There were four filaments placed in the combustion chamber attached to the inner ring and the hybrid vane at the varying ratios of axial distance aft of combustion chamber front wall over the total combustion chamber width (z_{comb}/c_{comb}) of 0.13, 0.31, 0.61 and 0.88 (labeled 4, 3, 2, 1 respectively in Figure 3.22) over a 25° sector. The vanes were placed also not along the centerline, but rather staggered on either side of it in order to ensure complete visual access through the large aft quartz window. Pilot holes were drilled into the top part of the hybrid vane less than 0.5 mm in diameter to act as anchor points. Seven additional pilot holes of the same size were drilled all the way through the trailing edge of the aft section of the hybrid vane to make guide holes for seven filaments in the exit plane. These holes were drilled at distance of from the inner diameter of 4.8 mm, 8.8 mm, 12.1 mm, 15.2 mm, 18.4 mm, 22.3 mm, and 25.9 mm, or (in % span) 15.7%, 28.8%, 39.6%, 49.7%, 60.2%, 72.3% and 84.7%. The spatial resolution for this method was previously determined to 120 micron per sample point by Vilimpoc, Goss and Sarka [32] and for this experiment the resolution was equivalent. The resolution within the combustion cavity was around 100 μm and at the exit plane the resolution was 190 μm. The filaments were secured in place with Cotronics © 907 Regular Grade (fireproof) Adhesive. These holes and filaments can be seen in Figure 3.22.

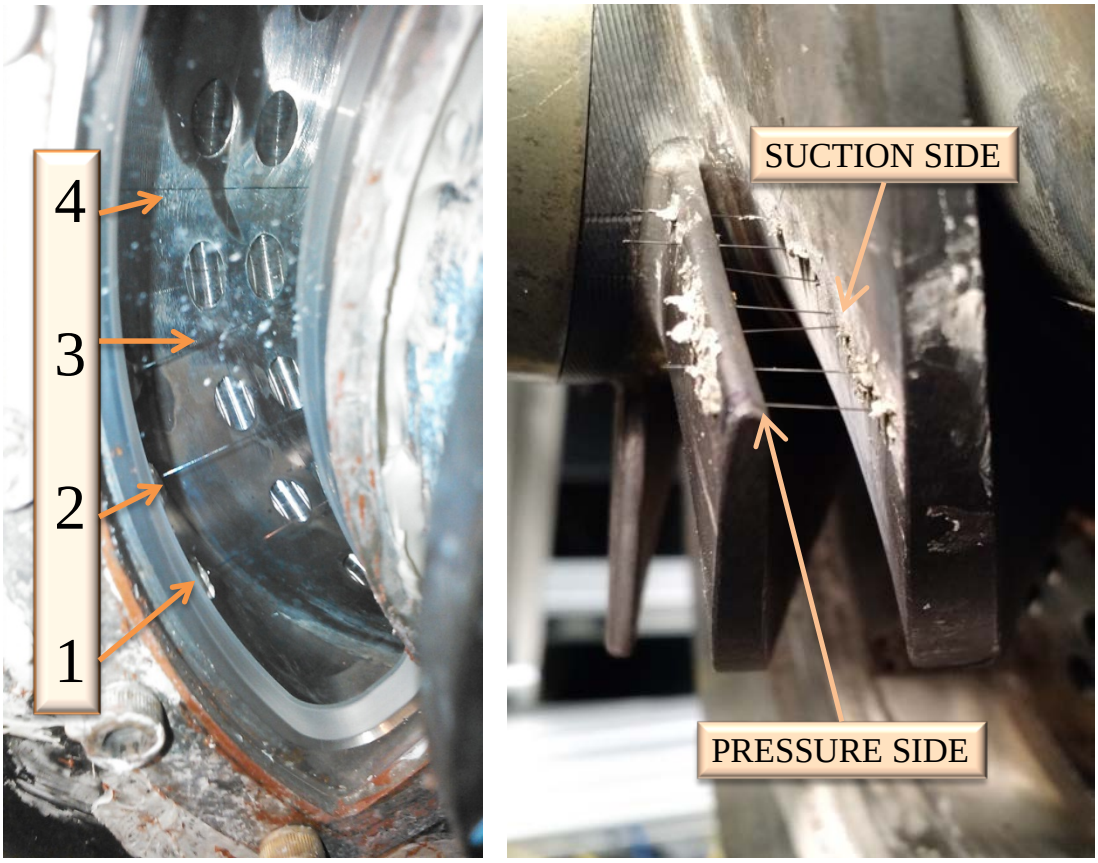

(a) (b)

Figure 3.22: β-SiC TFP Filaments glued in (a) combustion cavity and (b) exit plane

Error analysis for this method was previously determined by Goss [33] for the AFRL SABER-Rig and is equally applicable to the UCC since none of the error terms are effected by geometry. The primary sources of error are those associated with determining filament temperature and those associated with radiation losses (i.e. the filament to gas correction factor). From this realization, Goss [33] found that the error equations for the measurement of the intensity ratio, radiation correction, and gas correction (respectively) were:

$$\delta T_f = \sqrt{\left(T_0 \frac{\partial T_f}{\partial T_o}\frac{\delta T_o}{\delta T_o}\right)^2 + \left(I_R \frac{\partial T_f}{\partial I_R}\frac{\delta I_R}{\delta I_R}\right)^2} \tag{22}$$

$$\delta\Delta T = \sqrt{\left(h\frac{\partial \Delta \mathrm{T}}{\partial h}\frac{\delta h}{\delta h}\right)^2 + \left(T_f\frac{\partial \Delta T}{\partial T_f}\frac{\delta T_f}{\delta T_f}\right)^2} \tag{23}$$

$$\delta T_{gas} = \sqrt{\left(\delta T_f\right)^2 + (\delta \Delta T)^2} \tag{24}.$$

3.2. COAL Laboratory Equipment

The Combustion Optics Analysis and LASER (COAL) Laboratory at the Air Force Institute of Technology (AFIT) is the current location of the AFIT UCC in Dayton, Ohio. The improvements to the UCC, the COAL Lab, and its equipment have been led by a series of different individuals since its last major upgrade. This section describes those improvements and the individuals primarily responsible for their completion.

3.2.1. Air Supply

The air fed into the UCC is supplied primarily by an Ingersoll Rand H50A-SD, 50 hp, oil-free industrial compressor, capable of delivering a mass flow of 1 kg/s of air at atmospheric pressure, or up to 0.1 kg/s at 862 kPa (8.53 atm). The compressor is located in a portable trailer outside but adjacent to the eastern wall of the COAL Lab, as seen in Figure 3.23. The H50A-SD has built-in dryers and filters to remove humidity and dust particles but delivers the air at outside ambient conditions. The air is routed to the diffuser through a series of pipes 7.62 cm in diameter. Previously, a Flowserve MaxFlo 3 valve was installed which limits the inlet flow into the UCC to a maximum flow rate of 0.6 kg/s [25]. To accommodate the mass flow controller, a Fisher 99 pressure-reducing valve was installed that reduces the pressure from the compressor to the appropriate mass flow. A FT2 Fox Thermal Instrument measures and transmits the mass flow to the control station.

Figure 3.23: Ingersol Rand H50A-SD Compressor trailer located outside the COAL Lab

An additional air source is available to the COAL Lab. This source is fed from the AFIT general facility air supply line (3.81 cm in diameter) that the COAL Lab shares with 5 other rooms, each with several experiments within them. The COAL Lab splits the air from this source into two pipes 3.81 cm and 1.90 cm in diameter. A Fisher 299H presssure reducer on this line limits the maximum mass flow rate to 0.3 kg/s in the 3.81 cm pipe, as well as a combination of an ITP and Badger control valve with a Cashoo pressure reducer to limit the 1.91 cm line to a max flow rate of 0.03kg/s [25]. When all three of these pipes are used, the total system mass flow rate delivered to the UCC is 1 kg/s. These two lines also report their mass flows through FT2 Fox Thermal instrument flow meters to the control station. These latter two lines was used extensively by Wilson et al. [5] and Damele *et al.* [37] during experiments with the discretely-sourced-air configuration to supply the six air injection ports on the outer cavity ring. The flow control valves and entry points into the lab for the two sources are shown in Figure 3.24. If both source (yellow handle) lines are open, the red handle must remain in the closed position since there currently exists no other means to prevent backflow between the two sources.

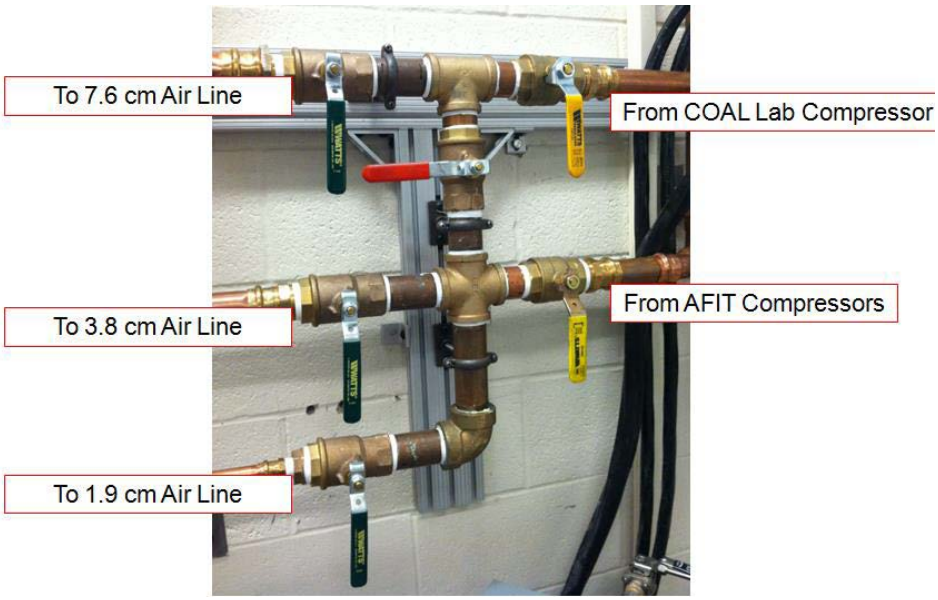

Figure 3.24: Off Position for Mass Flow Control Valves to UCC [25]

3.2.2. Tank Farm

The AFIT Tank Farm is located outside the COAL Lab approximately 100 meters south of the building and 3 meters from the east wall. It is a secured, covered enclosure that stores all the pressured gas and fuel used in the UCC experiments. The CAI uses the six, span gas tanks located in the back right side of the farm to calibrate and purge the emissions line during operation. Further explanation of the CAI tanks is located within the CAI section. The UCC uses four liquid propane reservoirs to fuel its experiments; the reservoirs were located in the front right corner of the tank farm. These reservoirs were piped into the lab via 1.27 cm copper lines. The two propane tanks each were attached to a single Zimmerman LPG liquid-to-gas vaporizer to convert the fuel state, and requires 20 min to heat up. On cold days, previous users found that some of the gas would reliquify prior to entry into the combustion chamber. Therefore, an Omega heat tape was wrapped around the internal copper tubes at the propane tube entry point behind the HVOF experiment shack. A setting between 15% – 25% power was found to be sufficient to prevent any liquid fuel from entering into the cavity. The gaseous fuel

flow was controlled by the Brooks SLA 5853 mass-flow control, which was located within the COAL Lab.

3.2.3. CAI

The California Analytical Instruments (CAI) machine is the primary means of emissions analysis at the COAL Lab. The CAI takes the emissions sample collected by a probe and analyzes that one signal for the concentrations of Total Hydrocarbon present (THC), CO_2, CO, NO_x, and O_2 gas. The CAI uses a flame ionization detection method to determine the number of carbon-hydrogen bonded ions by passing the sample through a hydrogen based flame. Then this number of ions is processed by the CAI and reported as a concentration of propane in the sample. The NO_x sampler uses a heated chemiluminescence process to convert NO to NO_2 and based on the light emitted, the concentration can be determined via a proportional relation. This CAI analyzer also can determine the amount of NO_2 in the flow by converting it to NO in a pre-mixer stage and then adding this additional light to that produced by the original NO in the sample. CO_2, CO and O_2 are determined by the same module using nondispersive infrared spectroscopy to determine the concentration values for each individual gas. All these concentrations are reported originally as concentration values to the displays on the CAI and are then converted to mA values by previously installed circuitry and recorded by the LabView VI.

With respect to the two carbon-oxygen based emissions, there is a wide range of potential values that can be measured, so two calibration gases are used for the CO_2 and CO emission analyzer (termed “spans” on the CAI knobs). The CAI can also report its measurements as current values to a “remote” data recorder that enables a time-averaged value to be obtained for later post-processing. Due to the length of time between uses of the CAI, institutional knowledge was lost on how to operate, maintain and use the California Analytic Industries (CAI) Emissions Analyzer. Calibration procedures and pictures were originally written by Conrad [28]

but maintenance procedures and operating instructions omitted certain steps. Therefore in addition to diagnosing the CAI system to determine solutions for the several problems, new procedures were written and included in Appendix B.

The first problem discovered was that all filters internal to the CAI, as well as those between the CAI and the gas canisters, had been clogged. Once they were replaced, the CAI required an initial calibration. The CAI requires daily calibration and purging of its systems to function properly. Also, the calibration point changes daily, so the machine must be zeroed and spanned before each test. It was discovered through these experiments however that the CO_2 sensor however required significantly more time to warm up than the other four channels (2.5 hours instead of 1.0 hours) and required regular calibration throughout the day. The other channels however would not diverge at all, even when left on for an 8 hour observation period. For this reason, the daily calibration error component was only included for the CO_2 analyzer and not the other four.

During these calibration efforts, three of the gases were exhausted and required replacement. As the gases are a hazardous material, their procurement requires a different process than normal part buys. Finally, the pump motor was no longer in alignment and required maintenance, in which Mr. Josh DeWitt played a key role. Due to the fragmented nature of the existing operating guidance for the UCC and the lack of maintenance guidance, a new consolidated operating procedure and maintenance schedule was drafted and is included in Appendix B.

After the CAI was properly calibrated, a new LabView Visual Instrument (VI) was created and placed upon the main UCC control interface. This VI reads the differential amperage on a scale from 4 mA to 20 mA supplied by the CAI data readout display. To capture

a representative value, a series of 50 samples was taken at a rate of 10 Hz. This data was then output to a .csv file and post-processed by a Matlab script, included in Appendix C. When the CAI is properly calibrated, the different span ranges report their readings as different values. For example, a CO reading of 1600 ppm would read 17 mA for span 1 and 6 mA for span 2. However, the span selected on the CAI is not reported to the data acquisition computer. Therefore a user specified input was placed on the UCC operating VI to capture what span is selected. This value must be inputted by the user each time he changes the span on the computer. This interface, along with the AtmoSeal control panel, can be seen in Section 3.2.4.

The average mean and standard deviation were then calculated in order to consolidate the data into a single point and aid in further error analysis. The first three points taken were always the daily calibration points: a zero reading point and then one or two "span" readings. From these initial points, a linear trend line was established that was used to convert the mA data given by LabView into units of ppm of the exhaust species (ratio of molar concentration). Due to the ambiguity of two point correlations, a way to ascertain more data was sought to validate the assumption that there is a linear relationship between the ppm reading and the mA recorded by LabView. Ideally, multiple samples of each gas would be required to achieve a sufficient amount of points. However, due to cost constraints and the number of ports available to the CAI, an alternative solution was developed. The skew dial for the span was adjusted to alter the reading around each span gas. For example, the CO gas was taken at 0 ppm, 1200, 1600 ppm, 2000 ppm, 4400 ppm, 4800 ppm and 5200 ppm. The current values for each of these points was taken, and then their mean and standard deviation were calculated. As the charts in Appendix A show, the amperage data shows linear agreement with the concentration readings displayed by the CAI over the same time frame. This test also confirmed that the linearity error of the CAI

was near the reported number of 1.0%. Therefore, a linear trend line was calculated after this by simply using the daily zero and span values for each gas.

3.2.4. LabView

Much of the COAL Lab's equipment and data collection is run through a series of Virtual Interfaces within National Instruments LabView 2011. These processes are all centralized in two NI 9178 cDAQs that are populated NI modules dedicated to specific processes. Three, NI 9213 16-channel thermocouple input modules are used for temperature acquisition, a NI 9472 module controls the Atmoseal regulator, an OPTO-22 circuit board reads the differential amperage readings of the CAI analyzer and reports it to LabView data via a NI PCI-6209 series bank isolator. Propane is not controllable by LabView without additional software driver installation so its control has remained on the Brooks Instrument flow controller. The same applies to the flow control settings with the MKS flow controller, but the solenoids for all 8 channels were designed to be controlled in LabView by Wilson [25].

Some VIs had already been developed by Wilson [25], Damele [47], Cottle [50] and others. These legacy VI's were able to acquire data but only as a text file and required the operator to push a radial button multiple times to get the required number of sample points. The frequency of acquisition was also limited by both the operator and the computer's ability to write the data; a process that required multiple seconds to pass between sample points. This irregularity of sample had not been rectified due to the thermocouple acquisition rate being set to "high-resolution", which limits the maximum sample rate to only 1 Hz. However, the CAI amperage reader is capable of a 50 Hz sampling rate, so a more regimented sample collection was required.

In order to acquire the CAI data while also outputting to the VI to ensure that LabView was receiving correct measurements, a series of software loops were constructed. The final design uses nested Boolean logic to output a single value during normal, non-data collecting operations (titled “1 sample (On Demand)”) that LabView continuously reads and then dumps. This is pivotal, as any other setting will cause the values to be stored indefinitely and quickly use up the available RAM. The other settings also cause a lag in the data collection time, so that when the “take data” button was pressed, it would take data from minutes prior. The purpose of the nested “if statements” are to only activate the data saving and writing commands only when prompted. This saves the RAM, and overwrites the data after each use. A windows dialogue box appears each time to prompt the user to save the data as a separate file type, and can be saved as a text, .csv, or .xls file per the desires of the user. This also improves upon the previous VI which only allowed for a single text file to be saved with all the data points, now the data can be more easily segregated into separate files. The original number of samples taken was 30 at a rate of 3 Hz in order to match the duration of the temperature measurement.

The same logic was used to improve the temperature measurements. It was also noted during this reconfiguration of the temperature DAQ Assistant that the NI 9213 modules were interpreting the voltage signals as J-type thermocouples, not the K-types used. Upon investigation, it was discovered that this was a legacy issue that had resulted in measured values consistently lower than CFD predicted values. A Matlab function titled “J2K” was developed using the calibration coefficients provided by Omega that could convert the published data back into a mV value, and then correctly convert it to a K-type value. This file is located for future student use on the common L:/ drive at: L:\Research\COAL LAB\Softwares & Manuals\Matlab Code.

It was previously assumed that the mismatch between the CFD and experimental data was due to a large gas correction factor, but upon correcting the correlation curves the values were shown to be much closer to previous and new predictions. It was also discovered that when using the high resolution mode, the number of samples is limited to 10, resulting in only 10 samples at 1 Hz being recorded automatically by the VI. It is possible to have more samples for a longer duration of time, but requires the VI to switch the collection mode from "high resolution" to "high speed". With the increased speed comes increased error, specifically an increase in the maximum measurement error from 1.64% to 1.78% which occurs at the lowest temperature measurements (around 560 K). Due to the small amount of error, the high speed option was selected as the future COAL Lab standard with a setting of 50 samples over 10 seconds. However, this setting was implemented late in the process and the initial data presented in Sections 4.1.2 and 4.2.1 were taken using the high resolution setting.

3.3. Data Collection

Data collection run conditions and equipment positions were informed by the Cottle CFD Model [50]. An example test point for a single hybrid vane geometry is provided below in Table 3.1. Pressure and temperature data is collected by the pitot-static probes and thermocouples (respectively) at the different locations of the engine. The profile and pattern factor data is collected with the instrumentation ring and silicone-carbide filament strands. Emissions data is collected by the four-channel emissions probe and routed to the CAI gas analyzer. All this information is reported and recorded by two National Instruments cDAQ busses which communicate and process the controls and data via the UCC LabView V11 SP1 user interface. As stated earlier, the CAI user interface was incorporated onto the UCC interface to streamline the data collection process. This software is run on a Dell desktop computer using the Windows

XP operating system located at the COAL Lab control station. The set points for the user interface are located within the bold box and the corresponding mass flow values have been calculated to determine the cavity equivalence ratio (Φ) for those conditions.

Table 3.2: Sample Test Card for Single Geometry Test Point

Geometry	Air Set Point	Fuel SLPM	Case #	Total Air [kg/s]	Fuel [kg/s]
LLCB 1	18	26	1	0.1080	0.00067
LLCB 1	18	33	2	0.1080	0.00134
LLCB 1	18	39.4	3	0.1080	0.00183
LLCB 1	18	46	4	0.1080	0.00064
LLCB 1	18	53	5	0.1080	0.00161
LLCB 1	18	59	6	0.1080	0.00220
LLCB 1	18	70	7	0.1080	0.00161
LLCB 1	18	90	8	0.1080	0.00220
LLCB 1	7 (idle)	15.4	9	0.1080	0.00141

3.4. Test Matrix

For these test matrices, and in the ensuing results, certain abbreviations are used. Those terms are clarified here for the reader as well as in the nomenclature section. UCCv3 is the most recent version of the combustion chamber but with holes 55° tangential to the flow and 0° tangent to the combustion cavity wall. The Cmpd Drvr, is the Compound Air Injection Driver scheme that adds the 10° tangential angle to the hole orientation within the combustion cavity. The term LLCB refers to the Low Loss Center-body designed and first tested by Wilson *et al.* [5] and used by Damele [37]. RVC is the Radial Vane Cavity design newly manufactured during the course of this thesis. All equivalence ratios mentioned in this paper and its charts are cavity equivalence ratios (Φ_{cavity}); to get the total equivalence ratio all one must simply do is divide the shown value by the appropriate cavity air split. Table 3.3 shows all the test points that were taken for this thesis. Note that one point constitutes data for pressure, thermocouple temperature, emissions and TFP data except for the idle condition, which was only taken during TFP tests.

Table 3.3: Complete Test Card for all data points, as well as date completed

Geometry			Air Set Point	Fuel SLPM	Total Air [kg/s]	Fuel (kg/s)	Date Emissions Completed
Geometry Number	Air Driver	Center-body					
1	UCCv3	LLCB	18	26	0.108	0.00067	17 Dec 15
1	UCCv3	LLCB	18	33	0.108	0.00134	17 Dec 15
1	UCCv3	LLCB	18	39.4	0.108	0.00183	17 Dec 15
1	UCCv3	LLCB	18	46	0.108	0.00064	18 Dec 15
1	UCCv3	LLCB	18	53	0.108	0.00161	18 Dec 15
1	UCCv3	LLCB	18	59	0.108	0.0022	30 Dec 15
1	UCCv3	LLCB	18	70	0.108	0.00161	30 Dec 15
1	UCCv3	LLCB	18	90	0.108	0.0022	30 Dec 15
1	UCCv3	LLCB	7 (idle)	15.4	0.108	0.00141	TFP (25 Jan 16)
2	UCCv3	RVC	18	26	0.108	0.00067	10 Dec 15
2	UCCv3	RVC	18	33	0.108	0.00134	10 Dec 15
2	UCCv3	RVC	18	39.4	0.108	0.00183	10 Dec 15
2	UCCv3	RVC	18	46	0.108	0.00064	10 Dec 15
2	UCCv3	RVC	18	53	0.108	0.00161	10 Dec 15
2	UCCv3	RVC	18	59	0.108	0.0022	10 Dec 15
2	UCCv3	RVC	18	70	0.108	0.00161	10 Dec 15
2	UCCv3	RVC	18	90	0.108	0.0022	10 Dec 15
2	UCCv3	RVC	7 (idle)	15.4	0.108	0.00141	TFP (21 Jan 16)
3	Cmpd Drvr	LLCB	18	26	0.108	0.00067	30 Jan 16
3	Cmpd Drvr	LLCB	18	33	0.108	0.00134	30 Jan 16
3	Cmpd Drvr	LLCB	18	39.4	0.108	0.00183	30 Jan 16
3	Cmpd Drvr	LLCB	18	46	0.108	0.00064	30 Jan 16
3	Cmpd Drvr	LLCB	18	53	0.108	0.00161	30 Jan 16
3	Cmpd Drvr	LLCB	18	59	0.108	0.0022	31 Jan 16
3	Cmpd Drvr	LLCB	18	70	0.108	0.00161	2 Feb 16
3	Cmpd Drvr	LLCB	7 (idle)	15.4	0.108	0.00141	TFP (2 Feb 16)
4	Cmpd Drvr	RVC	18	26	0.108	0.00067	6 Feb 16
4	Cmpd Drvr	RVC	18	33	0.108	0.00134	6 Feb 16

4	Cmpd Drvr	RVC	18	39.4	0.108	0.00183	6 Feb 16
4	Cmpd Drvr	RVC	18	46	0.108	0.00064	6 Feb 16
4	Cmpd Drvr	RVC	18	53	0.108	0.00161	6 Feb 16
4	Cmpd Drvr	RVC	18	59	0.108	0.0022	6 Feb 16
4	Cmpd Drvr	RVC	18	70	0.108	0.00161	6 Feb 16
4	Cmpd Drvr	RVC	18	90	0.108	0.0022	6 Feb 16
4	Cmpd Drvr	RVC	7 (idle)	15.4	0.108	0.00141	TFP (9 Feb 16)

3.5. Uncertainty Analysis

The measurements taken with this experiment were done by inputting the air mass flow setting and the fuel mass flow setting and then finding the pressure, temperature, and emissions within the combustion cavity as well as across the exit span of the center-body. Geometric measurements for the UCC rig were provided by the SolidWorks model with the machine shop tolerance of ± 0.05 cm and ± 1.0° for angle measurements on the wire EDM machine used to cut the air driver holes in the two front combustion cavity plates. The position of thermal and emission probes were determined by the process specified in Figure 3.15 using manufacture and SolidWorks provided measurements as reference lengths. Positions were marked at the beginning and end of each experiment to ensure marginal travel occurred, and if the deviation was too great, the point was discarded from analysis.

3.5.1. Input Parameter Error

Initial error assessment has been previously performed and annotated by previous master's students in the COAL Lab, most recently Damele [47]. He used the Constant Odds general form equation from Moffat [52] to determine the accuracy of measurement. This analysis is based on the equation:

$$\delta R = \left\{ \left(\frac{\partial R}{\partial x_1} \delta_{x_1} \right)^2 + \left(\frac{\partial R}{\partial x_2} \delta_{x_2} \right)^2 + \cdots \left(\frac{\partial R}{\partial x_n} \delta_{x_n} \right)^2 \right\}^{.5} \quad (25)$$

where R is the parameter of interest, x_n is the measured experimental result, and δx_n represents the measurement accuracy of the device used in the experiment. This equation also assumes a time averaged value is taken and then averaged together for a single value, which was done for all done for all data points in this experiment. Since the same air system and fuel system was used, the cavity equivalence ratio's error comes from the FT2 Fox Thermal Instrument and the Brooks Mass flow controller (respectively). Damele [47] found that the equivalence accuracy was ±0.6 % and this value also applies to all Φ_{cavity} values in this paper as well.

3.5.2. Calculated Data Error

3.5.2.1. Velocity

As previously mentioned in Section 3.1.7, Wilson [24] found the pressure error inherent to the Initium system propagated to a velocity error of 0.17 m/s. In order to reduce the error in the measurement, only the core flow measurement was taken where the flow is more uniform. The cavity flow is highly turbulent and has been shown to have large pockets of stagnant air, as well as highly variable velocity profile. Therefore, it is best to just subtract the core flow from the known total mass flow and have that be used as the cavity air flow value. As the max error will occur with the lowest measured velocity, this value was used to determine the maximum velocity error in the measurement. The slowest core velocity measured was 17.7 m/s, which means that the calculated velocity and mass flow values are within ± 0.96% of their true value.

3.5.2.2. Temperature – Thermocouple

For heat measurement devices, there are typically two main sources of error: the instrument error and the corrective gas factor. The former is characteristically a known quantity

provided by the manufacturer and dependent on the use range of the device. There is also error in the wiring and data collection device, which are values also provided (or accounted for) by the manufacturer. Omega, who manufactured the K-type thermocouples used in all these experiments, provides these values upon purchase as well as on their website [31]. Using this manufacture data, it was determined that the worst-case scenario for instrumentation error was 4.6 °C, or 2.34% of an individual probe's reading.

A repeatability study was also conducted to determine the ideal time to take temperature measurements. Normally, a single temperature measurement over ten seconds was taken. All temperature measurements were taken on the same day as their subsequent emissions measurements. As the CAI required approximately 2-5 min to reach an equilibrium reading, the temperature was taken during this transition wait time out of convenience. However, there are CAI probe channels, and therefore the equilibrium wait was required for all four locations. Therefore, the temperature was taken in between emission sample collection times, and as there are four emissions channels, four temperature points were also taken for this repeatability study. The two data points considered were the highest reading thermocouple and the lowest reading thermocouple, as typically these would provide the largest degree of error. This ensured that both the effects of colder and hotter thermocouple were considered. Also, the mean and standard deviation across each 10-second sample period are presented for reference. From this, the repeatability error for these experiments remained constant so long as the temperature measurement was taken after the first channel of emissions data and the resultant means, standard deviation, and confidence interval due to repeatability are presented in Table 3.4. In fact, the repeatability error was no more than ± 3.4% for these points and showed no distinct trends, suggesting that the reading had stabilized.

Table 3.4: Thermocouple Repeatability Study Results with Confidence Interval of Thermocouple reading for Lowest Temperature and Highest Temperature

Low Temperature Point	Run 1	Run 2	Run 3	Run 4
Time Averaged Temperature (°C)	302.4	313.5	305.0	288.3
Temperature Standard Deviation (°C)	1.42	3.45	2.95	1.10
Percent Deviation across sample	0.468%	1.101%	0.967%	0.381%
Sample Mean	302.3			
Standard Deviation	10.44			
95% Confidence Interval (n = 4)	291.179	313.44176	± 3.454%	
High Temperature Point	**Run 1**	**Run 2**	**Run 3**	**Run 4**
Time Averaged Temperature (°C)	788.1	784.0	775.4	817.2
Temperature Standard Deviation (°C)	4.11	4.92	3.57	7.00
Percent Deviation across sample	0.521%	0.628%	0.461%	0.856%
Sample Mean	791.2			
Standard Deviation	18.16			
95% Confidence Interval (n = 4)	773.016	809.338	2.295%	

3.5.2.3. Temperature – TFP

However, the second source of error requires considerably greater effort and knowledge of the flow field. Due to the nature of heat transfer, the actual temperature of the fluid (referred to as the gas temperature) will not be fully captured by the probe. Instead, it will lose this energy to conduction along the metal probe and radiation to the surroundings. For gases above approximately 1000 °C, the gas will begin to also radiate excess energy into the probe, which will further exacerbate the error. The advantage of TFP is that it has proven to be very

responsive to temperature fluctuations, account for this radiate loss very accurately, and it also has the error analysis well categorized. This error analysis, as previously determined by Goss [33] for the AFRL SABER-Rig, is equally applicable to the UCC since none of the error terms are effected by geometry. The primary sources of error are those associated with determining filament temperature and those associated with radiation losses (i.e. the filament to gas correction factor). From this realization, Goss found that the error equations for the measurement of the intensity ratio, radiation correction, and gas correction (respectively) were given by equations (21), (22), and (23) in Section 3.1.8.

These filaments had previously been analyzed under a Hencken burner for calibration and it was found that the $\frac{\delta T_o}{T_o}$ could be estimated to be 2.5% [33]. The uncertainty for the Irradiance term is dependent primarily on the camera measurement noise, as the long-term fiber degradation was shown to be negligible in previous studies [33]. The detectors provided by ISSI is known by them to have an error of $\frac{\delta I_R}{I_R} \approx 5\%$ [51]. Furthermore, when the reference temperature is 1580K and the detector wavelength is 990 nm, the partial $\frac{\partial T_f}{\partial T_0} \cong 1.0$ while $\frac{\partial T_f}{\partial I_R} = 175.7$. Therefore δT_f is approximately 36 K [51].

The greatest variance in the error for the second temperature term was a function of the velocity around the filament. When the velocity was high, the amount of time the gas has to radiate energy to and from the surround gas was reduced. Also, higher velocities cause greater magnitudes of the heat transfer coefficient (h). The h used for this analysis was taken from computational velocity values [50] and found to be 3600 W/m^{2}K. This, combined with a measured value of $T_f = 1580$ K, $T_\infty = 298$ K and ε=0.9, $\delta\Delta T$ is calculated to be ≈10K for the combustion cavity, which is the worst case scenario. Combining the uncertainty of the filament

measurement (δT_f) and the filament to gas temperature conversion ($\delta \Delta T$), the total uncertainty is off 38 K for the TFP measurements [51].

One other source of error was noted during the collection of TFP data. This error, depicted as the solid red line in Figure 3.25, shows a large spike in the temperature for this one geometry. This spike was due to a large blot of adhesive that altered the diameter of the filament across that location, which when processed by the ImageJ algorithm resulted a higher than correct value to be reported. The adhesive likely came from incidental contact with the applicator and dried on the filament. In order to correct for this, the data in between the effective points were removed and smoothed by taking the total difference between the two good data points and distributed the difference linearly across the affected filament span. This smoothing can be seen as the black dotted line in Figure 3.25, which are the results shown in Chapter 4.

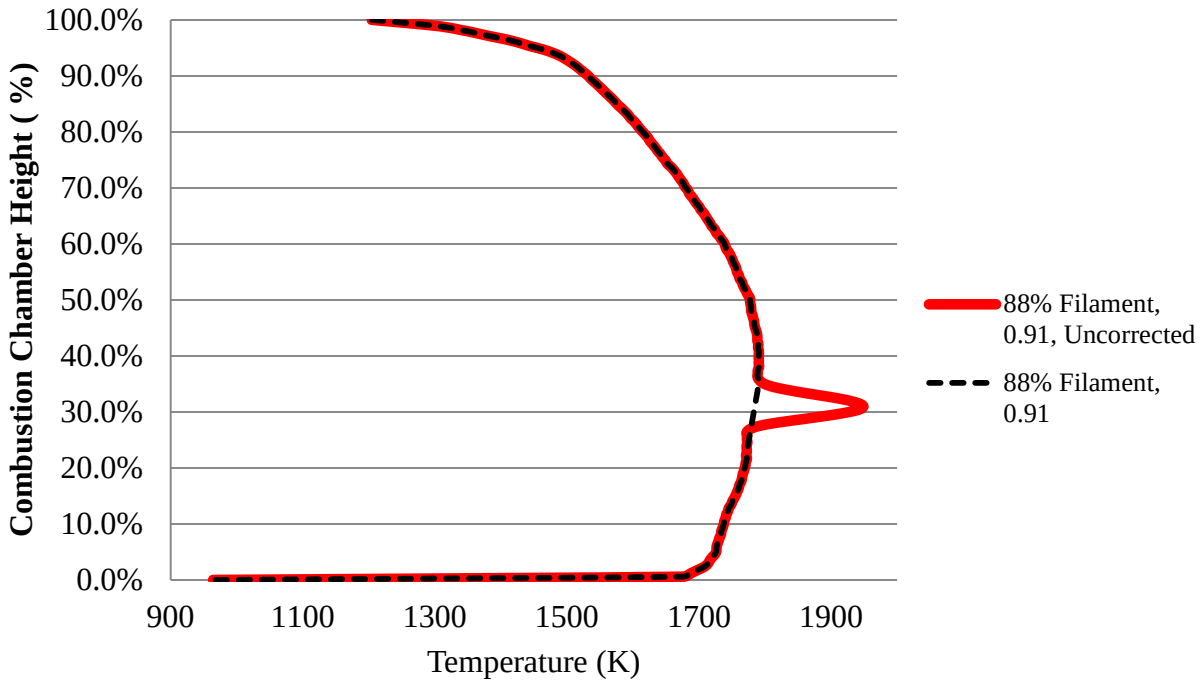

Figure 3.25: Data Smoothing Performed on TFP Temperature Values for Contamination of Wire due to Adhesive During Tests for the Compound Driver – LLCB geometry

3.5.2.4. Emissions

The California Analytic Emissions analyzer was the only quantified source of emissions error for this experiment. This was done primarily due to the error reduction tests and steps outlined in Sections 3.1.5 and 3.2.3 to quickly thermally quench the flow and maintain it at a constant temperature until it reached the analyzer. The analyzer itself has published values for its error, and all depend on the maximum measurable value (i.e. max range) of the specific span selected for each individual gas. Table 3.5 itemizes theses published sources of error, as well as the values that match to each span setting used during this experiment. Of note in this table is that an X means that there is no published error for that source corresponding to that analyzer, and a * means that this value was neglected due to measurements conducted over the course of these experiments. Also, the measurement of O_2 has been shown to have no effect on the error in calculating Emissions Indices.

Table 3.5: Published Sources of Error and Corresponding Value Relevant to these Experiments.

Source (X)	% Max Span	THC (ppm)	NO_x (ppm)	CO (ppm)	CO_2 (ppm)	O_2 (ppm)
Range Set		7	2	1	1	3
Max Range Value		10000	100	10000	50000	250000
Linearity	1.0%	100	1.0	100	500	2500
Repeatibility	0.5%	50	0.5	100	500	2500
O_2 Effects	1.0%	100	X	X	X	X
Noise	0.5%	50	0.5	100	500	2500
Zero/Span Creep	1.0%	***	***	***	500	X
H_2O effect	1.0%	X	1.0	X	X	X
CO_2 Effect	1.0%	X	1.0	X	X	X
RMS value		158.1	1.87	173	1000	4330
$\Delta[X]/X_{max\ range}$		1.58%	1.87%	1.73%	2.00%	1.73%

How to calculate emissions indices and efficiency was previously defined in ARP 1533 [42], but a simplified way to complete error analysis on these calculations was not included in them originally. Therefore, in 2000 Heneghan and Frayne [53] developed a means to quantify the error seen by emissions analyzers. They based their analysis on a standard, first order linear analysis and through a series of steps found a group of terms that would determine the error in the emissions indices. This analysis and terms was then incorporated to the CAI post-processing software designed and is both a text output to the main MatLab screen and the writeable Excel file. As each location and run condition has its own associated error value with it, the max and mean error value for each point was found. Those values can be seen in Table 3.6.

Table 3.6: Max and Mean Error for Emissions Index for each geometry tested

EI Considered	UCCv3 - LLCB		UCCv3 - RVC		C.D. - LLCB		C.D. - RVC	
	Max	**Mean**	**Max**	**Mean**	**Max**	**Mean**	**Max**	**Mean**
THC	3.36%	3.15%	2.37%	2.15%	3.28%	3.11%	2.43%	2.32%
NOx	3.66%	3.52%	2.58%	2.44%	3.57%	3.50%	2.63%	2.55%
CO	2.89%	2.75%	2.33%	2.02%	2.86%	2.75%	2.43%	2.28%
Efficiency	1.88%	0.27%	0.46%	0.15%	0.55%	0.29%	0.15%	0.058%

In addition to the error analysis performed with the CAI analyzer, the repeatability of these measurements were also considered. In order to quantify this effect, all five species of emissions were taken at the same air and fuel condition with a common geometry; specifically with the standard driver UCCv3 configuration at an air/fuel case of 0.108 kg/s and 39.4 SLPM Propane. However, as O_2 does not factor into the calculation of EI, its error analysis was excluded from all subsequent discussion. Each condition was sampled 30 times over a period of 10 seconds, from which a time-averaged single sample value was determined. This point was then repeated four times over three different days at different points in the test card in order to get a diverse sample. The probe orientation and position was not altered at all between the three

test runs. Table 3.7 shows that the original repeatability with the CAI was low, and highly dependent on both the levels of CO_2 read and the CO read. The CO_2 issue was later discovered to occur because the CO_2 analyzer component required significantly longer time to warm up than the manual instructions specified (2.5 hours instead of 1.0) and fluctuated much more in its sampling readings than the other emissions. Once the requisite 2.5 hours, a later comparison was accomplished for three points at the same air/fuel setting, but with the Compound Air Driver and LLCB geometries over the course of 3 different days. The probe orientation was moved slightly between test runs but returned to the same position. As seen in Table 3.7, the repeatability for these points was much higher, and consequently it was determined that the CAI should require at least 2.0 hours of warm up time once the THC sampler has been ignited. The worst case for the new procedures was 8.0% while the worst case for the old procedures was

Table 3.7: Repeatability Comparison for All 3 Emissions Indices Species and Efficiency for 4 different conditions using UCCv3 – LLCB Geometry

EI_{THC}				Mean	STD	EI_{NOx}				Mean	STD
0.736	0.736	0.736	0.736			0.736	0.736	0.736	0.736		
59.1	89.6	65.4	43.4	64.41	19.20	0.987	1.109	1.211	1.008	1.08	0.10
47.7	76.3	67.9	33.2	56.36	19.52	0.978	1.219	1.397	1.059	1.16	0.19
39.3	67.9	67.0	26.5	50.22	20.60	1.229	1.445	1.705	1.229	1.40	0.23
36.2	***	49.1	22.4	35.98	13.34	1.216	***	1.265	1.065	1.18	0.10
*** Removed b/c of bad CO reading ***		Worst Case		50.22	20.60	*** Removed b/c of bad CO reading ***		Worst Case		1.40	0.23
		95% Confidence Range		28.26	72.18			95% Confidence Range		1.16	1.64
		Percent off from Mean		- 43.7%	43.7%			Percent off from Mean		- 17.2%	17.2%

EI_{CO}				Mean	STD	$EI_{Eff\%}$				Mean	STD
0.736	0.736	0.736	0.736			0.736	0.736	0.736	0.859		
270.6	321.4	303.5	233.5	282.30	38.73	88.6	90.9	87.3	84.5	87.90	2.66
249.7	301.6	297.2	208.7	264.34	43.89	90.2	92.4	87.2	86.3	89.06	2.83
217.8	274.6	265.1	174.1	232.96	46.42	91.6	93.8	87.9	87.6	90.30	2.98
264.9	***	262.6	260.9	262.86	2.04	91.0	93.6	87.3	89.8	90.47	2.65
*** Removed b/c of bad CO reading ***		Worst Case		232.96	46.42	*** Removed b/c of bad CO reading ***		Worst Case		90.3	2.98
		95% Confidence Range		183.48	282.44			95% Confidence Range		87.12	93.48
		Percent off from Mean		- 21.2%	21.2%			Percent off from Mean		-3.5%	3.5%

Table 3.6: Second Repeatability Comparison Using Compound Driver, LLCB Geometry with Longer Warm-Up Period

EI_{THC}			Mean	STD	EI_{NOx}			Mean	STD
0.672	0.672	0.679			0.672	0.672	0.679		
76.473	70.515	59.792	68.93	8.45	1.037	1.054	0.917	1.00	0.07
56.602	60.473	47.104	54.73	6.88	1.037	1.033	0.999	1.02	0.02
53.418	***	45.675	49.55	5.47	1.035	***	1.096	1.07	0.04
49.230	65.639	57.141	57.34	8.21	1.061	1.104	1.183	1.12	0.06
Missed Point	Worst Case		68.93	8.45	Missed Point	Worst Case		1.00	0.07
	95% Confidence Range		59.92	77.94		95% Confidence Range		0.92	1.08
EI_{CO}			Mean	STD	$EI_{Eff\%}$			Mean	STD
0.672	0.672	0.679			0.672	0.672	0.679		
339.189	327.598	298.073	321.62	21.20	85.547	82.502	89.147	85.73	3.33
314.291	318.878	278.073	303.75	22.35	88.034	84.656	89.710	87.47	2.57
293.330	***	271.926	282.63	15.13	88.773	***	89.976	89.37	0.85
266.153	306.383	296.862	289.80	21.02	89.737	84.458	88.329	87.51	2.73
Missed Point	Worst Case		303.75	22.35	Missed Point	Worst Case		87.33	3.33
	95% Confidence Range		279.92	327.58		95% Confidence Range		83.78	90.88

IV. Results

By combining the existing UCC rig with the newly manufactured geometries, two newly designed temperature measurement options, as well as the revitalized multi-port probe emissions system, the research objective of determining the effect of altering the geometry of the combustion cavity, geometry of the hybrid vane, and air driver scheme could be accomplished. The results show that altering the combustion cavity geometry, as well as that of the hybrid vane, has an effect that communicates itself upstream into the diffuser. The temperatures at different points within the UCC were taken, and then their profile factors and local pattern factors were calculated. The increased aspect ratio in the combustion cavity was used for all experiments in this thesis, though a comparison to the previous UCC in the discrete air configuration was also made. For these same geometric changes, the emissions indices for the three major pollutant species were taken and compared to show that the RVC produced significantly more emissions than the original smooth walled Low Loss Center-Body (LLCB) design.

The emissions characteristics of the new UCC geometries were also investigated with the new emissions probe detailed in Section 3.1.5. The three emissions emphasized by ARP 1533 [9] are the total unburned hydrocarbons (THC), Nitrous-Oxide chains (NO_x), and carbon monoxide (CO). The CAI is able to determine the molar concentration of these species within the exhaust when collected with the new multi-port probe assembly. From this, the emissions indices can be determined and are presented in this section for the four geometries considered. No emissions data was previously produced for the discrete source configuration or UCC v2 and its collection was considered outside the scope of these experiments.

Of note is that the UCC efficiencies calculated are significantly lower than those of traditional jet engine combustors. All the point efficiencies were between 50% - 95%, which is

considerably lower than those seen in traditional combustors (i.e. > 99% efficiency). This is due to the AFIT UCC air source providing flow at atmospheric conditions (i.e. pressure is around 1 atm). Modern combustors use compressors to do work on the flow before it enters into the chamber in order to increase efficiency. Zelina *et al.* [4][11][18] ran a similar combustor at atmospheric conditions and found that the peak efficiency were between approximately 50%-97% consistent with this work.

4.1. Combustion Cavity Comparison: UCCv3 Versus UCC v2– LLCB Vane

The first configuration tested for this thesis was the one that would best enable a comparison to previous work: the UCCv3 combustion cavity with the smooth body LLCB. This work established the baseline for all other cases in this thesis. By increasing the cavity height and therefore the radial distance between the fuel injectors and the core flow, Wilson [25] hoped that the residence time of the fuel could be increased. This would then lead to higher exit temperatures, more heat release, and better efficiency. The effects on the exit temperature profile were not considered at the time of design.

In this section, a comparison of these results to the previous results of Damele [46] with the smaller combustion cavity (UCCv2) was accomplished. As previously noted by Damele [46], the observed temperature profile was biased toward the outer diameter. The Damele data was corrected by using the calibration coefficients provided by J2K program specified in Section 3.2.4. This allowed the exit temperature results from UCCv2 to be compared The UCCv3 data then served as the baseline for the three other configurations tested in this thesis to evaluate the merits of each design. Since the Damele data and all preceding data did not correct for radiative heat loss effects, this thermocouple data also neglected this analysis in order to make a more appropriate qualitative comparison. Quantitative temperatures were instead measured with Thin

Filament Pyrometry as discussed in Section 3.1.8. An emissions baseline condition was also established for the UCCv3 with the LLCB vane as there was no emissions data available for the UCC v2 geometry.

4.1.1. Mass Flow Comparison Between UCCv3 and UCCv2

The first aim for evaluating the new UCCv3 geometry was to evaluate the impact of the larger circumferential cavity. To accomplish this, flow conditions were compared to the previous UCC v2 investigations of Damele [37]. Initial mass flow splits were assumed to be equivalent between original common core combustion chamber and the increased aspect ratio combustion chamber (UCCv2 and UCCv3 respectively). However, initial experiments with the UCCv3 geometry revealed that the acoustics issued by the UCC were behaving as if it was operating at a far greater cavity equivalence ratio than expected. Therefore, two total ports were placed in the diffuser core flow and oriented with their probe heads normal to the upstream air flow at the mid-channel height. A single static port was also placed through a hole and flush with the splitter plate wall. Using Bernouli's equation, a velocity was calculated. This calculation assumed incompressible, 1-D which is a reasonable assumption since the flow is a low speed (< 20 m/s or $M \cong 0.06$). This assumption does not apply in the outer core flow where the large recirculation region makes velocity profile measurements difficult. Therefore, no measurements were taken in the outer annulus; rather the calculated core flow was subtracted from the known total inlet mass flow (which was approximately 0.108 kg/min).

Cottle *et al.* [23] previously showed how a change in the combustion cavity geometry would affect the back pressure seen by the flow, and therefore the mass distribution between the cavity and core passages. This phenomenon was confirmed with the increased aspect ratio combustion cavity geometry; the same blockage plate used to achieve a 70/30 split in the

previous cavity geometry (UCC v2) resulted in an average cavity-core split of 76/24 for UCCv3. This phenomenon is explained by the decrease in total area of the air driver holes into the combustion cavity. This altered split resulted in the range of equivalence ratios being between 0.45 and 1.75 versus the expected range of 0.40 and 1.37. The pressure measurements were also taken at the same air and fuel settings for the RVC hybrid vane geometry, showing that the average flow split for this geometry was 77/23, and are included in the below table to ease reference. The same experiment type was completed for the compound driver configuration and was to be 74/26 and 76/24 for the LLCB and RVC geometries. The equivalence ratios for each air and fuel set point were then ascertained by multiplying the known inlet air flow by the average percent, and those values are displayed in Table 4.1.

Table 4.1: Stoichiometric Ratios of tested geometry with LLCB and RVC Center-body Geometry with a $\lambda = 5$, with Average Cavity Split Shown on Bottom

Air Set (kg/s)	Fuel Set (SLPM)	UCCv3 - LLCB	UCCv3 - RVC	Compound Driver - LLCB	Compound Driver - RVC
0.108	26	0.49	0.51	0.45	0.49
0.108	33	0.62	0.64	0.57	0.62
0.108	39	0.74	0.77	0.68	0.74
0.108	46	0.86	0.90	0.79	0.86
0.108	53	0.99	1.03	0.91	0.99
0.108	59	1.10	1.15	1.02	1.10
0.108	70	1.31	1.36	1.21	1.31
0.108	90	1.68	1.75	1.55	1.68
Average Cavity Split		**24%**	**23%**	**26%**	**24%**

As discussed with Table 3.1, this phenomenon was primarily the result in the change of the combined area of the air jet driver holes from 9.52 cm^2 to 9.15 cm^2. Even though the holes are larger than the original configuration, the reduced combined area restricts the mass flow into the combustion cavity. This blockage then propagates upstream, reducing the pressure drop across the splitter plate and reducing the mass flow diverted by the splitter plate. In order to

overcome this, the core flow has to be restricted even further; originally a $\lambda = 5$ (as defined by Cottle [6] and discussed in Section 2.4.2.2) was used but through CFD analysis performed with the Cottle Computational Model, it was postulated that a blockage plate with a $\lambda = 4$ with the gap positioned directly aft of the support vanes was required. However, due to time constraints the confirmation of this analysis will have to be accomplished in later work.

4.1.2. Temperature Profiles

The purpose of changing the combustion cavity geometry was to determine if the change was effective at improving the exit temperature profile. This data will be shown for both raw uncorrected thermocouple data as well as the Thin Filament Pyrometry (TFP) data which corrects for heat transfer effects. The former is shown in order to establish a qualitative comparison with data from previous UCC iterations, which also did not account for the heat transfer effects. The latter allows for quantitative values to be ascertained and used to guide future analytic models. To understand the formation of emissions, the temperature within the combustion cavity also was investigated with TFP.

4.1.2.1. Combustion Cavity Temperature Profile

Combustion cavity temperatures had previously been collected within the UCC by instrumenting one of the small access ports on the back ring panel with thermocouples. However, these values were only for a single point at a fixed circumferential and radial position. While this was fine for comparative studies of common hybrid geometries, changing any geometry or flow characteristics change the temperature distribution within the cavity, both axial and circumferentially. As Cottle [23] originally depicted (and is reprinted in Figure 4.1) the temperature profile within the combustion cavity varies by as much as 1000 K both circumferentially (left hand figure) and axially (as shown by the right figure which is further

downstream in the combustion cavity). The geometry shown is for UCCv2 but the same trends exist in UCCv3. The interaction of the air (exiting from the small blue circles) and fuel (exiting along the OD where indicated and every 60° from there) are too complex for a single thermocouple position (black circle) to capture. Therefore, an alternative method was required to experimentally categorize the combustion cavity temperature.

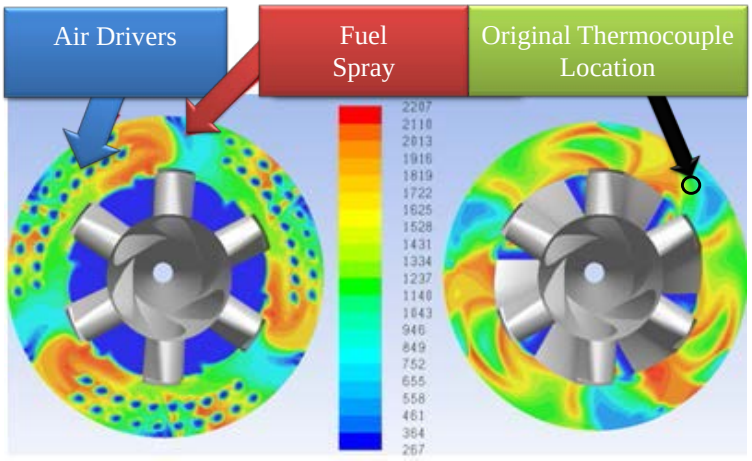

Figure 4.1: Axial cuts of Temperature Contours (K) within the UCC v2 LLCB geometry [23]

The new Thin Filament Pyrometry (TFP) method was ideally suited to capture temperature data within this region. The filaments were attached in accordance with Figure 3.22 with the intensity of wire being captured by the Bobcat cameras mentioned in Section 3.1.8. Once these images were collected, they were post-processed by Dr. Larry Goss using ImageJ to reduce the picture intensity and algorithms he had previously developed [32] and recently implemented on AFRL's SABER-RIG [33]. Dr. Goss lent AFIT these cameras, performed the image reduction, and error analysis himself, which then resulted in the reported time averaged data across the entire span of the filament. The span captured was the 18.17 mm aperture visible through the quartz window, and this typically resulted in the filament being represented with 160-170 pixels. Reflections against the air injector plate were sometimes seen, as seen in Figure

4.2, and were filtered from the data. Also in this figure, the red circle shows the gap in data caused by the flameproof epoxy at the bottom of the filament (wall is yellow) and how the filament does not glow if the temperature is too low to register (blue band). Each pixel of the picture (an example of which can be seen in Figure 4.2) had an intensity value associated with it that was converted into a temperature using Equation (12).

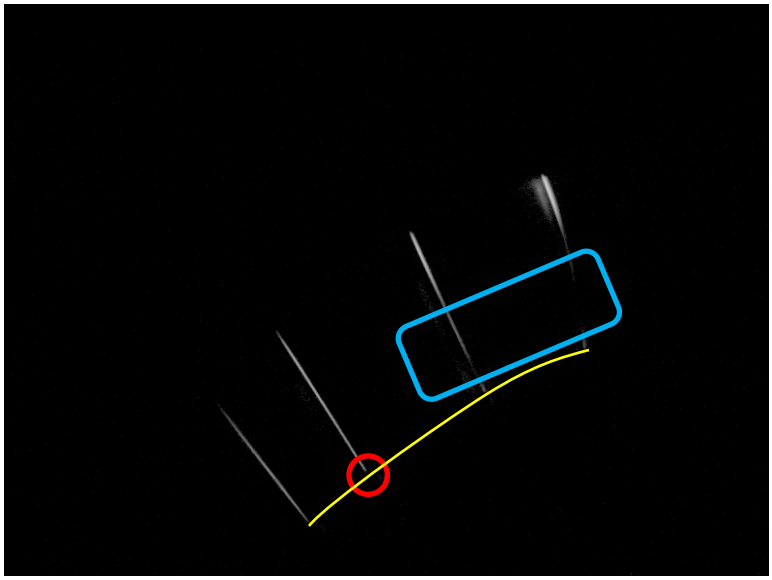

Figure 4.2: Example Image of Filament Irradiation within Combustion Cavity

Finally, the radiative heat effects were accounted for in order to get accurate temperature profiles across the entire combustion cavity. The top 5% and bottom 5% of the combustion cavity were not able to be captured with this technique however due to the need to use adhesive to secure the filament. The axial position filaments were taken by measuring from the front of the cleft of the hybrid vane that mates to the front wall of the combustion cavity to the filament anchor hole on the hybrid vane body.

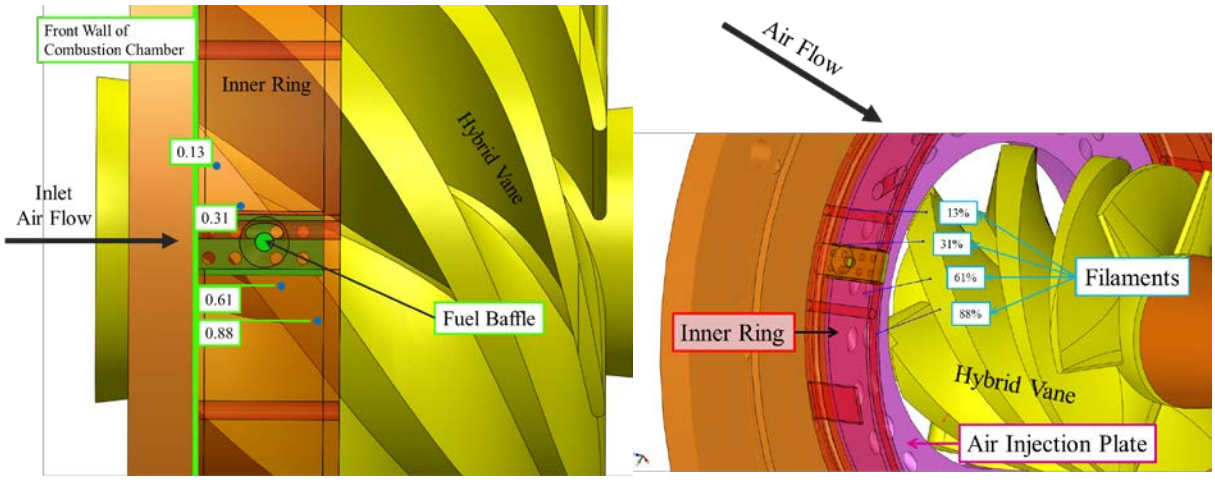

Figure 4.3: Axial and Isometric View of Filaments (Blue Lines), Placed at Their Attachment Points.

Note: All dimension lines drawn to base of filament, where it is attached to center-body

Figure 4.4 is the time-averaged temperature for each pixel point and each filament strand. Each filament in the figure links to the number specified in Figure 3.22. Figure 4.4 shows how with higher cavity equivalence ratio (Φ_{cavity}) the temperature in the front half of the combustion cavity are significantly reduced. The error (±38 K) that is present for all TFP data sets is shown with the black dotted lines showing the error bounds for the $\Phi_{cavity} = 0.99$ case. Also, the majority of the combustion in the front half of the cavity occurs in the upper 20%, which matches with past CFD analysis [55]. The starkest changes with respect to changing the Φ_{cavity} are at the 31% position (Figure 4.5). By the time the gases have migrated to the aft axial half of the LLCB to the lower 50% of the combustion channel height, with the maximum temperatures seen were around 1730 K seen in both the 31% and 61% axial displacement positions.

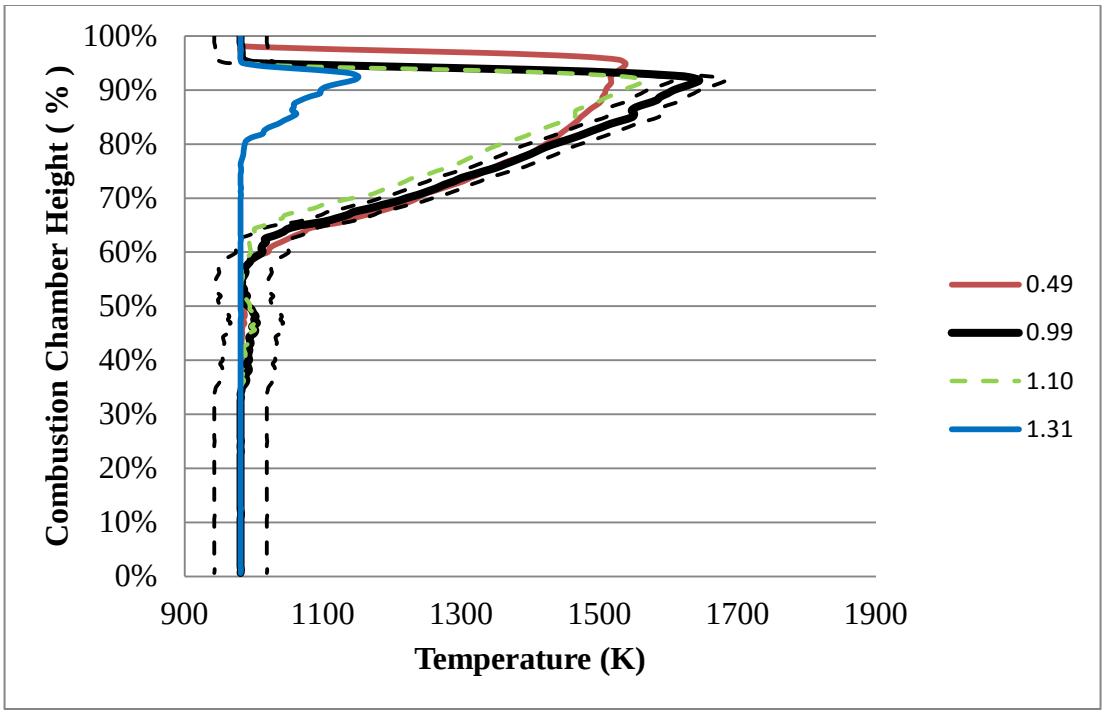

Figure 4.4: Filament Temperature Profile at 13% Axial Displacement with UCCv3 - LLCB Combustion Cavity. Values in Legend are Φ_{cavity} for This Geometry.

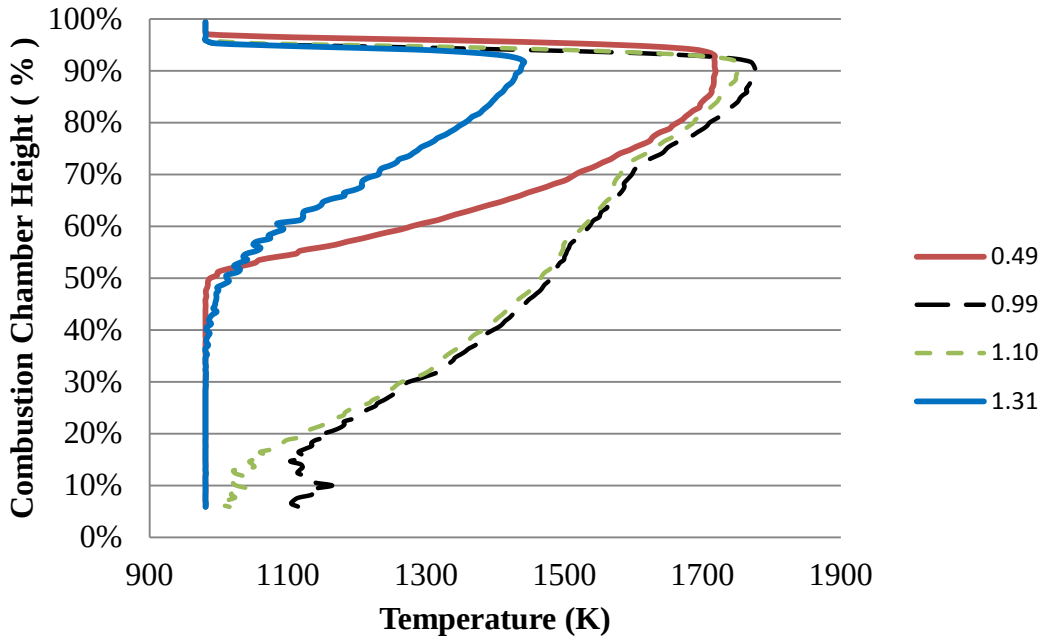

Figure 4.5: Filament Temperature Profile at 31% Axial Displacement with UCCv3 - LLCB Combustion Cavity. Values in Legend are Φ_{cavity} for This Geometry.

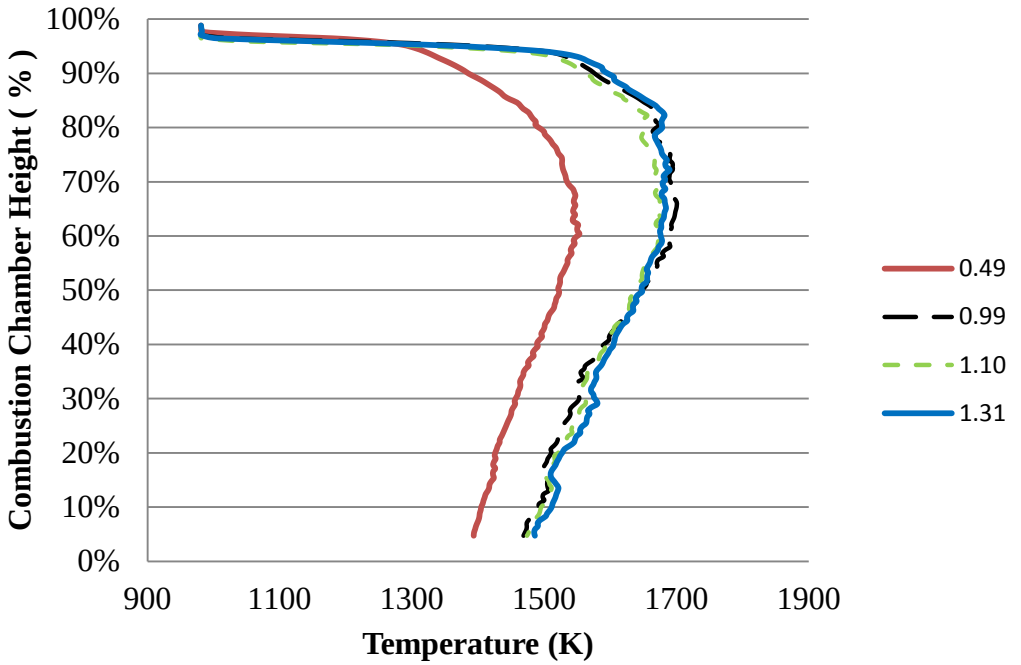

Figure 4.6: Filament Temperature Profile at 61% Axial Displacement with UCCv3 - LLCB Combustion Cavity. Values in Legend are Φ_{cavity} for This Geometry.

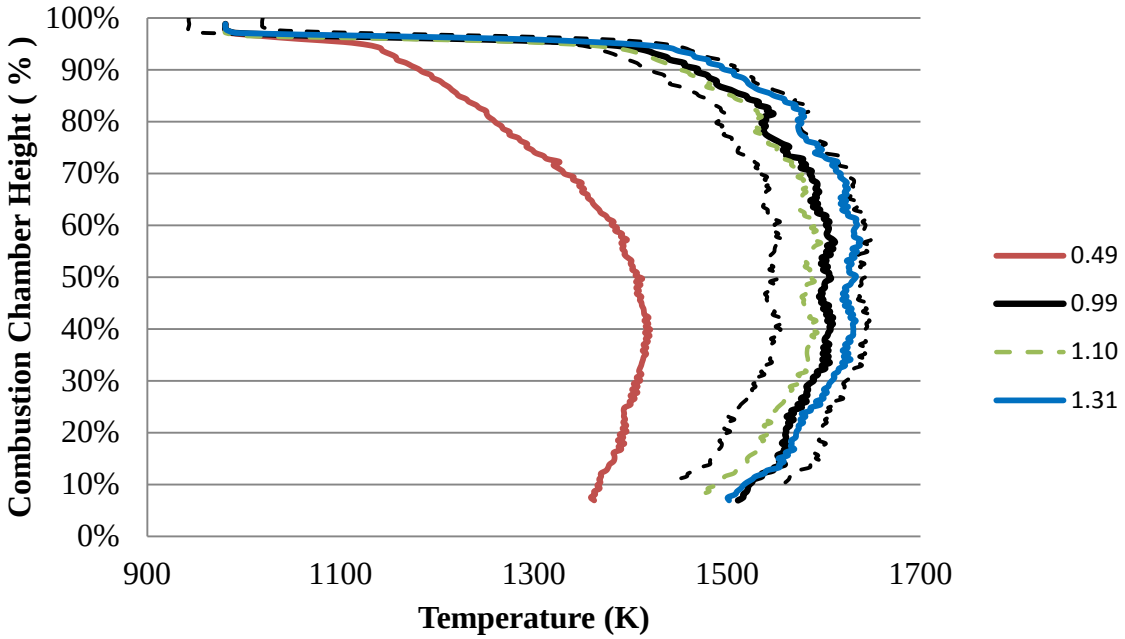

Figure 4.7: Filament Temperature Profile at 88% Axial Displacement with UCCv3 - LLCB Combustion Cavity. Values in Legend are Φ_{cavity} for This Geometry.

Finally, the temperature profiles of each of the four filaments were plotted against each other. Figure 4.8 shows more conclusively how the hot gases start in the upper 10% near the fuel rich portion of the cavity and migrates down. It is worth mentioning that front (13% axial displacement) filament was actually placed just upstream of a fuel baffle, meaning that this wire is further downstream than the other three filaments and its temperature profile represents the section that has the highest resident time. The other filaments were positioned just after one of the fuel baffles, but the combusting fuel that produced temperature migrated down and was measured by these filaments. The largest temperature for this configuration and air-fuel setting occurred at the flame front which was strongest at the 31% filament and stoichiometric condition.

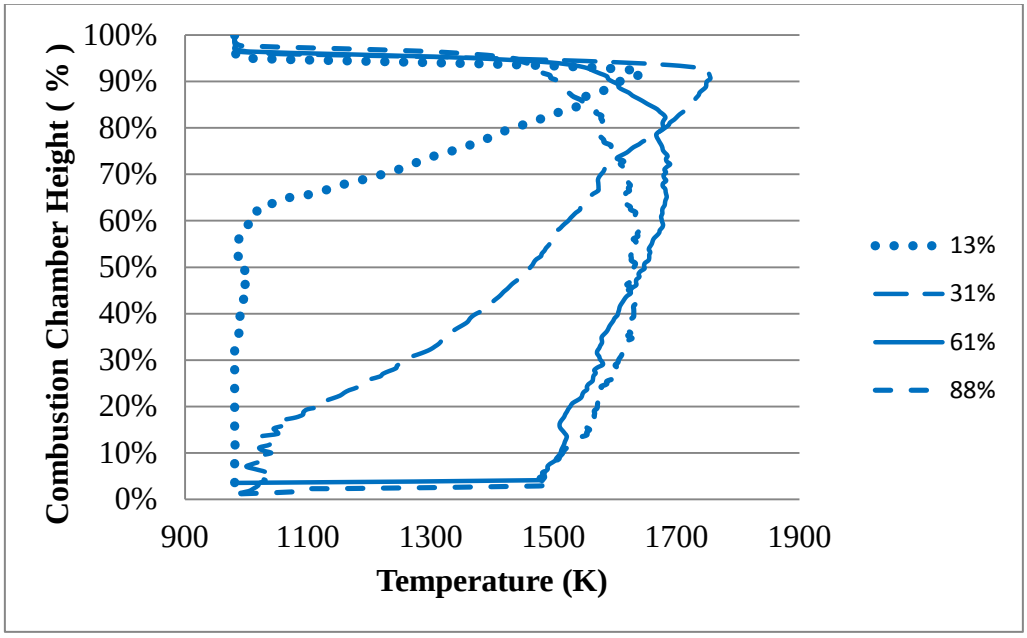

Figure 4.8: Four Filament Temperature Profiles at $\Phi_{cavity} = 0.99$ for UCCv3, LLCB Geometry

4.1.2.2. Exit Temperature Data

With the determination of the temperature field within the combustion cavity, the exit temperature profiles were investigated and compared with previous results of Damele [47].

Initial temperature measurements were taken with a rake of seven Omega, K-type thermocouples to ascertain the effect of altering the geometry on the overall combustion process. Data with and without the RVC was compared against Damele's [37] discrete source data taken within UCC v2. This data taken from flow splits of 70/30 and 75/25, depending on which stoichiometric ratio was closest to the set-point within the UCC version3 geometry. The reason the 75/25 split was not used exclusively, was because the available data ranged from a ratio of Φ_{cavity} between 0.99 and 1.99, but as Table 4.1 shows the range tested for this geometry was approximately between 0.5 and 1.7. Both of Damele's conditions however were near the same total mass flow rate (6.48 kg/min and 6.47 kg/min, respectively) as the one used within the current UCCv3 rig (6.48 kg/min).

Figure 4.9 shows this trend with the dashed green line; the peak temperature is seen in the outer 10% of the span with the largest gradient in between the outer two most points. For ease of convection, Damele's data will always be colored green and UCCv3 – LLCB data will be colored with a blue line. Of note is the Damele's data in the left figure (green line) was taken for a core/cavity split of 70/30, and resulted in temperatures approximately 100 K higher than the 75/25 displayed in the right figure (also green line) at the stoichiometric fuel condition (which theoretically should yield higher temperatures than a fuel lean case). This difference in temperature was attributed to the higher ratio of cooling core flow in the 75/25 (right-hand figure) case. The increased aspect ratio combustion cavity along with the transfer of the air injection holes from the outer ring to the front plate both were hoped to reduce pressure losses in the cavity and therefore encourage the peak temperatures to migrate more into the mid-span. Figure 4.9 juxtaposes the individual temperature profiles of the UCCv2 and UCCv3 data for two

different stoichiometric conditions. The total mass flow for the system was also held at approximately the same total air settings (6.47 kg/s discrete vs. 6.48 kg/s common core).

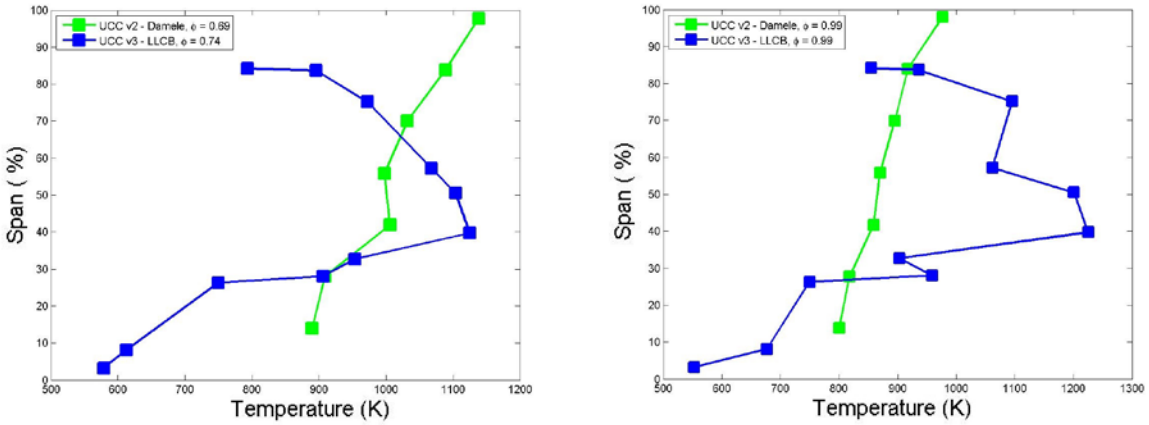

(a) (b)

Figure 4.9: Comparison of temperature values between discrete source UCC v2 and UCCv3 with the LLCB vane geometry at (a) $\Phi_{cavity} \cong 0.70$ and (b) $\Phi_{cavity} \cong 1.00$

Overall, the increased combustion cavity size resulted in greatly increased temperature magnitudes when compared to the same cavity-to-core ratio. Figure 4.9b shows how the peak increased nearly 300 K. Most importantly, the temperature peaks were migrated from the span region between 90%-100% to 35%-55%. This indicates that the larger cavity allows for better mixing and more complete combustion of the flow before exiting the cavity. Furthermore, the resultant profile has a shape more consistent with traditional combustors with a peak temperature between 40%-60% span. As desired, the flow closest to the inner core has the coolest temperature while the flow on the outer wall is on average 37% cooler than the peak temperature value. This verifies that increasing the aspect ratio of the combustion chamber does impact both the heat release and the exit temperature of a UCC. While only these two cases are presented in Figure 4.9, all the exit temperature profiles cases can be seen in Figure 4.10. The peak temperature for this configuration was routinely measured between the 40% – 60% span

thermocouple and occurred between a Φ_{cavity} of 0.99 and 1.10. This conforms with expectations since peak temperatures are typically seen around a $\Phi \cong 1.05$

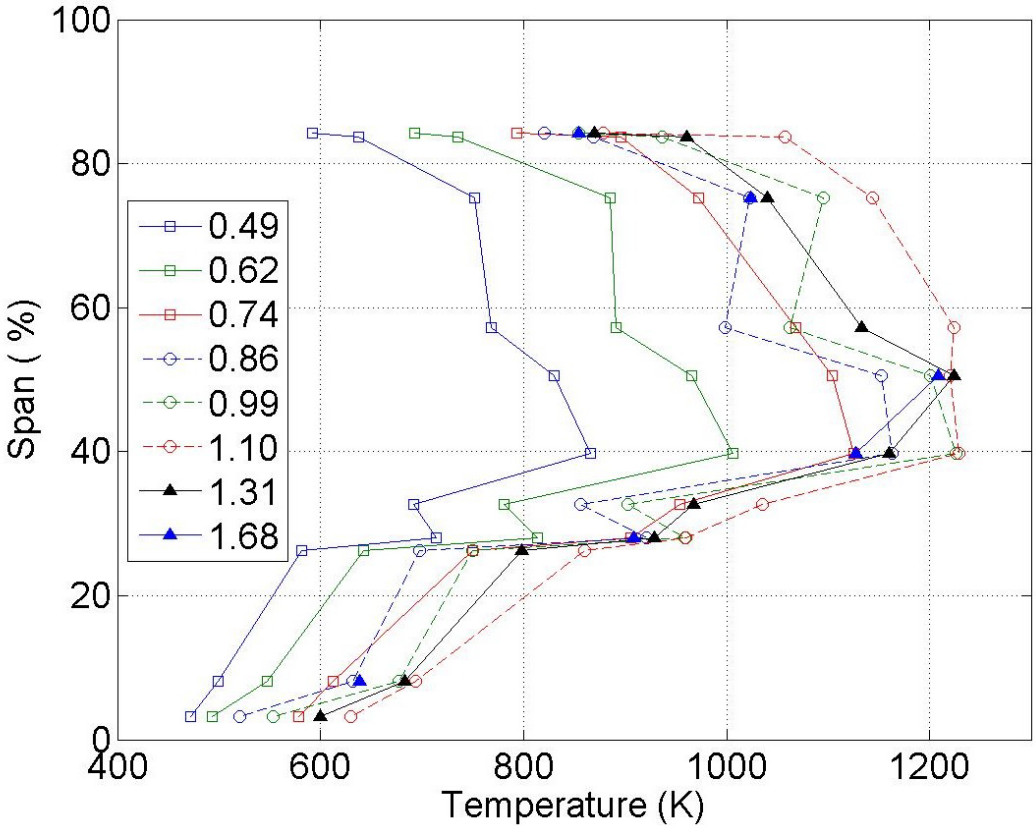

Figure 4.10: Span-Wise Exit Temperature Distribution for All Measured Thermocouple Values for the UCCv3 – LLCB Geometry. Values in Legend are Φ_{cavity} for This Geometry.

.

4.1.2.3. Filament Exit Plane Data

The same process as detailed above was then applied to the exit plane of the UCC in order to accurately determine the temperature profile of the baseline UCCv3 – LLCB vane configuration. Again, adhesive was used to secure the filaments on the suction side of the opposing airfoil and strung through a series of 0.51 mm holes drilled through the "top" airfoil. This adhesive caused more blockage of the filament then within the combustion cavity. The need for more adhesive was the increased velocity between the two environments, which was

analytically determined to be approximately 20 m/s to 200 m/s respectively [50]. Also, some of the filaments would routinely blow out of their holes and their data would be lost on all subsequent points.

Figure 3.10 shows an example of the image taken at the exit plane as well as the blockage caused by the adhesive. The adhesive does emit light energy, but is doing so at a different wavelength than the filament. The filtered image on the right shows how only the filaments are visible and none of the adhesive on "top" suction side (far right) of the airfoil is visible. The inner two most filaments in this picture are very dim; in fact the innermost filament (yellow circle) is barely visible in the picture. This low intensity means the data could not be collected, and that the filament temperature at this point was below 900 K, the minimum temperature that can register for this method. Consequently, most of the filament data charts do not include values for the span inside 40% as there was none collected, and thermocouples will have to be used in this area.

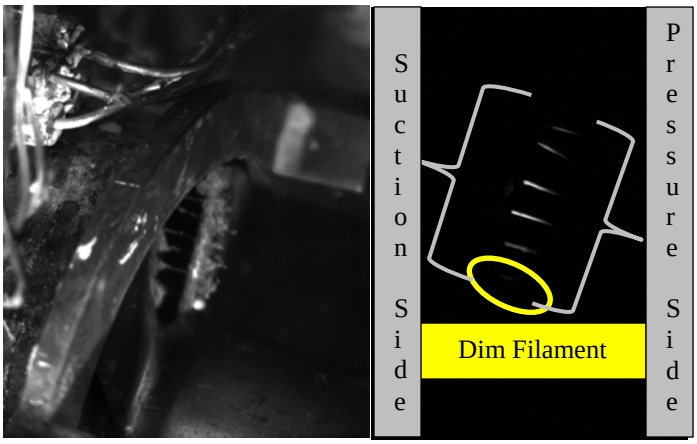

Figure 4.11: Example Image Capturing Light Intensity for Four Filaments at Exit Plane, both unfiltered (left) and filtered with the 990 nm lens (right)

The filaments provide data over the entire pitch, (referred henceforth as the channel "height") minus the obstructions of the adhesive. The filaments were reduced to 20 – 50 pixels and this varied because the height varies from 3.0 mm at the inner diameter to 8.0 mm at the

outer diameter. Three typical temperature profiles for the can be seen in Figure 4.12: the inner span, mid-span and outer span locations. Note that 100% corresponds to the suction side of the channel (right airfoil in Figure 3.22). All these temperature profiles are relatively uniform for the first 50%, but the mid-span filaments have higher values on the pressure side. This preference had been noted previously in the work by Lebay *et al.* [36] as the result of the flamelet's vertical momentum penetrating into the core flow mix. In order to account for this bias, the height-averaged mean of the filament was taken and used in all graphs presented after this. This idealization is similar to the method proposed by Lefebvre and Ballal [14] about how to represent values over the span of an axial combustor. The average values of the two parabolic shapes are also plotted to show how their magnitudes.

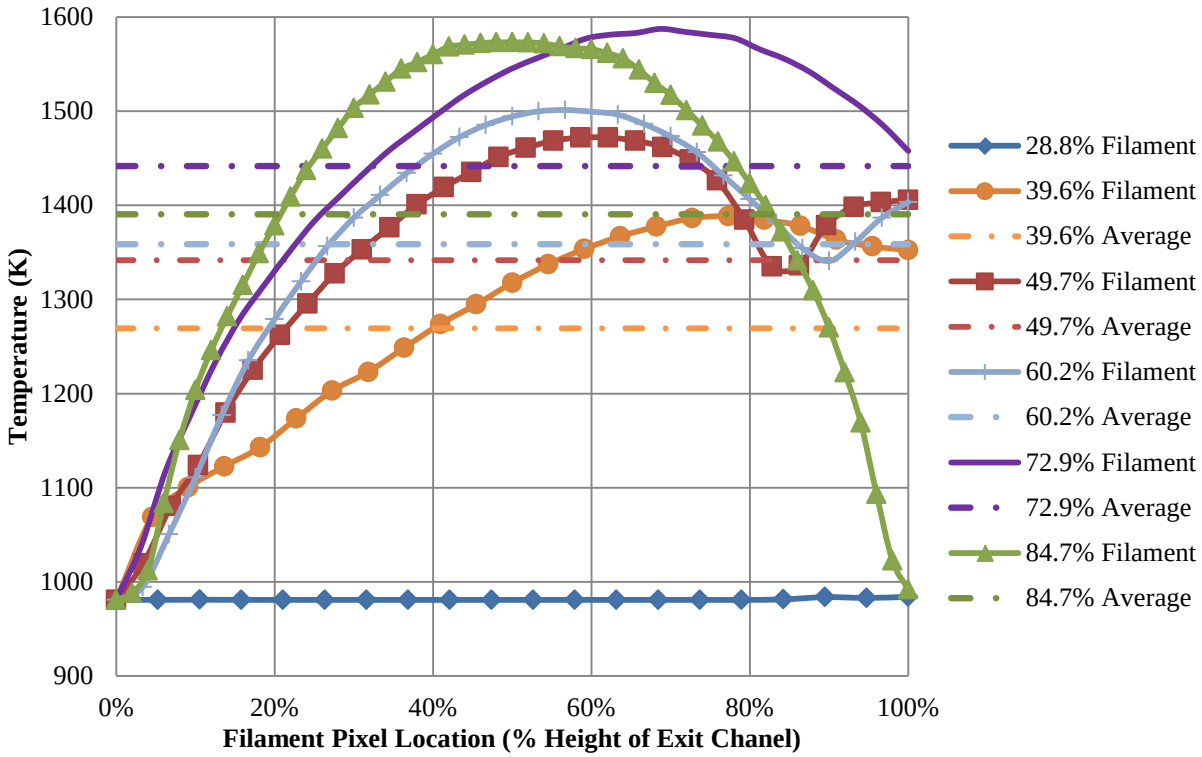

Figure 4.12: Temperature Distribution across the Entire Height of the Exit Plane, Taken for $\Phi_{cavity} = 0.99$ within UCCv3 – LLCB Vane

Figure 4.13 shows the results of the TFP analysis upon the exit plane. Overall the values were typically higher than those measured by the thermocouples; the inner filament was off the most by as much as 386 K while the peak values were still off by as much as 250 K. The maximum average temperature measured for this configuration was 1600K which occurred at a **Φ** of 1.31 at the 72.9% filament. The most significant finding of the TFP Data was that the temperature profiles measured by the thermocouples were skewed to the incorrect points. The thermocouple data read the highest temperatures occurring in the 40-60% range, while the TFP data shows it occurring between the 60%-80% span. TFP is considered the more accurate method due to the filaments' location at just before the trailing edge of the vane airfoil and because it corrects for the gas temperature effects. Since the thermocouples are skewed to the pressure side just aft of the exit plane by their natural resting placement, it appears that the circumferential swirl from the vane is enough to displace the flow roughly 20%. While this seems overly large, it actually equates to a displacement of 6 mm radially for approximately 1 mm of displacement downstream, which is not much since the circumferential skew at the exit plane is predicted by a computational model developed by Cottle [50] to be 100-250 m/s. Using this data, the maximum error of 38 K for TFP measurements is shown as error bars on the below figure. These bars are omitted from other figures, but the difference is the same for all points.

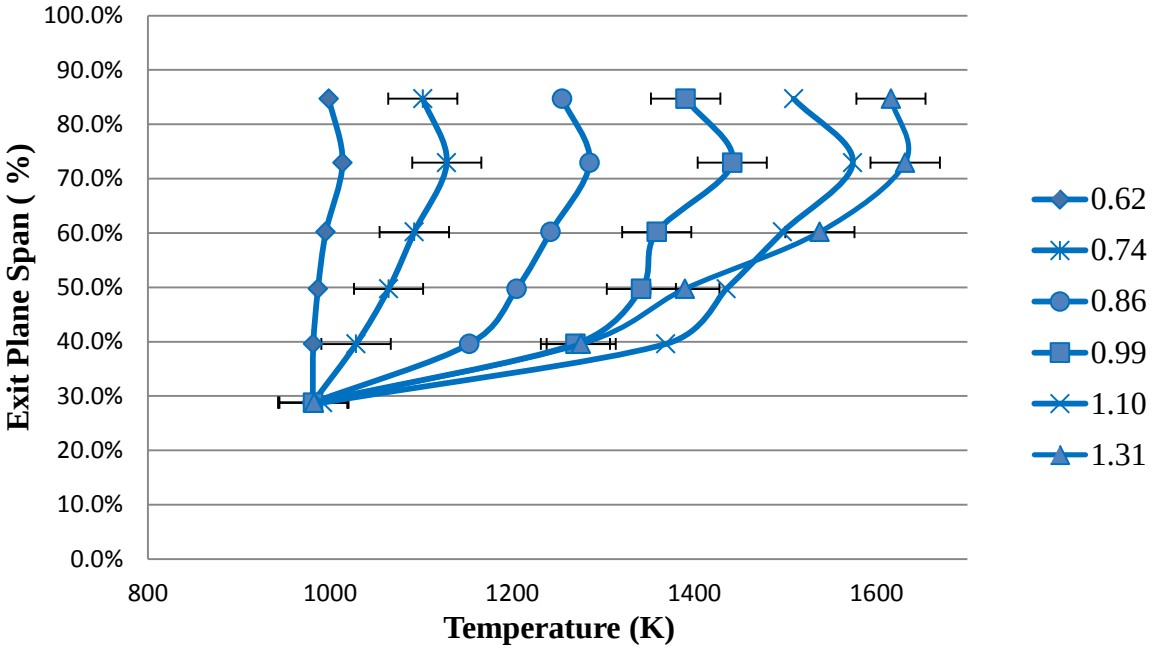

Figure 4.13: Span-Wise Temperature Distribution for Select Equivalence Ratios for UCCv3 – LLCB Geometry with Error Bars

4.1.2.4. Profile Factor Comparison

The local profile factor was next used to normalize the difference between the local time-averaged temperature ($T_{4_{Local}}$) and the average temperature across the span ($\overline{T_4}$) for a single Φ_{cavity} condition. Due to the higher accuracy of the TFP data, it was the only data normalized to the local profile factor. Equation (16) adapted from Lefebvre and Ballal [14] describes the divergence of the local value from the span-wise temperature average and helps locate where the peak temperatures are seen. It is desirable to avoid large peaks in the outer span and inner span in order to improve the fatigue life of turbine blades. The local profile factor ($\theta_{profile}$) for UCCv3 – LLCB geometry is shown in Figure 4.14, which shows how the temperature along the outer span is most divergent from the mean at the 72.9% filament location. This divergence results in a maximum profile divergence (i.e. maximum value for the profile and the highest temperature spike) of 0.154. However, the LLCB design does show a decrease in profile factor

along the inner diameter, which is preferable as it will not increase the effect of the centripetal load on the blade root. The minimum divergence (i.e. coolest temperature point) results a profile factor value of -0.295.

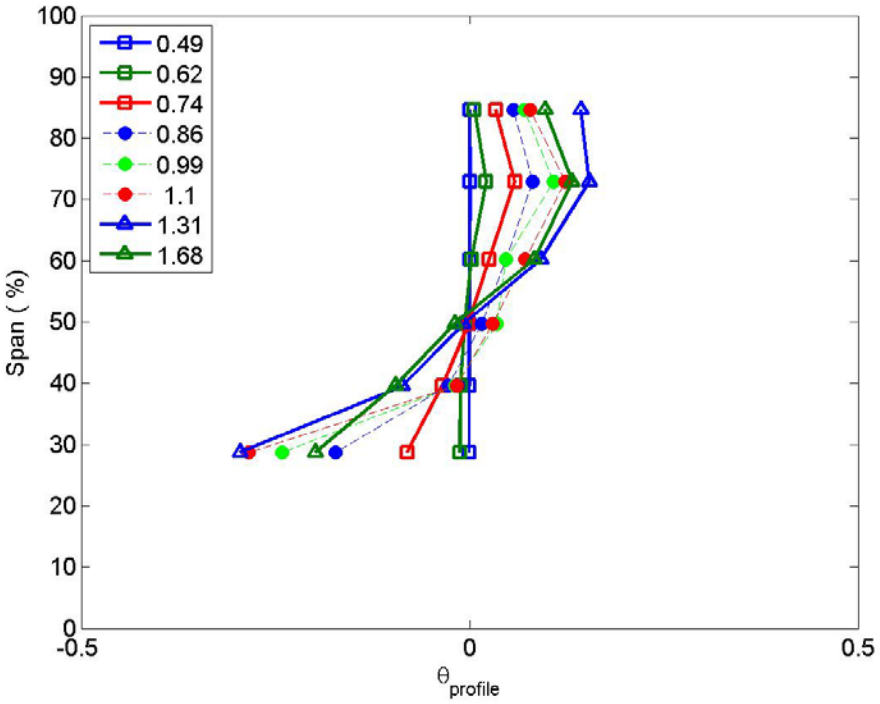

Figure 4.14: Local Profile Factor for All Equivalence Ratios for UCCv3 – LLCB. Values in Legend are Φ_{cavity} for This Geometry.

4.1.3. Emissions Baseline for UCCv3

Accurate emissions measurements were first made with the increased combustion cavity aspect ratio combustion cavity (UCCv3) with the Low Loss Center-Body (LLCB). These measurements were the first to use the emission analyzer for results with the AFIT UCC rig. Figure 4.15 shows some of the general trends between the two types of pollutant emissions that traditionally are regulated. The individual points in these diagrams show the NO_x output compared to the CO output at a specific point for a certain run condition (i.e. air flow setting and cavity equivalence ratio). These types of figures assist combustor designers by visually displaying emissions operating regions and trade spaces for a specific design.

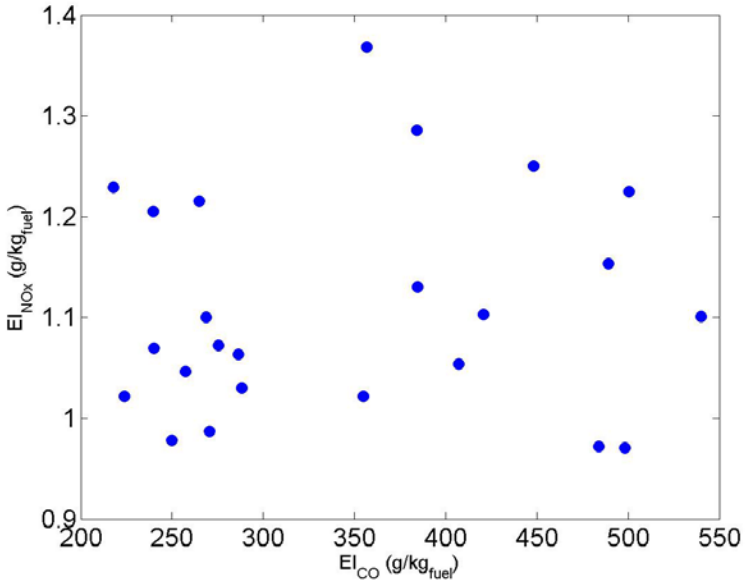

Figure 4.15: Emissions Baseline of CO and NO_x for UCCv3 Air Driver Configuration. Data Points Shown are for All Fuel Settings at All Positions.

4.1.3.1. Total Unburned Hydrocarbons (THC) Production

Also plotted were the point values of the emissions indices for THC, NOx, and CO. Figure 4.16 shows the Emissions Index of Total Unburned Hydrocarbons at the exit plane of one vane of the UCC. The highest concentration of propane for the LLCB geometry was found to occur at the outer most position, followed by the inner position, 41% span position, and the lowest being the mid-point. Of note in these results is the omission of certain data points; these values were excluded to the concentrations exceeding the maximum sample range of the CAI analyzer for either CO (most typical) or THC. The points of lowest unburned fuel tend to occur at the locations associated with the peak temperature values. This suggests that higher efficiencies exist in the mid-span region and decrease substantially at spans closer to the inner and outer wall. The minima for emissions for this geometry occurred between a Φ_{cavity} between 0.74 – 0.86, likely right around 0.80. The error bars for select points are also included to show the potential range of values in Figure 4.16.

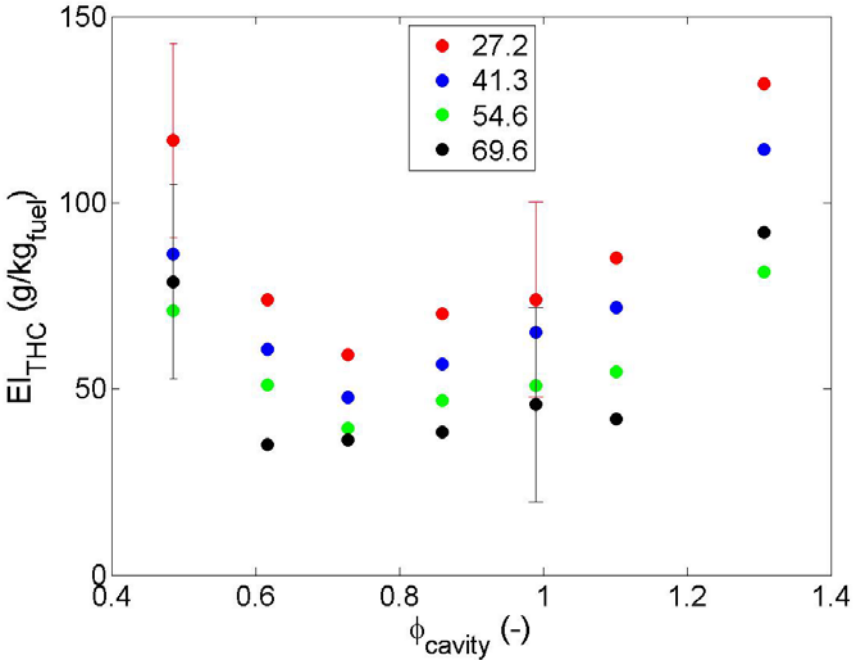

Figure 4.16: Emissions Index Baseline of THC for the UCCv3 – LLCB Geometry at Various Φ_{cavity} (x-axis) and % Span Locations (in legend) with Select Error Bars Shown

4.1.3.2. NOx Production

Turns [2] stipulates that the maximum production point for NO_x occurs where the maximum equilibrium point for O^- atoms which is near a $\Phi = 0.9$; right by the range of peak combustion temperatures and the largest radical production. Figure 4.17 conforms to this expected trend as the peak production of NO_x occurs between a Φ of 0.86 and 0.99. The highest amount of NO_x is also seen at the 54.6% span location, suggesting that the most oxygen radicals migrate to this location. This location also corresponds with the peak temperatures seen by the thermocouples. The EI values however are very close to each other due to the point with the highest reading in ppm of NO_x also corresponding to the point of max CO_2 production. For the LLCB this point of max reading occurred in the 69.6% span location, but the amount of CO_2 produced was nearly four times as high as at the mid-span points. The large concentration of CO_2 was due to the most combustion occurring within this point, and with increased combustion

comes increased production rate of products (specifically the measured CO_2 and not measured H_2O). EI is a molar ratio of the emissions product to fuel, and the carbon for the fuel was tracked in the summation of CO, CO_2 and THC. Therefore, EI helps normalize the emissions produced to the amount of combustion that actually occurs by seeing if a large amount of CO_2 is produced. A large CO_2 concentration increases the denominator of EI and reduces the resultant indices. Since there was little noted heat release in the filament data in this region, little combustion likely occurred here, which is why there are low amounts of CO_2 measured at these locations.

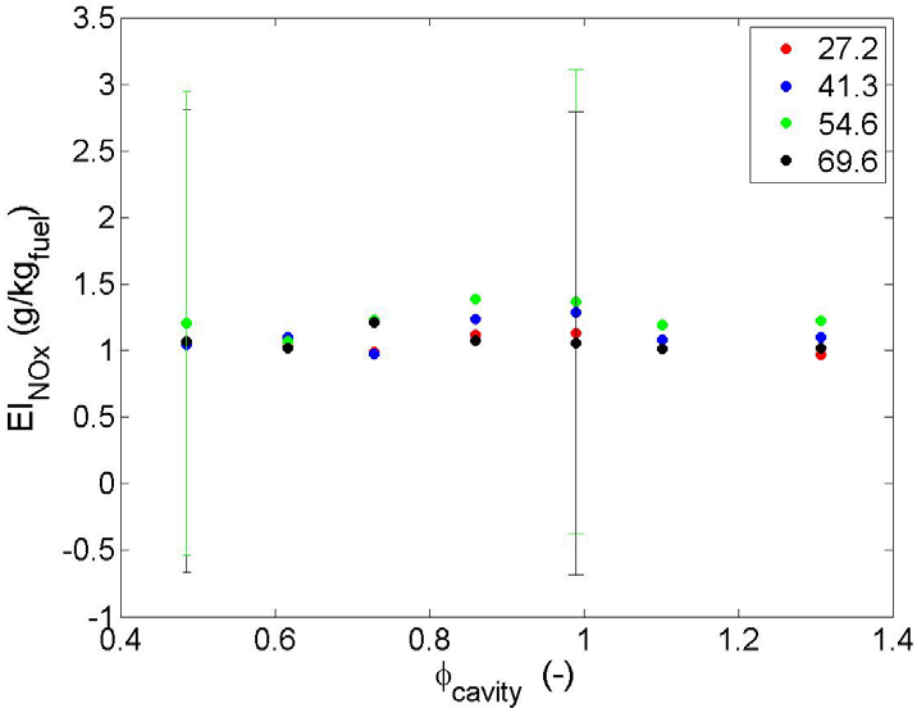

Figure 4.17: Emissions Index Baseline of NO_x for the UCCv3 – LLCB Geometry at Various Φ_{cavity} (x-axis) and % Span Locations (in legend) with Select Error Bars

4.1.3.3. CO Production

CO production, in contrast to NO_x production, occurs as a result of the products encountering conditions that arrest combustion. These conditions arise from quenching from either a lack of oxygen being available to complete the formation of CO_2 or cooler temperatures

removing the required activation energy [2]. This means that CO forms to the detriment of CO_2 and will occur in regions that are not heavily populated with Nitrous Oxides. This was shown to be the case for the different span location within the UCC in Figure 4.18. The highest EI for CO was noted at the 27.2% span for conditions of $\Phi < 0.8$ and 41.3% span for most $\Phi > 0.8$, with the minima occurring in between the two points around 0.8. The lowest value occurred consistently across all conditions at a span location of 54.6% which is exactly opposite of the trend seen for NO_x. It would therefore appear that EI for CO and NO_x are inversely related as the dedication of an oxygen radical to one restricts the formation of another: in other ones, when one of the pollutants is high, the other one will be low.

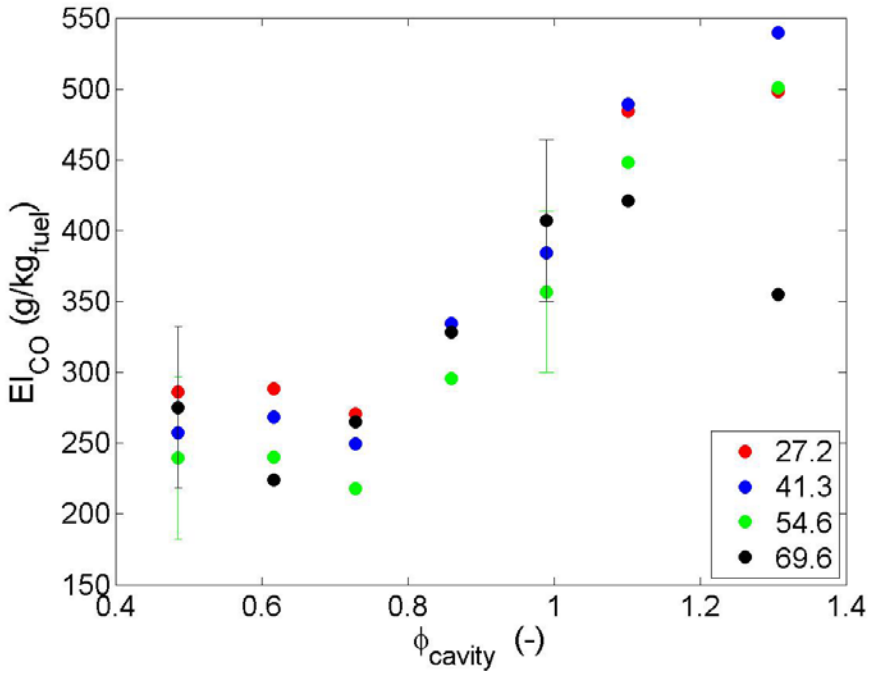

Figure 4.18: Emissions Index Baseline of CO for the UCCv3 – LLCB Geometry at Various Φ_{cavity} (x-axis) and % Span Locations (in legend) with Select Error Bars

4.1.3.4. Efficiency

Finally, the chemical efficiency of the reaction was calculated from the Emission Indices of Total Unburned Hydrocarbons, Carbon Monoxide, and Nitrous Oxide using Equation (21).

According to ARP 1533 [42], the optimal efficiency will occur at the point of maximum temperature as it will correspond to the point of maximum heat release. Therefore, if taking a single point measurement, the efficiency should be calculated by placing the probe in this one position. However, this experiment used a multiple channel probe in order to determine the span-wise trend of emissions and therefore span-wise values for efficiency can also be determined. Span-wise efficiency and emissions measurements are used both at AFIT and AFRL for this geometry [54] and are taken due to the high exit swirl of this combustion engine. Also for this experiment, multiple emissions points were desired because the peak temperature was not known *a priori* and could not be assumed to be located exactly at the 50% span location. By considering multiple span locations with the four-channel probe that was designed for this thesis, the span temperature and emissions measurements could be accomplished during the same test runs and correlations between temperature profile and emissions could be drawn.

Figure 4.19 shows these values across the span are on average within ± 6% Efficiency for this geometry. The peak efficiency alternates between the outer two span locations. The peak temperature occurs around the 72.9% span location according to the TFP data, and this is supported by the emissions data which has the peak value or near peak value occurring at the 69.6% span location. The efficiency also appears to remain relatively constant between the outer 15% ports as they never vary by more than 2% efficiency. As expected, efficiency peaks at a specific condition and tapers as the mixture is made too lean or too rich. However, peak efficiency normally occurs near stoichiometric conditions and typically in a range between a $\Phi_{\text{cavity}} = 0.8 - 1.0$, but for this geometry the peak occurred between a ratio of 0.62 and 0.74. This would suggest that the combustion chamber is not optimized like a traditional combustor with respect to emissions and further geometric alterations are necessary.

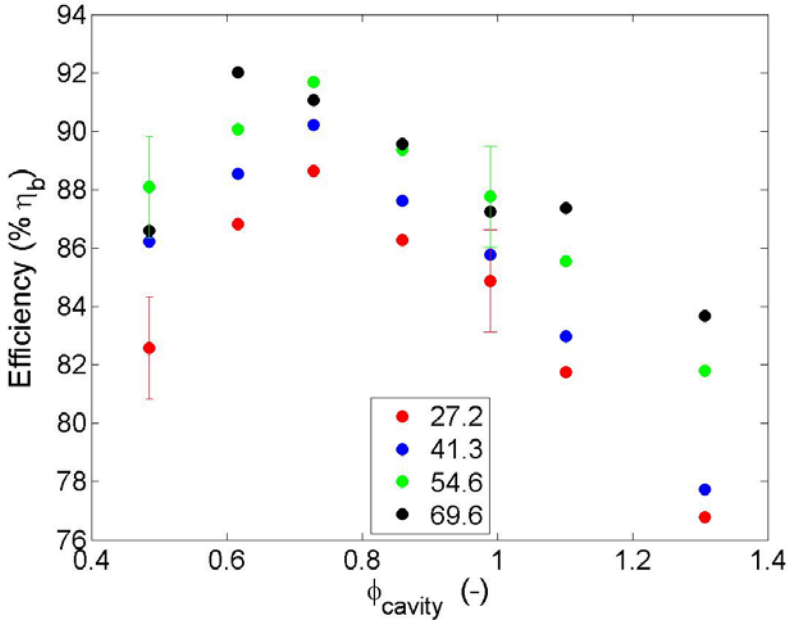

Figure 4.19: Efficiency Baseline of THC for the UCCv3 – LLCB Geometry at Various Φ_{cavity} (x-axis) and % Span Locations (in legend) with Select Error Bars Shown

4.2. Analysis of UCCv3 – RVC Center-body

The second geometric configuration considered was the placement of a radial vane cavity (RVC) into the basic LLCB vane geometry. As shown in Figure 3.11, the RVC was a channel placed into the center piece of the LLCB vane stack. The intent was to direct some of the hot gases out of the circumferential cavity and drive them into the mid-span region. Ideally this would increase the peak temperature at mid-span, thereby conforming to modern combustor exit profiles.

4.2.1. Temperature Profiles

The first investigation into the impact of the addition of the Radial Vane Cavity to the LLCB was to understand the impact on the temperatures within the cavity and at the exit plane. Both thermocouples and TFP was utilized to characterize the impact. Comparisons were made to the baseline condition, smooth body, LLCB to understand if the RVC offered benefits to this design. It was found that the RVC further concentrated the peak in the mid-span region but

overall had lower peak and average temperatures. The temperature profiles for this geometry will be colored with black lines throughout this thesis.

4.2.1.1. Combustion Cavity Temperature Profile

Within the combustion cavity, increased peak and average temperatures occurred for all conditions and filament positions. As Figure 4.20 and Figure 4.21 show, the dashed lines of the LLCB were consistently lower than the solid lines of the RVC for both fuel lean and fuel rich cases. The shape of the temperature curves also does not appreciably change between the two geometries, outside the change in magnitudes. This means that the RVC was better suited to concentrating the highest temperature gases into a compact region than the smooth body LLCB. However, as will be discussed noted in the exit plane data (Section 4.2.1.2 and 4.2.1.3), the temperature values observed at the exit plane were lower than the LLCB value for fuel lean conditions for all the points in outer span (>55%). Furthermore, the emissions data suggest that less overall combustion occurred.

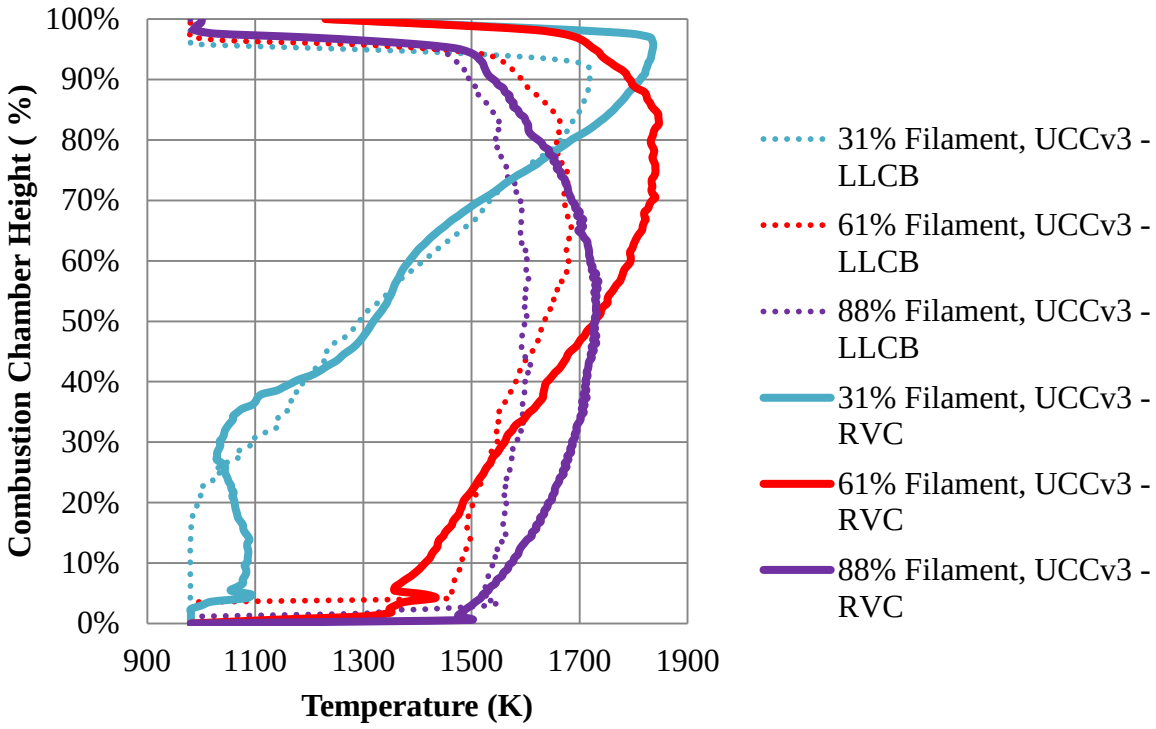

Figure 4.20: Comparison of Filament Temperature Profiles at $\Phi_{cavity} \cong 0.75$ for UCCv3 - RVC and LLCB Geometry

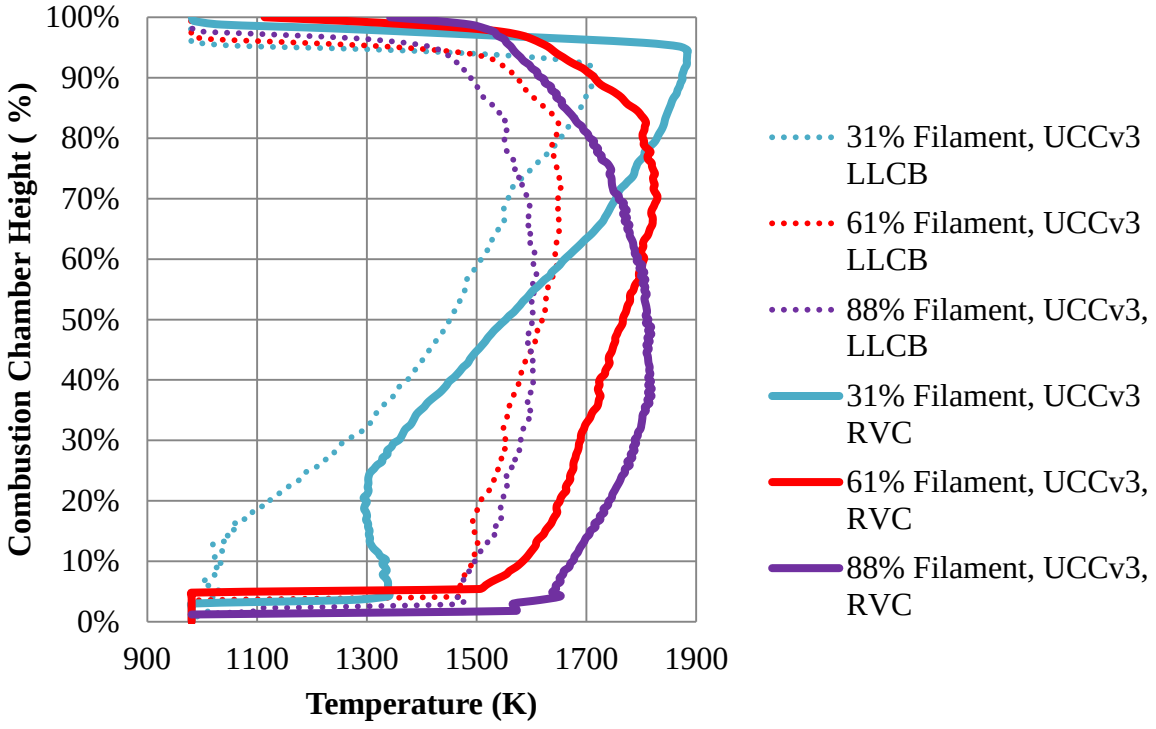

Figure 4.21: Comparison of Filament Temperature Profiles at $\Phi_{cavity} \cong 1.10$ for UCCv3 - RVC and LLCB Geometry

The computational fluid dynamics model developed by Cottle *et al.* [23][30] provides further insight into the physics of the cavity. This model had the RVC geometry inserted into as specified by Cottle *et al.* [55] in order to gain appreciation of the velocity flow fields and interactions within the cavity. Figure 4.22 shows how the RVC geometry entrains the combustion cavity flow within the core flow. The bottom two figures have a red circle drawn around the radial vane cavity while the top two have the LLCB and the colors seen in the vane are merely the heads of the velocities impacting the wall (the tails denote particle location). The increased density of velocity vectors in the cavity show the formation of a vortex that increases the mixing in the passage and swirls in upon itself. This vortex is shown at positions further axially upstream (Figure c) to propagate into the cavity and funnels the products out. These funnels have been shown to evacuate the fuel out of the combustion cavity more effectively, thereby reducing residence time. However, they also act as pressure seals that disturb flow "up" into the combustion cavity [50], which concentrates combustion and temperature more in the cavity. This helps explain the increase in cavity temperatures seen in the TFP data in Figure 4.20 and Figure 4.21.

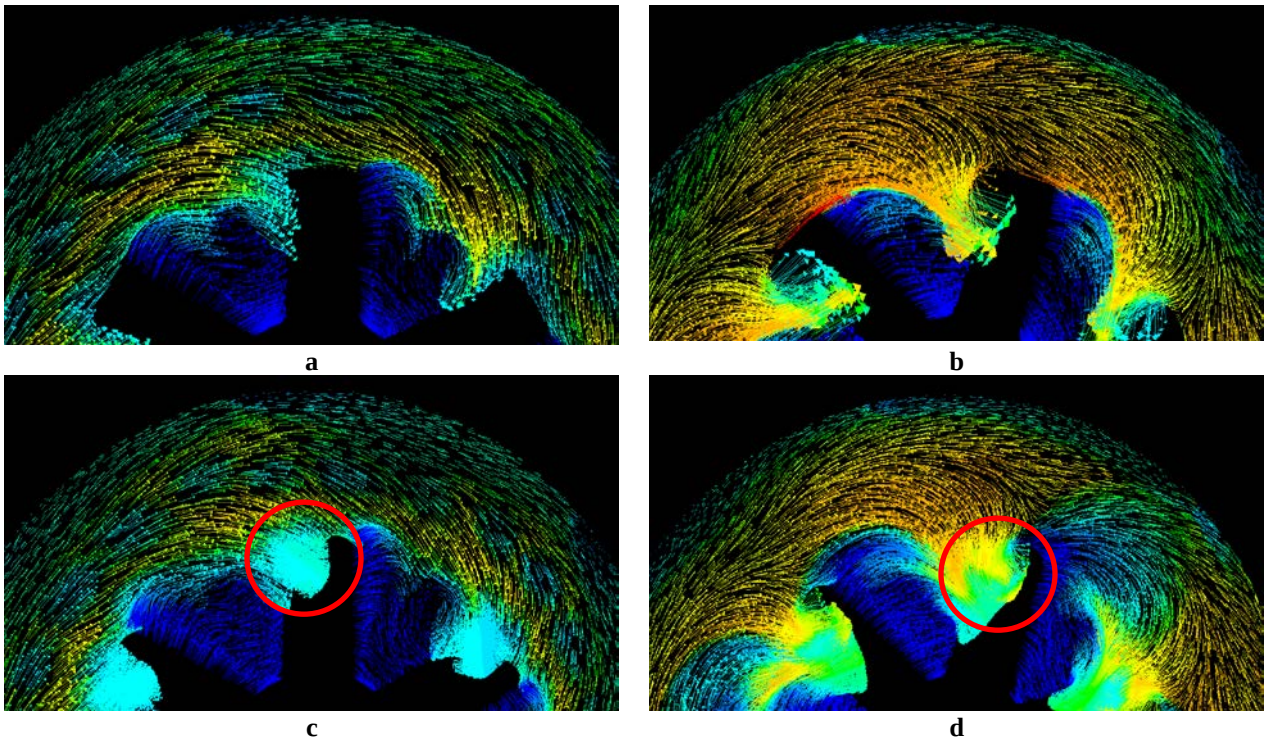

Figure 4.22: Velocity Vectors Colored by Temperature within Combustion Cavity at Axial Location $\bar{z}$=0.60 (left); 0.61 (right);. Combustion Chamber Geometry is altered between UCCv3 – LLCB (top) and UCCv3 – RVC (bottom) [55]

This is similar in behavior to the forward facing step used by Mawid et al. [38] in their analysis. This vortex increases the stirring of the hot combustion gases entrained and increases the distance traveled by some of the hot gases while maintaining the same axial displacement. Increased distance means increased time to cool, which then suggests that the exit temperature will be cooler. The vortex also sucks the products lower into the stream, meaning that the "cold" core flow dominated the temperature profile more in this region. These theories were confirmed by measuring the exit temperature profiles and seeing that the regions where in fact cooler. The lower peaks than seen with the LLCB can also be explained by the amount of un-combusted fuel lost out of the RVC. This fuel was quenched before it could react, thereby eliminating any of the heat release potential of this fuel. This theory was confirmed in the emissions analysis (Section

4.2.2) which saw the concentration of propane in the exhaust increase approximately 20% in the outer span.

4.2.1.2. Exit Temperature Profiles

Thermocouples were initially utilized to characterize the exit profile factor. Figure 4.23 illustrates how the radial vane cavity (RVC) increases the temperature gradient toward the peak temperature point, which occurs at the 44% probe position. The fuel-lean condition shows how the peak temperature location remains relative constant across multiple settings as can be seen in Figure 4.23 . Temperatures continue to rise until a Φ_{cavity} of 0.90 is reached at which point they stagnate around 1200 K – 1300 K. Later comparisons also showed that the UCCv3 – RVC data possessed a much more pronounced peak than baseline UCCv3 – LLCB data (see Figure 4.24).

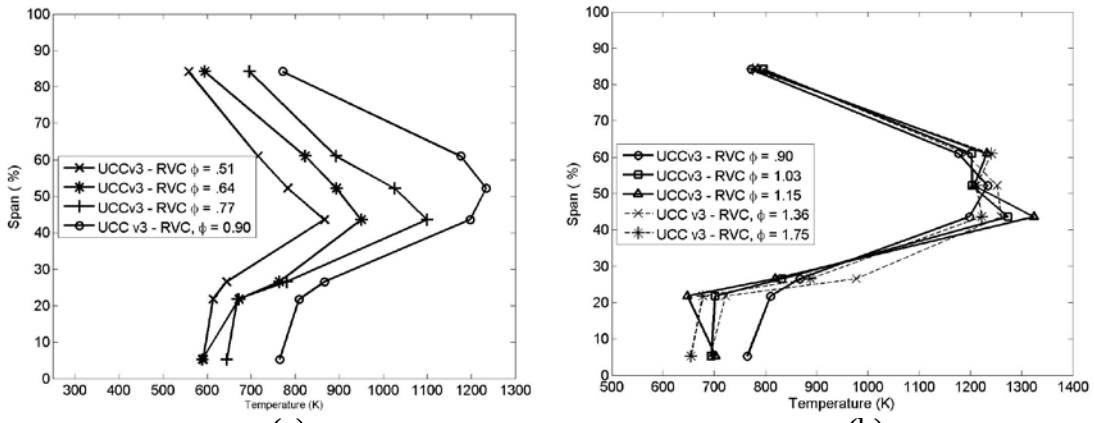

(a) (b)

Figure 4.23: Comparison of Temperature Values for UCCv3 – RVC Geometry at (a) Fuel-Lean Conditions and (b) Fuel-Rich Conditions

The temperature magnitude increased as well with fuel equivalence ratio until it reaches its maxima between 1.03 and 1.15. This trend follows the LLCB data as well as expected results. A unique characteristic of the RVC temperature profile is the sudden increase in span temperature between the 61% and 80% span locations as seen at $\Phi \cong 1.00$ case in the Figure 4.23b. This phenomenon presents itself around a $\Phi_{Cavity} \approx 0.90$ and continues through all the

test points taken for this experiment. This increase would suggest that the RVC successfully migrated more of the hot gas effect the outer 20% of the span and more effectively concentrated it within the middle span. Figure 4.23b also most clearly illuminates where the RVC cavity outlets its hot gases. However, as Figure 4.24 shows, the RVC peak temperatures (all black lines) tend be at the same span-wise location as the LLCB for the depicted fuel rich case (blue solid circles). The thermocouple profiles for the UCCv3 – LLCB did not agree well with the filament data, and so more certain determination about the peak can be made with those. Also, the RVC had reduced temperature values in the outer span, while being roughly equivalent in value at the inner diameter. This was due to the reduced chemical efficiency for the UCCv3 – RVC geometry that are discussed more in depth in Sections 4.2.2.1.

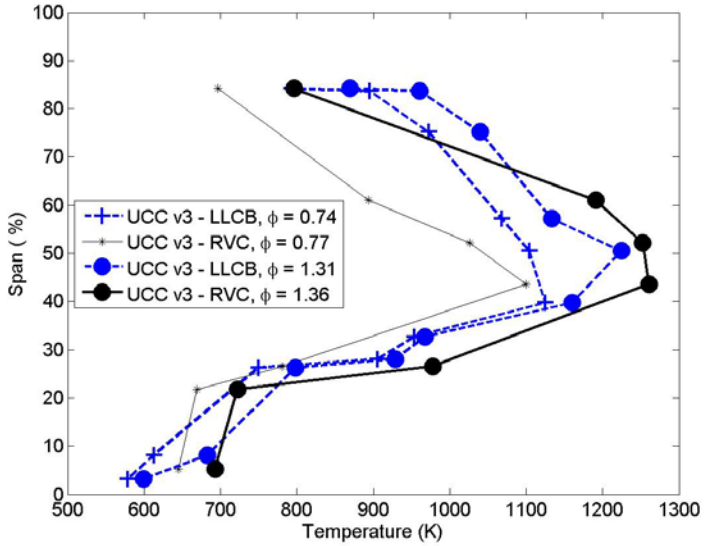

Figure 4.24: Comparison of Two Similar Φ_{cavity} Temperature Values for LLCB (blue) and RVC (black) within the UCCv3 Combustion Cavity

4.2.1.3. Filament Exit Plane

For this data, it was discovered during post-processing that the inner two filaments had been obstructed by adhesive and therefore were not useable. Also, the third filament (39.6% span location) snapped off during the seventh run and therefore data is only available for

$\Phi_{cavity} \leq 1.15$. Due to time constraints, these data points were not repeated, and were omitted from Figure 4.25. The maximum average temperature measured was 1619 K at the 39.6% filament position during a $\Phi_{cavity} = 1.15$. The RVC's success in migrating the flow is much more visible in Figure 4.25 which compares the filament measured temperature profiles at various stoichiometric ratios. At the fuel lean states, the transport of hot gases is diminished but for richer conditions the magnitude of the hot gas bump grows until the hot spot along the outer diameter is eliminated. This local hot spot in the outer-most filament location is likely the result of not all of the hot cases being fully entrained into the RVC. If combustion products are entrained in the core flow before the combustion flow can impact the RVC, it will be swept out by the core flow right at the outer radius. At the higher fuel conditions, it appears that this fuel either does not combust as much or leaks out of the RVC less. The reason for this requires further investigation into the velocity field within the UCC.

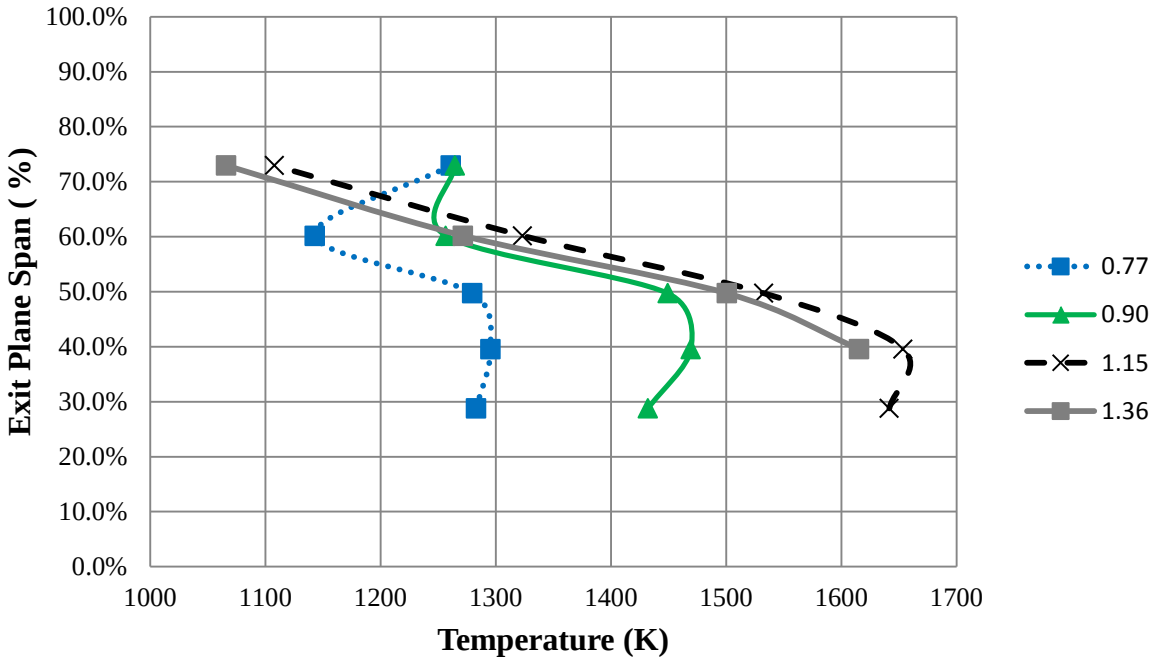

Figure 4.25: Span-Wise Exit Temperature Distribution for Select Stoichiometric Ratios for UCCv3 – RVC Geometry. Numbers in Legend are Φ_{cavity}.

Next, the exit temperature profiles were also compared between the Φ where the maximum temperature occurred as well as the thermocouple data discussed in Section 4.2.1.1. This occurred at a Φ of 1.15 for the RVC and 1.10 for the LLCB. Figure 4.26 shows how the peak temperatures migrated down the span with the addition of the RVC, and the RVC achieved a higher peak temperature than the LLCB configuration (1600 K compared to 1619 K). The difference between the filament data and the thermocouple data was again around 300 K for all points, with the greatest discrepancy again occurring at the wall temperature measurement. The difference in gas and probe values matches the peak difference seen with the UCCv3 – LLCB geometry (blue lines in Figure 4.26) and experiments performed on AFRL's SABER-Rig [33]. It is worth noting that while the SABRE-Rig saw discrepancies between the thermocouple data and the gas temperatures, the thermocouples used upon the UCC were greater. This was a result of the probes for the SABRE-Rig being coated with a thermal protective coating that reduced their conduction error, as well as being smaller in diameter than those used upon the UCC. Therefore, it is expected that the difference between the thermocouple and gas temperature would increase between these two set-ups.

This chart unmistakably demonstrates that the RVC was successful in migrating the temperature peak down the span for this particular equivalence ratio. Consideration of all the points also confirms that the temperature peak remains focused in the mid span region, and created a preferred profile (i.e. one without a second hot spot on the outer diameter) for those Φ_{cavity} in excess of 0.9. The lower average exit temperatures can be explained by the RVC shown in Figure 4.22. These vortices have been shown to evacuate the fuel out of the combustion cavity more effectively [38], thereby reducing residence time. Furthermore, the vortices created by the RVC mix the products with the cool core flow earlier and more

effectively than the LLCB geometry. This reduces the amount of burning in the vane passages, and therefore the effective length of the combustor is shortened. This means that the reactions in the vane where propane would have further broken down and CO progressed to CO_2 no longer occur, leading to decreased efficiency and average exit temperatures.

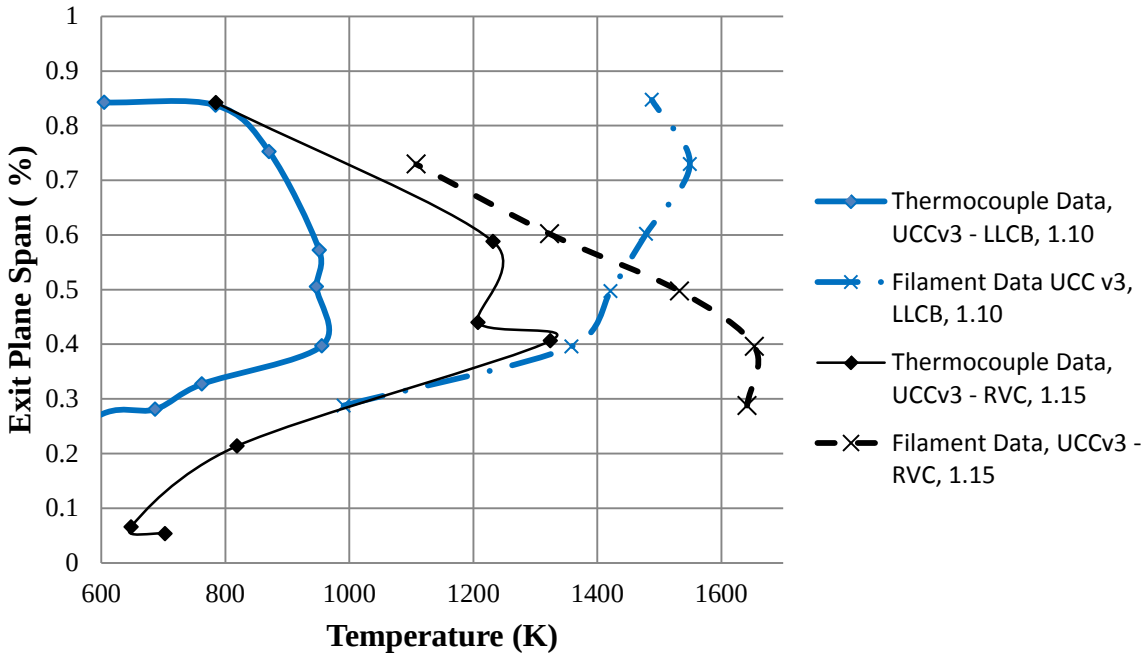

Figure 4.26: Span-Wise Exit Temperature Distribution Comparison for Different Geometries and Collection Methods. Numbers in Legend are Φ_{cavity}

4.2.1.4. Profile Factor Comparison

The local profile factor for the UCCv3 – RVC was more pronounced in the mid-span unlike the trends previously seen with the UCCv3 – LLCB configuration. Figure 4.27 depicts the local profile factor for the UCCv3 – RVC geometry across all sampled equivalence ratios. The peak divergence from the mean resides in the mid-span as intended, specifically at the 49.7% filament location. This maximum divergence is 0.176, slightly higher than previously noted values for the UCCv3 – LLCB geometry due to the lower bulk temperatures. However,

this increase in profile peak is focused in the desired region now as opposed to the outer diameter. The minimum divergence noted was now -.214 at the outer span value. It is worth reiterating that the inner diameter temperatures were lower than 900 K and therefore not readable with the TFP method. Because of this, the peak local profile values are likely higher than reported here, however the trends and consistent overlay are the patterns that are of most importance when considering this diagram.

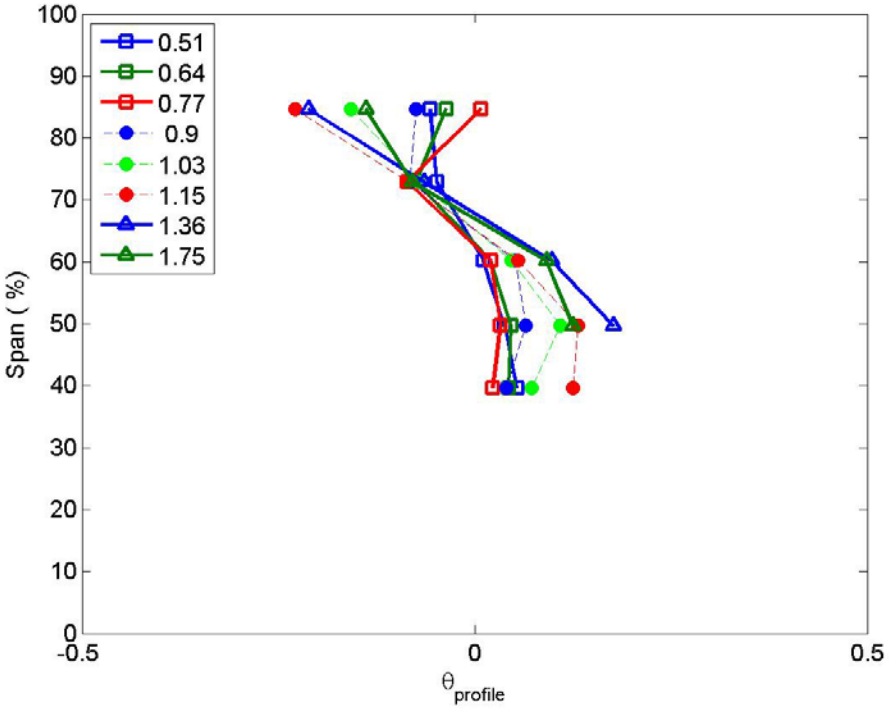

Figure 4.27: Local Profile Factor for All Equivalence Ratios for UCCv3 – RVC. Numbers in Legend are Φ_{cavity}

The consistency of the profile factor across multiple operating conditions is also desirable, and another aspect that the local profile factor can show. Advanced cooling schemes considered standard practice in modern aircraft turbine blade design [1] are supplied from the compressor and remain relatively constant in the pattern they can cool. Because of this, the exhaust from the combustor must also be cool across multiple flight conditions, otherwise the bleed air from the compressor will not be distributed accordingly during variable throttle settings

or perturbations to the engine flow. The UCCv3 – LLCB had a shape that continued to get more divergent from the mean at both the inner and outer diameter. However, UCCv3 – RVC had a shape that remained relatively constant between 50%–73% span, making the design of a cooling scheme easier for this exit temperature profile.

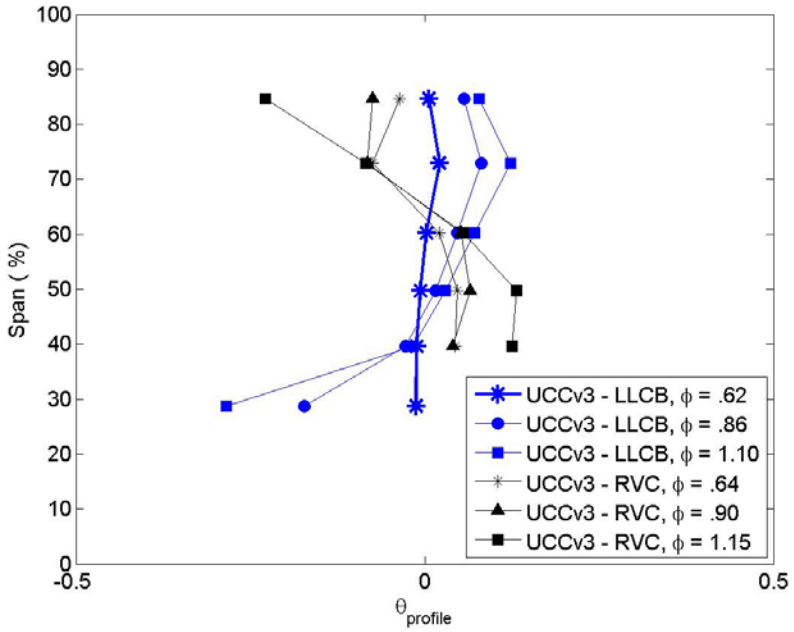

Figure 4.28: Local Profile Factor Comparison for Select Conditions for both Center-Body Geometries and Common UCCv3 Combustion Chamber

4.2.2. Emissions Trends for RVC

Emissions comparisons were made between the increased combustion cavity aspect ratio with the increased aspect ratio combustion cavity (UCCv3) with both the Low Loss Center-Body (LLCB) and the Radial Vane Cavity center-body (RVC) to determine the comparative differences between the two geometries. Figure 4.29 shows some of the general trends between the two types of pollutant emissions that traditionally are regulated. Figure 4.29 shows that the RVC geometry produced approximately twice as much Nitrous Oxide (NO_x) and Carbon Monoxide (CO) than the smooth vane LLCB geometry. Also, for the LLCB, NO_x production is

relatively stagnant across all operating conditions, while for the RVC there is a much stronger correlation between CO and NO_x production. There is also just more emissions with the RVC, both the concentration NO_x and CO increased a minimum of 100% between the two geometries. This was due to increased quenching caused by the RVC and the evacuation of fuel from the cavity into the thermally non-conducive environment of the core flow.

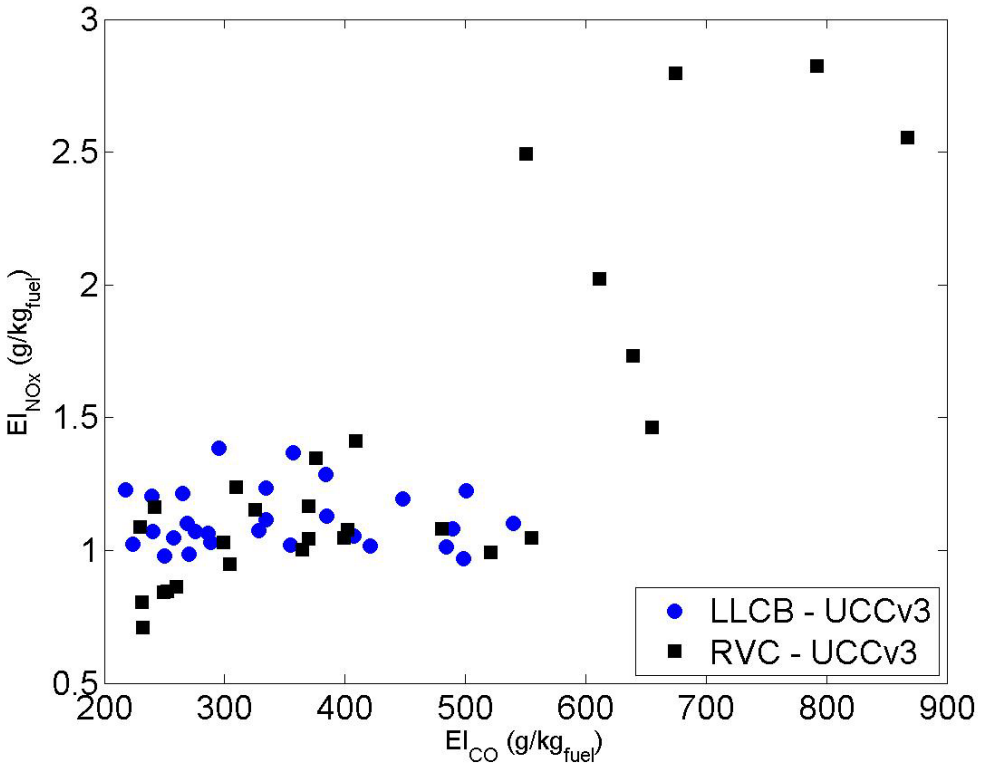

Figure 4.29: Emissions Comparison of CO and NO_x for UCCv3 Air Driver Configuration. Data points shown are for all fuel settings at all positions.

4.2.2.1. Total Unburned Hydrocarbons (THC) Production

Also plotted were the point values of the emissions indices for THC. Figure 4.30 shows the Emissions Index of Total Unburned Hydrocarbons (Propane) at the exit plane of one vane of the UCC. The highest concentration of unburned propane for the LLCB geometry occurred at the 27.2%, while the RVC saw the highest concentrations at the 54.6% span. The points of lowest unburned fuel tend to occur at the locations associated with the peak temperature values.

This suggests that higher efficiencies exist in the mid-span region and decrease substantially at spans closer to the inner and outer wall. The minima for emissions for this geometry occurred between a Φ_{cavity} between 0.83 – 0.95, likely right around 0.85.

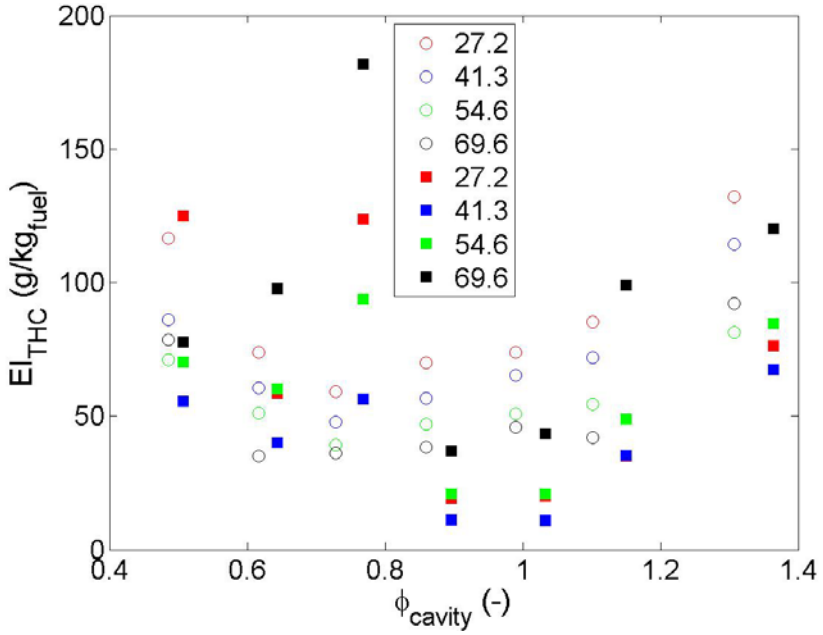

Figure 4.30: Emissions Index of THC for the UCCv3 Combustion Cavity Geometry at various Φ_{cavity} (x-axis) and % Span Locations (in legend) for LLCB (circles) and RVC (squares)

The RVC geometry followed some of the trends exhibited by the LLCB geometry; The RVC geometry followed some of the trends exhibited by the LLCB geometry; specifically they had minima of THC around the same cavity equivalence ratio. The divergence between Emissions Indices however was much greater for the RVC. This divergence led the RVC to perform more poorly than the LLCB at all equivalence ratios. This is likely due to the RVC having a reduced residence time with respect to the LLCB. CFD analysis by Cottle [55] has shown that the RVC creates a series of vortices that channels flow from the combustion cavity to the core flow. When this is done to hot gases, the temperature profile is improved as discussed in the previous section in Figure 4.24, but it would appear this is at the detriment of the chemical

reactions. CFD performed by Cottle et al. [55] traced the fuel particles from a single jet and found that the "average" number of vane passages it takes to entrain the fuel particle is approximately two vanes (120°) for the LLCB. It also had many of its fuel particles exit at the second vane, but an increased amount became entrained by the cavity induced vortex within the vane immediately following the fuel baffle. This all suggests that a RVC more effectively removes the products within the combustion cavity to the middle span, and the back wall created in this experiment's RVC design to combat the fuel loss noted by Mawid *et al.* [38] was insufficient to the task. It was therefore concluded that the RVC when placed in the straight driver UCCv3 combustion cavity produced undesirable results that would hamper its implementation in a traditional jet engine environment.

4.2.2.2. NOx Production

Turns stipulates that the maximum production point for NO_x occurs where the maximum equilibrium point for O^- atoms exist, which is near a $\Phi = 0.9$, right by the range of peak combustion temperatures and the largest radical production. As Figure 4.31 shows, both these geometries conform to this pattern, but the RVC has significantly increased NOx production. The concentration of NOx in the exhaust increased by a typical magnitude of two, which was approximately what the EI_{NOx} increased by as well.

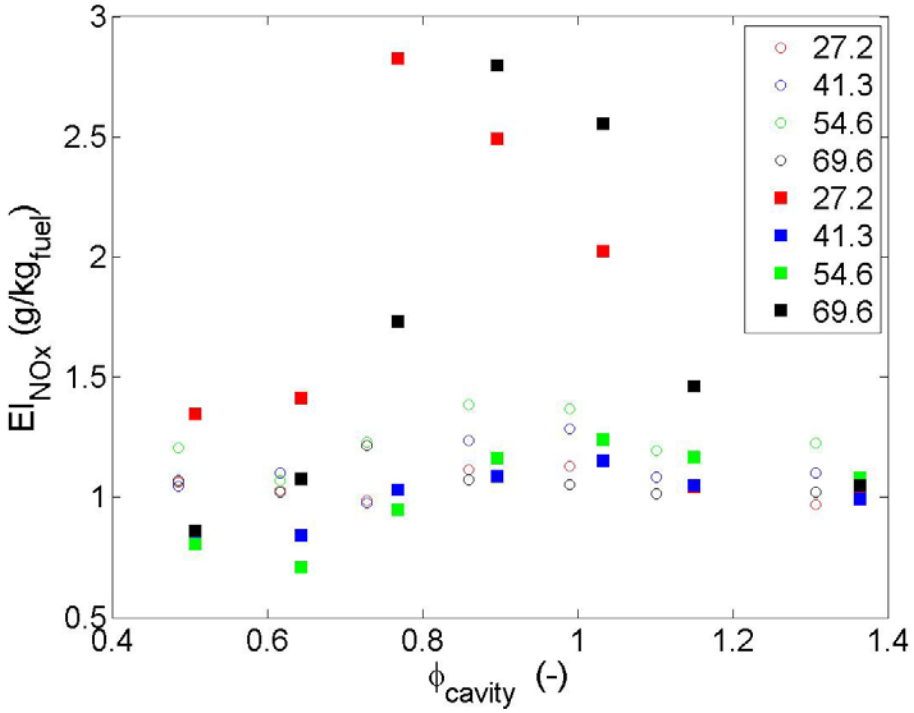

Figure 4.31: Emissions Index of NO_x for the UCCv3 Combustion Cavity Geometry at various Φ_{cavity} (x-axis) and % Span Locations (in legend) for LLCB (circles) and RVC (squares)

The relatively stagnant production of NO_x with the LLCB vane geometry is due to the failure of the flow to achieve the four mechanisms required for NO_x production. Turns [2] lists the four mechanisms as the Zeldovich (thermal) mechanism, Fenimore mechanism, N_2O-intermediate mechanism, and the NNH mechanism. The N_2O-intermediate mechanism only applies in low temperature applications (which the UCC combustion chamber is not) and the NNH mechanism is important mostly for hydrogen and fuels with large Carbon to hydrogen ratios (which propane is not). The Fenimore mechanism, or prompt NO_x, is important for fuel rich combustion, such as those that occur in the outer radial portion of the UCC combustion chamber and requires a laminar, premixed flame regime which the UCC has in certain portions of it. The Zeldovich mechanism meanwhile requires a large activation temperature of

approximately 1800 K to beget its limiting reaction. Both of these mechanisms also require a "super-equilibrium" of oxygen and hydroxyl radicals to enable NO_x formation.

The design of the UCC is specifically designed to create a region where heavy fuel particles and the radicals of combustion are entrained in the outer cavity flow. The work of Cottle *et al.* [23] shown in Figure 4.32 confirms that the fuel's highest concentration of fuel was in the upper 20% of the radial cavity height (red circle). This created another density gradient where there was fuel in the outer circumference, combusting flow in the inner portion, and a stable wrinkled layer that held the flame and most of the radicals. These radicals fit the Turns' description of a "super-equilibrium", especially considering the core flows oxygen as well. Normally when both the Zeldovich and Fenimore mechanism are activated together, some NOx disappears as they work in harmony to revert some of the formed NO_x back into more benign species.

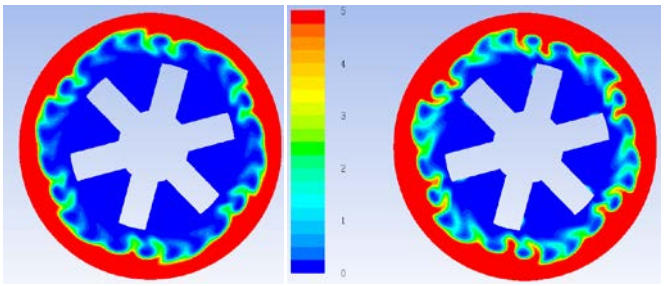

Figure 4.32. Local equivalence ratio contours in the combustion cavity (position C2) for the high-flow case at lean (left) and rich overall cavity equivalence ratios [23]

The temperature results of the TFP in Section 4.1.2.2 and 4.2.1.1 also show that there regions within the chamber that are near but do not exceed the 1800 K requirement. The LLCB has a maximum temperature of 1600 K so it is unlikely that there is sufficient thermal energy to beget NO_x formation. This means that the oxygen in this region is instead transferred to carbon monoxide and carbon dioxide formation. This makes the Fenimore mechanism the likely cause of NO_x formation within the LLCB geometry, and would become more of a factor if the inlet

pressure was increased or for higher equivalence ratios. However, the RVC geometry has even more NO_x formation suggesting that either a new mechanism has been activated or something is exacerbating the prompt NO_x mechanism more.

The temperature measured by the filaments within the combustion chamber registered near 1800K, suggesting that the Zeldovich mechanism could have been activated in addition to prompt NO_x. However, it is more likely that the vortex caused by the RVC cutout increased the NO_x production by creating more laminar premixed flame regimes. This RVC vortex disturbs and mixes the flow path enough that more laminar, pre-mixed flames occur and they do so over a longer distance. The core flow then quenches the reactions so much that the CO and NO_x formed is frozen and expelled out of the UCC before any progression can occur. The increase in NO_x is also present in CO emissions, suggesting that the RVC geometry produces more radicals in general than the LLCB. This not only makes the RVC problematic from an emissions standpoint, but reduces the efficiency in fuel lean conditions as well.

4.2.2.3. CO Production

The trend of increased emission concentrations and severely increased emissions indices from the LLCB to the RVC continued with carbon monoxide. Again this issue stemmed from the doubling of pollutant concentrations seen without a sufficient increase in combustion. The lack of CO_2 indicates an increase in THC which suggests that the fuel was being evacuated and quenched by the core flow before reactions could begin. As the velocity profiles suggest, this is due to the RVC vortex mixing the cool core flow into the exhaust stream and reducing the amount of burning occurring in the vane. Therefore, while more burning will occur in the combustion cavity, the effective length over which combustion can occur is reduced, leading to the decreased formation of CO_2. Because of this, the EI_{CO} increased up to nearly 900 g/kg at the

worst case point around a $\Phi_{cavity} = 1.03$. This maximum occurrence point of CO for the RVC did occur near the expected range of 0.8-1.0, however its high emissions still means the UCC does not behave like a traditional combustor in this configuration.

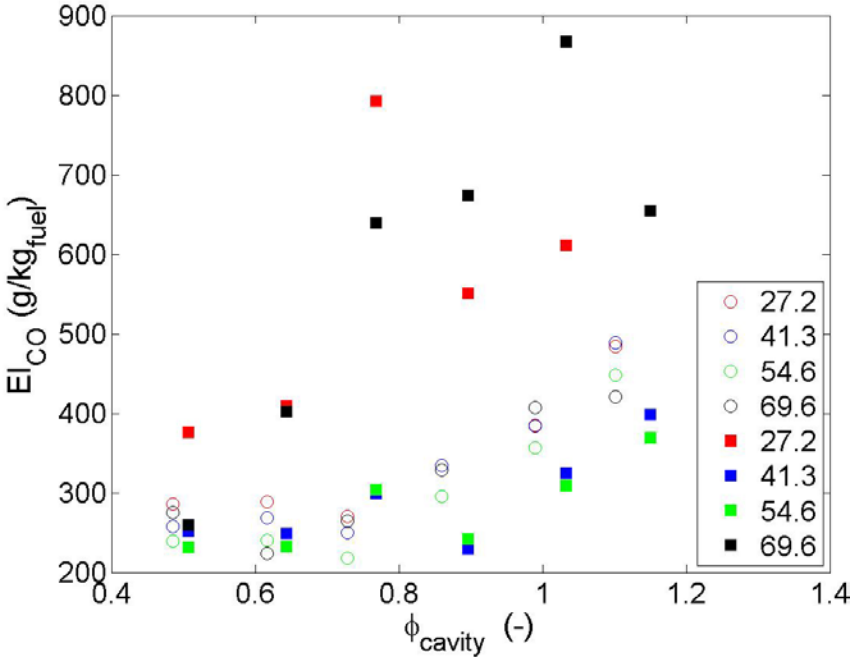

Figure 4.33: CO Emissions Index for the UCCv3 Combustion Cavity Geometry at various Φ_{cavity} (x-axis) and % Span Locations (in legend) for LLCB (circles) and RVC (squares)

4.2.2.4. Efficiency

All of the increased emissions of the UCC compounded upon each other to significantly degraded the efficiency for the UCCv3 – RVC geometry. While the efficiency for the LLCB peaked at 92%, the lowest values recorded were at the inner diameter at 76%. However, for the RVC, the highest efficiencies occurred at the inner diameter and outer diameter, places that were least affected by the RVC induced vortex. These peak values were also lower than those calculated for the LLCB geometry, with the peak efficiency of 94% occurring at a $\Phi_{cavity} = 0.90$ and the lowest being 69% at the outboard position with a $\Phi_{cavity} = 0.77$.

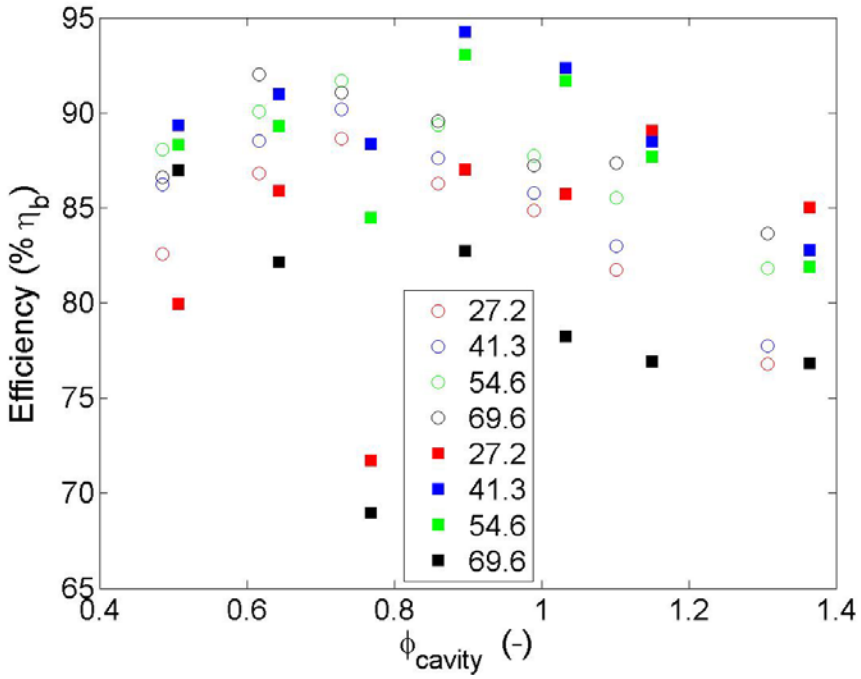

Figure 4.34: Efficiency for the UCCv3 Combustion Cavity Geometry at various Φ_{cavity} (x-axis) and % Span Locations (in legend) for LLCB (circles) and RVC (squares)

4.3. Analysis of Compound Driver – LLCB Vane to Other Geometries

The next design tested was the Compound Air Driver (Cmpd Drvr) air injection geometry as described in Section 3.1.2.4. This geometry was first developed by Capt Cottle as part of his work with modifying the flow within the combustion cavity [6][55]. It was hoped that this would increase the amount of air (and therefore oxygen) in the outer portion of the combustion ring, thereby keying more reaction. In addition to this, it was hoped that the velocity vectors would increase the residence time, and consequently the heat release, and efficiency. Initially the LLCB vane geometry was used in conjunction with the Compound Driver geometry in order to limit the number of geometric differences made between comparisons. Also, due to the poor emissions performance of the UCCv3 – RVC geometry, few comparisons were made between it and the Compound Air Driver geometry. The thermocouple data for all the fuel rich conditions were unable to be collected due to complications with the rig. It was shown that perturbations in

geometry from the baseline UCCv3 – LLCB case changed not only the temperature profile within the combustion cavity, but the volume within the primary zone that experienced combustion.

4.3.1. Temperature Profiles

The Compound Driver – LLCB configuration added a 10° radial component to the air drivers in the front plate of the UCCv3 combustion cavity. The effect of reorienting the air jet drivers was unknown, but it was postulated that this design might return the UCC exit temperature profile more to the flat, outer span biased profile seen by Damele [37]. Therefore its temperature profiles within the combustion cavity and at the exit plane were investigated. These experiments were therefore dual purposed: to determine if altering the combustion cavity air driver scheme would have more effect on the exit temperature profile than the RVC and to establish if the trends seen the computational results were valid. During comparisons to other geometries, the temperature profiles for the Compound Driver – LLCB configuration will be shown as magenta lines.

4.3.1.1. Combustion Cavity Temperature Profile

The Compound Air Driver geometry proved to yield more interesting results for the combustion cavity temperature profile. The first peculiarity observed in Figure 4.35 was the 17% filament actually registering temperatures below the 70% radial height points, which had not been seen in any of the previous results. If there is a heat signature at these points, it means the filament is actually surrounded by combustion that has managed to sustain in the front portion of the chamber. As the drivers were explicitly designed to achieve this benefit and the Cottle model predicted this behavior, the presence of hot gases in this area confirmed that the design was achieving its objectives. This increase in the lower span temperature is an excellent

sign that the redesign effort of the cavity air drivers was successful in increasing the residence time of the fuel within the combustion cavity. The experimental results therefore indicate that the fuel particles are now traveling around more than an average of two vanes as was the case for the UCCv3 geometry.

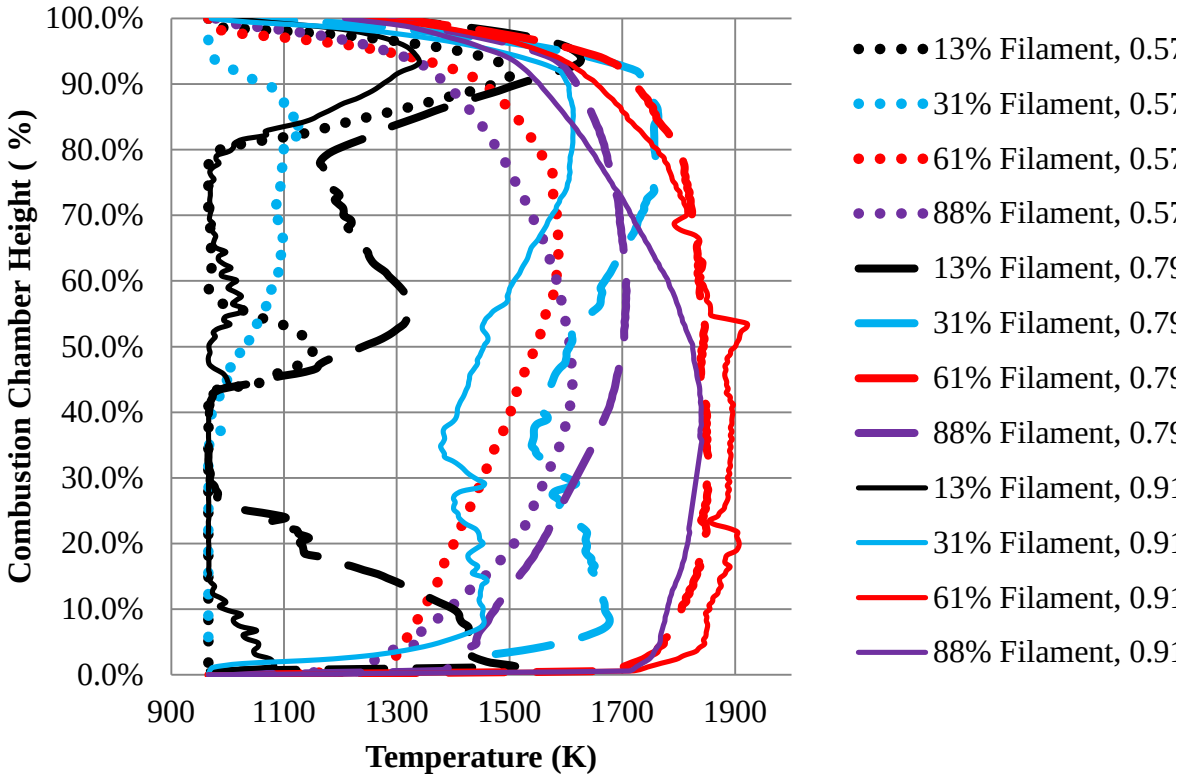

Figure 4.35: Comparison of Cavity Filament Temperature Profiles at Select Fuel Lean Conditions (number in legend) for Compound Driver – LLCB Geometry

The temperature behaved as expected with regards to fuel equivalence ratio: as fuel was increased, the temperature also did until it reached a peak value at a $\Phi_{cavity} = 1.02$, which can be seen in Figure 4.36. For most points in the cavity, the heat increase was relatively smooth but right at the around the 30% height point, a large temperature gradient appears that increased the temperature ≈ 170 K. This result was a new finding with the Compound Air Drivers, as the maximum temperature had previously been seen at the 61% filament. Indeed, the average

temperature of the 61% filament is still greater for the Compound Air Driver geometry, but the sudden spike at the 30% span region creates the highest values measured. This peak is present in most conditions, and is the least prevalent around $\Phi = 0.9$. This likely suggests that the hottest part of the flow, and therefore the flame itself, is surrounding this portion the vane. However when the conditions are most optimized for combustion, the flame front grows and therefore the temperature profile becomes more smooth again. The fact that such intense combustion is occurring for this geometry and not for the others suggests that the flow is leaving later than previously noted with the UCCv3 driver configuration.

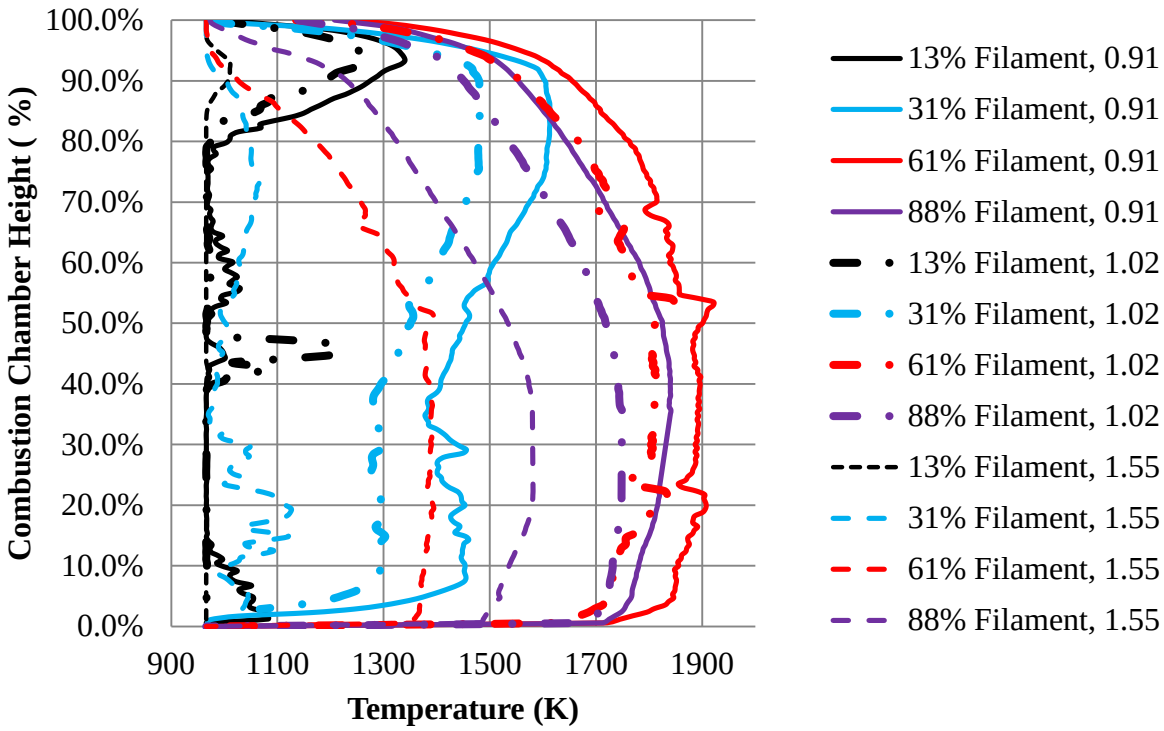

Figure 4.36: Comparison of Cavity Filament Temperature Profiles at Select Fuel Rich Conditions (number in legend) for Compound Driver – LLCB Geometry.
Note: Legend reads Location, cavity stoichiometric ratio

In addition to the aforementioned temperature spikes, the Compound Air Driver in general experienced much greater temperature values in the lower span region than either

UCCv3 configuration. As Figure 4.37 shows all the magenta lines denoting the Compound Air Driver configurations are hotter than the other two geometries. Consequently, the higher radial positions for this geometry are less than the other two, with the temperatures steadily increasing until the 30% span point. All of this suggests that the combustion event has moved radially inward due to a delay in the gases being entrained out of the chamber.

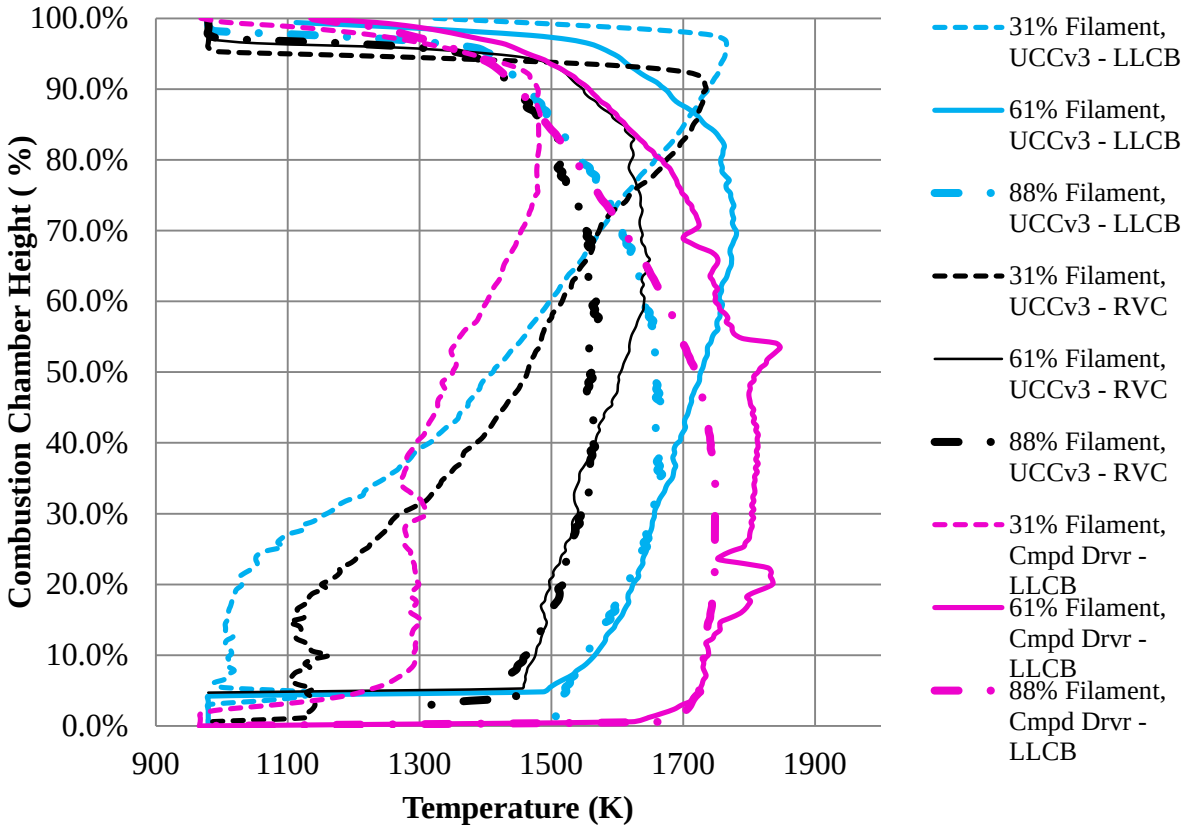

Figure 4.37: Comparison of Combustion Cavity Temperature Profiles for Three Previously Discussed Geometries at $\Phi_{cavity} \cong 1.00$

The explanation of this phenomenon can be explained by rudimentary drawings of the flow path and looking at the theoretical impact point. Figure 4.38 is the pictorial representation of the combustion cavity cross section looking towards the front two filaments. In order to ease the presentation of the material, the figure is not drawn to scale and the only two air drivers are shown with an exaggerated axial angle. This flow continually introduces more cold flow that

better mixes the upper portion of the cavity and lowers the temperature of the mixture in the top of the cavity. For this reason, it makes sense that the front half, which has less turbulent mixing and fresh air would have lower temperatures than the UCCv3 straight driver configuration.

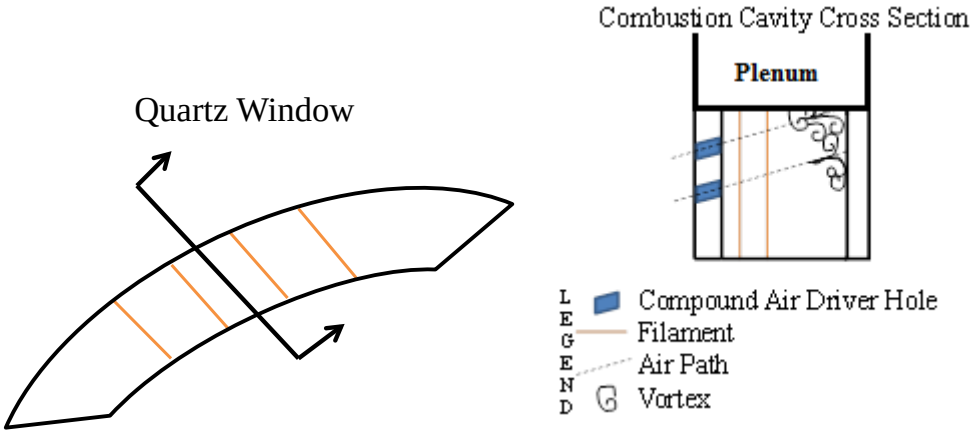

Figure 4.38: Explanation of Compound Driver Flow Path

This phenomenon also was analytically confirmed by Cottle *et al.* [23] in their 2016 IGTI paper. They traced the fuel particles through the combustion cavity to see if the residence time increased, as well as the progression of temperature through the cavity. In Figure 4.39, the left-hand figure is the baseline geometry while the right one shows the compound driver geometry. It is evident due to the increase in streamline distribution on the right figure that the residence time has been increased. However, this increase in residence time has not led to increased combustion at the outer radial heights, the temperature remains below 1000 K throughout the upper quarter which would not register on the filaments. Instead the heat release which correlates to combustion dominates in the lower half of the chamber.

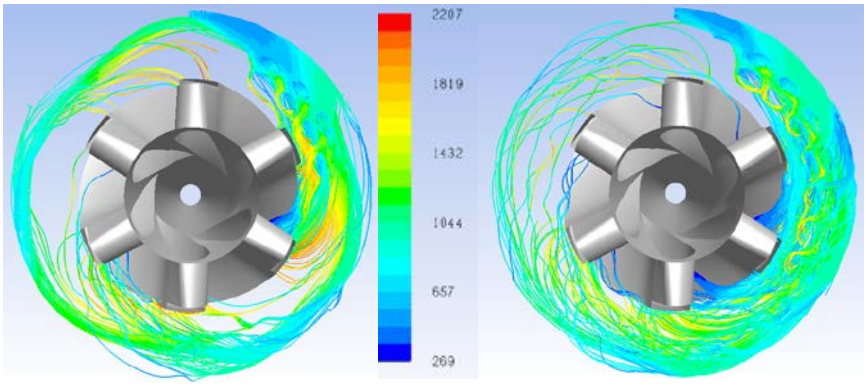

Figure 4.39: Front Looking Aft Cavity Fuel Injection Scheme Colored by Temperature for (left) UCCv3 – LLCB and (right) Compound Driver – LLCB [50]

Their results also found that the exit temperature declined at the exit profile between the normal UCCv3 air drivers and the compound air driver configuration. This configuration however increases efficiency as noted by Cottle [50] and proved in Section 4.3.2.4. This is also shown in Figure 4.39 with the cooler temperature of the flow in the outer diameter. The temperature is still increasing however suggesting burning. Therefore, the burning that is likely occurring in this geometry is extremely fuel-lean through the upper portion of the cavity with the additional oxygen. When the air becomes more vitiated in the bottom half, its temperature increases but due to the more distributed fuel-lean burning pattern, it is still lower than the average of the UCCv3 driver configuration. This means that the starting temperature that the core flow has to cool is lower, which means the final temperature at the exit will also be lower. However, more volume is consumed by combustion this way as the density of the fuel traces within the cavity show. By combining all this evidence, along with the increased temperature readings at the 13% filament, it can be concluded that the Compound Air Driver configuration with the LLCB confirmed the analytical determination that it would increasing the residence time within the UCC.

4.3.1.2. Exit Temperature Profile

The exit profile as measured with the thermocouples was much more biased to the outer diameter than the results seen previously in Figure 4.9, and resembled more closely the flat shape seen by Damele [47]. Figure 4.41 compares the observed flat profile (magenta line) with the temperature profile previously recorded for the UCCv3 – LLCB configuration (blue lines). The highest temperature is again noted around the 40% span location but the temperature holds relatively constant between the 20% and 60% cases for the fuel lean condition, while for the stoichiometric condition it is constant all the way to the 80% span probe. Also, the temperature magnitude is relatively constant between these two points, as opposed to the UCCv3 – LLCB geometry which saw a marked increase in all locations above 40% span.

When considering radial profiles, this geometric change was detrimental. The exit profiles presented in Figure 4.40 display higher temperatures in the outer span region and a shape that does not have the characteristic peak seen in the UCCv3 – RVC data. This trend is present for all the fuel lean and near stoichiometric conditions, with the peak in the fuel lean conditions actually having a consistent peak measured at the 41% span probe.

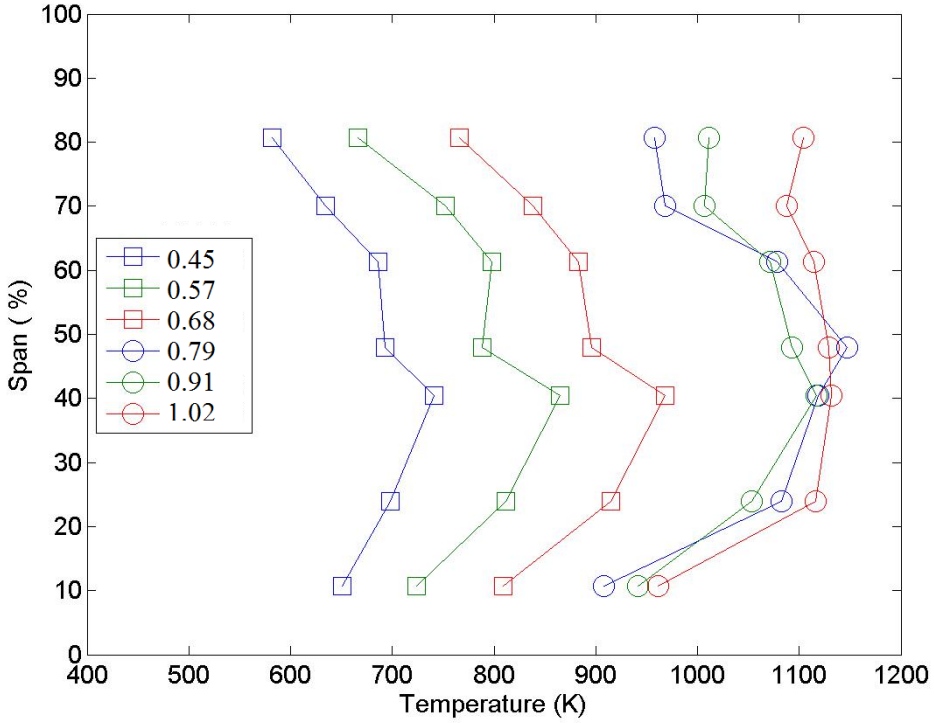

Figure 4.40: Span-Wise Exit Temperature Distribution for All Measured Thermocouple Values for the UCCv3 – LLCB Geometry

Also of interest is that even though the efficiency increased for this geometry (which can be seen in Section 4.3.2.4), the peak exit temperature was lower while the outer diameter temperatures were measured as warmer in the 60% – 80+% span probe locations. This likely occurred due to the increased residence time and distance traveled by the fuel stream within the combustion cavity. Looking at the cavity filament data in Figure 4.36 it also seems that while some combustion is occurring in the outer radial height of the chamber, the majority of it is concentrated in the bottom half. This delay in combustion allows for a more gradual heat release, but also shifts the flame location so that any burning in the core will be effected. This alters the flame length, which means the hottest part of the gases are not burning in the vane anymore, and the core has an increased cooling (quenching) effect. Due to this, the exit

temperatures will decrease as the core flow has less length (and therefore volume) of flow to cool.

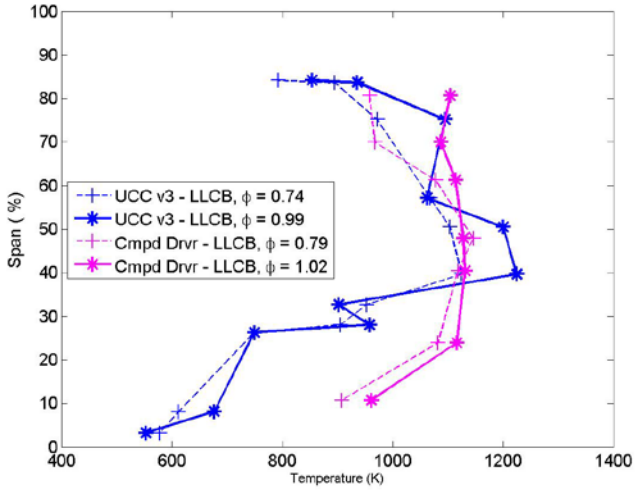

Figure 4.41: Span-Wise Exit Temperature Distribution for Select Φ_{cavity} Conditions within Compound Driver – LLCB and UCCv3 – LLCB

Comparing the Compound Driver – LLCB data with the UCCv3 – RVC in Figure 4.42 further illustrates the flat temperature profile. Though the peak temperature is lower due to the lower entry temperature inherent to the fuel-lean burning in the cavity, there is no discernable peak temperature in the mid-span. Rather, the temperature never varies more than 150 K from out-span point to the 40% (max temperature) point. If this design were to be placed in a traditional engine, the same temperatures would be seen in the outer span as the inner span. This temperature would impact the turbine blade evenly and raise the ductility across a large span of the blade. This, combined with the existing stresses on the turbine blade would cause it to elongate, strike the wall, and ultimately component failure.

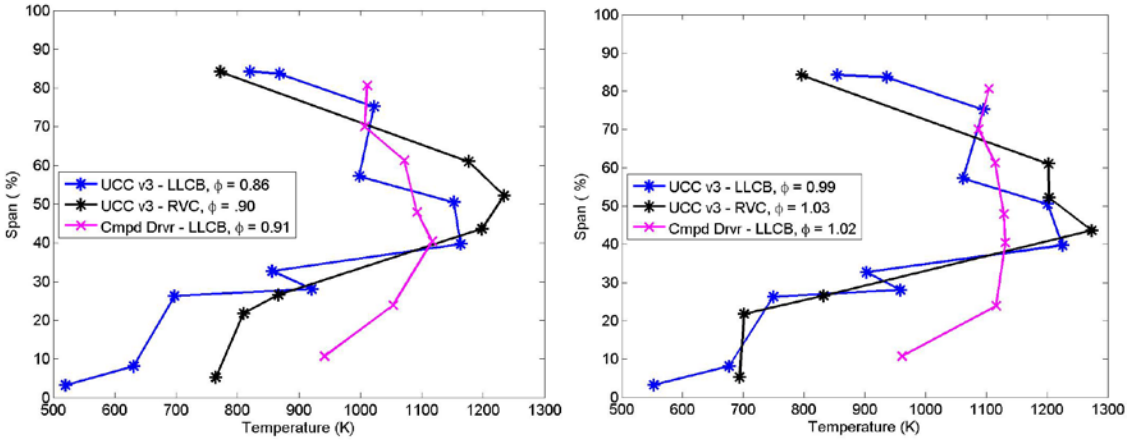

Figure 4.42: Comparison of Span-Wise Exit Temperature Distribution for Approximately Equivalent Φ_{cavity} of (left) 0.90 and (right) 1.00 for Three Previously Tested Geometries

The reason for this return to the flatter profile is the redirection of the flow into the upper cavity. The increase in measured temperature (i.e. heat release) is also likely due to the redirected air flow upward into the combustion cavity. Both of these increases likely come about due to the increase in combustion residence time which the air driver affords. Computational analysis [23] has shown that the residence time within the combustion cavity has increased from between 3-5 ms to 6-8 ms, or roughly one additional vane passage. This caused there to be less of a driving force from the cavity as the air was preference to flow upward and remain in the upper portion of the cavity, rather than strike the back wall and then progress out into the core flow. From a heat release and efficiency standpoint, this is of great benefit.

4.3.1.3. Filament Exit Plane Data

The filament data confirms the outer span bias that was noted with the thermocouple probes measurements. For fuel lean conditions the temperature magnitudes increase until an air-to-fuel ratio of 1.02 is met. The profile also progresses from a relatively consistent value with two cool pockets of air seen at $\Phi = 0.68$, to having the hot gases begin to congregate first in the

60% location and eventually more up the span to their maximum recorded temperature at the 84.7% filament location.

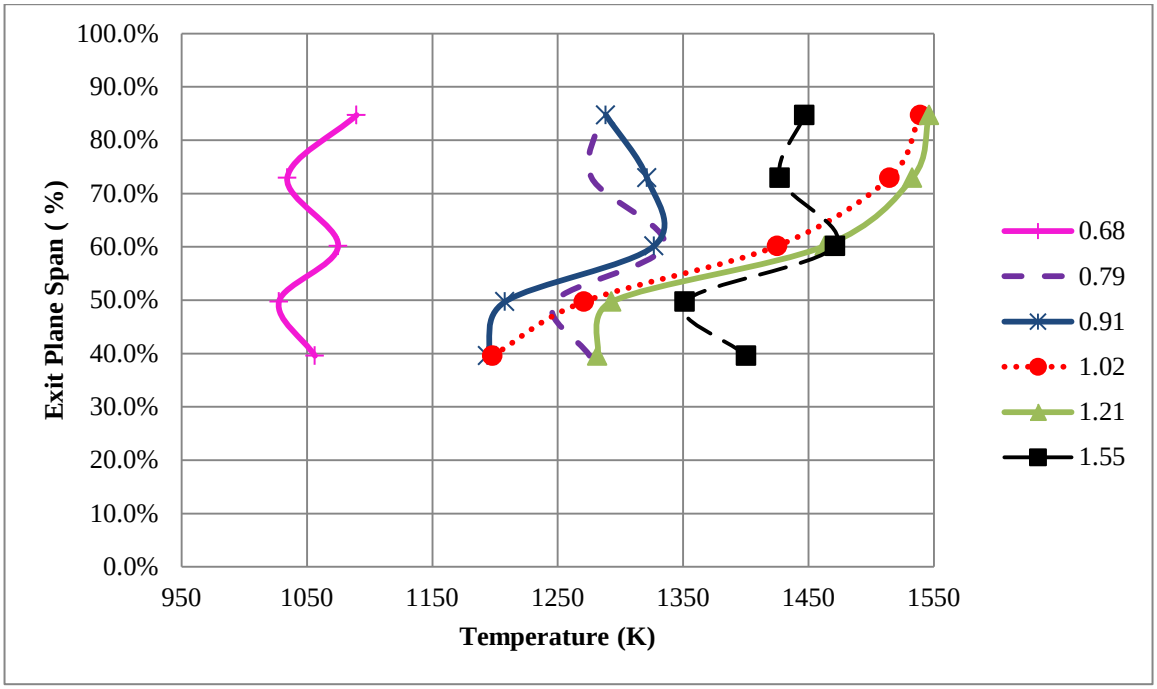

Figure 4.43: Span-Wise Exit Temperature Distribution for Select Stoichiometric Rations for Compound Driver – LLCB Geometry. Numbers in Legend are Φ_{cavity}.

Further comparisons were made between the compound driver values and those ascertained for the straight hole UCCv3 air driver arrangement. Both center-body geometries are

presented in

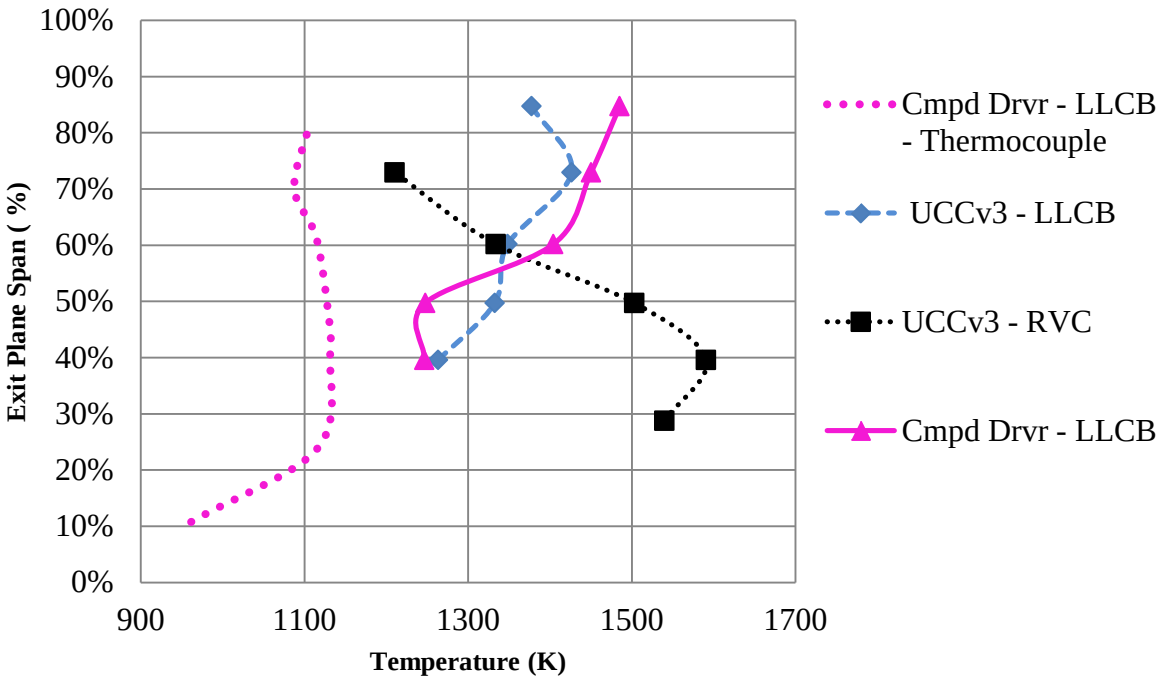

Figure **4.44** and the trends seen with the thermocouples (dotted line) are confirmed: the peak temperature grows from the middle to then dominate the outer span (>80% span) and the magnitudes of the measured temperature are within approximately 100 K of each other at all positions. The inner diameter temperature values are reduced for this case, and it is speculated that the temperatures in the outer 20% of the span would be even higher for the Compound Driver than those with the UCCv3 driver scheme. This is postulated due to the maxima appearing to have been reached at 73% filament location for the UCCv3 – LLCB geometry, but the Compound Driver scheme is still increasing at the 84.7% filament position. Also, as previously noted the filaments register decidedly higher temperatures than the thermocouples at all locations.

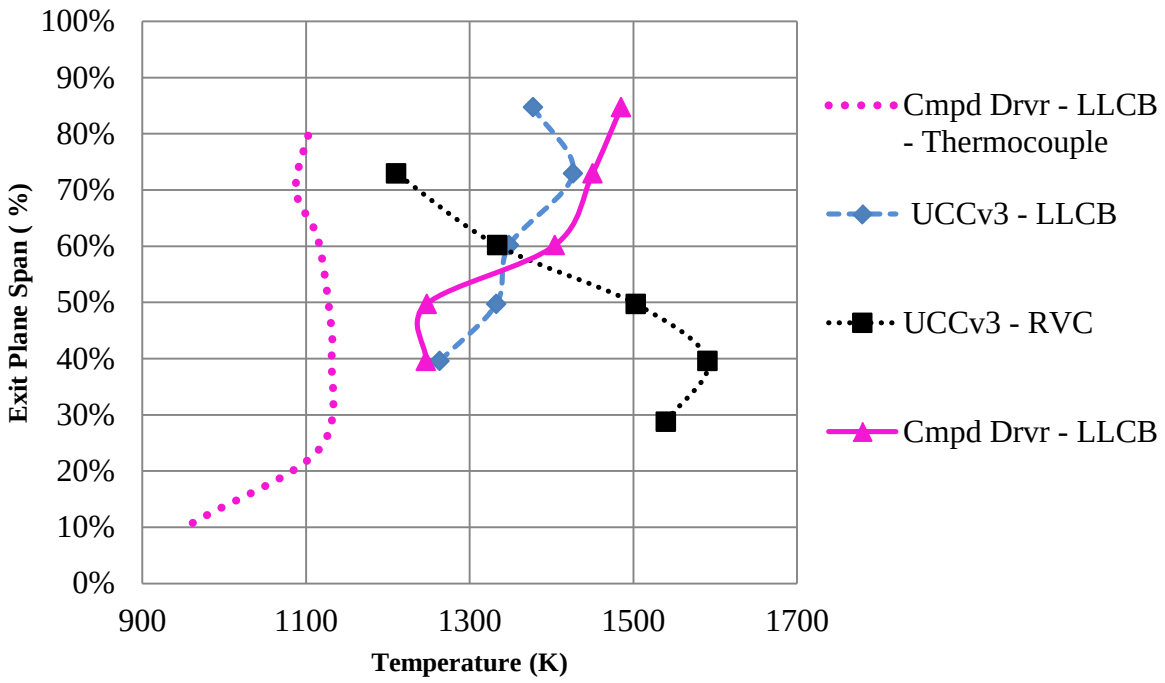

Figure 4.44: Comparison of Exit Filament Temperature Profiles at $\Phi_{cavity} \cong 1.02$ for Three Previously Mentioned Geometries

4.3.1.4. Profile Factor

The local profile factor for the Compound Driver – LLCB was extremely consistent; however, the profile values were consistently near the average line ($\theta_{profile} = 0$) at all measured locations. Figure 4.45 shows (on the same scale of all the previously shown local profile factors) how little the filament temperature diverged from the bulk temperature. This chart reveals that the ranges of all points were between -0.13 and +0.10, with the maximum temperatures being seen at the 84.7% filament at near stoichiometric conditions and at the 60.2% filament for all other conditions. The coolest documented temperatures happen at the 39.6% filament, which means that the turbine blade tips are going to experience the majority of the thermal loading. The local profile factor confirms that the temperature bias in the outer diameter has returned and must be moved to the mid-span again.

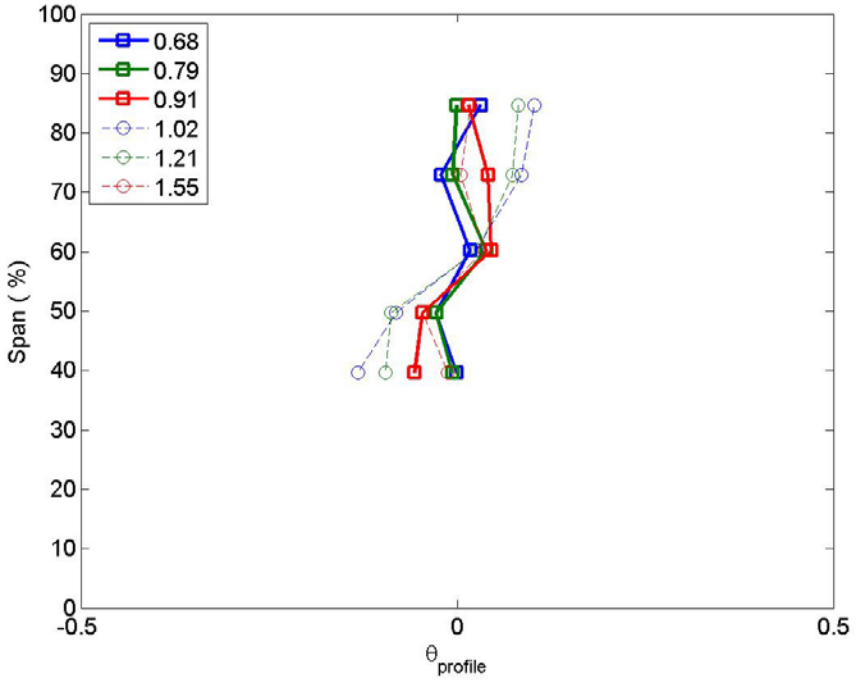

Figure 4.45: Local Profile Factor for All Equivalence Ratios, Compound Driver – LLCB

4.3.2. Emissions Trends for Compound Drivers

The Compound Driver air injection scheme also behaved similarly to the original UCCv3 injection scheme with respect to emissions. The EI for all measured species followed the same trends and had the same magnitude for their calculated values. Figure 4.46 shows how the Compound Driver was within the same range for both NO_x and CO production as the UCCv3 geometry, and that there was the same behavior of constant low NO_x emissions when additional CO was produced. The two mid-span channels tended to detect lower concentrations for all emissions at the exit plane of the Compound Air Driver geometry, but also had less CO_2 detected which kept the EI profiles very similar. This resulted in slightly higher span-wise efficiency values that were very tightly grouped. One other noticed difference is that before the results exceeded the capabilities of the CAI Analyzer, the Compound Driver performed less efficiently at fuel-rich conditions. Also note that emissions analysis stops for the compound driver data at a

$\Phi_{cavity} = 1.21$ because all subsequent points exceeded the maximum sample range of the CAI's THC analyzer (3000 ppm). This behavior led to an assumption that Compound Driver had degraded performed at fuel rich conditions that was borne out in the data.

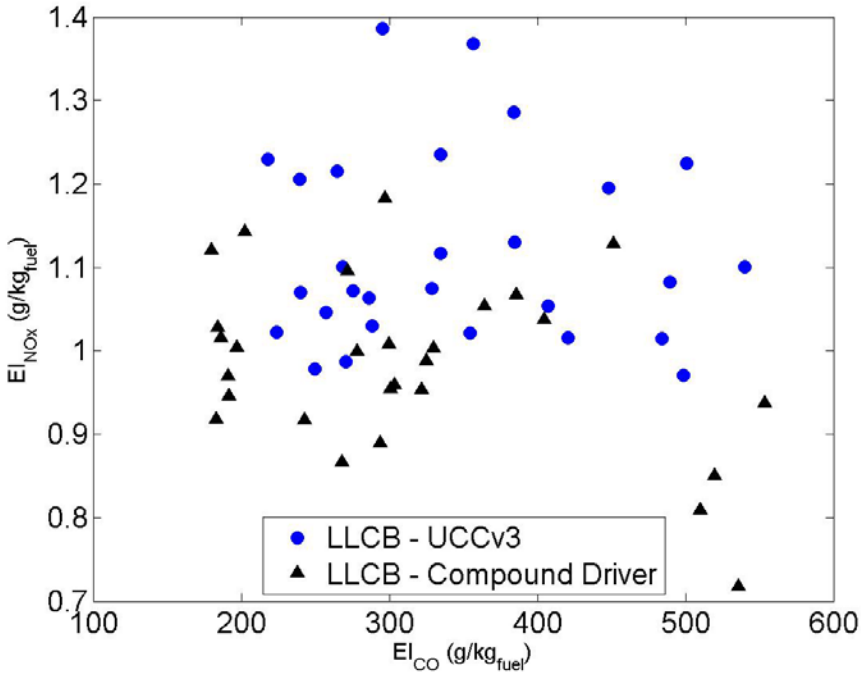

Figure 4.46: Emissions Comparison of CO and NOx for UCCv3 and Compound Air Driver Configuration with the LLCB as a Common Element.

4.3.2.1. THC Production

The total amount of unburned propane remained relatively proportional to the performance of UCCv3 combustion cavity geometry. The same span locations read the highest readings (27.2%) and the lowest readings (69.9%), hinting at where the most combustion was occurring. The Compound Air Driver performed slightly better at leaner fuel conditions and achieved the lowest value of hydrocarbons around the more traditional Φ of 1.05. The span-wise values of the EI for THC were also more uniformly grouped for this geometry. As can been in Figure 4.47, the triangular values often overlap each other or cover them up (as happens in the case of $\Phi = 0.57$ condition). The UCCv3 geometry has a much greater variance, with its

maximum and minimum value often being separated by as much as 40 g/kg at the most efficient locations and conditions. Also interesting in this figure is the sudden increase in EI of THC at the fuel rich point. This shift greatly alters the shape of the emissions curve with a large gradient not seen anywhere else on the figure, and suggests that the compound air driver does not operate well at fuel rich conditions. Also revealing the degraded performance is the fact that the outermost span location suddenly goes from being the best performing condition to the worst. This occurs due to the preponderance of the hot flow being concentrated in the upper span. The hotter the exit temperature flow, the more combustion has occurred typically upstream of that location and the more fuel is present in that area. If the fuel becomes too rich to burn, the remainder should be present at the same location as the highest temperature readings, which is what is demonstrated in the figure below.

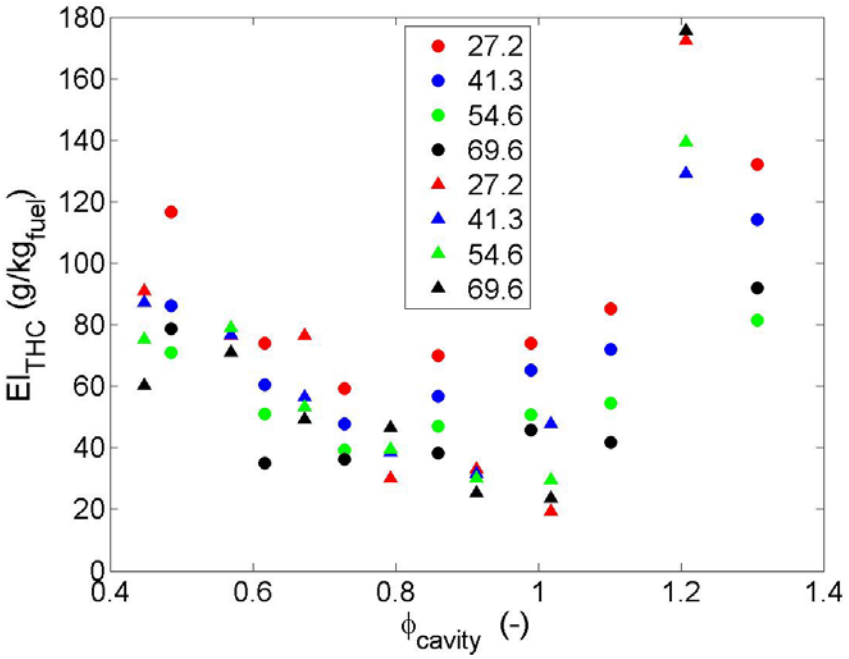

Figure 4.47: Emissions Index of THC with Common LLCB Geometry; UCCv3 (circle) and Compound Air Driver Cavity (triangle) at various Φ_{cavity} and Span Locations

4.3.2.2. NOx Production

Just as with THC, the Compound Air Drivers reduced the amount of NO_x normalized to the mass flow of fuel. The compound air driver also shared several similarities with the UCCv3 geometry: the lowest values tended to occur at the 27.2% span location; the highest values occurred at the 54.6% span location; and the maximum occurred at Φ = 0.91 while some local span values occurred at 1.02 where the maximum temperatures were seen in the cavity and exit profile. Also similar to the patterns observed with THC, NO_x suffered a sudden decrease in concentration for the fuel rich case, likely due to reduced flame size and combustion within the cavity which would reduce the effect of prompt NO_x.

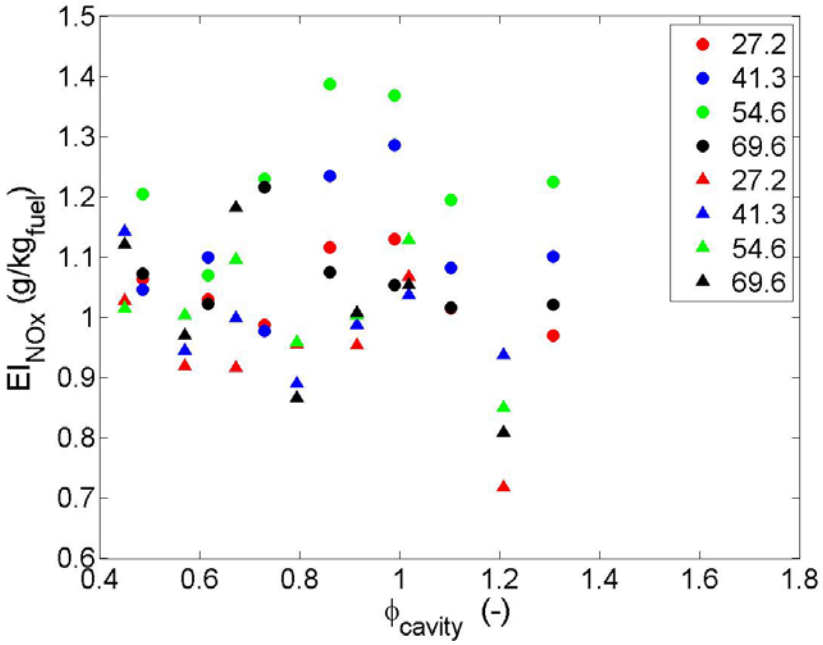

Figure 4.48: Emissions Index of NO_x with Common LLCB Geometry; UCCv3 (circles) and Compound Air Driver Cavity (triangles) at various Φ_{cavity} and Span Locations

4.3.2.3. CO Production

Carbon Monoxide production for the Compound Air Driver geometry followed almost the same identical trend as the UCCv3 geometry between the range of $\Phi = 0.62 - 1.21$. The

amount of CO produced was lower for fuel lean cases where $\Phi < 0.62$, and the amount of CO present in the exhaust gas exceeded the CAI's capability to quantify after conditions where $\Phi > 1.30$ for the Compound Air Drivers. There was no minima for the production of CO for the Compound Driver Configuration with the LLCB vane; rather it steadily increased once the equivalence ratio was greater than 0.57. When $\Phi = 0.91$ there seemed to be a gateway value where the difference between each subsequent point changes at a $\Phi = 0.91$. Since there is no minimum, there is no target value that can be aimed for with this geometry, so determining how the characteristics of the flow changed CO production is of interest to figure out how to potentially alleviate this problem, and should be the focus of further investigation.

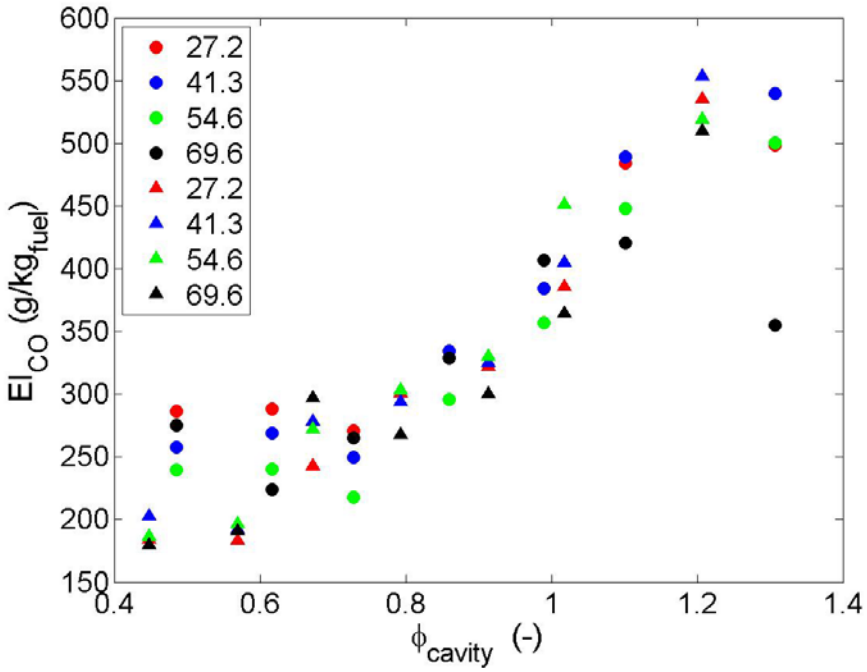

Figure 4.49: Emissions Index of CO with Common LLCB Geometry; UCCv3 (circles) and Compound Air Driver Cavity (triangles) at various Φ_{cavity} and Span Locations

4.3.2.4. Efficiency

As could be expected, the efficiency of the Compound Air Driver configuration offered slight improvement over the UCCv3 – LLCB Geometry and followed the same trend. Since the

trends for THC and NO_x shared many similarities between the two, it would make sense that these trends would carry over into the efficiency. Peak efficiency was calculated to be 93% which occurred a later equivalence ratio than the UCCv3 geometry at $\Phi_{cavity} = 0.91$. This most outboard position corresponds with the peak temperature zone at the exit plane of the Compound Air Driver geometry. The efficiency greatly suffered at the fuel rich data point taken due mostly to the sudden increase in THC. This characteristic is worrying as the UCC has previously been envisioned as an ITB, which would perform in a fuel rich, highly vitiated environment. Therefore, it was determined that even though the greatest efficiency occurred with the Compound Air Driver combustion cavity with the LLCB vane, the exit temperature profile was too concentrated in the outer diameter and too inefficient at fuel rich conditions to be considered ideal for implementation within the UCC.

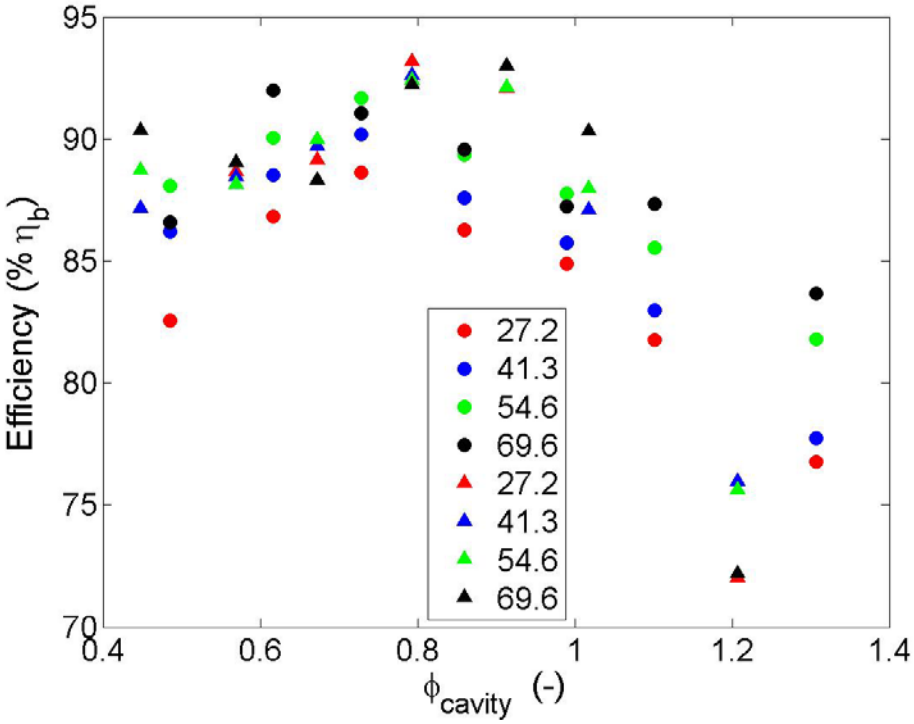

Figure 4.50: Emissions Index of CO with common LLCB Geometry and both UCCv3 (circles) and Compound Air Driver Cavity (triangles) at various Φ_{cavity} and span

4.4. Analysis of Compound Driver, RVC vane to Other Geometries

Due to the success of the Compound Air Driver in increasing efficiency and residence time, the RVC center-body was again placed within the UCC. It was hypothesized that the increased residence time and increased flame duration within the cavity would provide enough counter-balance to the losses incurred by the RVC and offer improvements with respect to the Compound Driver – LLCB geometry. In order to accomplish this, data was collected and primarily compared to the previous best case scenario: the Compound Driver – LLCB geometry. The thermocouple data confirmed that he RVC did succeed in successfully migrating the gases from the outer span. More surprising was that the even with the RVC, the residence time was sufficiently increased by the new air driver geometry that efficiency remained high. In fact the peak efficiency was 97%, the highest yet calculated. These results suggest that the ideal configuration for future research and quantification should use geometries based on these design concepts.

4.4.1. Temperature Profiles

The exit temperature profile with the RVC regained the desired peak in the mid-span region. This peak was originally located in the 60% region but transitioned to around the 50% location for all $\Phi_{cavity} > 0.86$ when there was a greater combustion within the cavity. This design also had the highest peak temperature of 1320 K any of the four geometries. All the Compound Driver – RVC geometry temperature profiles will be shown in red when comparing to other geometries.

4.4.1.1. Combustion Cavity Temperature Profile

The filament data confirmed the seen migration trend, but had increased values. The data taken within the combustion cavity for the Compound Air Driver – RVC maintained a similar profile throughout the tested equivalence ratio range.

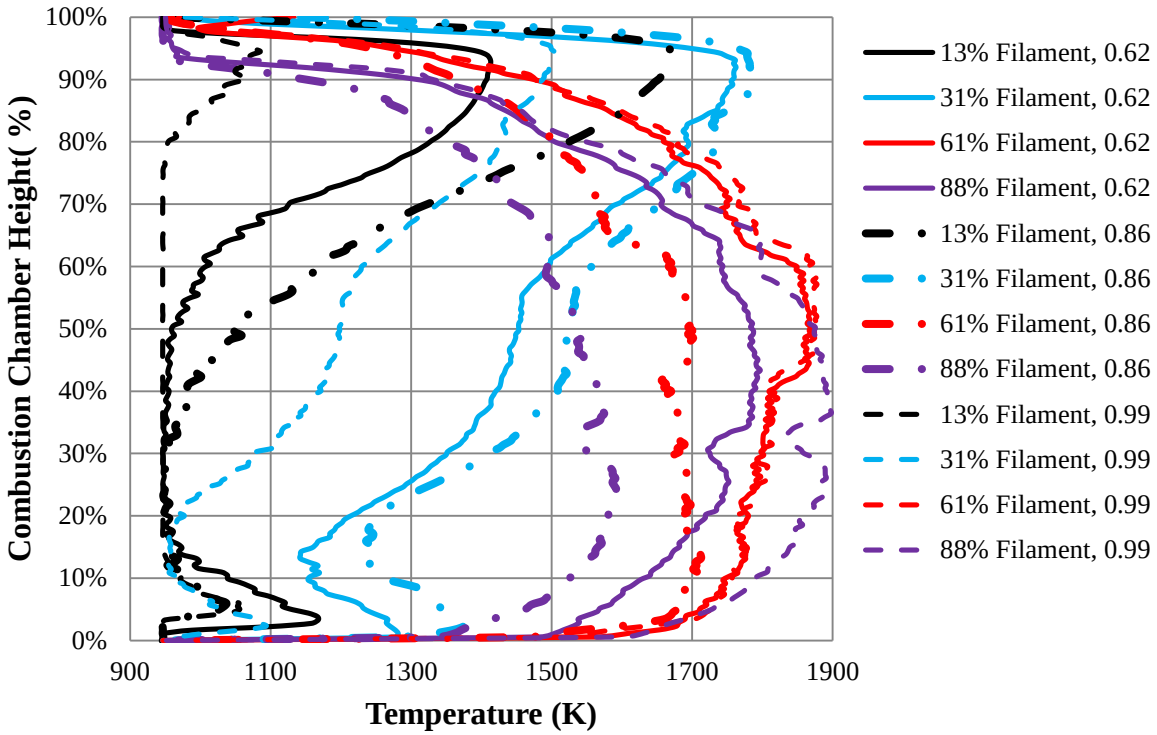

Figure 4.51 and Figure 4.52 show the progression of the thermal profile from a fuel lean condition to a fuel rich one. The near stoichiometric condition is plotted on both in order to provide a common profile to compare on both. The 13% filament maintained the dual temperature registration seen with same air driver scheme with the LLCB. The temperature on the inner filament increased until it registered across the entire filament, something that had never been accomplished before. This would suggest that at a high cavity equivalence ratio there was a change with the combustion cavity pressure that either pushed the products to the inner wall, or was reduced sufficiently to allow more gas to migrate into this region. As this transferal of combustion gases into the inner portion of the cavity was to the detriment of the heat release at

the other filament positions, it is likely the later. The peak temperatures were seen again in the lower portion of the chamber height, with the 61% having its highest temperatures from the 60% – 40% radial height positions while the 88% filament peaked between the 40% – 0% height. Furthermore, the peak temperatures occurred around a $\Phi_{cavity} = 1.00$.

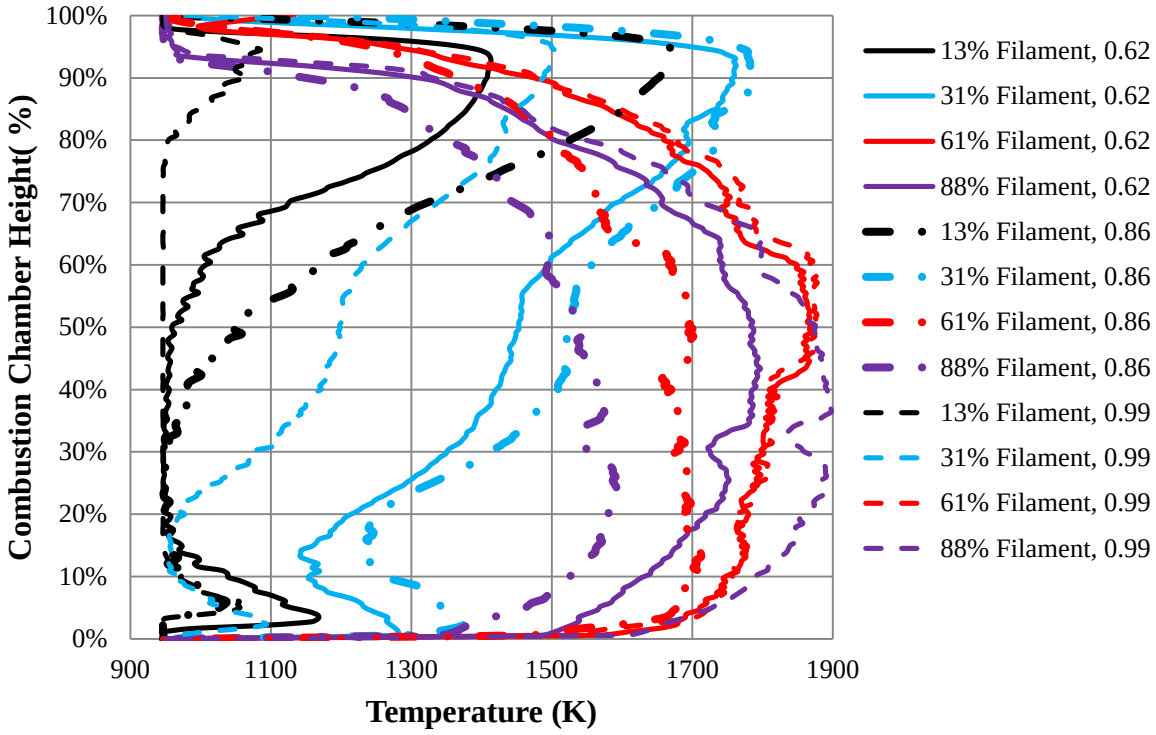

Figure 4.51: Comparison of Cavity Filament Temperature Profiles at Select Fuel Lean

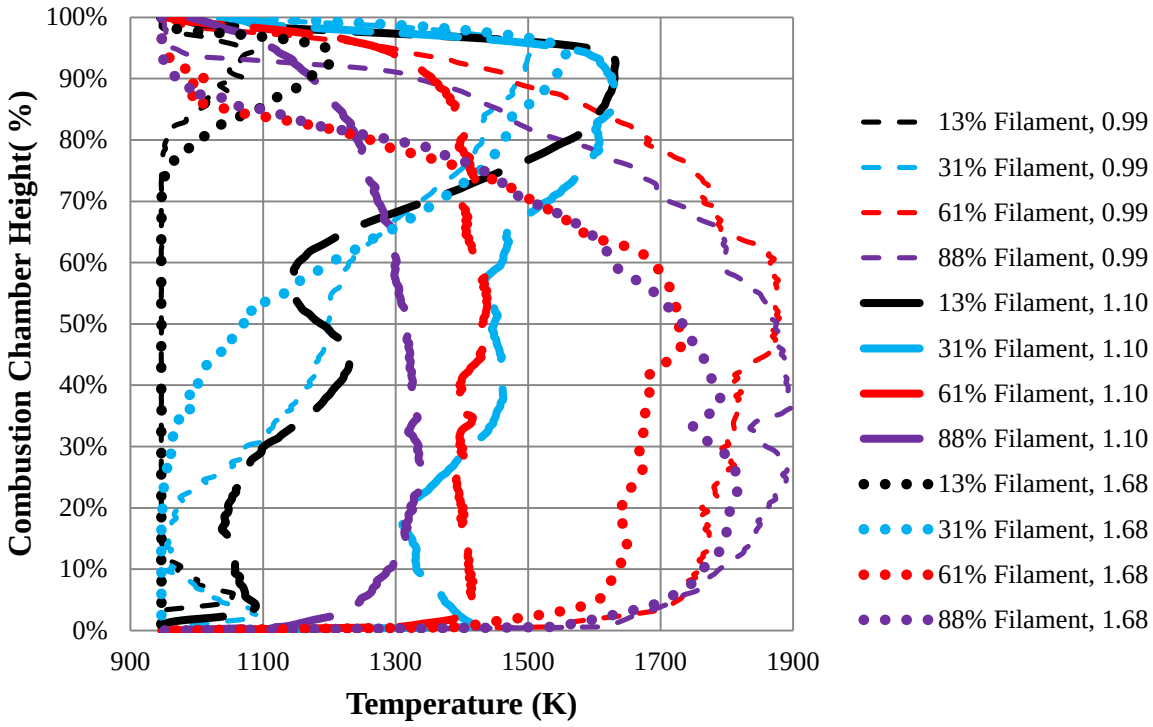

Figure 4.52: Comparison of Cavity Filament Temperature Profiles at Select Fuel Rich Conditions (number in legend) for Compound Driver – RVC Geometry

As was done with the thermocouple data, the combustion cavity temperature profile was compared at the near stoichiometric conditions The RVC data had the highest temperature at this common condition in the lower 50% span, and the highest peak temperatures as well for the both the 61% and 88% filament. This suggests that the RVC migrated the bulk of the combustion even away from the middle portion of the chamber, as the LLCB profiles had their highest temperatures in the upper 20% of the 31% filament and 61% filament. Since the combustion event (and therefore temperatures) were more radially outward for the LLCB than the RVC, it would appear that the RVC was successful in affecting the flow within the cavity and moving the combustion event down the span of not only the exit, but the primary zone as well. It is also clear from this chart that the Compound Driver was extremely increasing residence time. The UCCv3 temperature profiles all had their maximum temperatures along the 31% filament.

However this filament had cooler temperatures when the Compound Driver was introduced and both of the aft filaments read at higher temperatures across all height locations. Therefore, the combustion cavity data showed that residence time had indeed been increased due to preponderance of the hot gases into the back of the cavity and the increased temperatures recorded.

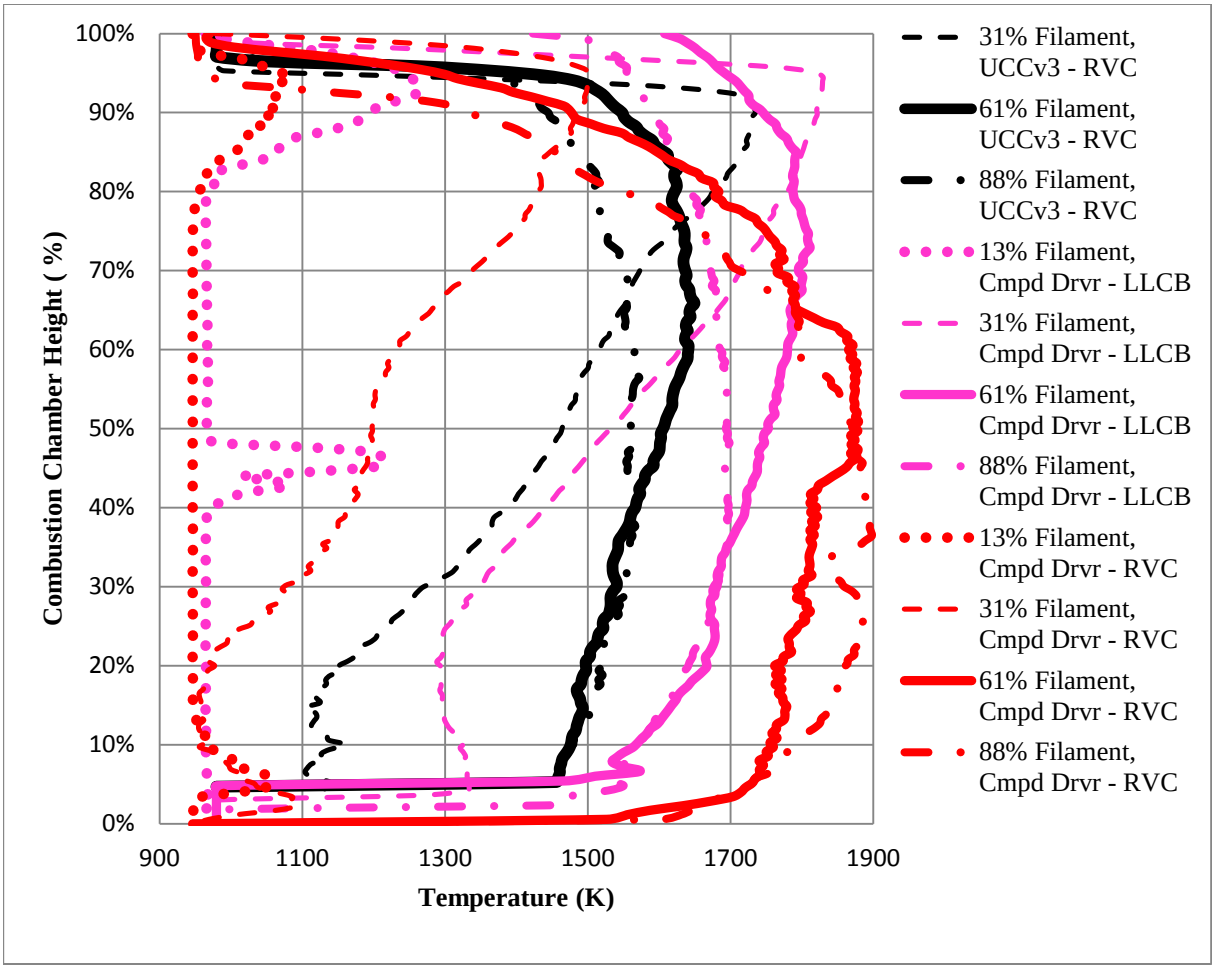

Figure 4.53: Comparison of Combustion Cavity Temperature Profiles for Three Previously Discussed Geometries at $\Phi_{cavity} \cong 1.00$

4.4.1.2. Exit Temperature Profile

The exit temperature profile with the RVC regained the desired peak in the mid-span region. This peak was originally located in the 60% region but transitioned to around the 50%

location for all $\Phi_{cavity} > 0.86$ when there was a greater combustion within the cavity. This design also had the highest peak temperature of 1320 K any of the four geometries. This was due to the high concentration of all the exhaust products being concentrated in the mid-span by the RVC and the Compound Air Driver allowing for sufficient residence time of the fuel. Also, the peak temperature occurred at equivalence ratios higher than normally expected. However, this could be due to a number of factors. One could be the chemical reactions changing the amount of air flowing into the combustion cavity and having a lower condition than calculated. Another is that this fuel condition imparted the highest g-load on the cavity, therefore increasing the turbulent mixing or Raleigh-Taylor instability sufficiently to increase combustion and heat release. In order to determine this, further investigation should be conducted on the geometry using PIV to investigate the velocity field within the cavity and the interface between the combustion cavity and core flow.

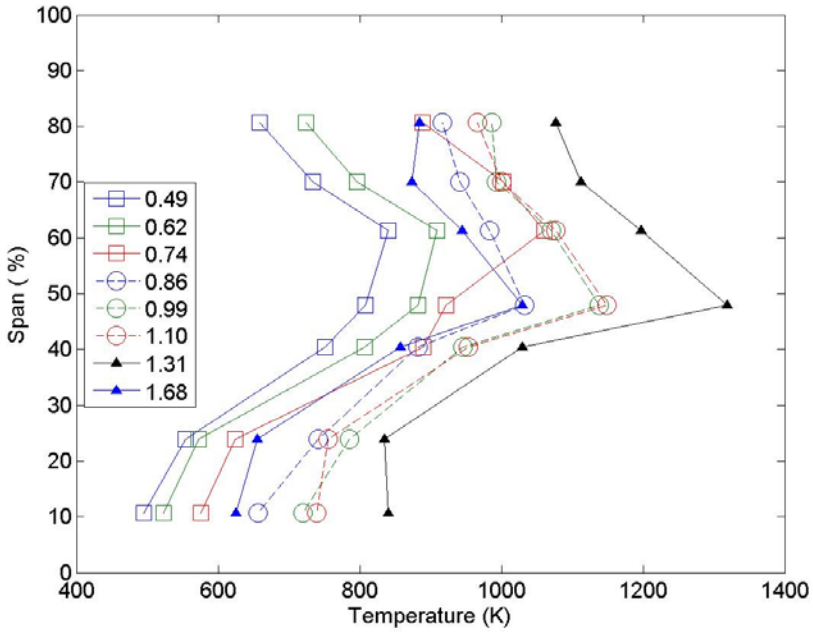

Figure 4.54: Span-Wise Exit Temperature Distribution for Select Stoichiometric Ratios for UCCv3 – RVC Geometry

With the conclusion of temperature testing, the merits of all four geometries thermal profiles could be compared. The profiles obtained using the thermocouple rake for fuel lean, stoichiometric, and fuel-rich cases are included in Figure 4.55, Figure 4.56, and Figure 4.57. In the fuel lean case, the success of the RVC funneling the heat into the mid-span region can clearly be seen in both the UCCv3 (black) and RVC data (red). Both geometries have much steeper gradients and much more focused points than the LLCB geometry. The LLCB seemed to have a flatter plateau in the mid-span region that reduced the prominence of the peak. Further, the peak temperature values for all four geometries were roughly the same, with only 100 K separating the hottest and coldest measurements. While the greatest temperature release was seen in the Compound Driver – LLCB geometry (magenta line), the Compound Driver – RVC geometry (red line) ensured that the focus of the flow was much more pronounced and decreased the temperature impacting the inner radius by 330 K and the outer radius by 70 K. This characteristic is desirable for aircraft engines as it will increase the life expectancy of the turbine rotor blades. The prominence of the peak for the three most fuel-lean cases was noted around the 61% span probe, but for all subsequent points it transitioned to the 47% span probe. Seeing if this result is repeatable and the explanation of this phenomenon should be the focus of future research. Either way, the RVC was shown to migrate the flow into the mid-span and away from the outer diameter, and provided the excellent benefit of protecting the Inner Diameter for excessive temperatures.

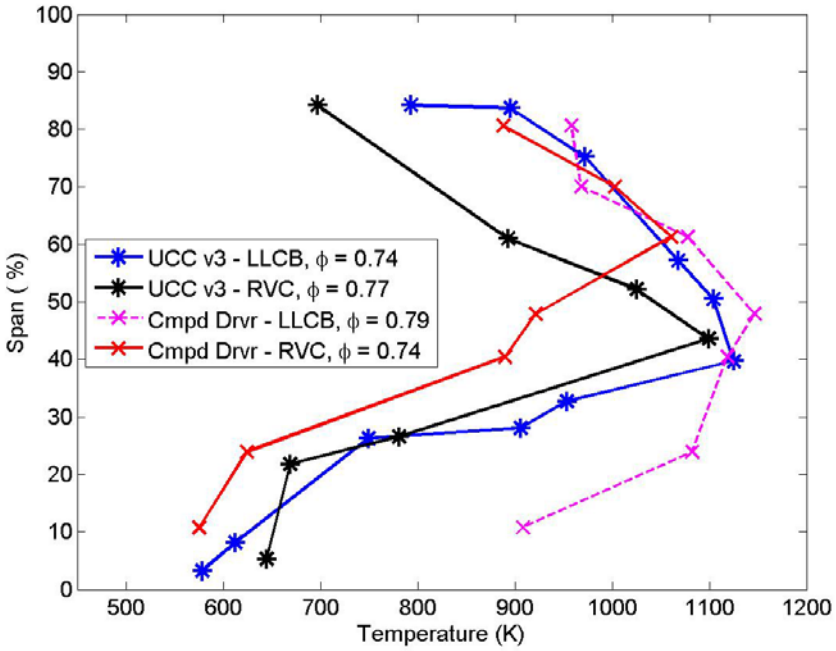

Figure 4.55: Comparison of All Four Tested Geometries' Span-Wise Exit Temperature Distribution for $\Phi_{cavity} \cong 0.75$

This trend became even more pronounced and favorable when the engine began operating near stoichiometric conditions. Figure 4.56 shows how at richer conditions the observed peak temperature for both RVC geometries occurred in 40% – 50% range, and maintained its easily discernible temperature peak. The peak temperature values for both Compound Driver Air injection schemes was lower by a minimum of 70 K, with the greatest distance coming once again at the ID location where there was a 240 K difference. This shows that the compound air drivers did increase combustion residence time so that the some of the combustion events were removed from the vane passages. This in turn improved the effectiveness of the core flow in cooling and quenching reactions, as its cool air rapidly reduced the gaseous temperature. The RVC also improved the core flows effectiveness in cooling the inner diameter flow by creating a vortex that concentrated all the reacting, hot gases in the mid-span region.

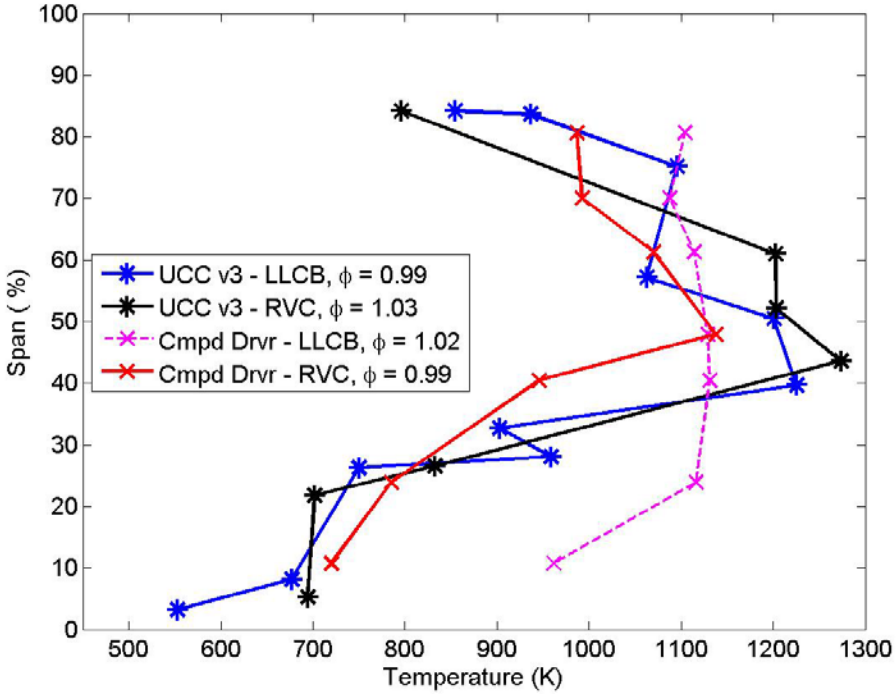

Figure 4.56: Comparison of All Four Tested Geometries' Span-Wise Exit Temperature Distribution for $\Phi_{cavity} \cong 1.00$

Finally the thermal performance of the UCC in fuel-rich conditions was plotted in Figure 4.57. As there was no high-Φ values for the Compound Driver – LLCB configuration, none appear in this chart. In this chart the peak value, as well as all the outer span values, of the Compound Driver – RVC configuration is greater than the other two. The inner span values however remain relative similar in value and pattern throughout the inner 40%. It would also appear that the interplay between the Compound Driver and the RVC yields the most effective evacuation of gaseous particles as well. Not only are the temperatures the highest, suggesting that the most combustion occurs at this point, but the peak is the most prominent for this geometry as well. This seems to suggests that the compound air drivers place the bulk of the combustion near where the RVC is able to funnel it out, leaving the rest of the core flow relatively un-heated. The Compound Air Driver – RVC temperature profile, and the associated physics that enabled it, is exactly the improvement that was desired at the beginning of this experiment.

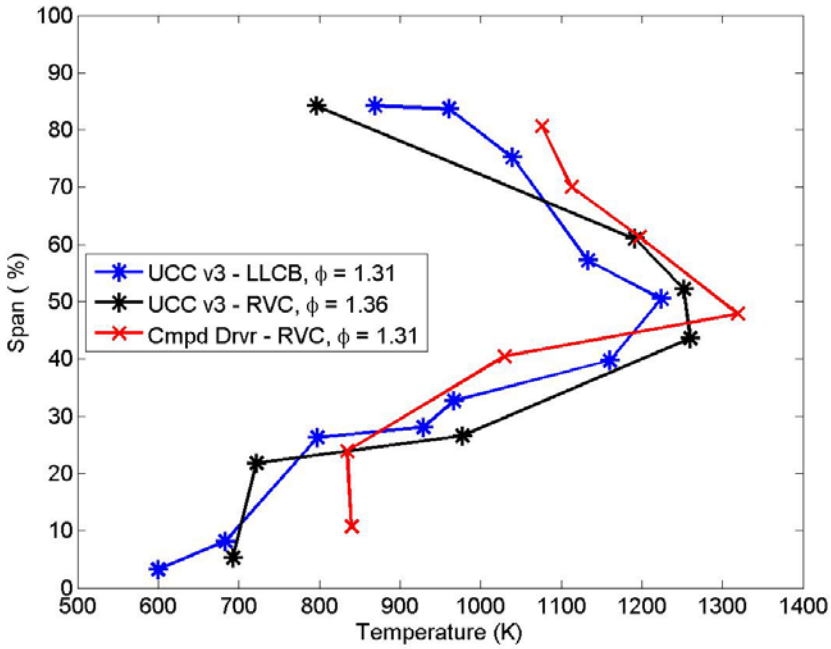

Figure 4.57: Comparison of All Three Tested Geometries' Span-Wise Exit Temperature Distribution for $\Phi_{cavity} \cong 1.35$

4.4.1.3. Filament Exit Plane Data

The filament data confirms the trend observed by the thermocouples that the peak temperature value transitions between two span locations, but it also suggests that this occurs for only fuel rich conditions and that the peak temperature locations are between 30% – 50% span locations. Figure 4.58 shows a steep increase along the outer span until the peak values are reached at the 40% span location. The inner diameter with a similarly steep slope returns to cooler temperature. The only condition where the RVC did not create a peak temperature was at $\Phi_{cavity} = 1.68$. However, since the temperature magnitude decreased to equalize with the two outer most filaments, the same temperature was observed at the other conditions. This decrease in temperature is expected with fuel-rich conditions as there is less combustion that occurs due to insufficient oxygen necessary for efficient combustion. One improvement that could be made in

this design would be to maintain the peak location, but flip the profile so that the coolest temperature was long the inner diameter as opposed to the outer diameter.

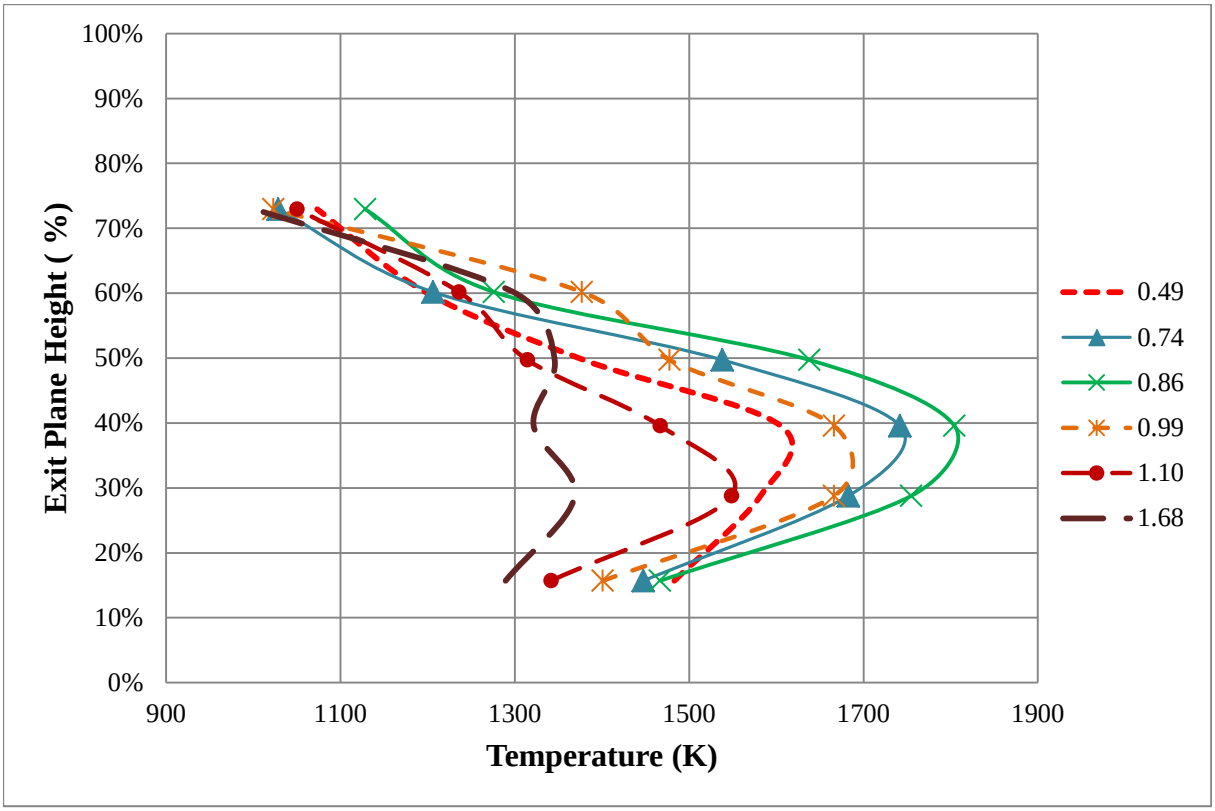

Figure 4.58: Span-Wise Exit Temperature Distribution for Select Stoichiometric Ratios for Compound Driver - RVC Geometry

However, this one improvement is a minor matter, as Figure 4.59 shows performance benefit of the Compound Driver – RVC geometry. As can clearly be seen, the filaments found that the peak was lower in the span than detected by the thermocouples, and was able to determine that the gas temperature was 500 K greater than originally measured by the thermocouple. As previously mentioned, the SABRE-Rig experiments performed by Goss [33] showed corrections of approximately 250 K when the thermocouples were placed correctly. This larger error is likely a confluence of factors reducing the thermocouple value further. First, the large diameter of the UCC probes increases the conduction error between the shielded weld for

the thermocouple and the probe tip. Secondly, the probes were very tightly packed within this space, which will distort the flow and reduce the probes' temperature measurements. Thirdly, these probes were metallic across their entire span, unlike the SABRE-Rig set-up which had a ceramic coating on the exterior that also lowered the conduction losses. When considering these additional sources of error, and noting that the probe location may have drifted during the data collection, the large difference is reasonable, and reinforces the belief that the TFP data is more accurate. The RVC (black and red lines) migrated the temperature peak in both combustion cavities to the 30-50% span region, as they were designed to do. The addition of the compound driver increased the residence time within the combustion cavity, which proved sufficient to alleviate the lost efficiency with the simpler UCCv3 driver scheme, and produced the most thermally beneficial geometry. As a reminder, the error for each of these points is ±38 K.

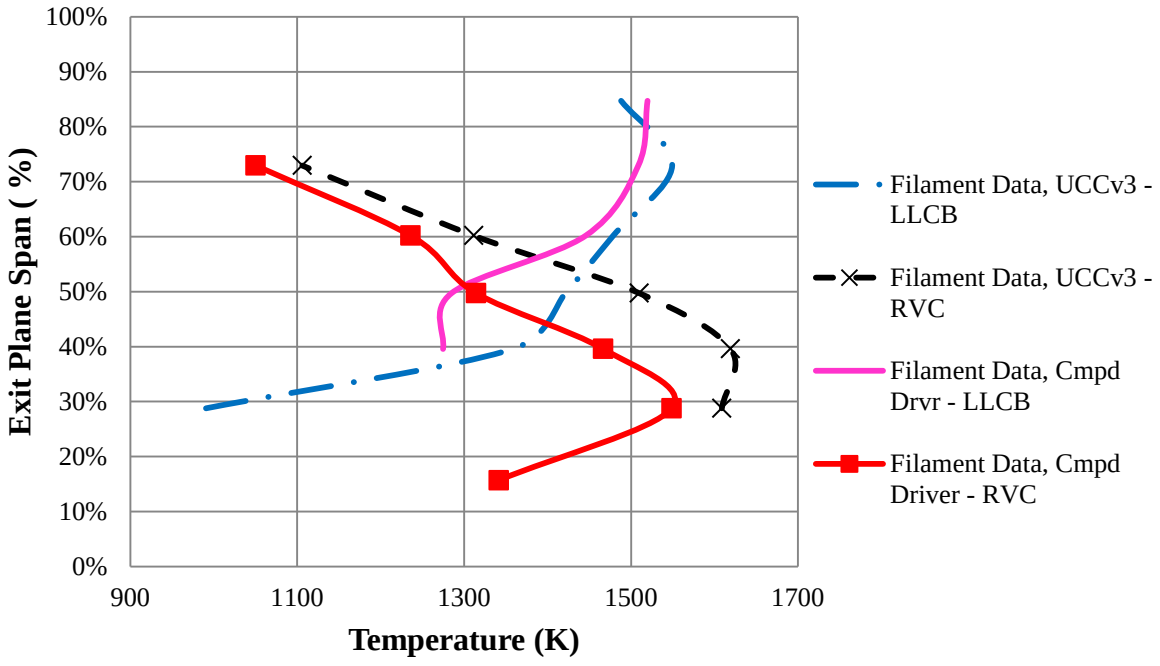

Figure 4.59: Comparison of Exit Filament Temperature Profiles at $\Phi_{cavity} \cong 1.15$ with the Compound Air Driver Cavity Common and Center-Bodies Varied

4.4.1.4. Profile Factor

The addition of the RVC center-body into the Compound Driver geometry was sufficient to improve the shape of the local profile factor. Figure 4.60 shows a consistent profile across all operating conditions with peak divergence occurring between the desired filament positions of 39.6% and 49.7%. Furthermore, the profile factor is low at the inner diameter and outer diameter, with a peak calculated divergence of -0.209 at the 84.7% location. The mid-span peak divergence value was maximized around a cavity equivalence ratio of 1.10, with the local profile factor being found as 0.187 at this point.

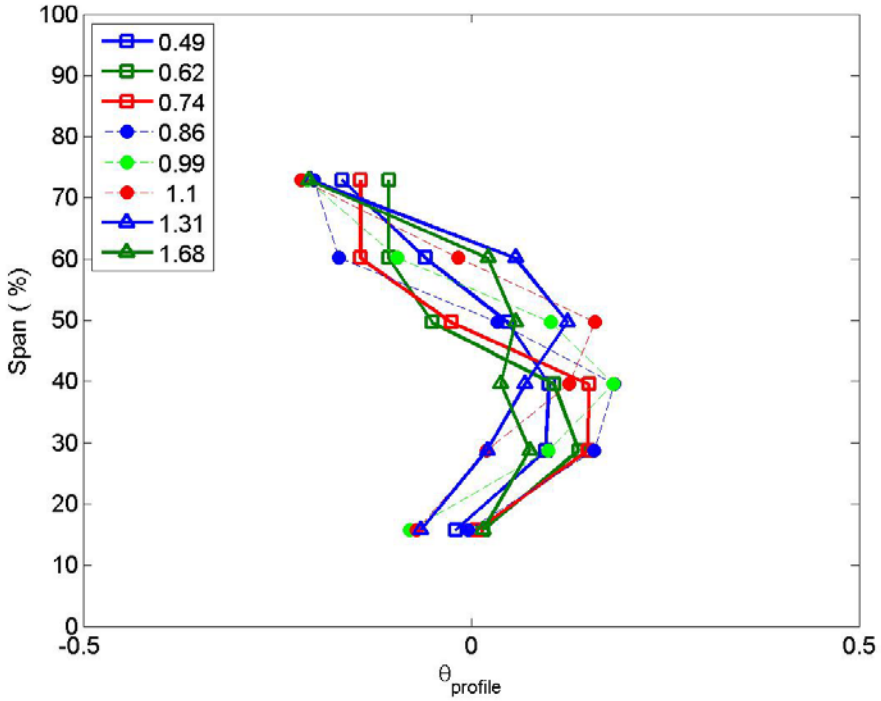

Figure 4.60: Local Profile Factor for All Equivalence Ratios, Compound Driver – RVC

Finally, a comparison between all four profile factors was made at a representative fuel condition. The conditions chosen for Figure 4.61 were those around the stoichiometric condition as these have the ideal conditions for combustion and because they had the smallest difference between the four values. Again, the divergence from the mean and the consistency of the profile

factor across operating conditions determined desirability. Though only one case is shown, the Compound Driver – RVC configuration routinely had the best profile factor at all equivalence ratios. Figure 4.61 shows the profile factor peak is greatest for this geometry, and it occurs at the lowest filament span location (39.6%). It also has the greatest negative divergence at the outer diameter, indicating that it successfully migrated the greatest amount of hot cavity gases. This chart also shows how little gas migration the UCCv3 – LLCB geometry accomplished; it had the lowest inner diameter value suggesting that this configuration had almost no migration into the lower 30% of the span. While this is advantageous for the inner diameter, this profile would still decrease the lifecycle of the turbines by growing the turbine blade tips.

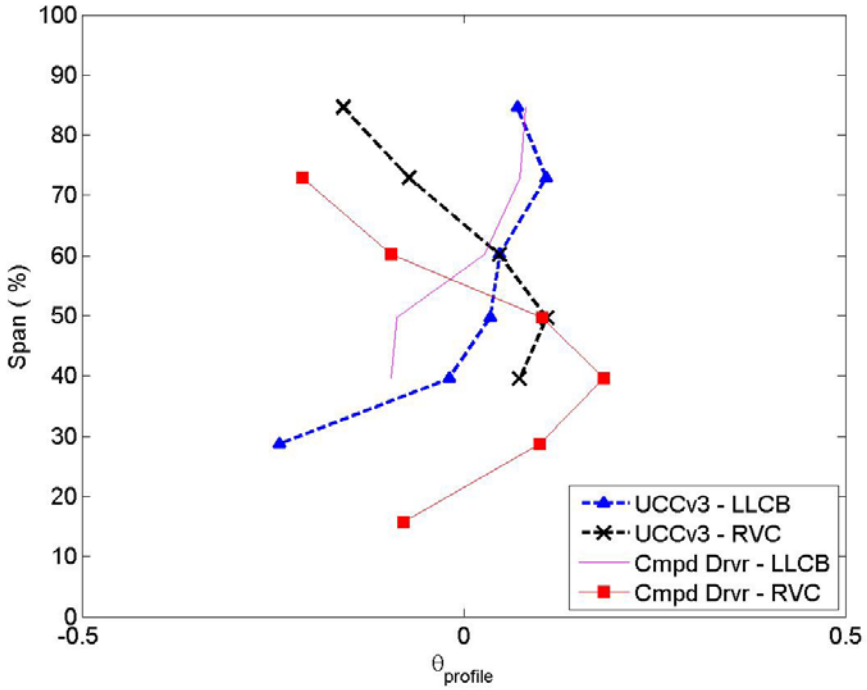

Figure 4.61: Local Profile Factor Comparisons for All Geometries at $\Phi_{cavity} \cong 1.0$

4.4.2. Emissions Trends for RVC

As was seen in the previous radial vane cavity, the concentration of pollutant emissions greatly increased with the introduction of the RVC. In fact, the emissions were so high that the

geometry exceeded the CAI's capabilities at the lowest recorded equivalence ratio yet. At $\Phi = 1.02$, which occurs at a fuel set point at 6.48 kg_{air}/min and 59 SLPM of propane, the measured CO was approximately at 1.00%. As this is the maximum range of the CAI analyzer, progressing to 60 SLPM of propane pushed the concentration reading over the CO maximum reading and therefore no more emissions measurements were possible with this method. Because of this, none of the EIs could be calculated for any of the fuel-rich conditions and thus were omitted from all the subsequent charts.

Offsetting this increased emissions however was also the largest amount of combustion to date. The first sign of this increased combustion was the reduction of THC in the exhaust, with the values routinely being seen at 100-300 ppm across multiple conditions. Previously this low concentration had only noted at the point of maximum efficiency and at one probe location, but with the Compound Driver – RVC configuration this was seen at multiple ports across multiple operating conditions. The increase in combusted propane also increased the amount of carbon radicals available, which contributed to the highest average CO_2 and CO concentration readings for this geometry. Again, EI_{CO} was reduced due to the increase in CO_2 offsetting the slight increase in CO production. The average concentration of CO_2 was the highest measured of any of the four geometries, with the two middle probe ports seeing up to 300% increases in CO_2. For perspective, while the average amount of CO_2 produced by the baseline UCCv3 – LLCB configuration was 22,800 ppm and 15,400 ppm for the UCCv3 – RVC, the average value was 28,000 ppm for the Compound Driver – RVC configuration. As CO_2 only forms when combustion is complete, and there is only normally only 3.2 ppm in ambient air, these results suggest that the RVC increased combustion throughout the entire UCC while also migrating the flow into the mid-span region.

This increase in complete combustion helped mitigate the effect of losses due to incomplete CO formation and the effect was accounted for by lower EI values for CO and NOx. As Figure 4.62 shows, the RVC (diamonds) showed the same, non-correlated relation between CO and NOx production as the LLCB geometries. Also, the values of EI for CO and NO_x were of the same order of magnitude as for both air driver schemes with the LLCB vane. The NOx values tended to be a little higher however than the Compound Driver – LLCB configuration suggesting that the vortex caused by the RVC again increased the amount of NO_x produced by the UCC. Also, by comparing the Compound Driver – RVC geometry to the UCCv3 – RVC geometry, the effect of the increased CO_2 production with the former configuration could clearly be seen. The concentrations of NO_x and CO were close when the vane geometry was held constant and the two air driver configurations were altered. The increased residence time of the Compound Driver enabled more complete combustion and this in turn lowered emissions index as more fuel had been combusted. Also, the improved CAI collection procedures were implemented for both Compound Driver geometries and the new error bar ranges are shown on the specific species graphs for the stoichiometric conditions as an example condition.

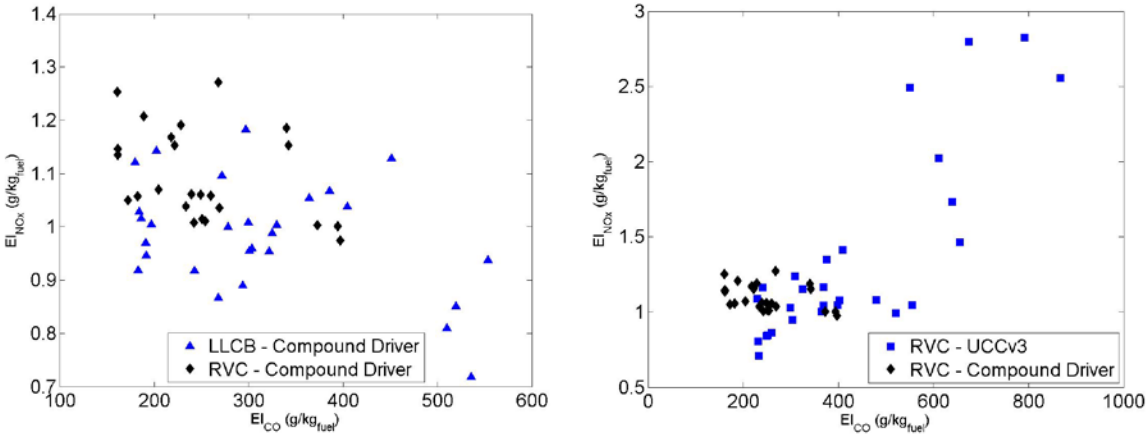

Figure 4.62: Emissions Comparison between Compound Air Driver – RVC configuration and both the Compound Driver – LLCB (left) and UCCv3 – RVC geometries (right)

4.4.2.1. THC Production

Figure 4.63 continues to demonstrate how this configuration was the most efficient of the four. The amount of THC measured was consistently lower than the Compound Driver – LLCB, which had previously been the best design. Even when CO exceeded the collection capability of the CAI, THC was still less; the measured concentrations at the points where CO was exceeded were recorded at 4,600 ppm, 4,300 ppm, 3,800 ppm, and 3100 ppm, while the Compound Driver – LLCB had values of 5800 ppm, 4600 ppm, 5200 ppm, 6300 ppm for the 27.2%, 41.3%, 54.6% and 69.7% span locations (respectively) at the same Φ_{cavity}. The nadir shifted to a more lean condition around 0.86, with the 69.6% and 54.6% probe location alternating the distinction for lowest EI. The most unburned fuel could be found in the 27.2% probe location, again suggesting that the least amount of burnt particles is transferring to the inner most part of the span, which is desired in order to prevent high temperature from striking the root of the turbine rotor.

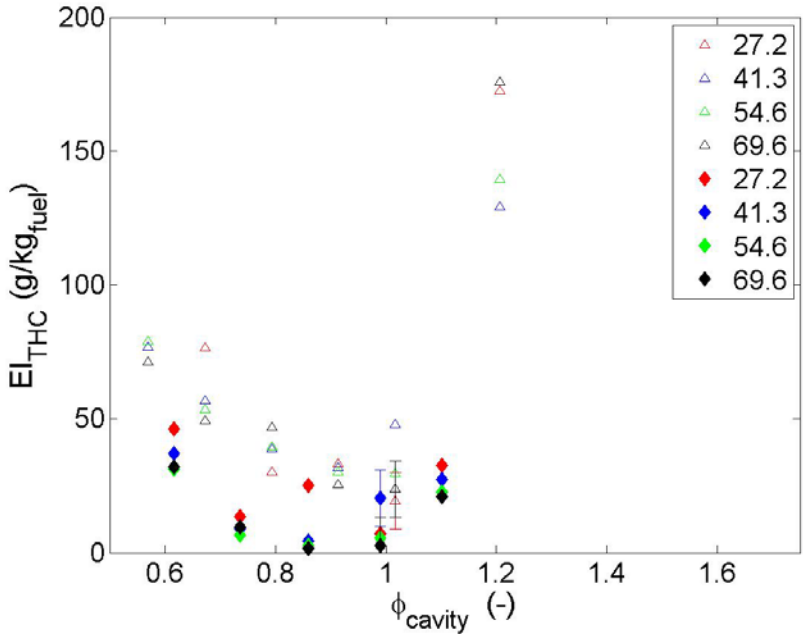

Figure 4.63: Emissions Index of THC for the Compound Air Driver Geometry; LLCB (triangle) and RVC (diamond) Center-Bodies was considered at various Φ_{cavity} (x-axis) and % Span Locations (in legend)

4.4.2.2. NOx Production

NO_x production for the Compound Air Driver – RVC configuration again peaked near the most stoichiometric conditions, and these peak values were higher than any of the values previously seen with the LLCB, though not the UCCv3 – RVC. However, as previously discussed, the EI_{NOx} for the Compound Air Driver was substantially lower with the RVC than with the UCCv3 driver scheme. In fact, at leaner conditions, the RVC emitted less NOx per kg of propane than the LLCB geometry, suggesting that this increase was probably a byproduct of the increased amount of combustion and radicals present, rather than some intrinsic change to the characteristics of the flow field. Furthermore, the quenching effect which had previously caused the high problems with NO_x in the mid-span region with the UCCv3 air driver configuration have disappeared with the compound driver. Instead, the position with the worst NOx performance is the most radially inward probe location, with an equivalent magnitude to the LLCB configuration. This low NO_x production rate suggests that the NO_x output for this region is now due to thermal conditions as the temperature is high enough to activate the Zeldovich mechanism. This also suggests that the residence time within the cavity is now sufficient that the quenching effect of the core flow is introduced at the desired point, and not so early that the reactions are frozen before they can complete. The CFD of the Cottle model [50] supports this as the fuel residence time is increased and the velocity contours hold the flow in the middle of the chamber now as opposed to the UCCv3, which has the velocity contours route the flow closer to the cavity-vane (primary zone–intermediate zone) interface.

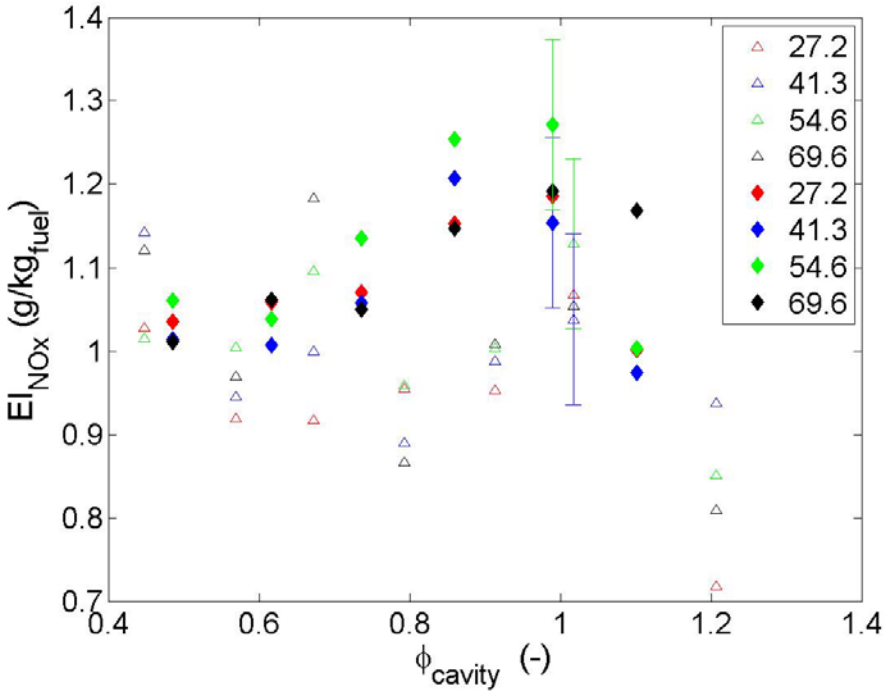

Figure 4.64: Emissions Index of NO_x for the Compound Air Driver Geometry; LLCB (triangle) and RVC (diamond) Center-Bodies was considered at various Φ_{cavity} (x-axis) and % Span Locations (in legend)

4.4.2.3. CO Production

Holding with the trends seen with THC, the emissions index of CO was reduced for all positions when compared to the previous three cases. Figure 4.65 shows the comparison of the Compound Driver – RVC cavity to the Compound Driver – LLCB design, but as the later was shown previously the most efficient, the same improvements exist between this fourth geometry and the other three. The CO production rate again resembles a more parabolic shape than the LLCB geometry, but this may be due to the fact that no measurements were available after a $\Phi_{cavity} = 1.10$. It should be noted however that the CAI maximum span value was almost achieved by this point, so the measured concentrations were already very high while achieving this low EI. The minima for all the points also occur around 0.86, just like with THC. It can be expected that the maximum efficiency will occur here.

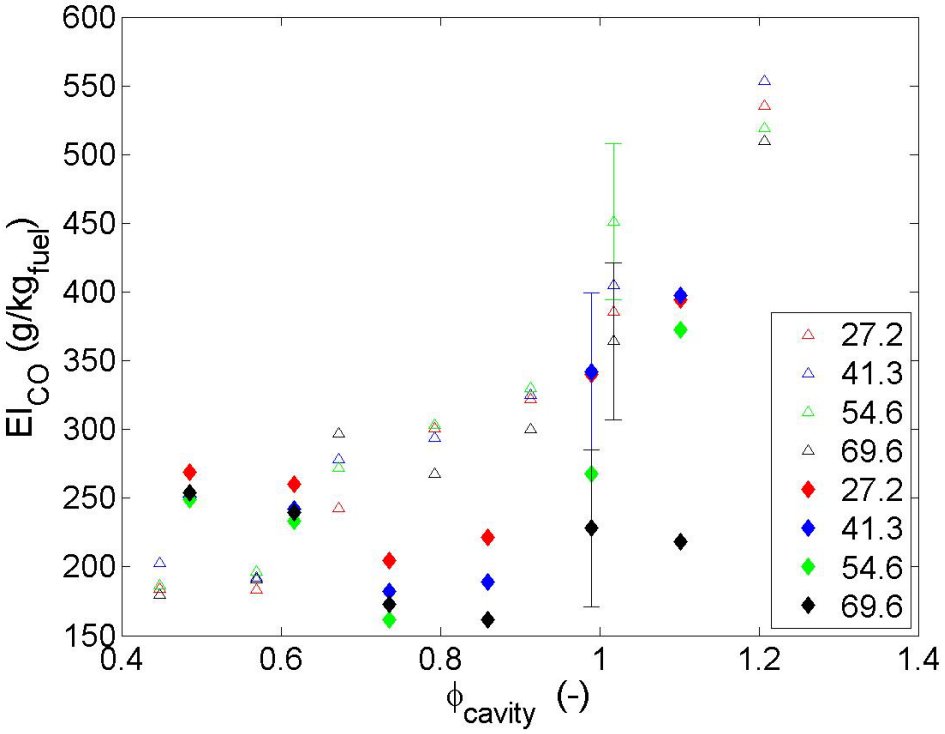

Figure 4.65: Emissions Index of CO for the Compound Air Driver Geometry; LLCB (triangle) and RVC (diamond) Center-Bodies was considered at various Φ_{cavity} (x-axis) and % Span Locations (in legend)

4.4.2.4. Efficiency

Finally, it was shown that with the reduction in EI that the Compound Air Driver – RVC configuration created, the efficiencies measured were also the highest. Figure 4.66 depicts how the RVC cavity created sufficient back pressure and optimized the residence time to produce a peak efficiency value of 97% at atmospheric conditions. This value occurred at both the mid span region where the maximum temperature was and in the outer span, suggesting that the combustion efficiency was very high for over half span. The lowest span efficiency values occurred at the lowest temperature region as well at the 27.2% span but were still no less than 85.6%, which is equivalent to some of the peak points seen in the baseline UCCv3 – LLCB configuration. Also, the efficiency values for the 69.6% span probe and the 54.6% probe are almost equal across most operating conditions. Assuming the efficiency across the span

resembles a curve with a single maximum value, this trend suggests that the peak efficiency actually occurs somewhere in between these two points. Finally, there is no sudden drop off in efficiency for this geometry during fuel rich conditions, although this phenomenon could be outside the range of the collectable data.

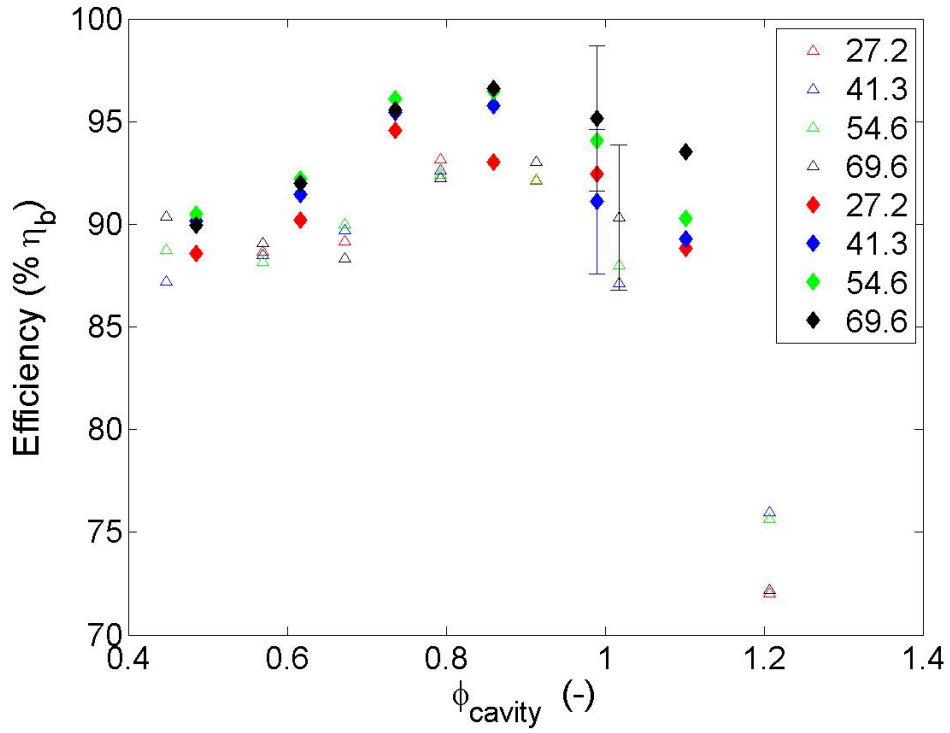

Figure 4.66: Efficiency for the Compound Air Driver Geometry; LLCB (triangle) and RVC (diamond) Center-Bodies was considered at various Φ_{cavity} (x-axis) and % Span Locations (in legend)

4.5. Temperature Conclusion: Thermocouple Exit Pattern Factor

Concluding the temperature based analysis is a categorization on the effect of changing the geometry with respect to the pattern factor. According to Lefebrve and Ballal [14], the pattern factor shows the maximum deviation of a combustor's exhaust from its ideal, uniform exit temperature and the value actually seen. Greater deviations lead to larger variations in the heat load to the turbine section, but if the deviation is not great enough then the temperature distribution will cause increased loads on the critical sections of the turbine blade, specifically

the inner radius and the tip. The pattern factors for the newer AFIT UCC combustion cavity featuring both the LLCB and RVC can be seen in Table 4.2. All configurations utilized the same inlet air and fuel mass flow, and the equivalence ratios altered based on the pressure distributions recorded in Table 4.1.

Table 4.2: Comparisons of Pattern Factors and Alternate Center-Body Vane and Air Driver Designs

Fuel Setting (SLPM)	UCCv3 - LLCB	UCCv3 - RVC	Compound Driver - LLCB	Compound Driver - RVC
26	0.512	0.281	0.235	0.400
33	0.515	0.327	0.210	0.385
39.4	0.428	0.404	0.209	0.381
46	0.504	0.384	0.163	0.263
53	0.472	0.380	0.109	0.300
59	0.338	0.391	0.052	0.309
70	0.464	0.427		0.351
90		0.424		0.381

From this table, it is again easy to see how the compound driver has reduced the temperature gradients between span-wise locations. The LLCB within the Compound Air Driver arrangement is at least a factor of two less than its corresponding values for the straight hole drivers. The RVC also showed lower magnitudes for all Φ_{cavity} greater than 0.74. This was likely due to the overall decreased temperatures seen within the UCC with the Compound Air Driver configuration. In other words, if there is a lower peak temperature then the difference between the peak and all other temperatures, to include the mean, will also be lower. Also of note is that with the combustion volume within the cavity increased, the profile again resembled the profile factor seen by Damele *et al.* [37], especially at high conditions. Only with the RVC was the profile factor above 0.25, and even though the peak was higher up on the span it still created the desired increase in profile magnitude.

V. Conclusions

This experiment successfully quantified the thermal effects and efficiency changes of varying the geometry of multiple components of the combustion chamber within the AFIT UCC. The hybrid-vane geometry and the combustion chamber air driver configuration were altered with their measured exit temperature profiles compared against each other as well as previous configurations to determine if any improvement occurred. The effect of varying the hybrid-vane geometry and combustion air driver injection angle was also quantified using emissions and efficiency measured at the exit plane to ensure the most efficient design was considered. The compound driver increased residence time, resulting in higher efficiency values and lower temperature values at the exit plane. However, this also placed more of the hot exhaust gases in the upper span region, and the Radial Vane Cavity (RVC), which had previously been highly ineffective with just the tangential air driver, successfully migrated these gases to the mid-span while increasing efficiency.

5.1. UCCv3 – LLCB

The first investigation compared the UCCv2 geometry to the enlarged UCCv3 combustion cavity. The new cavity utilized a full 360° ring of air driver holes angled at 55° tangential to the bulk flow. The cavity height was increased from 5.2 cm as used previously by Damele [47] to 6.4 cm for these experiments. Both configurations utilized the smooth LLCB vane constructed by Wilson and Polanka[5]. This geometry experienced a peak thermocouple temperature value of 1229 K at the 41% span probe position and peak temperature value of 1600 K at the 73% filament location. The thin filament pyrometry (TFP) proved to be much more accurate in both determining temperature profile shape and temperature magnitude. The exit temperature profile observed was greater in magnitude than Damele's [47] data at a comparable

equivalence ratio An accurate baseline of the emissions of the AFIT UCC was determined for THC, NOx, and CO. By also acquiring the CO_2 at these conditions, Emission Indices were computed for the UCC at different span locations and run conditions. From this the efficiency range of each geometry could be determined. The efficiency range for the UCCv3 – LLCB was 76.7% – 93.8%, with the lows occurring in the inner span region (27.2%) and the peaks occurring at the outer span locations ($\geq$ 54.7% locations). This UCCv3 – LLCB geometry then became the baseline case for the other comparisons in this thesis.

5.2. Impact of Adding a Radial Vane Cavity to the Hybrid Vane

Next the UCCv3 – RVC geometry was presented as a viable option to migrate the high temperatures seen in the outer span in previous test rigs [37], as well as the UCCv3 – LLCB configuration. It utilized the same air driver angle scheme, but introduced a cutout directly under the aft 50% of the combustion cavity that turned the flow into the core. This sweep was used to reduce hot spots and pressure losses. This geometry experienced a peak thermocouple temperature value of 1324 K at the 43.6% span probe position and peak temperature value of 1629 K at the 39.6% filament location. Here the thermocouple data began to exhibit the same patterns as the TFP data, though still much lower in magnitude. The average efficiencies for the RVC were lower than the LLCB, and the efficiency range for the UCCv3 – RVC was found to be between 69.0% and 94.26%. The lows occurred at the outer- and inner-span locations, or where the combustion products had not been funneled by the RVC.

5.3. Impact of Compound Angled Holes on Cavity Combustion

The second major change made to the combustion cavity was the alteration of the air driver scheme on the front plate of the UCC. These holes maintained the 55° tangential angle but added a radial angle of 10° so that the air was injected radially upwards towards the fuel

injectors. The intent was to increase mixing between the air and fuel and begin the combustion process radially higher in the circumferential cavity. This geometry experienced the most constant temperature profile and cooler temperatures than the straight driver UCCv3 configuration at the exit plane. A peak thermocouple temperature of 1147 K at the 48.0% span probe position and peak temperature value of 1520 K at the 84.7% filament location were recorded. The efficiency between the UCCv3 and the Compound Driver remained relatively constant, with an observed range of 72.0% – 93.2%, though the difference in efficiencies at different span locations was reduced when compared to the other two geometries.

5.4. Compound Driver – RVC

Finally, the hybrid vane with the RVC cavity was placed behind the Compound Driver air injection scheme to understand the combined effects. The goal was to discover if the RVC could alleviate the flat profile noted in the Compound Driver – LLCB configuration. This geometry yielded the highest peak temperatures and highest efficiencies, showing that it fulfilled its design goals of high efficiency and favorable profiles. The peak thermocouple temperature observed by the thermocouples was 1320 K at the 47.9% span probe position, while TFP found 1652 K at the 39.6% filament location. The efficiency range for this geometry was the highest due to the most fuel being burned, and was found to be between 88.5% – 96.6%. These peak values were found by the 54.6% probe and 69.6% probe, which suggests that the true peak occurs between these two points. The only place where adverse performance was noted was at richer fuel conditions, which might make this design unfavorable for highly vitiated airfoils. It is therefore suggested that this geometry, or a design similar to it, be used as the baseline for future fuel lean to stoichiometric fuel-to-air ratio experiments as it possess both the thermal profile and high efficiency desired from modern jet combustors.

5.5. Future Research

As a result of this research two major areas of future effort are required. These can be split into future experiments and lab improvements. The former resulted in the inability to repeat data points to reduce the repeatability error of measurements by taking more independent samples over a wider range of values. The latter suggestions focus on ways to improve the ventilation system and standardize the temperature measurement locations for the thermocouple rake. Some of these facility improvements are more important and should be completed as soon as practical in order to ease future test efforts. This section seeks to outline the required changes and potential ways to expand the research efforts of this work.

5.5.1. Facility Improvements

The first thing that must be addressed is improving the ventilation of the COAL Lab around the UCC. During the course of these experiments, is was noted that the existing ventilation network could not remove sufficient amounts of the sulfur-dioxide smell additive. This caused the smell to "leak" into the hallways and adjoining storage rooms. In order to prevent this, a new exhaust shed has been purposed. Once built, the enclosure should capture all the emissions out of the rig and successfully vent them to the roof. The enclosure however must be able to have sufficient room and sufficient visual access to allow LASER diagnostic beams to enter the rig and high-resolution optical devices to capture the images. Furthermore, the exhaust gases that are spilling out of the UCC are above 1300 K so a medium to high-temperature material must be used for all walls. It would also be advisable to increase the roof clearance of the exhaust system on the roof so the gas is more effectively blown away.

Another improvement to the UCC test rig would be the construction of a temperature rake and mounting strut to the test rig stand. Such a device would set the thermocouples right at

the exit plane at the same channel height position and same span-wise position for each test. This would greatly reduce the time needed to place the probes in the correct position and ensure accurate readings. It would also allow for the much easier tracking of thermocouple signals to the LabView Data Acquisition software. Past efforts have needed to keep a "Rosetta stone" key for which channels were which probes, and during reconfigurations of the UCC, these have sometimes altered. The probe would allow for all seven channels to constantly be dedicated to this device and purpose, and allow for quicker post processing.

Finally, efforts should be enacted to improve pitot-static and total pressure probe access into the diffuser section to ensure accurate measurement of the mass flow splits. Currently the holes drilled into the diffuser can only accommodate 1/16 inch metal tube that must be bent into place after installation. Due to the compact nature of the diffuser core and cavity passages, this is very difficult and results in crimping the lines. Also, pitot-static probes cannot currently be installed because they are pre-bent and cannot be altered, lest they crimp the collection tubes and distort the data. For this reason, it is not currently possible to collect information about the complex velocity profile within the diffuser cavity passage. By expanding the clearance, these measurements might become possible in future research.

5.5.2. Future Experiment Ideas

The first round of additional tests includes emissions and filament tests at lower and higher air flow conditions. This would determine if the profile factors seen were consistent across multiple air inlet conditions and fuel settings. This would also help determine if there was an optimal air inlet point for the UCC, and if the core-to-cavity split altered with the air setting used. However, in order to go to higher air and fuel settings, the emissions enclosure would need

to be assembled first. Also, for accurate pressure data the diffuser should be re-instrumented first.

Secondly, several different vane geometries prototypes were created during this thesis. While some are similar to the single modification made to the LLCB, others have increased complexity that incorporate channels and passages throughout the entire length of the vane. Therefore, it would be advantageous to first computationally determine which complex geometries show promise in acting as flow control devices for the entrainment of hot gas into the mid-span region. Then, the efficiency of these models could also be determined using the same combustion scheme. Some examples include the crescent hybrid vane, or potentially incorporating an air cooling scheme into the hybrid vane that would allow for quicker quenching of the flow within the core flow.

Lastly, PIV experiments should be done with all four geometries at the same test conditions run for this thesis. This would aid in understanding the velocity fields and flow migration within the combustion cavity. It could help explain the peak variance seen with the Compound Air Driver – RVC data, as well as prove that the residence time had increased.

Appendix A: Linearity Study of CAI CO_2 Span

The below figure shows the results of the linearity study performed on the CAI Emissions Analyzer. It was assumed that the CO_2 Analyzer output would behave similarly as all other emissions readouts. The published value for this error is 1% of maximum span, which for this species and span setting was 20.00%. Six point were taken with three gases, one each at zero, 4.75% and 9.75%, which are the actual concentrations of the gases. In order to increase the number of points sampled, the span was deliberately skewed away from the known values to a reading of 2.5%, 6.0% and 7.5%. The measured output in mA was then compared to the CO_2 readout on the CAI. From this, a linear trend line was drawn, and shown to be perfectly correlated (R^2 = 1.0). Because of this, it was proven that the relationship between the display readout and the transmitted value to LabView were linear and a simple, 2 point correlation with the line could be used for all subsequent daily calibrations.

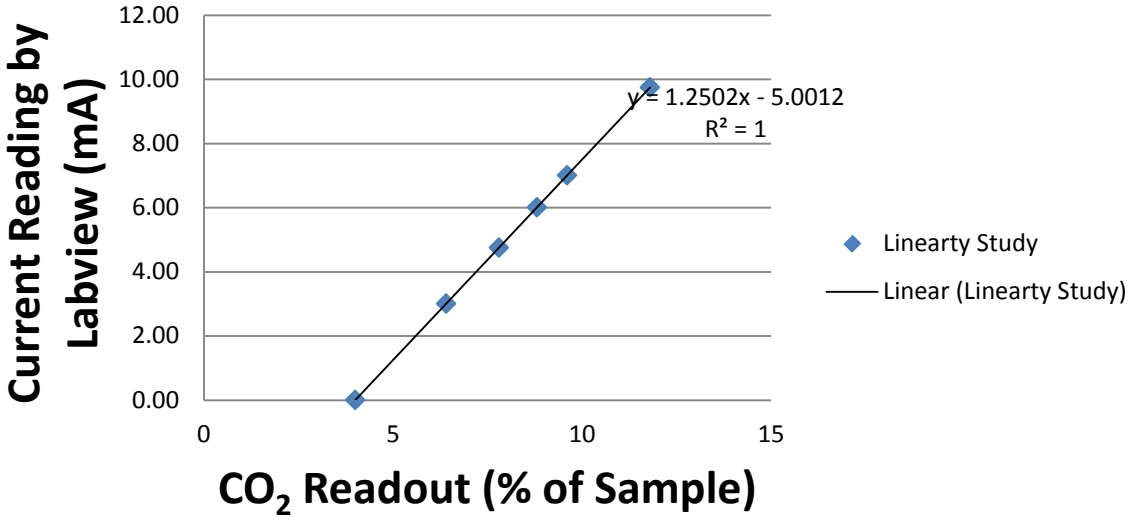

Figure A. 1: CO_2 Linearity Study

Appendix B: CAI Maintenance Procedures and Operating Procedures

Note: these procedures use some photographs, information and other information were taken from Matthew Conrad's Thesis [56]. A copy of the new procedures has been included in the CAI Procedure Continuity Binder.

The operating ranges of the AFIT COAL Lab California Analytic Instruments (CAI) emissions analyzer were re-investigated and found to diverge from previously noted ranges. The table below has the updated maximum values for each range, as well as the normal ranges where values were taken in these experiments were highlighted to allow for future use. The minimum value for all ranges are zero (0), however the higher the upper span value, the greater the error due to maximum span and the less precise the mA readout will be during post-processing. Also, the machine can only hold one range per use. For example, if during a day of testing the UCC was run at lean conditions so that the original CO span selected was Range 1 (2000 ppm), but later that day the upper range was calibrated using the second gas span, then the calibration for span 1 is no longer good. This is due to the compounding error within the two gas samples, as well as the electrical distortion error. Therefore, use the range that requires no changing during the course of a full day of testing AND has the lowest range value that can be successfully read.

Table A.1: CAI ranges

Range	THC (ppm)	NOx (ppm)	CO2 (%)	CO (ppm)	O2 (%)
1	10.00	30.	5.000	2000.	5.000
2	30.0	100.	20.00	10,000	10.000
3	100.	300.		1.000%	25.00
4	300.	1000	N/A	N/A	N/A
5	1000.	3000	N/A	N/A	N/A
6	3000	N/A	N/A	N/A	N/A
7	10000	N/A	N/A	N/A	N/A
8	30000	N/A	N/A	N/A	N/A
RMT					

"The CAI emissions machine is made up of several modules. They are the Power / Machine Diagnostics, Emissions Analyzers, Flow Meters, Flow Switches, and Sample Oven and can be seen in Figure A.2. The power and diagnostics panel shown in Figure A.3 is where the power to the CAI machine is turned on. It also has the power switch for the pump. The diagnostics on the panel are used to ensure different parts of the machine are operating at the correct temperature. The CAI analyzer controls are where the emissions outputs are controlled and display on the machine. The different knobs on the analyzers are shown in Figures A.4 – A.6 The CAI flow meter panel, is where flow rate are adjusted and displayed." [56]

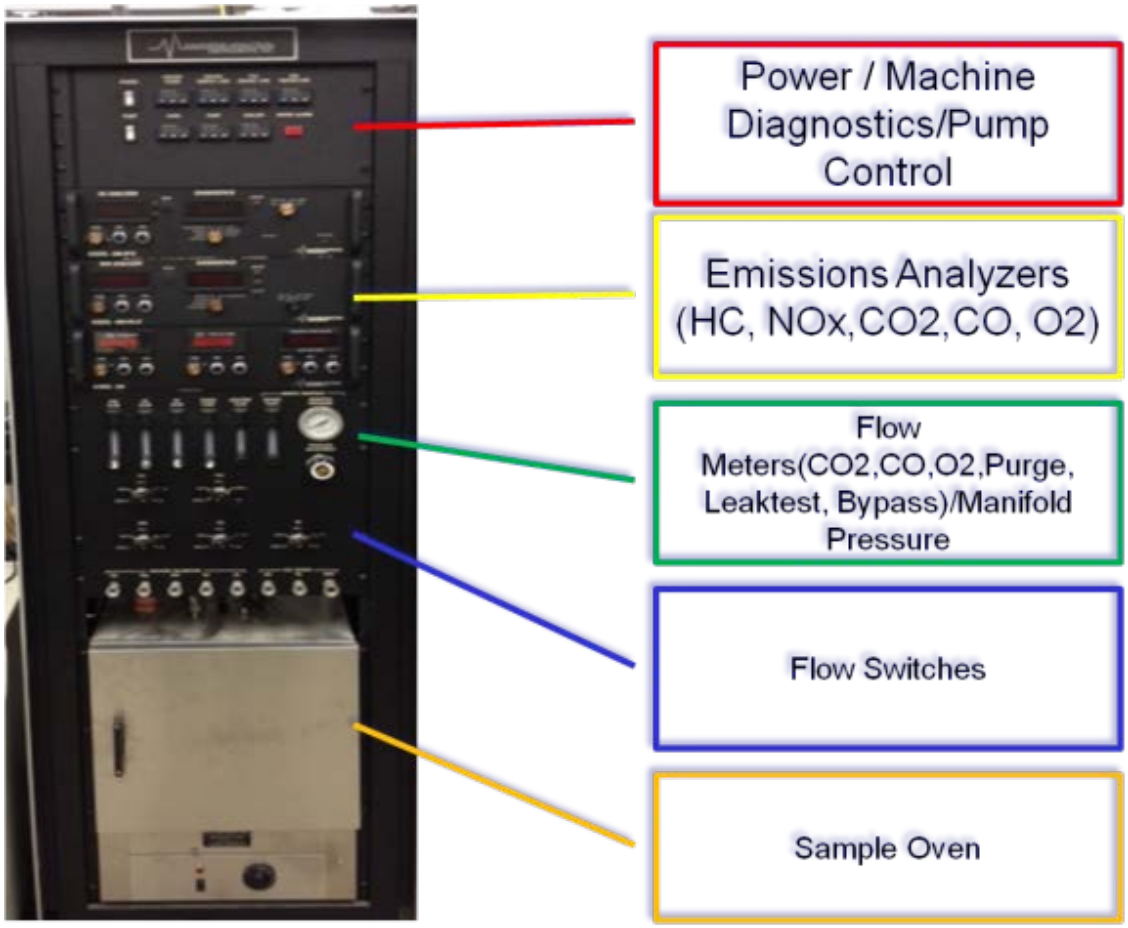

Figure A.2: CAI modules [56]

Figure A.2: CAI power and diagnostics panel [56]

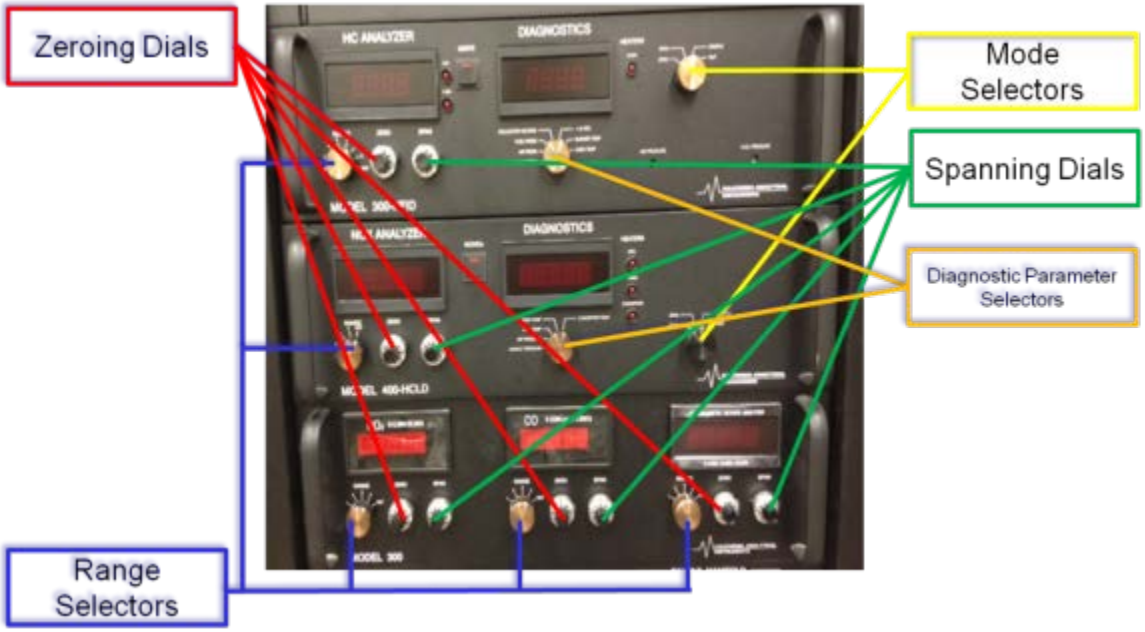

Figure A.3: CAI analyzer controls

Figure A.4: CAI flow meter panel

Figure A.5: CAI flow switch panel

The CAI flow switch panel shown in Figure A.6 is where the source gas can be selected to go to the analyzers. Sample is the setting used for taking data. Zero, Span 1 and Span 2 are for calibration of the CAI emissions machine. The CAI emission machine is equipped with an oven, the insides of which can be seen in Figure A.7.

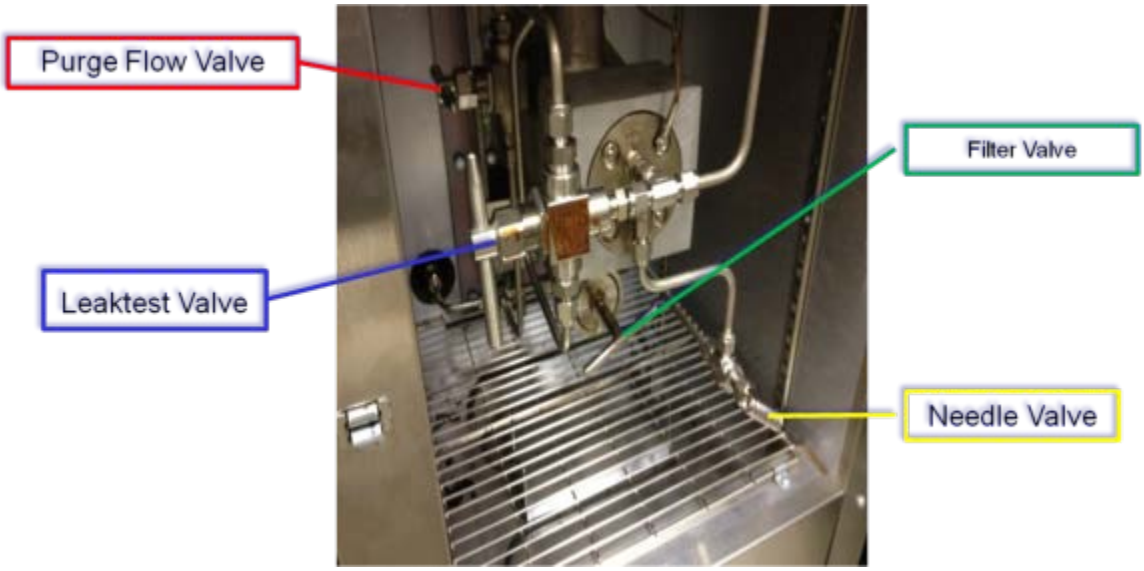

Figure A.6: Inside CAI sample oven

Tank Farm Upkeep

Calibrating the CAI emissions machine is a fairly simple process. Before beginning calibration it is important to ensure span gases are available in the tank farm shown in Figure A.9 and Figure A.10. The span gases are short tanks and can be seen in Figure A.9. In addition to the span gases, a 99.9+% N_2 gas is needed to purge the CO_2, CO and O_2 lines, and a hydrogen-helium fuel blend are also required to complete the calibration shown in Figure A.10. ENSURE THAT THE HYDROGEN/HELIUM BOTTLE IS KEPT AWAY FROM THE O_2 BOTTLES BY THE SOLID BRICK WALL! Specifics on the composition of span gases and hydrogen-helium blend can be found in the CAI binder in the COAL laboratory as they will change with each new bottle that is used. It is very important to have accurate records of these gases as it has a direct impact on the calibration of the CAI machine.

Figure A.7: Tank Farm

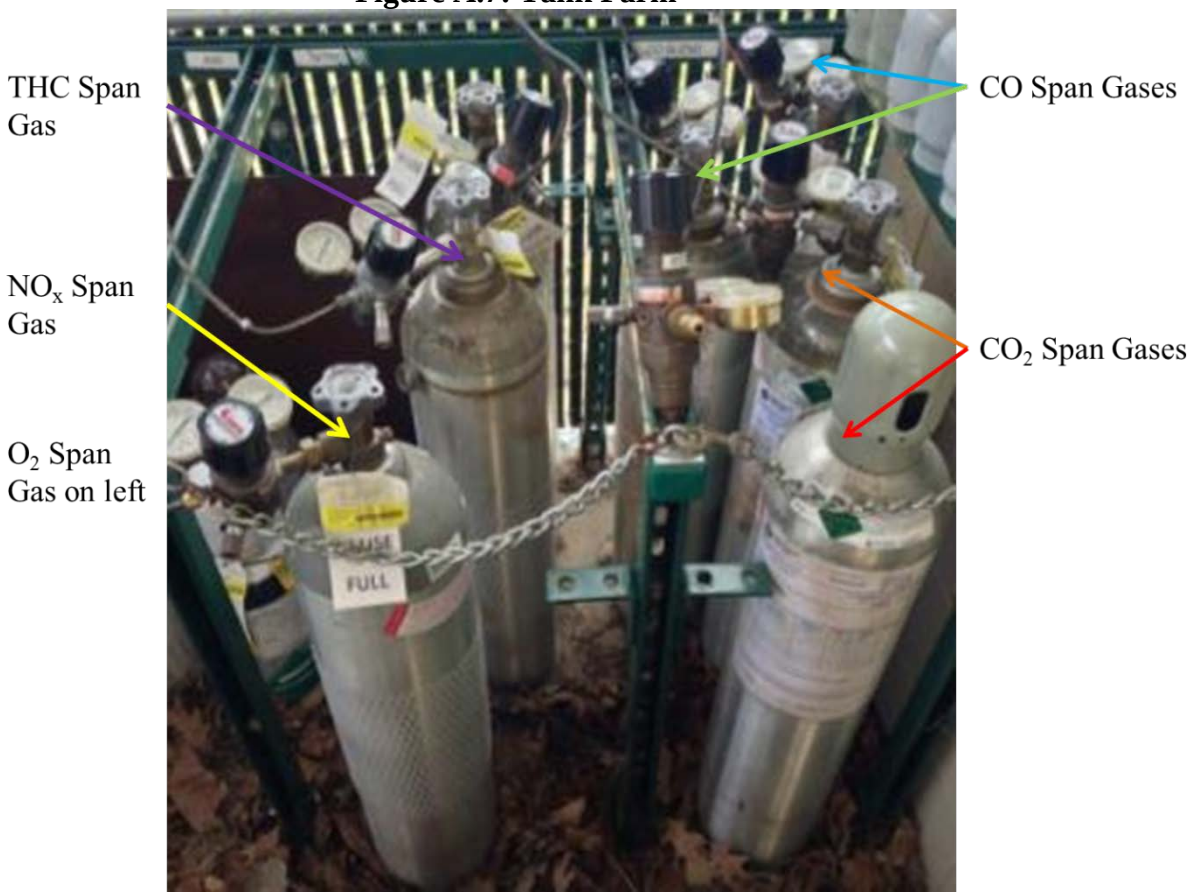

Figure A.8: Span gas tanks, O_2, CO, CO_2

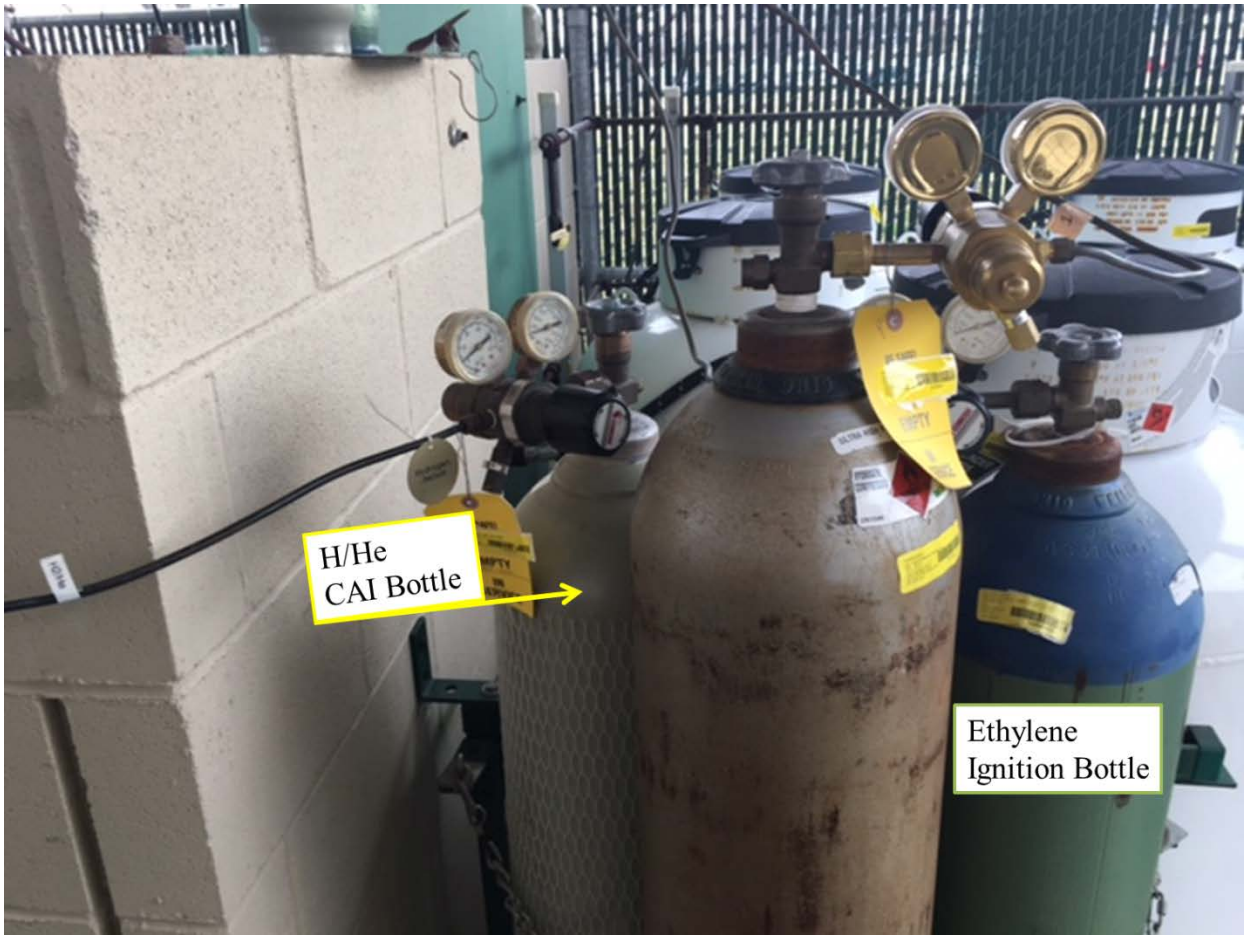

Figure A.9: Hydrogen/Helium (CEM) Air Tank
WARNING: Ensure bottle is by other flammable gases and not O_2!

During the initial development of the multi-channel emissions probe, several maintenance actions were required in order to return the California Analytic Instruments gas analyzer (CAI) to working order. It was also discovered that no manual or operational instructions existed for the CAI outside of daily calibration procedures. Therefore, a consolidation of maintenance procedures and operating instructions are required for future research efforts so as not to lose the institutional knowledge of how to run the CAI.

Below summarizes the procedures used and codified during the course of this thesis in order to make the CAI work. It is divided into two sections: Maintenance Requirements and Operational Procedures. Both MUST be maintained in the CAI Continuity Binder in addition to the Calibration Gas Sheets and it is the hope that they may be altered, improved, and supplemented with further procedure in the future.

Maintenance Requirements

Initial System Requirements

Purchase Calibration Gases

1. Obtain quote from off-base supplier for specific gases. Order should be for one (1) bottle of the calibration gas at the concentration specified in Table B.2. The bottle should be 70 cubic ft in sized, filled until the internal pressure at 2000 psi and "balanced" (i.e. diluted with) N_2 .
   - Note that as of Jan 2016 all calibration gases have been purchased from Natural Valley Gas, a subsidiary of Matheson Gas. The large propane comes from Weiler.
2. Obtain the MSDS or SDS (Safety Data Sheet) from Matheson Gas' website. All SDS's for gases in the tank farm currently are located on the L://Drive:
   - Link: <L:\Research\COAL LAB\Students\Gilbert\Lab Equipment\Tank Farm>
3. Fill out the top portion the AFIT HAZMAT GPC Form with the required information. The ALFI of the COAL Lab is 06-12. The form is located on the SharePoint on the L:\ Drive at: <L:\Research\COAL LAB\Hazmat_GPC_Form.docm>
4. Send the SDS, Quote, and AFIT HAZMAT GPC Form to Dr. Marc Polanka to fill out the funding allocation information. Dr. Polanka should then forward the three documents to Mr. John Hixenbaugh, AFIT/EN Hazardous Material expert.
5. Upon Mr. Hixenbaugh approving the package, notify Mr. Josh DeWitt, COAL Lab's dedicated technician, and his supervisor that a gas order has been placed.
6. After the end of the wait time, the gas should be delivered either to Mr. Hixenbaugh (who will call the COAL Lab to come pick it up) or directly to the Tank Farm. If delivered to the Tank Farm, it will be placed against the back side of the concrete wall on the left.
7. ***If canister empties before delivery of new canister, proceed to Replace and Return Gas Canister

Span Gas	THC	NO_x	CO2	CO	O2
Span 1	900 ppm	-	4.75%	1600 ppm	5.00%
Span 2	2700 ppm*	98.4 ppm (98.2 recommended)	9.75%*	4800 ppm*	-

Note: routing between the two tanks of THC span gas is required out in the tank farm.

\

Replace and Return Gas Canister

- Note: All the gas canisters in the Tank Farm are rented from either Matheson Gas or Weiler Gas, and therefore AFIT is paying a monthly fee for their use. Upon the gas being emptied the canisters are returned to the appropriate vendor. In order to maintain fiscal responsibility, please immediately notify Mr. John Hixenbaugh of any empty canisters.

TOOLS REQUIRED

- One 9/16" crescent/combination wrench
- One 13 inch (handle size) adjustable crescent wrench

1. Notify Mr. Hixenbaugh that the canister is empty and is ready for pick-up. Include the gas name, cylinder number, MSN and company that originally supplied tank.
2. Proceed to Tank Farm and empty cylinder.
3. Using the 9/16" wrench, unscrew and remove the ¼" copper line from valve.
4. It is good practice to ensure the lines are unobstructed and not leaking at this time. Perform Blowout the Lines and Leak-Check Copper Lines procedures.
5. Using the 13" wrench, unscrew and remove the pressure regulator from the used canister.
   - **Note**: some of the regulators are lefty-loosey (Left Hand Thread) and some are righty-loosey (Right Hand Thread). If the last number on the regulator valve is even, they are Left Hand Screws, if it is odd, they are Right Hand screws. Be careful not to over-tighten.
6. Unscrew the protective cover from the new gas.
   - **Note**: SAVE THE SPECIFICATION SHEET CONTAINED WITHIN. You will need this for the CAI Continuity Binder.
7. Re-attach the pressure regulator to the new canister.
8. Re-attach ¼" copper tubing to the end of the pressure regulator
   - **Note**: some of the regulators are lefty-loosey (Left Hand Thread) and some are righty-loosey (Right Hand Thread). If the last number on the regulator valve is even, they are Left Hand Screws, if it is odd, they are Right Hand screws. Be careful not to over-tighten.
9. The CAI requires the gas to be delivered at a pressure of 30 psig ± 5 psi, therefore, open valve and adjust flow regulator reading until it equals 30 psi.
   - Note: If the flow regulator does not initially read 30 psig, a continuous flow (i.e. open system) is required to perceive adjustments to the system.
   - Tests performed during Sept-Oct 2015 found that the pressure loss within the emission span-gas tubing was no more than 1.0 psi up to the filters. Therefore, it is desired for the setting on the pressure gauge to equal 30 psig.
10. Remove empty canister from span gas area and place in rack against the front of the concrete wall on the left hand side (see Figure Y).
11. Three-hole punch the gas canister specification sheet and place in the Active Gas tab of the CAI Continuity Binder. Remove old sheet and place on top in the Past Orders tab.

Blowout the Lines

TOOLS REQUIRED

- One 9/16” crescent/combination wrench
- One adjustable crescent wrench

1. In COAL Lab, remove SwageLok fitting from sample gas routing board (Figure Y).
2. Open AFIT Shop Air 5/16” line (red handle, plastic line on the bottom in Figure Y). Ensure black switch is closed and pressure regulator is set to a minimum of 120 psi.
3. Attach ¼” shop line tube to open fitting so that air goes through copper line out to Tank Farm.
4. Go to Tank Farm. Remove 9/16” SwageLok attaching ¼” copper tube to canister pressure regulator
   - Note: color of tube inside and label of routing board should match tanks outside.
5. Open black switch within COAL Lab. Leave open for a minimum of 15 seconds.
6. Close AFIT Supply Line switch, allow pressure to bleed out through line.
7. Close black switch.
8. This is the best time to also perform a Leak-Test of the Copper Lines.
9. Disconnect ¼” shop line tube from routing board.
10. Reattach sample gas SwageLok fitting to routing board.
11. Reattach copper tube to canister pressure regulator.

Leak-Test Copper Lines

TOOLS REQUIRED

- One 9/16” crescent/combination wrench
- One adjustable crescent wrench
- One 0-150 psig pressure gauge (obtain from Lab-Techs)

1. In COAL Lab, remove SwageLok fitting from sample gas routing board (Figure Y).
2. Open AFIT Shop Air 5/16” line (red handle, plastic line on the bottom in Figure Y). Ensure black switch is closed and pressure regulator is set to round number (such as 80 psi or 120 psi).
3. Attach ¼” shop line tube to open fitting so that air goes through copper line out to Tank Farm.
4. Go to Tank Farm. Remove 9/16” SwageLok attaching ¼” copper tube to canister pressure regulator
   - Note: color of tube inside and label of routing board should match tanks outside.
5. Attach pressure gauge to open end of ¼” copper tubing. Ensure good seal.
6. Open black switch within COAL Lab.
7. Check reading on pressure gauge. Reading should be within ± 5 psi of COAL Lab regulator setting if set to 80 psig.
8. Close black switch and check pressure gauge again.

9a. If pressure is decreasing at rate > 4 psi per 10 seconds (.4 psi/s) then leak is present. Double check the two connections are good and re-test. If pressure still decreases too much, you will have to Leak Check with the entire line to find the crack/leak. Once found, you will need to seal over the crack with an epoxy and duct tape. Let sit for the prescribed time and then see if there are any more leaks. Re-perform this procedure once line is repaired

9b. If pressure does not decrease at a rate > 4 psi per 10 seconds, then the line is good. Proceed to step 10.

10. Close black switch.
11. Disconnect ¼” shop line tube from routing board.
12. Reattach sample gas SwageLok fitting to routing board.
13. Disconnect pressure gauge from copper tubing.
14. Reattach copper tube to canister pressure regulator.

External CAI Calibration Gas Filter Check

TOOLS REQUIRED

- One 9/16" crescent/combination wrench
- One adjustable crescent wrench
- Tin snips (for the zip-ties, it works better than scissors)
- One 0-150 psig pressure gauge (obtain from Lab-Techs)
- Spare filters (located in far white storage cabinet on the right, third shelf, next to the beakers and pipettes).
- Replacement 1/8" zip-ties
- Replacement 5/16 flexible Tygon tubing

1. Remove ¼ hard plastic line from top of Arco filter by pushing down of the gray ring surrounding the tube and pulling up on the line. Basically these plastic unions work like Chinese finger traps.
   - Note: The stripes of color should match the copper tubing color (excepting black which goes with purple) and the color code in the CAI Continuity Binder.
2. Attach a ¼" tube adapter to the pressure gauge with open (i.e. no SwageLok fitting) end.
3. Insert open end of ¼" pressure gauge adapter tube into top of filter.
4. Disconnect 9/16" Swagelok fitting corresponding to filter at sample gas routing board.
5. Attach via dual male SwageLok union to the AFIT shop line tube.
6. Open AFIT shop air-line (red handle).
7. Set pressure regulator to 30 psi.
   CAUTION: THE FILTERS ARE DESIGNED TO ONLY HANDLE 50 PSI. FAILURE TO DECREASE PRESSURE COULD TEAR FILTER.
8. Open black switch to shop line.
9. Check reading on pressure gauge. Pressure will decrease substantially across filter, but any reading over 20 psi is sufficient.
10. If reading is < 20 psi, Replace Filter.
11. Close AFIT shop air-line (red-handle). Allow air to bleed out.
12. Close black handle.
13. Disconnect AFIT shop line tube and reconnect end to appropriate node on routing panel.
14. Disconnect pressure gauge and re-insert ¼ striped tube.

Replace Filter

1. Cut all zip-ties off filter ends. DO NOT DAMAGE TYGON TUBE.
2. Remove filter alligator teeth valve end from tubing on both ends.
3. Inspect the flexible Tygon tubing for cracks or deformations. If no longer reusable, replace.
4. Insert new Arco filter into exposed ends of tube. Note the writing on the filter goes "up" towards the CAI analyzer.
5. Zip tie the ends down around the valleys of the teeth. One is required, two is preferred.
6. When turning on pressure, make sure seal is formed within 3 seconds. If not, tighten zip-ties or try to replace.

Vacuum Pump Inspection

During the course of inspection, it was discovered the pump was turning on but getting drawing no sample. Below follows the inspection logic tree that eventually resulted in most of the problems with the pump being resolved.

1. To tell if the pump is working, open gas exhaust ports on back side of CAI analyzer. These switches are on the bottom panel right by where all the span gas ports are located.
2. Turn the Mode Selector (bronze knob on right side of analyzer box) of the HCID-300F and HFID-400 (THC and Nitrogen analyzers, respectively) to SAMPLE.
3. Turn Mode Selector (black pointy knob) to SAMPLE.
4. Turn PUMP ON.
5. Inspect the MANIFOLD PRESSURE dial on the Flow Switch Panel.
6. Adjust the MANIFOLD PRESSURE to 6-10 psig using the black Pressure Adjustment knob directly below MANIFOLD PRESSURE dial.
7. If the pressure is < 2 psi, then the pump has become disengaged.
    a. If pump is disengaged, turn off CAI oven and wait to cool.
    b. In gap between top of oven and bottom of the quick-disconnect panel, reach toward the large black cylinder. This is the CAI pump.
    c. The silver cylinder extending down from the black pump into the oven is the connector. At the top of this rod is a beveled gear that connects the rod to the pump.
8. Move the beveled gear up until the teeth are enmeshed (make full contact with) the gear at the bottom of pump
    a. Use 5/64 inch Allen wrench to loosen bottom gear (one on silver cylinder)
    b. Move gear up
    c. Tighten bolt with 5/64 inch Allen wrench

CAI Start-Up Procedure

PRECONDITIONS

- All span gas tubes are hooked up through gas switchboard, filters, and to the back of the CAI
- All Span gases are full and connected in the tank farm
- All Span gases and Hydrogen/Helium fuel are set to 30 psi
- 99.9+% Nitrogen gas tank is set to 40 psi

TOOLS REQUIRED

- One 9/16” crescent/combination wrench
- One adjustable crescent wrench
- Tin snips (for the zip-ties, it works better than scissors)
- One 0-150 psig pressure gauge (obtain from Lab-Techs)
- Spare filters (located in far white storage cabinet (RHS looking towards front of lab) with the distilled water and lab supplies, second shelf from the top, next to the beakers and pipettes).
- Replacement 1/8” zip-ties
- Replacement 5/16 flexible Tygon tubing

1. In tank farm, open 40/60, Hydrogen/Helium fuel bottle.

2. In tank farm, open all seven (7) span calibration tanks. CO and CO_2 have two tanks each.

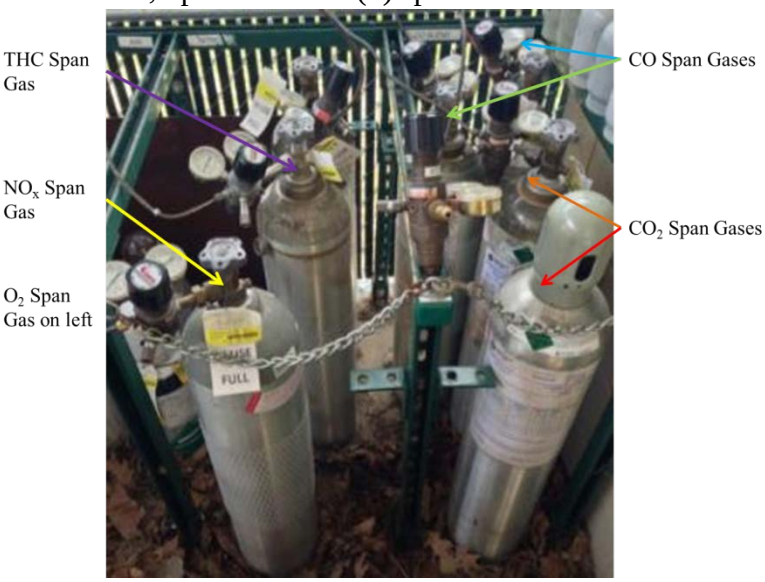

3. In tank farm, open 99.9+% Nitrogen tank.
4. In COAL Lab, ensure second clean air pressure regulator (big black tank by printer) is set to 40 psi.
5. Open gas four (4) exhaust ports on back side of CAI analyzer. These switches are on the bottom panel right by where all the span gas ports are located.

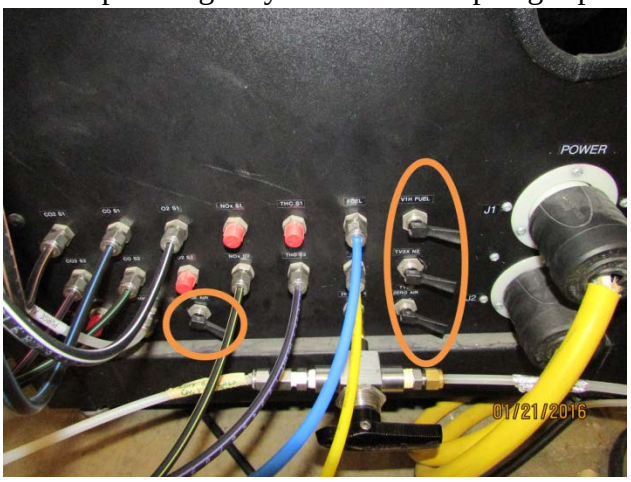

6. Turn the Mode Selector (bronze knob on right side of analyzer box) of the HCID-300F and HFID-400 (THC and Nitrogen analyzers, respectively) to ZERO.

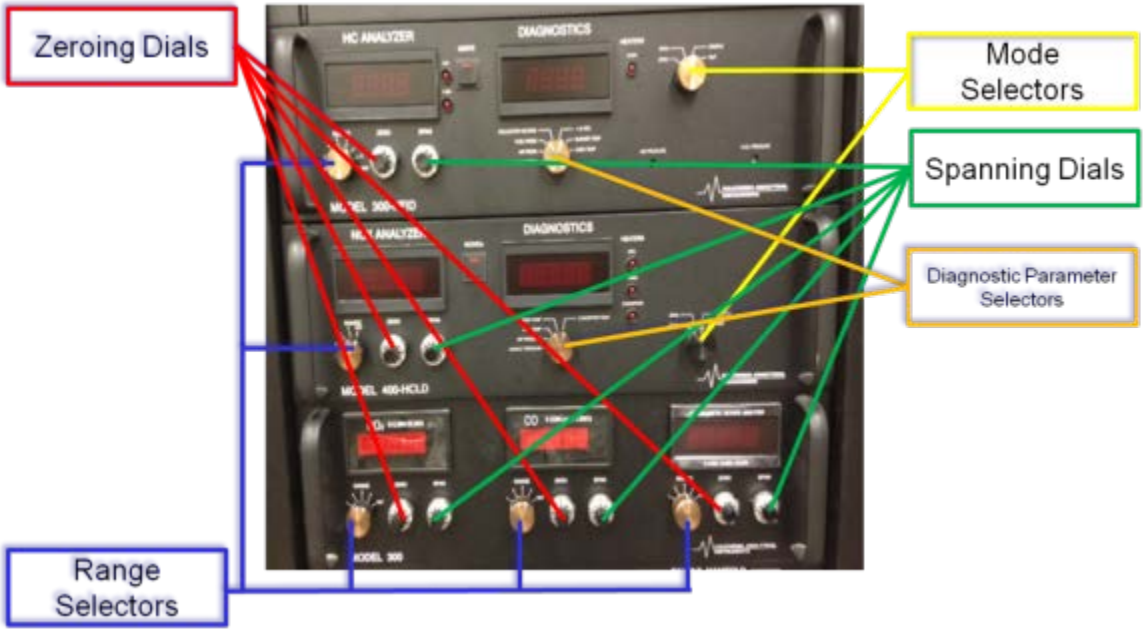

7. Turn all five Flow Switch Valves (black pointy knobs) to ZERO.

8. Turn on POWER switch in upper left corner of CAI Analyzer.
9. Turn on Oven Power switch on bottom front face of oven.
10. Set Oven Power Knob to 10.
11. Set Watlow Thermocouple Control unit to following settings.

	Heated Filter	Sample Line	THC Heated Line	NOx Heated Line
Setting (°C)	Error	150°C	150°C	65°C
	Oven	Pump	Chiller	Water Alarm
Setting (°C)	190°C	190°C	5°C	

12. Wait until Oven Temperature reads >100°C. This should take 20+ minutes.
13. Once temperature is > 100°C, ensure (double-check) that the back exhaust port for fuel and clean air are open.
14. Push IGNITE button on HCID-300F. You should hear a click, see the THC rise from 0 to 2-4, then come down. This is the auto-ignition sequence programed in the CAI. Once the flame is lit, the red light on the button will come on. This can take anywhere from 5 seconds to 5 minutes. If after 5 minutes it has not relit, ensure you set it up properly. If set upt properly, turn off CAI for five seconds and then turn back on. Ensure oven is above 130°C and then retry.
15. Once hydrogen flame is lit, wait a minimum of 2.0 hours for CAI to heat up and come to sample balance.
    a. Note: all samplers except CO_2 require only one hour to heat up. If calibrating CO_2 throughout the entire experiment, then it is permissible wait only 1.0 hours.
16. To perform daily calibration of CAI with LabView, start and run "0 UCC RIG CONTROL_Working_2016" LabView VI in RIG CONTROL Folder on Desktop.

- Note: the "0" at the beginning just puts this VI at the top of the list
- Note: the Pump should be off during all calibrations.

17. Open all three mass flow regulators to 1 mL/min setting and ensure THC and NO_x Analyzer have Flow Setting Valve and Flow Selector Valve set to ZERO.

18. Loosen all ZERO-ing dials and set adjust all five knobs until displays 0.000. Do not take a measurement with LabView at this time.
19. Turn Range Selector Switches to 7 / 2 / 2 / 2 / 1 for THC, NO_x, CO_2, CO and O_2.
20. Once all 5 channels read zero, switch THC, NO_x, CO_2, and CO Flow Selector Valves (black knobs) to Span 2 position (2 o'clock) and Span 1 for O_2.

a. Note: Span 2 is the only gas sample input for THC and NO_x values. However, "Range 6" should be used if THC concentration is expected to be below 3000 ppm. Otherwise, "Range 7" is required for experiments between a range of 3,000-10,000.
b. Only Span 1 works for O_2.

21. Turn Mode Selectors (brass knobs) to Span Mode.

22. Loosen Spanning knobs and adjust until each display reads the corresponding value to the sample gas (i.e. NO_x sensor reads and holds 98.4 ppm). It will take a few moments for the reading to stabilize.
23. Lock in spanning knob hard set.
24. Once all 5 samples are stable and reading correct value, collect "Span 2" data. File Format is "CAIData_DD_MMM_YY_Span2.csv"
25. Repeat Step 19-24 for Span 1 data. Turn Range
    a. Selector Switches to 6 / 2 / 1 / 1 / 1 for THC, NO_x, CO_2, CO and O_2 (note, NO_x and O_2 are the same).
    b. Record readings of CO_2 and CO if using these channels and calibrating to Span 2 (i.e. if you have a 1600 ppm CO sample gas but you read 1592 ppm, record 1592 and use this as the curve value in post processing program code).
    - Note: altering the span calibration for these values will mess up the Span 2 calibration curves. This would be the time to change THC range from 7 to 6 if that is desired for the day.
    - File Format is "CAIData_DD_MMM_YY_Span1.csv".
26. Turn all Flow Switches to Zero position and Mode Selectors to Zero.
27. Readjust Zero knobs if there was any change in displays so that they now again read "0"
28. Collect "Zero" data. File Format is "CAIData_DD_MMM_YY_Zero.csv".
29. CAI is now calibrated. Place collection probe in the desired location in the exhaust wake.
30. Turn on Mokon Oil Pump to 250°F – 300°F.

- ***CAUTION: Flipping these steps will burn your hands.***

31. Turn off Flow Meters for CO_2, CO, and O_2.
32. Start UCC up and get rig into desired run condition.
33. Open desired channel/sample position (IN, MID-IN, MID-OUT, OUT) at the manifold using the push buttons in the LabView UCC Rig VI.
34. Turn pump on by flipping PUMP switch on CAI.
35. Turn two (2) Mode Selectors to Sample setting.
36. Turn five (5) Flow Switches to Sample position (7 o'clock).
37. Adjust Pressure Adjustment knob until manifold pressure reads a minimum of 6.0 psi.

- CAUTION: In order to get good data for THC and NO_x, the Sample Pressure digital display MUST read 1.8 psi and 3.8 psi (respectively). Failure to do so will cause under-estimates of data.

38. Turn on one of the flow meters (recommend CO_2 or CO as you need those to calculate EI) until it reads 1.0 mL/min.
39. If this causes the Manifold Pressure to dip below 6.0 psi, adjust flow meter until manifold Pressure again reads > 6.0 PSI.

- Note: that according to CAI sales representative, only 0.5 mL is required to get an accurate reading.
- Note: if you cannot do this, then you need to enlarge the probe hole to get more mass flow. Also, exhaust gases are hotter than normal gases, so your density will go down. Sufficient mass flow at atmospheric conditions does not equate to sufficient mass flow at test conditions.

40. Turn on second flow meter (recommend CO_2 or CO as you need those to calculate EI) until it reads 1.0 mL/min.
41. If this causes the Manifold Pressure to dip below 6.0 psi, adjust flow meters until manifold Pressure again reads > 6.0 PSI.

- **Procedural Work-Around: If you can only get one sample at a time, what you can do is take three sets of data at the same point. This will give you three files 150 THC and NOx points, and then 50 CO_2, 50 CO and 50 O_2. Combine the CO_2, CO and O_2 data with the common THC and NO_x values and you will have a "all" file of representative values for all 5 species. Proceed to step 38.**
- Note: that according to CAI sales representative, only 0.5 mL is required to get an accurate reading.
- Note: if you cannot do this, then you need to enlarge the probe hole to get more mass flow. Also, exhaust gases are hotter than normal gases, so your density will go down. Sufficient mass flow at atmospheric conditions does not equate to sufficient mass flow at test conditions.

42. Turn on third meter until it reads 1.0 mL/min.
43. If this causes the Manifold Pressure to dip below 6.0 psi, adjust flow meters until manifold Pressure again reads > 6.0 PSI.

- **Procedural Work-Around: If you can only get one sample at a time, what you can do is take three sets of data at the same point. This will give you three files 150 THC and NOx points, and then 50 CO_2, 50 CO and 50 O_2. Combine the CO_2, CO and O_2 data with the common THC and NO_x values and you will have a "all" file of representative values for all 5 species. Proceed to step 38.**
- Note: that according to CAI sales representative, only 0.5 mL is required to get an accurate reading.
- Note: if you cannot do this, then you need to enlarge the probe hole to get more mass flow. Also, exhaust gases are hotter than normal gases, so your density will go down. Sufficient mass flow at atmospheric conditions does not equate to sufficient mass flow at test conditions.

44. Press Collect UCC Data radial button on LabView VI.
45. Name file when window pops up. File format

-THE FILE SAVER WILL NOT AUTOMATICALLY SAVE THE FILE AS A .CSV, BUT THIS IS WHAT THE POST PROCESSING SCRIPT REQUIRES. YOU MUST HAND TYPE .CSV AT THE END OF EACH FILE EVERY TIME YOU SAVE.

- **If you forget to do this, it will save a generic file type. Simply double-click on file, open with NotePad and "Save As" a .csv file extension.**

46. Repeat for as many points as required.
47. Sporadically re-zero all channels during test breaks. Recommended interval is 20 minutes. If the channels wander more than 0.5% (which CO_2 does all the time), write down what the change was and apply an adjustment factor to each sample point in the post-processing of the data.
48. Once all data points are completed turn off pump. **DO NOT TURN OFF CAI.**
49. Shut down UCC and bleed out propane/air lines.

50. Turn Pump back on for at least 10 minutes to clear out all lines and CAI of exhaust gases.
51. Turn Pump off. Flow zero gas (99.9+% N_2) through all channels for at least 5 minutes.
52. Turn off Flow Meters.
53. Turn off Span Gases and Hydrogen/Helium gas in Tank Farm.
    - Note: it takes about 15 min for the Hydrogen/Helium fuel to burn off
54. Turn Off CAI Power
55. Flip closed exhaust ports to seal off system.

Appendix C: Legacy MatLab Code

1) J2K

```
function [ K_Temp ] = J2K(J_Temp)
% J2K converts readings taken by a thermocouple that was set to analyze
% those readings as coming from a J-type thermocouple when in actuallity a
% K-type thermocouple was used.
% Temp is a matrix of Temperature, must be in units of °C

[ROW, COLM] = size(J_Temp);
K_Temp = zeros(ROW,COLM);

% Conversion Factors taken from https://www.omega.com/temperature/Z/pdf/z198-
201.pdf
c760 = [0, 5.0381187815E1, 3.047583693E-2, -8.568106572E-5, 1.3228195295E-
7,...
    -1.7052958337E-10, 2.0948090697E-13, -1.2538395336E-16, 1.5631725697E-
20];
c1200 = [2.9645625681E5 -1.4976127786E3, 3.1787103924, -3.184768670E-3,...
    1.5720819004E-6, -3.0691369056E-10];

for r = 1:ROW
  for c = 1:COLM

 if J_Temp(r,c) <= 760
    Volt(r,c) = c760(1) + c760(2)*J_Temp(r,c)^1+ c760(3)*J_Temp(r,c)^2 +...
     c760(4)*J_Temp(r,c)^3 + c760(5)*J_Temp(r,c)^4 +c760(6)*J_Temp(r,c)^5
+...
     c760(7)*J_Temp(r,c)^6 + c760(8)*J_Temp(r,c)^7 + c760(9)*J_Temp(r,c)^8;
 elseif J_Temp(r,c) <= 1200
     Volt(r,c) = c1200(1) + c1200(2)*J_Temp(r,c)^1+ c1200(3)*J_Temp(r,c)^2
+...
     c1200(4)*J_Temp(r,c)^3 + c1200(5)*J_Temp(r,c)^4 +c1200(6)*J_Temp(r,c)^5;
 else
     Volt(r,c) = 'ERROR value too large';
 end %if

 end % Column For
end % Row For

% Error = - 0.05 °C to .04 °C

d500 = [0, 2.508355E-2, 7.860106E-8, -2.503131E-10, 8.315270E-14, ...
   -1.228034E-17, 9.804036E-22, -4.41303E-26, 1.057734E-30, -1.052755E-35];

d1372 = [-1.318058E2, 4.830222E-2, -1.646031E-6, 5.464731E-11,...
    -9.650715E-16, 8.802193E-21, -3.110810E-26];

for r2 = 1:ROW
    for c2 = 1:COLM
```

```
        if  Volt(r2,c2) <= 54886
            if Volt(r2,c2) <= 20644
     K_Temp(r2,c2) =
d500*[1,Volt(r2,c2),Volt(r2,c2)^2,Volt(r2,c2)^3,Volt(r2,c2)^4,Volt(r2,c2)^5,V
olt(r2,c2)^6,Volt(r2,c2)^7,Volt(r2,c2)^8,Volt(r2,c2)^9]'   ;
            else
     K_Temp(r2,c2) =
d1372*[1,Volt(r2,c2),Volt(r2,c2)^2,Volt(r2,c2)^3,Volt(r2,c2)^4,Volt(r2,c2)^5,
Volt(r2,c2)^6]';
            end

        else
     K_Temp(r2,c2) = 15;

        end %if

    end % Column For
end % Row For


end % J2K function
```

2) CAI Data Compiler

```
%%
% Original work by Nicholas A. Gilbert

clc
clear all
close all
%%%%%%%%%%%%%%%%%%%%%%%%%%%%%%%%%%%%%%%%%%%%%%%%%%%%%%%%%%%%%%%%%%%%%%%%%%%%%%%%
%%%%%%%%%%%%%%%%%%%%%%%%%%%%%%%%%%%%%%%%%%%%%%%%%%%%%%%%%%%%%%%%%%%%%%%%%%%%%%%%
%%%%%%%%%%%%%%%%%%%%%%%%%%%%%%%%%%%%%%%%%%%%%%%%%%%%%%%%%%%%%%%%%%%%%%%%%%%%%%%%
%%%%%%%%%%%%%%%%%%%%%%%%%%%%%%%%%%%%%%%%%%%%%%%%%%%%%%%%%%%%%%%%%%%%%%%%%%%%%%%%
%% Import Data
% CONSTANTS
% humidity taken from
% http://www.timeanddate.com/weather/usa/dayton/historic and converted to
% ppm by http://www.humcal.com/index.php
humidity = 4578.81/10^6;

span ={['27.2% span'] ['41.3% span'] ['54.6% span'] ['69.6% span']}';


% Taken from Matheson Gas Data for 21.1°C, 1 atm, who supplies our gas
rho_propane = 1.8580; %kg/m^3, assumed constant
% http://webbook.nist.gov/cgi/cbook.cgi?ID=C74986&Mask=1#Thermo-Gas
propane_Hc = 21660; % BTU/lb: 44.0956 = MW_Propane

% INPUTS--FILES
% ***Copy and paste each name of file and then add one index to
% each.  Be sure to use {X} brackets and enclose string in [] in order for
% the syntax to work correctly

filename{1} = ['CAIData_6_Feb_16_Calib_Zero.csv'];
filename{2} = ['CAIData_6_Feb_16_Calib_Span1.csv'];
filename{3} = ['CAIData_6_Feb_16_Calib_Span2.csv'];

filename{4} = ['CAIData_6_Feb_16_18_26_in_all5.csv'];
filename{5} = ['CAIData_6_Feb_16_18_26_mid_in_all5.csv'];
filename{6} = ['CAIData_6_Feb_16_18_26_mid_out_all5.csv'];
filename{7} = ['CAIData_6_Feb_16_18_26_out_all5.csv'];

filename{8} = ['CAIData_6_Feb_16_18_33_in_all5.csv'];
filename{9} = ['CAIData_6_Feb_16_18_33_mid_in_all5.csv'];
filename{10} = ['CAIData_6_Feb_16_18_33_mid_out_all5.csv'];
filename{11} = ['CAIData_6_Feb_16_18_33_out_all5.csv'];

filename{12} = ['CAIData_6_Feb_16_18_39_in_all5.csv'];
filename{13} = ['CAIData_6_Feb_16_18_39_mid_in_all5.csv'];
filename{14} = ['CAIData_6_Feb_16_18_39_mid_out_all5.csv'];
filename{15} = ['CAIData_6_Feb_16_18_39_out_all5.csv'];

filename{16} = ['CAIData_6_Feb_16_18_46_in_all5.csv'];
filename{17} = ['CAIData_6_Feb_16_18_46_mid_in_all5.csv'];
filename{18} = ['CAIData_6_Feb_16_18_46_mid_out_all5.csv'];
```

```
filename{19} = ['CAIData_6_Feb_16_18_46_out_all5.csv'];

filename{20} = ['CAIData_6_Feb_16_18_53_in_all5.csv'];
filename{21} = ['CAIData_6_Feb_16_18_53_mid_in_all5.csv'];
filename{22} = ['CAIData_6_Feb_16_18_53_mid_out_all5.csv'];
filename{23} = ['CAIData_6_Feb_16_18_53_out_all5.csv'];

filename{24} = ['CAIData_6_Feb_16_18_59_in_all5.csv'];
filename{25} = ['CAIData_6_Feb_16_18_59_mid_in_all5.csv'];
filename{26} = ['CAIData_6_Feb_16_18_59_mid_out_all5.csv'];
filename{27} = ['CAIData_6_Feb_16_18_59_out_all5.csv'];

% filename{28} = ['CAIData_6_Feb_16_18_70_in_all5.csv'];
% filename{29} = ['CAIData_6_Feb_16_18_70_mid_in_all5.csv'];
% filename{30} = ['CAIData_6_Feb_16_18_70_mid_out_all5.csv'];
% filename{31} = ['CAIData_6_Feb_16_18_70_out_all5.csv'];
% ------------------------------------------------------------------------
% ------------------------------------------------------------------------
% ------------------------------------------------------------------------

%% HERE STOPS THE INPUTS-------------------------------------------------
% INPUTS--Run conditions of data points
% fuel_set = input('fuel setting (SLPM) as array: ');
% air_set  = input('\nfuel setting (percent setting) as array: ');
% fuel_set = [0 0 0 1st point 2nd setpoint 3rd setpoint ...]; SLPM
% air_set  = [0 0 0 1st point 2nd setpoint 3rd setpoint ...]; % max flow
% fuel_set = [0 0 0 26,26,26,26, 33,33,33,33, 39.4,39.4,39.4,39.4,...
%                   46,46,46,46, 53,53,53,53, 59,59,59,59, 70,70,70,70]; %
SLPM-->kg/s
fuel_set = [0 0 0 26,26,26,26, 33,33,33,33, 39.4,39.4,39.4,39.4,...
                  46,46,46,46, 53,53,53,53, 59,59,59,59]; % ,70,70,70,70
split=.26;        % .30 ideal

air_set  = 18.*ones(1,length(fuel_set)); % mass air flow (% 3" line -> kg/s)
    F_A_stoich = 44.1/28.97/5/4.76;



    air_set_mass  = air_set(1,1:end).*.006.*split; %kg/s
    fuel_set_mass = fuel_set/60/1000*rho_propane; %kg/s
    phi = (fuel_set_mass./air_set_mass)./F_A_stoich;


%%%%%%%%%%%%%%%%%%%%%%%%%%%%%%%%%%%%%%%%%%%%%%%%%%%%%%%%%%%%%%%%%%%%%%%%%%%
%%%%%%%%%%%%%%%%%%%%%%%%%%%%%%%%%%%%%%%%%%%%%%%%%%%%%%%%%%%%%%%%%%%%%%%%%%%
%%%%%%%%%%%%%%%%%%%%%%%%%%%%%%%%%%%%%%%%%%%%%%%%%%%%%%%%%%%%%%%%%%%%%%%%%%%
%%%%%%%%%%%%%%%%%%%%%%%%%%%%%%%%%%%%%%%%%%%%%%%%%%%%%%%%%%%%%%%%%%%%%%%%%%%
%% This is where the magic happens
% ------------------------------------------------------------------------
% Splitting the Arrays
THC = zeros(50,length(filename));
NOx = zeros(50,length(filename));
CO2 = zeros(50,length(filename));
CO = zeros(50,length(filename));
O2 = zeros(50,length(filename));
```

```
for i=1:length(filename)


data=dlmread(filename{i},',',1,0);
THC_Span(i) = csvread(filename{i},0,0,[0,0,0,0]);
CO2_Span(i) = csvread(filename{i},0,2,[0,2,0,2]);
CO_Span(i)  = csvread(filename{i},0,3,[0,3,0,3]);

THC(:,i) = data(:,1)*1000;
NOx(:,i) = data(:,2)*1000;
CO2(:,i) = data(:,3)*1000;
CO(:,i)  = data(:,4)*1000;
O2(:,i)  = data(:,5)*1000;

end

% Time average data of each measurement point
THC_point = mean(THC);
NOx_point = mean(NOx);
CO2_point = mean(CO2);
CO_point = mean(CO);
O2_point = mean(O2);
% ------------------------------------------------------------------------


%% Convert mA --into--> ppm
% 2 Dec Data

THC_convert1  = polyfit(THC_point([1 2]),[0,900],1); % Range 6
THC_convert2  = polyfit(THC_point([1 3]),[0,900],1); % Range 7
NOx_convert  = polyfit(NOx_point([1 3]),[0,98.4],1);
CO2_convert1 = polyfit(CO2_point([1 3]),[0,4.75*10^4],1);
CO_convert1  = polyfit(CO_point(1:2),[0,1600],1);
CO_convert2  = polyfit(CO_point([1 3]),[0,4800],1);
O2_convert   = polyfit(O2_point([1 3]),[0,5.00*10^4],1);


NOx_ppm = NOx_convert(1).* NOx_point + NOx_convert(2);
O2_ppm = (O2_convert(1).*  O2_point  + O2_convert(2)); %convert from % to ppm
CO2_ppm = (CO2_convert1(1).*  CO2_point  + CO2_convert1(2)); % If Linear
Adjustment not required

for j=1:length(THC_point)

    if round(THC_Span(j)) == 6
        THC_ppm(j) = THC_convert1(1).*THC_point(j) + THC_convert1(2);
    else
        THC_ppm(j) = THC_convert2(1).*THC_point(j) + THC_convert2(2);
    end %if CO

end %for
```

```
for j=1:length(CO_point)

    if round(CO_Span(j)) == 1
        CO_ppm(j) = CO_convert1(1).*CO_point(j) + CO_convert1(2);
    else
        CO_ppm(j) = CO_convert2(1).*CO_point(j) + CO_convert2(2);
    end %if CO

end %for

for k=4:length(CO2_point) % CO2 linear adjustment (if required)

    if k <= 11
        CO2_ppm(k) = CO2_ppm(k) - 820*(k-3)/8;
    elseif k <= 19
        CO2_ppm(k) = CO2_ppm(k) - 1000*(k-8-3)/8;
    elseif k <= 27
        CO2_ppm(k) = CO2_ppm(k) - 1300*(k-16-3)/8;
    end %if CO

end %for

% The first three data points in each set should be your all zero values
% followed by all spanned values (span1 is sample 2, span 2 with the rest
% of span 1 values is sample 3)
% using y = m*x+b for each
% THC_convert1  = polyfit(THC_point2(1:2),[0,900],1); %Value taken after
switching to span 6

m = 3;
n = 8;
alpha = n/m;
MW_CO2 = 44.01;
MW_O2 = 2*15.9994;
MW_CO = 28.010;
MW_C = 12.0107;
MW_H = 1.00794;
MW_air = 28.966; % kg/kmol
MW_propane = 44.0956; % kg/kmol
MW_THC =  MW_C + MW_H*8/3;
MW_NOx = 46.0055;
Carbon_SUM = (THC_ppm/10^6 + CO_ppm/10^6 + CO2_ppm/10^6);
% T = .00032 = molar ratio of CO2 naturally in air
X = m.*((1-alpha/4.*(Carbon_SUM))./...
    ((1+humidity).*(Carbon_SUM)-.00032));

%
EI_THC = (THC_ppm/10^6)./Carbon_SUM * (MW_THC*10^3/(MW_C+alpha*MW_H)).*
(1+.00032*X/m);
EI_NOx = (NOx_ppm/10^6)./Carbon_SUM * (MW_NOx*10^3/(MW_C+alpha*MW_H)).*
(1+.00032*X/m);
% EI_CO2 = (CO2_ppm/10^6)./Carbon_sum * (MW_CO2*10^3/(MW_C+alpha*MW_H)).*
(1+.00032*X/m);
EI_CO  = (CO_ppm/10^6) ./Carbon_SUM * (MW_CO*10^3/(MW_C+alpha*MW_H)).*
(1+.00032*X/m);
```

```
% EI_O2  = (O2_ppm./10^6)./Carbon_sum * (MW_O2*10^3/(MW_C+alpha*MW_H)).*
(1+.00032*X/m);
Efficiency = (1.00 - 4.346*EI_CO./propane_Hc - EI_THC./1000).*100;


%% Plots

figure(11)
plot([EI_CO(4:4:end) EI_CO(4:4:end)],[EI_NOx(4:4:end)
EI_NOx(4:4:end)],'o','MarkerFaceColor','b')
hold on
plot([EI_CO(5:4:end) EI_CO(5:4:end)],[EI_NOx(5:4:end)
EI_NOx(5:4:end)],'ko','MarkerFaceColor','k')
plot([EI_CO(6:4:end) EI_CO(6:4:end)],[EI_NOx(6:4:end)
EI_NOx(6:4:end)],'ro','MarkerFaceColor','r')
plot([EI_CO(7:4:end) EI_CO(7:4:end)],[EI_NOx(7:4:end)
EI_NOx(7:4:end)],'mo','MarkerFaceColor','m')


legend(span,'Location','SouthEast')
xlabel('EI_C_O (g/kg_f_u_e_l)')
ylabel('EI_N_O_x (g/kg_f_u_e_l)')
% axis([0 200 0 .2])
hold off
%% EI_THC
figure(12)
plot(phi(4:4:end),EI_THC(4:4:end),'bo','MarkerEdgeColor','b','MarkerFaceColor
','b')
hold on
plot(phi(5:4:end),EI_THC(5:4:end),'ko','MarkerEdgeColor','k','MarkerFaceColor
','k')
plot(phi(6:4:end),EI_THC(6:4:end),'ro','MarkerEdgeColor','r','MarkerFaceColor
','r')
plot(phi(7:4:end),EI_THC(7:4:end),'mo','MarkerEdgeColor','m','MarkerFaceColor
','m')


% axis ([.5 2.2 0 200])
legend(span,'Location','East')
xlabel('\phi (-)')
ylabel('EI_T_H_C (g/kg_f_u_e_l)')
hold off

%% EI_CO
figure(13)

plot(phi(4:4:end),EI_CO(4:4:end),'bo','MarkerEdgeColor','b','MarkerFaceColor'
,'b')
hold on
plot(phi(5:4:end),EI_CO(5:4:end),'ko','MarkerEdgeColor','k','MarkerFaceColor'
,'k')
plot(phi(6:4:end),EI_CO(6:4:end),'ro','MarkerEdgeColor','r','MarkerFaceColor'
,'r')
```

```
plot(phi(7:4:end),EI_CO(7:4:end),'mo','MarkerEdgeColor','m','MarkerFaceColor'
,'m')

legend(span,'Location','NorthEast')
title('Emissions of UCC at \phi setting')
% axis ([.4 1.8 0 200])
xlabel('\phi (-)')
ylabel('EI_C_O (g/kg_f_u_e_l)')
hold off

%% EI_NOx
figure(14)
plot(phi(4:4:end),EI_NOx(4:4:end),'bo','MarkerEdgeColor','b','MarkerFaceColor
','b')
hold on
plot(phi(5:4:end),EI_NOx(5:4:end),'ko','MarkerEdgeColor','k','MarkerFaceColor
','k')
plot(phi(6:4:end),EI_NOx(6:4:end),'ro','MarkerEdgeColor','r','MarkerFaceColor
','r')
plot(phi(7:4:end),EI_NOx(7:4:end),'mo','MarkerEdgeColor','m','MarkerFaceColor
','m')


% axis ([.4 1.8 0 .3])
legend(span,'Location','NorthEast')
xlabel('\phi (-)')
ylabel('EI_N_O_x (g/kg_f_u_e_l)')
hold off

%% EI_THC
figure(26)
plot(phi(4:4:end),THC_ppm(4:4:end),'bo','MarkerEdgeColor','b','MarkerFaceColo
r','b')
hold on
plot(phi(5:4:end),THC_ppm(5:4:end),'go','MarkerEdgeColor','g','MarkerFaceColo
r','g')
plot(phi(6:4:end),THC_ppm(6:4:end),'ro','MarkerEdgeColor','r','MarkerFaceColo
r','r')
plot(phi(7:4:end),THC_ppm(7:4:end),'ko','MarkerEdgeColor','k','MarkerFaceColo
r','k')

% axis ([.5 2.2 0 200])
legend(span,'Location','East')
xlabel('\phi (-)')
ylabel('EI_T_H_C (g/kg_f_u_e_l)')
hold off

%% EI_CO
figure(27)

plot(phi(4:4:end),CO_ppm(4:4:end),'bo','MarkerEdgeColor','b','MarkerFaceColor
','b')
hold on
plot(phi(5:4:end),CO_ppm(5:4:end),'go','MarkerEdgeColor','g','MarkerFaceColor
','g')
```

```
plot(phi(6:4:end),CO_ppm(6:4:end),'ro','MarkerEdgeColor','r','MarkerFaceColor
','r')
plot(phi(7:4:end),CO_ppm(7:4:end),'ko','MarkerEdgeColor','k','MarkerFaceColor
','k')

legend(span,'Location','NorthEast')
title('Emissions of UCC at \phi setting')
% axis ([.4 1.8 0 200])
xlabel('\phi (-)')
ylabel('EI_C_O (g/kg_f_u_e_l)')
hold off

%% EI_NOx
figure(28)
plot(phi(4:4:end),NOx_ppm(4:4:end),'bo','MarkerEdgeColor','b','MarkerFaceColo
r','b')
hold on
plot(phi(5:4:end),NOx_ppm(5:4:end),'go','MarkerEdgeColor','g','MarkerFaceColo
r','g')
plot(phi(6:4:end),NOx_ppm(6:4:end),'ro','MarkerEdgeColor','r','MarkerFaceColo
r','r')
plot(phi(7:4:end),NOx_ppm(7:4:end),'ko','MarkerEdgeColor','k','MarkerFaceColo
r','k')


% axis ([.4 1.8 0 .3])
legend(span,'Location','NorthEast')
xlabel('\phi (-)')
ylabel('EI_N_O_x (g/kg_f_u_e_l)')
hold off

%% Efficiency
figure(28)
plot(phi(4:4:end),Efficiency(4:4:end),'bo','MarkerEdgeColor','b','MarkerFaceC
olor','b')
hold on
plot(phi(5:4:end),Efficiency(5:4:end),'go','MarkerEdgeColor','g','MarkerFaceC
olor','g')
plot(phi(6:4:end),Efficiency(6:4:end),'ro','MarkerEdgeColor','r','MarkerFaceC
olor','r')
plot(phi(7:4:end),Efficiency(7:4:end),'ko','MarkerEdgeColor','k','MarkerFaceC
olor','k')


% axis ([.4 1.8 0 .3])
legend(span,'Location','NorthEast')
xlabel('\phi (-)')
ylabel('EI_N_O_x (g/kg_f_u_e_l)')
hold off

%% Error Analysis
Delta_THC = sqrt(100^2 + 50^2 + 100^2 + 50^2)/10000;
% Delta_CO  = 1% Repeatability = 100 ppm, 1% scale = 100 ppm, Linearity
Delta_CO  = sqrt(100^2 + 100^2 + 100^2)/10000;
% Delta_NOx = Repeatability =.5 ppm, Noise = .5 ppm, <1% error with CO2 and
```

```
% H20 effects
Delta_NOx = sqrt(.5^2 + .5^2 + 1^2 + 1^2 + 1^2)/100;
% Delta_CO2 = 1% Repeatability = .01% = 1000 ppm, 1% scale = 1000 ppm
Delta_CO2 = sqrt(500^2 + 500^2 + 500^2 + 500^2)/50000;
% Linearity always 1% full scale, Drift < 1% per 24 hrs
T = .00032;
m = 3;
n = 8;
alpha = n/m;

Carbon_SUM = (CO_ppm + CO2_ppm + THC_ppm)./10^6;
common_term = (T./(m+T.*X)).*(-m).*(1+humidity-
T*alpha/4)./((1+humidity).*(Carbon_SUM)-T).^2;

CO_Term1 = ((CO2_ppm+THC_ppm)/10^6)./Carbon_SUM + common_term.*CO_ppm./10^6;
CO_Term2 = ((-CO2_ppm)/10^6)./Carbon_SUM + common_term.*CO2_ppm./10^6;
CO_Term3 = ((-THC_ppm)/10^6)./Carbon_SUM + common_term.*THC_ppm./10^6;
CO_Error = (CO_Term1.^2*Delta_CO.^2 + CO_Term2.^2*Delta_CO2.^2 +
CO_Term3.^2*Delta_THC.^2).^0.5;

NOx_Term1 = ((-CO_ppm)/10^6)./Carbon_SUM + common_term.*CO_ppm./10^6;
NOx_Term2 = ((-CO2_ppm)/10^6)./Carbon_SUM + common_term.*CO2_ppm./10^6;
NOx_Term3 = ((-THC_ppm)/10^6)./Carbon_SUM + common_term.*THC_ppm./10^6;
NOx_Term4 = 1;
NOx_Error = (NOx_Term1.^2*Delta_CO.^2 + NOx_Term2.^2*Delta_CO2.^2 +...
    NOx_Term3.^2*Delta_THC.^2 + NOx_Term4.^2*Delta_NOx.^2).^0.5;

THC_Term1 = ((-CO_ppm)/10^6)./Carbon_SUM + common_term.*CO_ppm./10^6;
THC_Term2 = ((-CO2_ppm)/10^6)./Carbon_SUM + common_term.*CO2_ppm./10^6;
THC_Term3 = ((CO2_ppm+CO_ppm)/10^6)./Carbon_SUM + common_term.*THC_ppm./10^6;
THC_Error = (THC_Term1.^2*Delta_CO.^2 + THC_Term2.^2*Delta_CO2.^2 +
THC_Term3.^2*Delta_THC.^2).^0.5;

Eff_Term1 = -EI_CO./(100.*propane_Hc./4.346 - EI_CO -
propane_Hc./4346.*EI_THC);
Eff_Term2 = -EI_THC./(1000-4346./propane_Hc.*EI_CO-EI_THC);
Eff_Error = (Eff_Term1.^2.*CO_Error.^2 + Eff_Term2.^2.*THC_Error.^2).^0.5;

Max_CO_Error  = max(CO_Error(4:end));
Max_NOx_Error = max(NOx_Error(4:end));
Max_THC_Error = max(THC_Error(4:end));
Max_Eff_Error = max(Eff_Error(4:end));

Mean_CO_Error  = mean(CO_Error(4:end));
Mean_NOx_Error = mean(NOx_Error(4:end));
Mean_THC_Error = mean(THC_Error(4:end));
Mean_Eff_Error = mean(Eff_Error(4:end));

StDev_CO_Error  = std(CO_Error(4:end));
StDev_NOx_Error = std(NOx_Error(4:end));
StDev_THC_Error = std(THC_Error(4:end));
StDev_Eff_Error = std(Eff_Error(4:end));

fprintf(['The max error for EI_THC is: '  num2str(Max_THC_Error*100) '%%\n'])
```

```
fprintf(['The max error for EI_NOx is: '  num2str(Max_NOx_Error*100) '%%\n'])
fprintf(['The max error for EI_CO is: '   num2str(Max_CO_Error*100) '%%\n'])
fprintf(['The max Efficiency error is: '  num2str(Max_Eff_Error*100) '%%\n'])
fprintf(['The mean error for EI_THC is: ' num2str(Mean_THC_Error*100)
'%%\n'])
fprintf(['The mean error for EI_NOx is: ' num2str(Mean_NOx_Error*100)
'%%\n'])
fprintf(['The mean error for EI_CO is: '  num2str(Mean_CO_Error*100) '%%\n'])
fprintf(['The mean Efficiency error is: ' num2str(Mean_Eff_Error*100)
'%%\n'])


%% Write File

Proceed = questdlg('Do you wish to output data to an Excel File?', 'Yes',
'No');

if length(Proceed) == 3

File_Name = inputdlg('What do you wish the Excel File to be called?');

THC_EI_data1 = [phi(4:4:end); EI_THC(4:4:end); EI_THC(5:4:end);
EI_THC(6:4:end); EI_THC(7:4:end)];
THC_EI_data = [[0 27.2 41.3 54.6 69.6]' THC_EI_data1];

CO_EI_data1 = [phi(4:4:end); EI_CO(4:4:end); EI_CO(5:4:end); EI_CO(6:4:end);
EI_CO(7:4:end)];
CO_EI_data = [[0 27.2 41.3 54.6 69.6]' CO_EI_data1];

NOx_EI_data1 = [phi(4:4:end); EI_NOx(4:4:end); EI_NOx(5:4:end);
EI_NOx(6:4:end); EI_NOx(7:4:end)];
NOx_EI_data = [[0 27.2 41.3 54.6 69.6]' NOx_EI_data1];

Efficiency_data1 = [phi(4:4:end); Efficiency(4:4:end); Efficiency(5:4:end);
Efficiency(6:4:end); Efficiency(7:4:end)];
Efficiency_data = [[0 27.2 41.3 54.6 69.6]' Efficiency_data1];

THC_ppm_data1 = [phi(4:4:end); THC_ppm(4:4:end); THC_ppm(5:4:end);
THC_ppm(6:4:end); THC_ppm(7:4:end)];
THC_ppm_data = [[0 27.2 41.3 54.6 69.6]' THC_ppm_data1];

CO_ppm_data1 = [phi(4:4:end); CO_ppm(4:4:end); CO_ppm(5:4:end);
CO_ppm(6:4:end); CO_ppm(7:4:end)];
CO_ppm_data = [[0 27.2 41.3 54.6 69.6]' CO_ppm_data1];

NOx_ppm_data1 = [phi(4:4:end); NOx_ppm(4:4:end); NOx_ppm(5:4:end);
NOx_ppm(6:4:end); NOx_ppm(7:4:end)];
NOx_ppm_data = [[0 27.2 41.3 54.6 69.6]' NOx_ppm_data1];


xlswrite(File_Name{1},THC_EI_data,'EI_THC')
xlswrite(File_Name{1},CO_EI_data,'EI_CO')
xlswrite(File_Name{1},NOx_EI_data,'EI_NOx')
xlswrite(File_Name{1},THC_ppm_data,'THC ppm')
```

```
xlswrite(File_Name{1},CO_ppm_data,'CO ppm')
xlswrite(File_Name{1},NOx_ppm_data,'NOx ppm')
xlswrite(File_Name{1},Efficiency_data,'Efficiency')
% Into xlswrite section
% xlswrite(File_Name,[['Max EI THC Error is:'],
Max_THC_Error],'EI_THC','A9:B9')
% xlswrite(File_Name,[['Max EI NOx Error is:'],
Max_NOx_Error],'EI_NOx','A9:B9')
% xlswrite(File_Name,[['Max EI CO Error is:'], Max_CO_Error],'EI_CO','A9:B9')
% xlswrite(File_Name,[['Max Efficiency Error is:'],
Max_Eff_Error],'EI_NOx','A9:B9')
%
% xlswrite(File_Name,[['Mean EI THC Error is:'],
Mean_THC_Error],'EI_THC','A10:B10')
% xlswrite(File_Name,[['Mean EI NOx Error is:'],
Mean_NOx_Error],'EI_NOx','A10:B10')
% xlswrite(File_Name,[['Mean EI CO Error is:'],
Mean_CO_Error],'EI_CO','A10:B10')
% xlswrite(File_Name,[['Mean Efficiency Error is:'],
Mean_Eff_Error],'EI_NOx','A10:B10')
% % Standard Deviation
% xlswrite(File_Name,[['StDev EI THC Error is:'],
StDev_THC_Error],'EI_THC','A11:B11')
% xlswrite(File_Name,[['StDev EI NOx Error is:'],
StDev_NOx_Error],'EI_NOx','A11:B11')
% xlswrite(File_Name,[['StDev EI CO Error is:'],
StDev_CO_Error],'EI_CO','A11:B11')
% xlswrite(File_Name,[['StDev Efficiency Error is:'],
StDev_Eff_Error],'EI_NOx','A11:B11')

else
    break
end
```

Bibliography

1. Mattingly, J. D., Heiser, W. H., Pratt, D. T., *Aircraft Engine Design*, 2nd edition, Reston, Virginia, AIAA, 2002.
2. Turns, Stephen R., *An Introduction to Combustion: Concepts and Applications* (3rd edition), New York, McGraw-Hill, 2011.
3. Lewis, G. D., Shadowen, J. H., and Thayer, E. B., "Swirling Flow Combustion," *Journal of Energy*, Vol. 1. 1977
4. Zelina, J., Sturgess, G. J. and Shouse, D. T., "The Behavior of an Ultra-Compact Combustor (UCC) Based on Centrifugally-Enhanced Turbulent Burning Rates," *40th AIAA/ASME/ SAE/ASEE Joint Propulsion Conference and Exhibit*, Fort Lauderdale, FL, 2004.
5. Wilson, J. D., and Polanka, M. D., "Reduction of Rayleigh Losses in a High G-Loaded Ultra Compact Combustor." *58th ASME International Gas Turbine Institute Exposition*, GT2013-94795, San Antonio, Texas, June 3-7, 2013.
6. Cottle, A. E. and Polanka, M. D., "Common Flow Source for a Full Annular Ultra Compact Combustor," *AIAA SciTech Conference*, AIAA-2015-0100, Orlando, FL, Jan 5-8, 2015.
7. Briones, A. M., Sekar, B., Shouse D.T., Blunck D.L., Thornburg H.J. Erdmann T.J., "Reacting Flows in Ultra-Compact Combustors with Combined-Diffuser Flameholder," *Journal of Propulsion and Power*, Vol. 31, No. 1, 2015
8. Spytek, C. J., "Application of an Inter-Turbine Burner using Core Driven Vitiated Air in a Gas Turbine Engine," *Proceedings of the ASME Turbo Expo 2012*, Copenhagen, Denmark, 2012.
9. SAE Aerospace, *ARP 1533: Procedure for the Analysis and Evaluation of Gaseous Emissions from Aircraft Engines*, SAE International Group, Rev. B, 2013
10 . Cottle, A.E, Polanka, M.D., Goss, L.P., Goss, C.Z. "Detailed Combustion Velocities and Temperatures under High G-Loading" ASME Turbo Expo 2016: Turbine Technical Conference and Exposition, Seoul, South Korea, July 13-17 2016, GT2016-56216
11. Zelina, J., Shouse, D. T., Neuroth, C., "High-Pressure Tests of a High-g, Ultra-Compact Combustor," *41st AIAA/ASME/SAE/ASEE Joint Propulsion Conference*, 10-13 July 2005, AZ, AIAA 2005-3779.
12. Briones, A. M., Sekar, B., Erdmann, T.J. "Effect of Centrifugal Force on Turbulent Premixed Flames," Jounral of Engineering for Gas Turbines and Power, Vol 137, Jan 2015
13. Erdmann, T.J., Burrus, D.L., Shouse, D.T., Gross, J.T., Neuroth, C., Caswell, A.W. "Experimental Studies of a High-g Ultra-Compact Combustor at Elevated Pressures and Temperatures," *54th AIAA SciTech Conference*, San Diego, CA, Jan 4-8 2016
14. Lefebvre, A. H., and Ballal, D. R. Gas Turbine Combustion: *Alternative Fuels and Emissions*, CRC Press, 3rd ed., Boca Raton, FL: 2010.
15. Sirignano, W. A., and Liu, F., "Performance Increases for Gas-Turbine Engines Through Combustion Inside the Turbine," *Journal of Propulsion and Power*, 15:1, pp.111-118, 1999.

16. Anthenien, R. A., Mantz, R. A. Roquemore, W. M., and Sturgess, G., "Experimental Results for a Novel, High Swirl, Ultra Compact Combustor for Gas Turbine Engines," *2nd Joint Meeting of the U.S. Sections of the Combustion Institute*, Oakland, CA March 2001.
17. Zelina, J., Shouse, D. T. and Hancock, R. D., "Ultra-Compact Combustors for Advanced Gas Turbine Engines," *49th ASME International Gas Turbine and Aeroengine Congress and Exposition*, Vienna, Austria, 2004.
18. Zelina, J. Greenwood, R.T., Shouse, D.T., "Operability and Efficiency Performance of Ultra-Compact, High Gravity (g) Combustor Concepts," *51st ASME International Gas Turbine and Aeroengine Congress and Exposition*, Barcelona, Spain, May 2006, GT2006-90119
19. Anthenien, R. A. and Zelina, J. "Experimental Results on the Turbulent Combustion Regimes within a Small-Scale Atmospheric Pressure High-g Combustor," *Spring Technical Meeting of the Central States Section: Combustion Institute*, Cleveland, OH, 2006.
20. Borghi, R. "Turbulent Combustion Modeling," *Progress of Energy and Combustion Science*, Vol 14, 1988, pp 245-292
21. K. D. LeBay, "Characterization of Centrifugally-Loaded Flame Migration for Ultra-Compact Combustors," Air Force Institute of Technology, Wright-Patterson Air Force Base, OH, 2011.
22. Bohan, B. T. and Polanka, M. D. "Analysis of Flow Migration in an Ultra-Compact Combustor," *J. Eng. Gas Turbines Power*, Vol 135:5, 2013.
23. Cottle, A.E, Polanka, M.D., Goss, L.P., Goss, C.Z. "Detailed Combustion Velocities and Temperatures under High G-Loading" ASME Turbo Expo 2016: Turbine Technical Conference and Exposition, Seoul, South Korea, July 13-17 2016, GT2016-56216
24. Wilson, J. D., Conrad, M, and Polanka, M. D. "Flame Structure Effects at High G-Loading," *Journal of Engine Gas Turbines Power*, Vol.136:10, May 2014.
25. Wilson, J. D. "Characterizing g-Loading, Swirl Direction, and Rayleigh Losses in an Ultra Compact Combustor," Air Force Institute of Technology, Wright-Patterson Air Force Base, OH, 2013.
26. Saad, M. "Compressible Fluid Flow," Englewood Cliff, NJ: Prentice-Hall, 1985.
27. Radtke, J. T., "Efficiency and Pressure Loss Characteristics of an Ultra-Compact Combustor with Bulk Swirl," Air Force Institute of Technology, Wright-Patterson Air Force Base, OH, 2007.
28. Conrad, M. M., Wilson, J. D., and Polanka, M. D., "Integration Issues of an Ultra-Compact Combustor to a Jet Turbine Engine," *49th AIAA/ASME/SAE/ASEE Joint Propulsion Conference*, San Jose, CA, 2013.
29 . Reneau, L.R., Johnston, J.P., and Kline, S.J., "Diffuser Design manual, Part I," Report PD-8, Stanford University, Sept. 1964.
30 Cottle, A.E, Polanka, M.D., Goss, L.P., Goss, C.Z. "Detailed Combustion Velocities and Temperatures under High G-Loading" ASME Turbo Expo 2016: Turbine Technical Conference and Exposition, Seoul, South Korea, July 13-17 2016, GT2016-56216
31. "Thermocouples: Using Thermocouples to Measure Temperature," *Omega Engineering Inc.*, Samford CT., http://www.omega.com/prodinfo/thermocouples.html [Accessed 23 Jan 2016]

32. Vilimpoc, V., Goss, L.P., Sarka, B. “Spatial Temperature-Profile Measurements by the Thin-Filament-Pyrometry Technique,” Optics Letters, Vol 13(2), Feb 1988
33. Goss, L.P. “SABER-RIG Experimental Campaign: Interim Report 2343” *Innovative Scientific Solutions, Inc.*, Dayton OH, Dec 2014
34 . Mossey, P.W., Shaffernocker, W. M., and Mulukutla, A. R., “1700°C Optical Temperature Sensor” 1986, *Final report NASA-CR-175108*.
35. Samuelsen, S., “Conventional Type Combustion” The Gas Turbine Handbook, U.S. Department of Energy, Office of Fossil Energy, National Energy Technology Laboratory, DOE/NETL-2006-1230. 2006.
36. LeBay, K. D., Polanka, M. D., and Branam R. D., “Characterizing the Effect of Radial Vane Height on Flame Migration in an Ultra Compact Combustor,” 56th ASME International Gas Turbine Institute Exposition, Vancouver, Canada, GT2011-45919, 2011.
37. Damele, C.J., Polanka, M.D., Wilson, J.D., and Rutledge, J.L. “Characterizing Thermal Exit Conditions for an Ultra Compact Combustor”, *2014 AIAA SciTech Conference*, AIAA-2014-0456, National Harbor, MD, Jan 13-17, 2014
38. Mawid, M. A., Thornburg, H., Sekar, B., Zelina, J. “Performance of an inter-Turbine Burner (ITB) Concept with Three-Different Vane Cavity Shapes”, *42nd AIAA/ASME/SAE/ASEE Joint Propulsion Conference*, Sacramento, CA, July 2006, AIAA 2006-4740
39. Thornburg, H., Sekar, B, Zelina, J., Greenwood, R. “Effect of Curved Radial Vane Cavity Arrangements on Predicted Inter-Turbine Burner (ITB) Performance”, *DoD High Performance Computing Modernization Program Users Group Conference*, 110-119, June 2007
40. Seinfeld, J. H., *Atmospheric Chemistry and Physics of Air Pollution*, John Wiley & Sons, New York, 1986.
41. Sturgess, G. J., Zelina, J., Shouse, D. T., Roquemore, W. M., “Emissions Recution Technologies for Military Gas Turbine Engines,” *Journal of Propulsion and Power*, Danvers, MA, March 2005. Vol 21.
42. SAE Aerospace, *ARP 1533: Procedure for the Analysis and Evaluation of Gaseous Emissions from Aircraft Engines*, SAE International Group, Rev. B, 2013.
43 . Fenimore, C. P., “Formation of Nitric Oxide in Premixed Hydrocarbon Flames,” *Proceeding of the Thirteenth International Symposium on Combustion, Combustion Inst.*, Pittsburgh, PA, 1971.
44. Anderson, W., Radtke, J., King, P. I., Thornburg, H., Zelina, J., and Sekar, B., “Effects of Main Swirl Direction on High-g Combustion,” *44th AIAA/ASME/SAE/ASEE Joint Propulsion Conference and Exhibit*, Hartford, Connecticut, AIAA-2008-4954, 2008.
45. C. J. Spytek, "Application of an Inter-Turbine Burner using Core Driven Vitiated Air in a Gas Turbine Engine," *Proceedings of the ASME Turbo Expo 2012*, Copenhagen, Denmark, 2012.
46. Jeschke, P., Penkner A., “A Novel Gas Generator Concept for Jet Engines Using Rotating Combustion Chamber,” *Journal of Turbomachinery*, Vol 137, July 2015.
47. Damele, C.J., “Operational Characteristics of an Ultra Compact Combustor”, Air Force Institute of Technology, Wright-Patterson Air Force Base, OH, 2014.

48. Cottle, A.E., Polanka, M.D. “Numerical and Experimental Results from a Common-Source High-g Ultra-Compact Combustor,” *Proceedings of ASME Turbo Expo 2016: Turbine Technical Conference and Exposition*, Seoul, South Korea, June 2016, GT2016-56215
49 . Parks, A.K., “Desensitizing Flame Structure and Exhaust Emissions to Flow Parameters in an Ultra-Compact Combustor,” Air Force Institute of Technology, Wright-Patterson Air Force Base, OH, 2012.
50 . Personal correspondence with Cottle, A.E. (PHD Student), Jun 2015 – Feb 2016.
51 . Personal correspondence with Goss, L. (PHD) and Goss, C., ISSI, Jan 2016.
52 . Moffat, R. J., “Contributions to the Theory of Single-Sample Uncertainty Analysis,” Journal of Fluids Engineering, vol. 104, 1982.
53 . Heneghan, S.P., Frayne, C.W. “ Propagation of Errors for Combustion Analysis Using Emission Analyzer Data,” 38th Aerospace Sciences Meeting & Exhibit, Reno, NV, Jan 2000, AIAA-2000-0955
54 . Erdmann, T.J., Burrus, D.L., Shouse, D.T., Gross, J.T., Neuroth, C., and Caswell, A.W., “Experimental Studies of a High-g Ultra-Compact Combustor at Elevated Pressures and Temperatures,” *54th AIAA Aerospace Sciences Meeting*, San Diego CA, 2016, AIAA 2016-0446
55 . Cottle, A.E., Gilbert, N.A., Polanka, M.D., Goss, L.P. “Mechanisms for Enhanced Flow Migration from an Annular, High-g Ultra Compact Combustor,”*2016 AIAA SciTech Conference*, San Diego, CA, Jan 2016, AIAA 2016-1392
56 . Conrad, M. M., “Integration of an Inter Turbine Burner to a Jet Turbine Engine”, Air Force Institute of Technology, Wright-Patterson Air Force Base, OH, 2014.

REPORT DOCUMENTATION PAGE

Form Approved
OMB No. 074-0188

1. REPORT DATE *(DD-MM-YYYY)*	2. REPORT TYPE	3. DATES COVERED *(From – To)*
24-03-2016	Master's Thesis	January 2015 – March 2016

TITLE AND SUBTITLE

Enhanced Flow Migration in Full Annular Ultra Compact Combustor

5a. CONTRACT NUMBER

5b. GRANT NUMBER

5c. PROGRAM ELEMENT NUMBER

6. AUTHOR(S)

Gilbert, Nicholas A., Captain, USAF

5d. PROJECT NUMBER

5e. TASK NUMBER

5f. WORK UNIT NUMBER

7. PERFORMING ORGANIZATION NAMES(S) AND ADDRESS(S)

Air Force Institute of Technology
Graduate School of Engineering and Management (AFIT/ENY)
2950 Hobson Way, Building 640
WPAFB OH 45433-8865

8. PERFORMING ORGANIZATION REPORT NUMBER

AFIT-ENY-MS-16-M-211

9. SPONSORING/MONITORING AGENCY NAME(S) AND ADDRESS(ES)

Dr. Chiping Li
875 N Randolph St
Ste 325 Rm 3112
Arlington AFB VA, 22203
426-8574, chiping.li@us.af.mil

10. SPONSOR/MONITOR'S ACRONYM(S)

AFSOR/RTA

11. SPONSOR/MONITOR'S REPORT NUMBER(S)

12. DISTRIBUTION/AVAILABILITY STATEMENT

DISTRUBTION STATEMENT A. APPROVED FOR PUBLIC RELEASE; DISTRIBUTION UNLIMITED.

13. SUPPLEMENTARY NOTES

This material is declared a work of the U.S. Government and is not subject to copyright protection in the United States.

14. ABSTRACT

Since combustion efficiency in modern jet engines has stabilized, attention has turned to improving the combustor by improving the thrust-to-weight ratio. The Ultra Compact Combustor (UCC) is a means to reduce the weight of the combustor while ensuring exhaust meets increasingly stringent government emission standards. Combustion occurs within the UCC under a g-load in the circumferential direction, which maintains combustion efficiency while decreasing axial combustor length. Previous analysis optimized the combustion chamber flame characteristics with a common upstream air source. Previously, issues for the UCC were inspired by integration into a traditional axial turbojet. The focus of this investigation was to increase migration of the hot combustion products to the middle of the hybrid vane's exit plane. This was done by varying the dimensions of the UCC combustion cavity, the air driver configuration into the cavity, as well as adding a radial vane cavity into the center-body guide vanes. In order to accomplish this, a temperature measurement collection technique called thin filament pyrometry was implemented to obtain high fidelity data. Also, the AFIT UCC required an accurate initial emissions baseline to be established; this baseline consisted of collecting five different gaseous species for each considered geometry. These data points were then compared against each other and previously collected temperature values. Optimal exit efficiency and temperature profiles were obtained through modifications to the hybrid vane passage and the air driver geometry.

15. SUBJECT TERMS

Ultra Compact Combustion, Thin Filament Pyrometry, Emissions

16. SECURITY CLASSIFICATION OF:			17. LIMITATION OF ABSTRACT	18. NUMBER OF PAGES	19a. NAME OF RESPONSIBLE PERSON
a. REPORT	b. ABSTRACT	c. THIS PAGE			Marcus D. Polanka, AFIT/ENY
U	U	U	UU	263	19b. TELEPHONE NUMBER *(Include area code)* (937) 255-6565, ext 4714 (marc.polanka@afit.edu)

Standard Form 298 (Rev. 8-98)
Prescribed by ANSI Std. Z39-18